UNIVERSITY of CALIFORNIA

Santa Barbara

A Search for Dark Matter Production with Jets and Missing Momentum Signature in Proton-Proton Collisions at 7 TeV

A dissertation submitted in partial satisfaction of the requirements for the degree of

Doctor of Philosophy

in

Physics

by

Sue Ann Koay

Committee in charge:

Professor Joseph Incandela, Chair

Professor David Stuart

Professor Mark Srednicki

June 2011

The dissertation of Sue Ann Koay is approved:

Professor David Stuart

Professor Mark Srednicki

Professor Joseph Incandela, Chair

June 2011

A Search for Dark Matter Production with Jets and Missing Momentum Signature in Proton-Proton Collisions at 7 TeV

by

Sue Ann Koay

For my father, who taught me to look at the horizon when I drive.
For my mother, who is the source of my persistence.
For my teachers, who asked me to think and not just to know.
For my mentor, who bade me run as fast and far as I can.
For my friends, who reminded me to be human.

Curriculum Vitæ

Sue Ann Koay

June 2011

Education

2011 Ph. D. (Physics), University of California, Santa Barbara
2002 B. S. (Physics) and B. S. (Computer Science), San Jose State University (*summa cum laude*)

Publications

Di-lepton $t\bar{t}H$ at the CMS, CERN-CMS-CR-2006-058, Geneva, September 2006. Hadron Collider Physics Symposium 2006 at Durham, NC, USA.

Observability of higgs produced with top quarks and decaying to bottom quarks. *Journal of Physics G: Nuclear and Particle Physics*, 34(5):N221, 2007. URL http://stacks.iop.org/0954-3899/34/i=5/a=N03.

Data driven estimation of the Z→invisible background for the early SUSY searches. *CMS-PAS-SUS-08-002*, 2008. URL https://twiki.cern.ch/twiki/bin/view/CMS/SusyAnalysisZtoinvisible

Search for new physics with the jets and missing momentum signature at the LHC. *CMS-PAS-SUS-10-005*, 2010. URL https://twiki.cern.ch/twiki/bin/view/CMS/SUS10005

ABSTRACT

A Search for Dark Matter Production with Jets and Missing Momentum Signature in Proton-Proton Collisions at 7 TeV

by

Sue Ann Koay

One of the largest mysteries in astronomy is that a vast amount of "dark matter"—more than four times as much as ordinary matter—is required to explain several observations and yet remain within Newtonian laws of gravitation. If dark matter does in fact exist, it should be possible to produce it at a high-energy collider experiment like the Large Hadron Collider (LHC) experiment. This document describes such a search utilizing $36\,\mathrm{pb}^{-1}$ integrated luminosity of LHC data collected by the Compact Muon Solenoid (CMS) detector, with fully hadronic jets plus missing transverse momentum signature. The search regions are designed to be simple, with high efficiencies for a wide variety of Beyond Standard Model signals that have dark matter candidate particles in the event final state. Standard Model processes with high cross-sections like top quark pair-production, W and Z boson production in conjunction with jets, as well as multi-jet production, all form significant backgrounds to these search regions, and are estimated using data-driven techniques. In particular, a novel method for predicting the multi-jet background has been developed, which is by construction highly safe against contamination from other processes including any signals that may be present. This method, called Rebalance and Smear, first unfolds events in an inclusive data sample back to a well-balanced, particle-level description of the jets per event, then smears the momenta of these jets to simulate detector-related measurement effects as would cause multi-jet events to contribute to the search regions. The collider data sample collected in 2010 is seen to be compatible to within one standard deviation of the predicted background yields in all search regions. Limits are set in some slices of the Constrained Minimal Supersymmetric Standard Model parameter space, which extend to gluino and squark masses of 700 GeV in some regions and gluino masses nearly up to 500 GeV for more or less arbitrary squark masses. The results are also interpreted in terms of Simplified Model Spectra signals, which furthermore provide an intuitive language in which strengths and weaknesses of the search are diagnosed.

Contents

Part I

Introduction to the Experiment

Chapter 1

Looking Beyond the Standard Model of Particle Physics

This document describes a search for Beyond Standard Model physics (BSM) excesses of events with jets and missing momentum in the final state, using $36\,\mathrm{pb}^{-1}$ integrated luminosity of data collected by the Compact Muon Solenoid (CMS) detector at the Large Hadron Collider (LHC) experiment. But first: why look for new physics? Why with such a signature? Why at a collider experiment? These questions go back to a review of the twenty-first century understanding of microscopic laws of the universe, and discontent with said understanding.

1.1 Theories of the Quantum World

One of the most disturbing axioms of the disturbing science of Quantum Mechanics (QM) is the wave-particle duality of matter/energy. Since this, particles can no longer be seen as simply very tiny versions of objects like those in daily human experience, obeying the mechanical laws of a clockwork universe. Instead the "fundamental stuff" is rather a quantum mechanical wavefunction that describes the probability to find one or more particles in a particular state, and the locality/quantization of interactions with this system (expected from experiment) is demoted to being properties of observations made on its wavefunction. The dynamics of a quantum system is predicted by Schrödinger's equation, $i\hbar(\partial/\partial t)\psi(\vec{x},t) = \mathbf{H}\psi(\vec{x},t)$, which governs the time evolution of the wavefunction $\psi(\vec{x},t)$ given a Hamiltonian operator $\mathbf{H}$. Here $\vec{x}$ is the vector of spatial coordinates, t the time coordinate, and operators are denoted in bold type.

The Quantum Field Theory (QFT) treatment of particle physics incorporates special relativity into the quantum description of particles, at cost of another layer of abstraction. Rather than directly trying to construct an equation of motion for $\psi(\vec{x},t)$ that satisfies Lorentz invariance and still maintains a wavefunction interpretation for ψ, one works with an intermediate (Lorentz scalar) field $\varphi(\vec{x},t)$. This field is required to satisfy relativistic equations of motion like the Klein-Gordon equation $(-\partial^2 + m^2)\varphi(\vec{x},t) = 0$,

which would not have worked for ψ due to pathologies like solutions that do not preserve unitarity versus time and that even have negative probability densities. The trick is to notice that the physical interpretation can be deferred: φ is instead to be regarded as a field of *coordinates*—in the sense of canonical variable conjugate to momentum—and $(\vec{x},t)$ simply labels that specify a particular $\varphi(\vec{x},t)$ in space-time. The prescription that follows is parallel to canonical quantization in QM, where one takes a classical Hamiltonian which is some function of coordinates x_i and momenta p_i as obtained from the Legendre transformation of the Lagrangian, and promotes them to operators $x_i \to \mathbf{X}_i$ and $p_i \to \mathbf{P}_i$ satisfying quantum commutation relations. In QFT, the same is done using the Hamiltonian density $\mathscr{H} = \pi\dot{\varphi} - \mathscr{L}$, which is a function of the coordinate field φ and momentum field $\pi = \partial\mathscr{L}/\partial\dot{\varphi}$ obtained from the Lagrangian density $\mathscr{L}$. These are densities because $\varphi = \varphi(\vec{x},t)$, so to obtain a total energy interpretation of the Hamiltonian one needs to integrate over all of space-time: $H = \int d^3x\,dt\,\mathscr{H}(\vec{x},t)$. This Hamiltonian is then quantized by promoting φ and π into fields of operators. But what has been gained by all this machinery? The φ field still suffers from the problems indicated above, and there is still no prescription for what is a physical state.

An understanding of H is obtained by considering its form. The Lagrangian density[1] consists of at least a kinematic piece $\mathscr{L} = -\partial^\mu\varphi\partial_\mu\varphi - m^2\varphi^2 + \ldots$, where the repeated μ indices indicate summation over all four space-time coordinates. After plugging in the expansion of φ in terms of the complete set of plane-wave solutions to the Klein-Gordon equation, $\varphi = \int \widetilde{dk}\,[a(\vec{k})\exp(i\vec{k}\cdot\vec{x} - i\omega t) + a^*(\vec{k})\exp(i\vec{k}\cdot\vec{x} + i\omega t)]$ where $\omega = (|\vec{k}|^2 + m^2)^{1/2}$ and $\widetilde{dk} \equiv d^3k/(2\pi)^3 2\omega$ is a Lorentz-invariant differential element, one obtains a simple form $H = \int \widetilde{dk}\,\omega\,[a(\vec{k})a^*(\vec{k}) + a^*(\vec{k})a(\vec{k}) + \ldots]$ [83]. This is evidently the Hamiltonian for an infinite series of harmonic oscillators, where the quantized operators $\mathbf{a}^\dagger(\vec{k})$ and $\mathbf{a}(\vec{k})$ respectively create and annihilate one quantum (particle) with momentum $\vec{k}$ (relativistic energy ω); also $\mathbf{a}^\dagger$ and $\mathbf{a}$ must satisfy commutation relations in order for the theory to be nontrivial. Lastly, since the number operator $\mathbf{n}(\vec{k}) \equiv \mathbf{a}^\dagger(\vec{k})\mathbf{a}(\vec{k})$ commutes with the Hamiltonian, the set of all possible states with definite numbers of particles forms a basis, and the number eigenvalues are of course time-independent. So long as one does not try to concoct states with negative numbers of particles, one does not run into the problem with negative probability densities. This can be enforced by always starting from a vacuum state $|0\rangle$ that is destroyed by any annihilation operator, and from which number eigenstates are obtained by applying some series of creation operators.

In other words, the QFT framework places the burden of dynamics on operator fields—which are allowed to satisfy equations of motion in flexible ways—yet maintains proper behavior of physical states by constructing them from vacua via sensibly interpreted particle creation/annihilation operators. This is a trick that neatly sidesteps several problems that arise whenever the equation of motion has to be generalized to

[1] It can be shown that the Klein-Gordon equation follows from this form of $\mathscr{L}$ (without extra terms) in the usual way i.e. by requiring that the variation of its action with respect to φ to vanish.

higher orders of space-time derivatives, but is also a somewhat profound shift in views of what constitutes fundamental building blocks of reality. The QM question is on how particular quantum *states* evolve under some universal set of laws. The QFT question is on possible configurations of underlying quantum fields, which in a sense concerns what combinatorial and dynamical rules *observations* (operators) must obey.

It is not the task of this chapter to delve into the mathematics of particle physics, but only to provide a global enough overview of the concepts and issues to understand the motivation of this research. There is in fact a beautifully intuitive (and yet calculationally equivalent!) way to think about the interactions predicted by quantum field theories—Feynman diagrams [84]—that will be relied on here. Figure 1.1.1 summarizes the main concepts of the diagrammatic approach. First, the Lagrangian gives rise to two types of building blocks: the *propagator* from the free-field piece $-(\partial^\mu \varphi^\dagger \partial_\mu \varphi + m^2 \varphi^\dagger \varphi) \to (k^2 + m^2)\,\mathbf{a}^\dagger \mathbf{a}$ which describes the kinematic properties of the φ field, and the *interaction vertices*. For example, the Lagrangian could have contained a term like $-(\lambda/4)(\varphi^\dagger \varphi)^2$, where λ is the coupling strength of this 4-way interaction. The vertex for this term is shown in Figure 1.1.1(b), where each of the solid lines represent one instance of the φ field. The arrows are used for fermions, where there is a distinction between particle (flowing one way into the vertex) and anti-particle (flowing the opposite way). Each of these vertices "cost" a factor of λ to create. As another example, the theory could contain another (vector) field A_μ, which may couple with the φ field via the terms $ieA_\mu[(\partial^\mu \varphi^\dagger)\varphi - \varphi^\dagger \partial^\mu \varphi]$ in the Lagrangian. The reason for this form is motivated below, but anyway this gives rise to a vertex shown in Figure 1.1.1(a). In this case the derivatives are converted to a coupling that depends on the momenta k and k' of the $\varphi^\dagger$ and φ fields. Finally, out of these propagators and vertices one can construct scattering diagrams like Figure 1.1.1(c), which describe how a set of initial states interact and produce a set of final states. The convention of time flowing from left to right in Feynman diagrams is used throughout this document. This means that the incoming states are a $\varphi^\dagger$ particle and anti-particle φ, which then scatter into three final states A, $\varphi^\dagger$ and φ. Such diagrams where none of the lines form a closed loop are called "tree level", and are to be contrasted to diagrams involving one or more loops like Figure 1.1.1(d). Evidently both (c) and (d) are of the same perturbative expansion order in the theory, i.e. $O(e^3)$, but it turns out that (d) is much more difficult to handle mathematically. It therefore happens that in the industry often only the tree-level diagrams are evaluated, and then only to leading order (LO) in the number of vertices. Even when more vertices are included, so long as the computation remains tree level, it cannot truly be next-to-leading order (NLO). As seen in Section 4.1 however, there are approximation methods that allow one to do significantly better than LO.

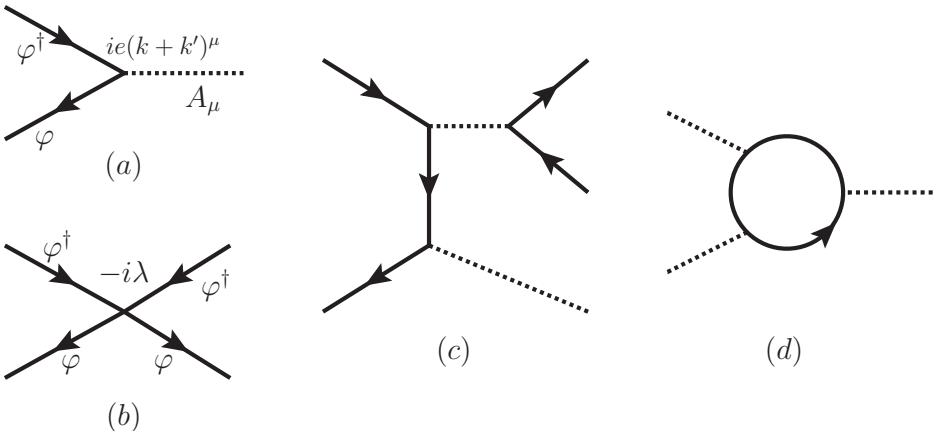

Figure 1.1.1: Example Feynman diagrams for a charged scalar field (φ) theory with a gauge field (A_μ). (a) and (b) are the interaction vertices. (c) and (d) are two possible $O(e^3)$ diagrams.

1.2 The Standard Model of Particle Physics (SM)

The SM is traditionally formulated as a relativistic quantum field theory. The number of quantum fields involved, whether they are commuting or anti-commuting, and their group theoretical properties, must all be experimentally constrained. The present theory consists of the smallest number of fields required to explain all observed particles and forces by which they interact, plus one non-observed field—corresponding to the Higgs particle—which provides a mechanism for explaining the masses of all particles[2]. Coincidentally or not, all these fields cover the four simplest irreducible representations of the Lorentz group, i.e. scalar, left- and right-handed spinors, and vector representations. The main ingredients in the construction of the SM are only sketched here:

Gauge invariant Lagrangians

Gauge invariance is not a fundamental requirement, but rather one that has been empirically found to fit observation, and the entire SM is comprised of gauge-invariant Lagrangians. Why local gauge invariance implies the existence of additional gauge fields can be seen schematically from the above scalar field theory example, pretending for a moment that φ had been a complex scalar field. The desire is for $\mathscr{L}$ to remain invariant under a local transformation $\varphi(x) \to \varphi(x)\exp[i\alpha(x)]$ for some function of space-time $\alpha(x)$, but it is easy to see that the derivative acting on φ would always produce an extra term via $\partial\varphi \to (\partial\varphi)\exp[i\alpha] + \varphi\exp[i\alpha]\cdot(i\partial\alpha)$. This is circumvented by trading in the coordinate derivative ∂_μ for a covariant derivative $\partial_\mu - ieA_\mu$, where $A_\mu(x) \to A_\mu(x) + \partial\alpha(x)/e$ under the local gauge transformation. The gauge field $A_\mu(x)$

[2]There are also many Higgs-less alternatives, but they are beyond the scope of this document.

that was required to compensate for the coordinate dependence of the gauge transformation appears in the Lagrangian in the form of terms like $-ie(\partial^\mu \varphi^\dagger) \cdot A_\mu \cdot \varphi$, thereby "naturally" mediating interactions between φ fields.

Group structure of matter and gauge fields

SM fields fall into two categories, one being matter fields that are roughly speaking what one puts in by hand, as distinct from gauge fields that arise from requiring that the theory remains invariant under local gauge transformations. It has long been experimentally established that there are two classes of matter fields: (a) leptons, which interact via weak and electromagnetic forces; and (b) quarks, which additionally interact via the strong force. Even within these classes they are not universal in their interactions, but rather seem to be grouped in some way. There are six flavors each of leptons and quarks, arranged in three increasingly heavy generations:

	Leptons		**Quarks**	
Generations	$\begin{pmatrix} e \\ \nu_e \end{pmatrix}$	electron electron neutrino	$\begin{pmatrix} u \\ d \end{pmatrix}$	up down
	$\begin{pmatrix} \mu \\ \nu_\mu \end{pmatrix}$	muon muon neutrino	$\begin{pmatrix} c \\ s \end{pmatrix}$	charm strange
	$\begin{pmatrix} \tau \\ \nu_\tau \end{pmatrix}$	tau tau neutrino	$\begin{pmatrix} t \\ b \end{pmatrix}$	top bottom/beauty

The final accounting is that the SM has gauge structure $SU(3)_c \otimes SU(2)_L \otimes U(1)_Y$, which are the color, weak isospin, and hypercharge gauge groups respectively. All matter fields are spin $1/2$ fermions and therefore come with anti-particles, whereas all gauge fields are spin 1 bosons and are their own anti-particles. The eight gauge bosons of $SU(3)_c$ are massless and are called gluons (g), and only quarks (q) have color charge; collectively they are referred to as the strong sector of the SM. The $SU(2)_L \otimes SU(1)_Y$ electroweak sector is more complicated because of observations that the gauge bosons mediating weak interactions must have large masses, whereas the photon which mediates electromagnetic interactions remains massless. Therefore the $SU(2)_L \otimes SU(1)_Y$ must be a broken symmetry at least at presently accessible energies, a mechanism for which is explained below. The gauge bosons of the broken theory are the massive $\mathrm{W}^\pm$ (charged) and Z (neutral), and the massless photon (γ).

Electroweak symmetry breaking

Mass terms for gauge bosons cannot be directly inserted into the Lagrangian because they violate gauge invariance. The Higgs mechanism is one of the simplest ways to

circumvent this problem, and starts by adding a complex scalar field ϕ to the $SU(2)_L \otimes SU(1)_Y$ sector of the Lagrangian. This means that the addition should have the form $\mathscr{L}_h = (D_\mu \phi^\dagger)(D_\mu \phi) - V(\phi)$, where D_μ is the covariant derivative that ensures that the ϕ field satisfies the $SU(2)_L \otimes SU(1)_Y$ gauge invariance, and $V(\phi)$ is some potential function that must be polynomial in $\phi^\dagger \phi$ in order to be sufficiently well behaved. If the minimum of V is at $\phi = 0$, then all that this does is to add an (unobserved) field to the theory. If the minimum of V is at $\phi = v \neq 0$ however, one must instead re-express ϕ in terms of an equivalent field h that is in fact zero at the location of the potential minimum: $\phi(x) = v + h(x)$; recall that all fields are eventually interpreted as creation/annihilation operators that act on the vacuum state—and the true ground state is at v. There is however a delicacy here that has been hidden by the over-simplistic discussion: ϕ is not only a complex scalar field, it also has $SU(2) \otimes SU(1)$ indices. This gives a total of four degrees of freedom, only one of which is constrained by the condition $V =$ minimum. Even though a particular choice of v can be made, it is degenerate with a 3-dimensional manifold of equally good minima. But these directions in which the theory is rotationally invariant are exactly what local gauge invariance allows gauging away, so it is without loss of generality that v and $h(x)$ can both be chosen to be real. The last detail to note is that v generates mass term proportional to v^2 for the gauge fields of $SU(2)_L \otimes SU(1)_Y$, when the gauge field terms in D_μ act on the v piece in $\phi(x)$. The same Higgs field $h(x)$ can be used to insert mass terms for the fermion fields into the theory, although the values of these masses are not calculable because of the unknown coupling factor.

1.3 Reasons for Dissatisfaction

Despite having successfully predicted and explained a wide variety of experimental results throughout the past forty years, there is also a clear case to be made for the SM not being the end of the quest for a fundamental theory of particle physics. Theoretical dissatisfactions include the inability to incorporate gravitational forces into the field theory framework, the weak vs. Planck scale hierarchy problem, the fact that 19 arbitrary parameters are required, and a desire to embed the SM in some larger theory so that the strong and electroweak (EWK) forces may be unified at some high mass scale. On the experimental side, neutrino oscillations and masses are not correctly predicted by the SM, the Higgs boson remains undiscovered, and there are no viable SM explanations for the abundance of dark matter/energy. It is the latter that this search is designed to probe.

Regardless of theoretical preferences, there is little dispute that astronomical data points to features of the universe that seem to be beyond the spectrum of particles and/or forces known in the SM. Almost eighty years ago, observations of the orbital velocities of galaxies in clusters provided the first experimental indication that most of the inferred mass in such a cluster is in fact not accounted for by luminous matter.

Decades later, the rotation curves of galaxies provided some of the most striking and direct evidence for this unseen source. These curves, defined as the circular velocities of stars/gasses as a function of distance from the galaxy center, deviate strongly from Newtonian gravity expectations given the observed matter density profiles. In particular, these curves flatten out at large radii instead of the $1/\sqrt{r}$ fall-off expected beyond the visible extent of the galaxies, which can be interpreted as the presence of a spherical halo of *in*visible a.k.a. "dark" matter. Present-day measurements of cosmic microwave background fluctuations in fact put only a small fraction (4.5%) of the total energy budget of the universe as being comprised of ordinary (baryonic) matter; instead 22% is thought to be dark matter, and the rest dark energy [54]. Of course, the popular label "dark matter" hardly means that this non-understood physics can only be resolved via the introduction of new particles or forms of matter into the theory. One may instead explore modifications to the laws of gravitation, e.g. as motivated by quantum corrections [74]. There are also schools that question the treatment of gravity in the same footing as the other fundamental forces of physics, instead regarding it as an "emergent" (macroscopic) law arising from entropic considerations [87]. One of the most conclusive evidences for the particle nature of so-called dark matter would be observations of behavior decoupled from that of visible matter. Hints of this are found in the merger dynamics of a class of colliding galaxies called "bullet-like", which have a clear separation of the visible baryonic component and the dark matter component as inferred from, say, gravitational lensing. [20] presents one such observation of a $> 4\sigma$ significance level separation between the two components of the MACS J0025.4-1222 cluster, as well as an upper bound on the interaction cross-section of dark matter indicating that it is almost collisionless; however tests of whether these observations are still consistent with modified gravity theories are still pending. Large-scale statistical analyses [64] of the average displacement between ordinary and dark matter components of galaxy clusters are also planned, a nonzero result of which would indicate differences in the collision cross-sections of the two types of matter, thereby possibly disfavoring models with non-particulate dark matter.

A natural complement to astronomical and cosmological data are experiments that attempt to produce dark matter and/or other associated BSM particles in a laboratory setting. One broad-range technique is to collide pairs of particles, out of which BSM states may be produced as allowed by their couplings to the incoming SM states and the center-of-mass energy at which the collision occurs. This cannot probe a BSM sector that is completely disassociated ("hidden") and only interacts via gravity, because the production cross-section would be infinitesimal. However if the BSM sector does couple to the SM sector in some nontrivial way, the constraint is then the required center-of-mass energy to produce these new particles. The mass scale at which to expect new physics can be estimated by considering the dark matter relic density, but this depends rather strongly on the nature of the dark matter candidate (DMC) itself. What is known is that the dark matter particle mass should be heavier than a few keV in order for it to be "cold", a.k.a. non-relativistic at the time of structure formation in the

universe; this is because without the presence of relatively slow-moving dark matter, ordinary matter would have had too high of a temperature and pressure to collapse into stars. A mostly model-independent but rough upper bound on dark matter particle mass is given by [48] to be around 34 TeV (using as input more modern WMAP data [19]), though for the weakly interacting variety the most motivated range is around the weak scale i.e. $\sim 100\,\text{GeV}$. Nevertheless, this wide range of possibilities motivates a desire to probe as high values as possible of center-of-mass energy in collision experiments. Furthermore, hadron collisions provide several advantages over e^+-e^- collisions in terms of discovery potential when the new particle spectrum is unknown, as will be discussed in Section 2.

1.4 Some "Popular" BSM Theories

If astronomical data are to be explained with particulate dark matter, the discussion above indicates that there are few experimental constraints on its nature, other than that it should not be electrically or strongly charged (which would make it visible), and that at least one species of dark matter should be non-relativistic and with mass in the keV-34 TeV range. This eliminates the one possibility already predicted by the SM—the neutrino—as the dominant component of dark matter. Astronomical observations [46] also rule out other "mundane" sources—black holes, neutron stars, faint stars, brown/white dwarf stars, and other low-visibility objects such as diffuse hot gases, cool neutral hydrogen, lumps/snowballs of hydrogen, rocks, and dust.

Fortunately, there has been no lack of speculation as to how the Standard Model of particle physics can be extended to include new particles and/or forces. Much of this work is motivated to address the theoretical dissatisfactions with the SM as mentioned above, but the ability of a proposed BSM theory to address the dark matter problem is nevertheless a strong constraint. One may roughly consider the following categories of extensions based on how ambitiously they modify the SM:

1.4.1 No change to the SM

Rather than modify the structure of microscopic physics as known to the SM, one may instead question the laws of space-time (relativity) that in the first place alluded to the presence of "dark matter". This is in fact probably a rather natural suspicion, given the fundamentally different nature and scale of gravity compared to the other known forces. In this direction people have attempted modifications to the laws of gravitation, as well as speculations that there is *no* microscopic gravity, as mentioned in the previous section. Direct testing of such hypotheses is however far beyond the scope of this document.

1.4.2 Addressing of specific SM issues/possibilities

Given that the SM neutrino mass is inadequate to explain the bulk of dark matter, one may simply ask whether there is some fourth generation of more massive neutrinos. These would have to be "sterile" in the sense of not having any SM interactions other than mixing with other neutrino species. Recently the MiniBooNE neutrino oscillation experiment observed a 3σ excess in the number of electron neutrinos [6], which might indicate the existence of sterile neutrinos. Other DMCs of note include so-called axions, which have been proposed to answer the question of why strong interactions are not experimentally seen to break CP symmetry even though allowed to by SM theory. Accelerator-based searches have already ruled out large couplings of axions to the rest of matter, although possibilities of "invisible axions" remain and are actively being looked for by dedicated experiments [77]. There are a plethora of other possibilities, some introduced particularly to explain dark matter, and not listed here. Instead it is only noted that many of these sources would seem to require more specific experimental setups to detect than afforded by the generic collider experiment described in this document.

1.4.3 Incorporation of the SM into a larger theory

The remaining class of SM extensions are much grander in scale, i.e. an overhaul of the theory to address conceptual discomforts and desires. Here, one overarching desire is to construct a "simple" fundamental theory out of which the various known forces and elementary particles arise as a low-energy effective theory—i.e. *without* the need for many arbitrary parameters and degrees of freedom in the particle zoo. The near-unification of the strong and electroweak gauge couplings in the 10^{14}-10^{15} GeV mass scale serves as a tantalizing hint that one may be able to construct a "grand unified" theory, including some symmetry breaking factor that causes an eventual phenomenological distinction of the three forces as well as the observed spectrum of particles in the low-energy limit. Such theories may also attempt to relate quark and lepton fields, explain why there are three generations of fermions, and so forth. They are often also required to solve the hierarchy problem, which concerns the Higgs mass obtaining large corrections from higher-order (loop) diagrams. In general, the correction to the squared Higgs mass has at least a quadratic dependence on the mass of the heaviest particle that it couples to, which is a problem since there are strong theory-experiment reasons to expect the Higgs mass to be small i.e. near the electroweak scale. This is often prohibitive when trying to incorporate BSM sectors into the theory[3], because then to maintain a small Higgs mass, either the allowed new particle masses must remain similarly small, or cancellations must somehow happen in the loop corrections to the Higgs mass... or

[3] Of course, there will not be this problem if the Higgs field simply does not couple to any of the high-mass BSM particles, even indirectly. However this requires the high-mass BSM sector to be completely dissociated from the SM sector, which is itself a strong constraint on the allowed structure.

the Higgs mechanism should simply not be required. In light of these theoretical considerations, some of the most widely pursued BSM models (that have DMCs detectable via collider experiments) are listed below:

Supersymmetry (SUSY) [63]

These class of models may be seen as arising from the observation that quantum corrections to the Higgs mass come with a negative sign if the particle in the loop is a fermion, versus a positive sign if the virtual particle is instead a boson. That is, if only each fermion (boson) in the theory came with a bosonic (fermionic) counterpart that had the same coupling to the Higgs boson, the loop corrections to the Higgs mass would cancel exactly. A symmetry that transforms particles of one spin to other particles that differ by half a unit of spin is called a "supersymmetry", and the counterparts are called "superpartners". Since none of the SM particles are suitable to be mutual superpartners, this means that the smallest supersymmetric model—the Minimal Supersymmetric Standard Model (MSSM)—must contain at least a doubling in the number of particles. The new particles introduced to the theory are referred to collectively as "sparticles", and a short exposition of the MSSM particle content is given in Section 1.5.1. One also typically adds "matter parity" or equivalently "R-parity" conservation to the MSSM in order to preserve baryon and lepton numbers, in particular since the proton has not been observed to decay. All SM particles and the Higgs bosons have even R-parity, while sparticles have odd R-parity. Conservation of R-parity ensures that every interaction vertex in the theory involves an even number of sparticles, which means that sparticles are pair-produced and every sparticle other than the lightest supersymmetric particle (LSP) must decay into an odd number of sparticles, and eventually into an odd number of LSPs. The LSP itself is prevented from decaying since there is by definition no kinematically allowed supersymmetric states into which it can decay; if electrically neutral, it is a good DMC. Lastly, the MSSM does manage to unify the strong and electroweak gauge couplings at a mass scale around 10^{16} GeV, and the allowed vertices and couplings in the theory are directly related to those in the SM thanks to supersymmetry. However there is a wide range of possible low-energy phenomenology depending on details of how supersymmetry is broken, and without further constraints one might expect almost any spectrum of sparticle masses[4]. For models that are not unduly contrived, the lightest sparticles are expected to be at most in the order of 1 TeV in mass, and sparticle masses should not differ by more than an order of magnitude or so. This makes the LHC quite a conclusive probe of at least a "garden variety" of MSSM models.

[4]The allowed decay modes remain SM-like up to mixing angles; the latter arise because the superpartners need not be mass eigenstates of the theory.

Little Higgs with T-parity (LHT) [52]

Here a minimal extension is made to the SM in order to preserve the smallness of the Higgs mass, by requiring that the Higgs field satisfies additional (approximate) symmetries. The intricacies of these theories are not discussed here, except to say that unlike SUSY, divergences in the low energy effective theory are canceled by new particles of similar spin statistics. There is however some tension between the original Little Higgs theories—which more or less bound new particles to be below about 1 TeV in mass scale in order to avoid residual fine-tunings—with precision electroweak measurements which expect new physics in the 5-10 TeV scale. One solution to this is to introduce a "T-parity" under which SM particles are even and most of the new particles are odd. Requiring T-parity conservation resolves the tension with the aforementioned measurements, plus provides a DMC if the lightest parity odd particle is neutral. On the other hand, LHT theories have a rather similar phenomenology to those arising from SUSY. Other than spin statistics, which is experimentally difficult to resolve, major differences include there being no gluon partner in LHT theories, but instead a heavy top partner exists which is T-even and can therefore be singly produced. The lack of strongly coupled new states means that the dominant T-odd production mode at the LHC would be for pairs of heavy gauge bosons, and sub-dominantly new scalar particles; each these decay via some combination of Higgs, W, and Z particles, and eventually into an odd number of the lightest (stable) new particle. The other high-cross section process is pair production of the T-odd heavy top partner.

Universal Extra Dimensions (UED) [75]

For these class of models, it is postulated that there are extra spatial dimensions on top of the four known space-time dimensions. Since extra dimensions are not observed in daily life, they could be "compactified" so the size of space along these dimensions are finite and presumably too small to be seen. One of the conceptually simplest ways by which a dimension can be compactified is to roll it up into a periodic space. Momentum along such a compactified direction is thus quantized, which means that a given quantum field can be decomposed in terms of the allowed excitation modes—these infinite number of modes are referred to as the tower of Kaluza-Klein (KK) states. In UED all fields are allowed to propagate along the extra dimensions, and at tree level the KK number is conserved because of momentum conservation. A SM-compliant geometry of compactification induces a breaking of the KK number conservation from loop corrections, but leaves a residual symmetry called KK-parity. In this way the collision of zero-mode states (identified as being SM particles) can only pair-produce excited KK modes; the latter are new particles of the theory and have the same quantum numbers and spin-statistics as the SM states. The excited mode states are prevented from decaying unless there is new physics beyond that encoded in the basic UED Lagrangian. The phenomenology of these models is strongly dependent on the nature of this new physics, so only options with DMCs are highlighted here. Of these, the obvious case

is where the excited KK modes are indeed stable. The collider experiment footprint in this case is nonzero because every SM particle has excited KK modes that can be produced, and those resulting in heavy stable charged particles would constitute a distinct experimental signature. Another case arises when the excited KK modes are allowed to decay to zero modes and a graviton, the latter of which is a viable DMC.

1.5 Distinguishing Between BSM Theories

It has been noted that a discovery in the missing momentum channel at the LHC *will* confirm SUSY. This statement is in fact not entirely facetious since most dark matter searches (at least of 2010) have been designed with SUSY theories in mind—but more importantly because most BSM models predict very similar missing momentum signatures. As explained in Section 1.4, presently very little can be assumed of potential BSM production processes except that most theories require presence of a symmetry that prevents some lightest BSM state(s) from decaying into SM particles. This symmetry also tends to ensure that BSM particles must be pair-produced—at least the sector possessing the same parity as which preserves the DMC. In light of these very minimal assumptions, one may then consider all possible ways in which DMCs may be produced from scattering two SM states. The trivial option is of course for two DMC particles to be pair-produced. Alternatively, it is possible that the DMC mass is lower than some of the heavier SM particles, i.e. the top quark and electroweak gauge bosons. Decay modes of the W [3] and Z [2] bosons are strongly constrained by electroweak precision measurements, though decays of the top quark may prove to be an interesting search channel [65]. Otherwise, or if the DMC mass is higher than all SM states, the only particles that would be kinematically allowed to decay into it are other BSM states. The simplest such topology would be a one-stage decay of the produced higher-mass BSM particle directly into a DMC and one or more SM particles. However the produced particle may also decay into an intermediate BSM state which itself decays and so forth (though not *ad infinitum*)—this distinctive feature of BSM event topologies is referred to as a "cascade decay". Examples of one-stage and cascade decays are illustrated in Figure 1.5.1. Although the length of a.k.a. number of stages in the decay chain depends on details of the new particle spectra and allowed couplings, especially the simpler topologies and final states tend to have analogies in most BSM theories. For example, the one-stage decay topology of Figure 1.5.1 could arise in SUSY theories from squark pair production where the squark decays into a jet and the LSP. It could also arise in UED theories from excited KK quarks decaying into zero-mode (SM) quarks and a graviton DMC.

The question of how to distinguish between various BSM models in the case of an observed excess is a nontrivial one, and has been extensively studied in literature [18]. The theoretically expected cross-section turns out to be one of the most discriminating

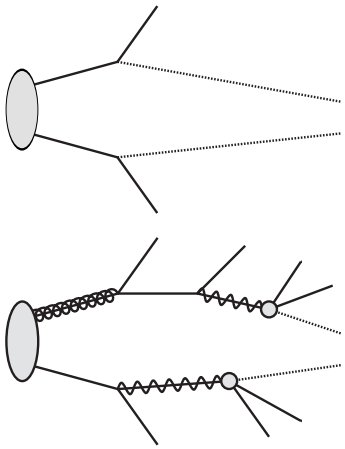

Figure 1.5.1: Example BSM pair-production and decay topologies. Top: Each of the produced BSM particles decays via a one-stage decay directly into DMCs (dotted line). Bottom: The produced particles undergo cascade decays i.e. via one or more intermediate stages.

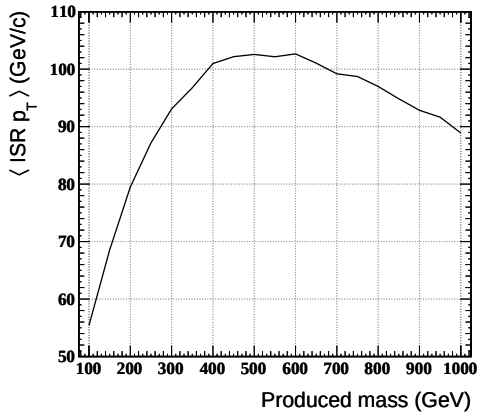

Figure 1.5.2: Average ISR recoil p_{T} as a function of the pair-produce particle mass, as simulated by the PYTHIA event generator [82].

features and can be used as a zeroth-order compatibility check; however cross-sections can depend quite significantly on model parameter details like the number of participating species. Roughly next on the feasibility list would be a thorough cataloging of all possible channels[5] in which excesses are/are not seen, since the expected types/flavors of new particles and reactions obviously depends on the BSM model; however it is noted that this argument applies to the minimal set of particles and forces required by the theory, but nothing actually requires reality to manifest as a minimal theory. Much useful information is also given by kinematic observables like event shape variables and edges/endpoints or lack thereof in the distributions of invariant masses of combinations of objects (typically multi-leptons); however this is may not be conclusive. In fact one piece of information that is probably necessary to deciding between at least SUSY versus LHT/UED models is the spin statistics of the BSM partners. This kind of measurement is experimentally very challenging, but may potentially be extracted from quantities like angular correlations between and polarization of objects in the final state.

1.5.1 The Supersymmetry Language

Since the major BSM theories have or can easily be extended to have very similar phenomenologies—at least to the extent of present experimental resolution—there is actually very little loss of generality in choosing to study dark matter searches in the SUSY language. The search itself of course makes no assumptions about the nature of potential signals, but it is often desirable to construct "test" signals in order to understand general kinematic features, benchmark the performance of the search, and so forth. As such, the MSSM particle content and allowed couplings are summarized here.

As mentioned in Section 1.4.3, the minimal SUSY model must at least double the particle content of the SM by postulating a superpartner for each SM particle. The symbols for all these superpartners have a tilde on top. The fermionic superpartners of SM bosons have their names modified to end with "-ino", and the bosonic superpartners of SM fermions have their names prefixed with "s":

SM particle	**Superpartner**	**Allowed branchings**
Quark (q)	Squark ($\tilde{q}$)	$q\tilde{g}$, $q\tilde{\chi}^0$, $q\tilde{\chi}^0$, $q'\tilde{\chi}^\pm$
Lepton (ℓ)	Slepton ($\tilde{\ell}$)	$\ell\tilde{\chi}^0$, $\nu\tilde{\chi}^\pm$
Neutrino (ν)	Sneutrino ($\tilde{\nu}$)	$\nu\tilde{\chi}^0$, $\ell\tilde{\chi}^\pm$
Gluon (g)	Gluino ($\tilde{g}$)	$q\tilde{q}$
$W^0, W^\pm$	Wino ($\widetilde{W}^0, \widetilde{W}^\pm$)	*(see mass eigenstates)*
B	Bino ($\widetilde{B}$)	
Photon (γ)	Photino ($\tilde{\gamma}$)	
Higgs (H)	Higgsino ($\widetilde{H}$)	

[5]The use of the term "channel" is somewhat context-dependent in this document. However here it refers to a detailed categorization of events by all observable properties of the final states: object type (jets or leptons), flavor, and multiplicities of these objects.

For theoretical self-consistency, the Higgs sector has to be extended from having one neutral scalar field to eight Higgses and Higgsinos. Moreover, in general the wino/zino/photino need not be the mass eigenstates of the broken supersymmetric theory. Instead, they mix with the Higgsinos to form four neutral mass eigenstates called neutralinos ($\tilde{\chi}_i^0$) and two charged mass eigenstates called charginos ($\tilde{\chi}_i^{\pm}$):

	Allowed branchings								
$\tilde{\chi}_1^0,\ldots,\tilde{\chi}_4^0$	$Z\tilde{\chi}^0$,	$W^{\mp}\tilde{\chi}^{\pm}$,	$h^0\tilde{\chi}^0$,	$\ell^{\pm}\tilde{\ell}^{\mp}$,	$\nu\tilde{\nu}$,	$A^0\tilde{\chi}^0$,	$H^0\tilde{\chi}^0$,	$H^{\pm}\tilde{\chi}^{\mp}$,	$q\tilde{q}$
$\tilde{\chi}_1^{\pm}$,$\tilde{\chi}_2^{\pm}$	$W\tilde{\chi}^0$,	$Z\tilde{\chi}^{\pm}$,	$h^0\tilde{\chi}^{\pm}$,	$\ell^{\pm}\tilde{\nu}$,	$\nu\tilde{\ell}$,	$A^0\tilde{\chi}^{\pm}$,	$H^0\tilde{\chi}^{\pm}$,	$H^{\pm}\tilde{\chi}^0$,	$q\tilde{q}'$

The mass eigenstates of the Higgs sector are h^0, A^0, H^0, and $H^{\pm}$, and they are R-parity even. The convention used here is to assume that the neutralinos and charginos are labeled in order of increasing mass, i.e. $\tilde{\chi}_1^0$ is the lightest neutralino and $\tilde{\chi}_1^{\pm}$ the lightest chargino.

1.6 Dark Matter Searches at a Collider Experiment

Section 1.4 highlights some extensions to the Standard Model of physics that also provide DMCs. Some of these can only be probed by dedicated experiments, but the large class involving full-blown BSM theories (Section 1.4.3) all predict new particles that may be produced at a high-enough energy collider experiment. If these new particles are or eventually decay into DMC states, a generic signature would be events with missing momentum in the final state, since DMCs do not interact with the detector elements and can only be inferred from what is *not* seen. Hadron colliders like the LHC are able to achieve the multi-TeV energies at which new physics is expected, without being plagued by synchrotron radiation problems which limit electron-positron colliders, and with unprecedentedly high collision rates. Table 1.1 shows how the rate of collecting events of various types at the present running conditions of the LHC compares to the total number of events collected in several previous experiments. Notably, six top-antitop pair production events occur per hour, and one and a half solid years of data collection will exceed the full $10\,\mathrm{fb}^{-1}$ integrated luminosity Tevatron data sample. Another feature of hadron collisions is that the parton spectrum is not fixed, but rather a wide range of center-of-mass energies are sampled as dictated by the parton distribution function of the hadron of choice (proton-proton in the case of the LHC). This is a blessing when the nature of the new physics to be discovered is largely unknown, because one may simultaneously probe a wide range of incoming states and collision energies without having to change the mechanical setup of the experiment. It is also somewhat of a curse because one now lacks full knowledge of the momenta and types of partons participating in the collision. In particular, since the incoming momenta of the colliding partons are not known, what may be assumed is only the conservation of momentum

Process	Events/hour	Total number of events (other colliders)
$W \to e\nu$	10^4	10^4 (LEP), $\sim 10^7$ (Tevatron)
$Z \to e^+e^-$	35	10^6 (LEP)
$t\bar{t}$	6	$\sim 10^5$ (Tevatron)
$\tilde{g}\tilde{g}$ (mass = 1 TeV)	10^{-4}	

Table 1.1: Expected numbers of events produced at the LHC per hour when running at instantaneous luminosity $\mathscr{L} = 10^{33}\,\mathrm{cm}^{-2}\,\mathrm{sec}^{-1}$ and center-of-mass collision energy $\sqrt{s} = 7\,\mathrm{TeV}$. The last column compares the total numbers of events collected at various other experiments.

in the direction perpendicular to the beams of colliding particles. This has direct consequences on a dark matter search, turning the signal footprint into one with missing transverse momentum ($\not{E}_T$), and further reducing the number of constraints available to resolve a system that is already under-constrained by the non-observability of the DMC—especially if always produced in pairs—and unknown BSM particle masses.

Using a "generic" set-up like the CMS detector, one can only collect events containing one or more DMCs if they are are created in conjunction with other visible particles. The first question when designing a dark matter search at such detectors is therefore the channel(s) in which to look. For all of the models discussed in Section 1.4.3, one feature that is almost guaranteed to be in a large portion of BSM events is jet activity from the fragmentation and hadronization of quarks and gluons. For theories with strongly interacting new particles, the strength of this coupling to the partons participating in the hadron-hadron collision typically ensures that these have larger production cross-sections than for electroweakly coupled new states. Color charge conservation also means that the strongly interacting new particles must eventually decay[6] into SM quarks and/or gluons with the same total units of color charge. Even without a strongly coupled BSM sector however, theories that allow weak decays of BSM states would result in jets from hadronic decays of W and Z bosons in the final state. Lastly, high-mass particle productions at a hadron collider is certain to be accompanied by substantial initial state radiation (ISR), which occurs when the natural emission-absorption of quarks and gluons by a colored particle is interrupted due to its participation in a scattering event. This radiation, which can no longer be coherently reabsorbed, enters in the final state of the event as one or more jets; it also acts as a recoil which gives the pair-produced system of particles a nonzero transverse momentum. It is seen in Figure 1.5.2 that the average value of this ISR-induced transverse momentum rises quite steeply as a function of the mass of the produced particles[7] up to masses around 600 GeV, which is expected since QCD radiation occurs at a strength proportional to the energy scale of

[6] Unless somehow stable/meta-stable, although one should surely not discount other exotic possibilities to be within the imagination of theorists.

[7] The ISR spectrum does not depend strongly on the type of particle produced, being a property of the incoming states.

the event. At higher masses it is restricted by the available center-of-mass energy for the collisions, but the fall-off is not rapid.

A choice of looking in the fully hadronic jets plus missing transverse momentum channel has been made for the search described in this document, due to its wide applicability and high discovery power in many BSM scenarios. After a description of the experimental set-up in Section 2, general concerns and design choices of this search are explained in Section 3. Section 4 discusses the use of Monte Carlo (MC) simulations and the motivation for data-driven analyses, before launching into details of the background estimation in Sections 5-7. Section 8 presents the statistical interpretation of the measurement as a test of SM-only versus SM+BSM hypotheses. Section 9 analyzes the efficacy of this search for various BSM models, and compares it to several other searches that have also been performed using the same data. Lastly, Section 10 offers a few concluding words about this search and potential future evolutions.

Chapter 2

The Experiment

2.1 The Large Hadron Collider (LHC)

The LHC is a proton-proton synchrotron collider of about 27 km in radius, 100 m underground on average, and situated at the Franco-Swiss border near Geneva, Switzerland. It was built by the European Organization for Nuclear Research (CERN) and is presently colliding beams at $\sqrt{s} = 7\,\text{TeV}$, although designed to reach up to an energy of $\sqrt{s} = 14\,\text{TeV}$ in asymptotic running. It is also capable of accelerating heavy (lead) ions, which although a more complicated system to analyze, nevertheless have the advantage of being able to reach collision energies of $\sqrt{s} = 1150\,\text{TeV}$. The machine itself comprises of eight arcs, which contain dipole magnets that bend the beam, and eight insertions which are long straight sections joined by transition regions at their two ends. The insertions have different uses: physics (beam collisions within an experiment), beam injection, beam dumping, beam cleaning.

Protons are obtained from a hydrogen bottle by stripping the orbiting electrons, and injected into the LHC in bunches from a pre-accelerator complex. The two beams are then accelerated in separate beam-pipes that intersect at the experiments (detectors) situated at various interaction points around the LHC. This acceleration is achieved by the use of eight superconducting radio frequency cavities (RF) per beam, grouped in fours and installed in insertion sections. The RF frequency is constrained to be an integral factor of 200 MHz due to the operating frequency of the upstream pre-accelerators, and has been chosen to be 400 MHz. This has a consequence that the minimum time spacing between bunches is 2.5 ns, although it is not foreseen to go below an operational value of 25 ns.

Since the protons are loaded in discrete bunches, collisions also happen at discrete points in time called bunch crossings. The bunch size is not constant as the beam circulates around the LHC ring, but rather gets squeezed around the interaction points to micrometers in radii by quadrupole magnets in order to increase the probability of a collision, and expanded to a few centimeters long and a millimeter wide when far from a collision point. The bunch structure and squeezing parameters control the instanta-

neous luminosity $\mathscr{L}$ delivered by the LHC, which is arguably the one number apart from the center-of-mass energy that represents the physics throughput of the machine. In particular $\mathscr{L} \propto k_B N_p^2/\beta^\star$, where k_B is the number of bunches and N_p the number of protons per bunch. The function controlling the amplitude of transverse motion of a single particle within the beam is called β, and $\beta^\star$ is its value at the interaction point. These three parameters are what the machine operations crew evolves in order for the machine to deliver higher instantaneous luminosities, and each have consequences in terms of physics seen at the detectors. Increasing N_p and/or decreasing $\beta^\star$ are very effective in increasing $\mathscr{L}$, but also lead to an increase in the average number of interactions per bunch crossing. The "extra" interactions are called in-time pile-up, and is often undesirable from the physics standpoint because having multiple collisions at the same time complicates the task of analyzing any one of them. The other option is to increase k_B, which unfortunately only has a linear effect, but can still be good enough. The bunches are injected in trains, so one way of doing this is to decrease the temporal spacing in between bunches of a single train. The bunch separation was 75 ns during the collection of all the 2010 data, but has since been reduced to 50 ns in the midst of 2011 data taking. A further reduction to 25 ns is possible, but is expected from detector simulation studies to strongly impact physics, because the signals seen by the calorimeter electronics would start to overlap between bunch crossings. That is, read-out electronics have a finite response time, different amongst various sub-detectors, and a small bunch spacing results in the tails of the signal response curves extending to the previous and next bunch crossings. This is called out-of-time pile-up, and has a magnified impact compared to in-time pile-up because both the previous and next bunch crossings contribute, and may themselves contain pile-up interactions. Furthermore, in-time pile-up can be identified and cleaned to a certain extent using tracking information in the recorded event, whereas out-of-time pile-up would only appear as extra energy in the calorimeter systems because the tracker read-out electronics have a much faster response time and are insensitive to out-of-time pile-up. The cleanest option by which to increase $\mathscr{L}$ is simply to increase the number of bunch trains, but maintain a healthy bunch spacing like 50 ns. Of course, this can only be exploited so far as allowed by the maximum bunch-train occupancy of the machine, given the fixed RF frequency and need to maintain gaps between trains to accommodate rise times of devices used to inject/dump the beams.

Beams circulate for many hours under normal operating conditions, the duration of which is called a "fill". The duration in which a particular detector experiment is actively recording and processing events is called a "run", which may or may not be exactly the period of the fill because the data-taking might need to be restarted in order to change running parameters or troubleshoot problems. Furthermore the instantaneous luminosity falls over the course of a fill, because of a decrease in the number of protons per bunch. Therefore each run is further divided into "luminosity blocks" small enough such that the instantaneous luminosity should be approximately constant throughout, which facilitates measurement. As such, each event collected

by the detectors are uniquely indexed by three numbers: run, luminosity block, and a consecutively assigned event number. For brevity, this is often written in the form "run-number:luminosity-block:event-number".

2.2 The Compact Muon Solenoid (CMS) Detector

CMS is one of two general-purpose detector experiments at the LHC, the other being A Toroidal LHC Apparatus (ATLAS). The reason to have two experiments with similar purviews follows from a long tradition in high energy physics to ensure that results may be cross-checked with setups utilizing different technologies. For the CMS experiment a compact design with a strong central magnet has been chosen, with the goal to retain a resolution of 10% on muon momenta measurements at 1 TeV. The superconducting solenoid, which is 13m long and with 5.9m inner diameter, creates a 3.8T magnetic field along the LHC beam line. The diameter of the magnet's coil is large enough such that inner tracker and calorimetry systems are both accommodated inside. On the outside an iron return yoke closing the field hosts the CMS muon spectrometer. The detector is cylindrically symmetric insofar as possible, and has a layout as shown in Figure 2.2.1. In order to ensure a high degree of hermeticity, the barrel-type sub-detector sections are typically supplemented with endcap-type sections. The coordinate system convention used by the CMS collaboration is such that the z axis is along the beam-line, and the x and y axes define the transverse plane perpendicular to the beam, with x pointing radially inwards towards the center of the LHC ring and y pointing upwards towards the surface of the earth. Physicists often work with a cylindrical coordinate system (ρ, ϕ, z), where ρ is the radial distance and ϕ the azimuthal angle in the transverse plane. A spherical coordinate system (r, θ, ϕ) is also in common use, except that instead of the polar angle θ the pseudo-rapidity $\eta \equiv -\ln[\tan(\theta/2)]$ is preferred for its invariance[1] under Lorentz boosts along z. As a consequence, the solid angle $\Delta R \equiv \sqrt{\Delta\eta^2 + \Delta\phi^2}$ in (η, ϕ) space is also invariant under longitudinal boosts.

To understand experimental hadron collider physics, one must understand the detector and its capabilities. The large number of sub-detector systems in CMS is in order that it should be possible to measure—and ideally distinguish—as many conceivable types of interacting final-state particles as may originate from a collision. Nevertheless, its capabilities are limited by the state of the art of detector technology around the time of conception (about 20 years ago), and finite financial resources. The measurement process is illustrated in Figure 2.2.2. The particles produced in a collision travel outward from the interaction point, traversing several sub-detectors along the way. Depending on how these particles interact with material, they leave behind footprints a.k.a. "hits" in one or more active elements. Since the allowed interactions are fully specified by the type of particle, one may more or less deduce what it was by trying to *recon-*

[1] This is exact for massless particles, and approximate for massive particles. As such, theorists often prefer to use the rapidity $y \equiv 1/2 \ln[(E + p_z)/(E - p_z)]$, which is exactly Lorentz invariant.

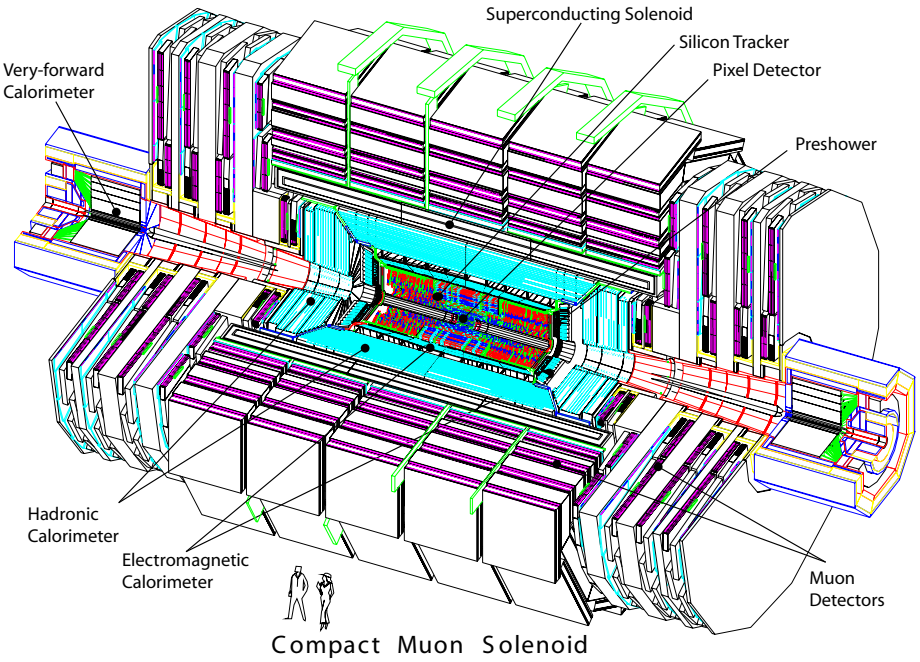

Figure 2.2.1: Layout of the Compact Muon Solenoid detector, with one quadrant removed.

struct particle trajectories or traces in the various systems—this process is detailed in Section 2.3.

A charged-particle tracking system is typically the innermost sub-detector, since these are designed to non-destructively measure particle trajectories. As such they are also commonly referred to as the "inner" tracking system, in order to distinguish them from other tracking detectors that may also be present, e.g. for muons. The CMS inner tracker utilizes semiconductor detection technology throughout, and with a radius of 110 cm and length of 540 cm provides tracking coverage up to $|\eta| < 2.5$ with a total of 66 million pixel-type channels plus 9.6 million strip-type channels. The pixel detectors form the three innermost barrel layers, where their small sizes of $100\,\mu\text{m} \times 150\,\mu\text{m}$ provide point resolutions of $10\,\mu$m in r-ϕ and $20\,\mu$m in z. This resolution is required for vertex reconstruction, i.e. locating the points in space where several tracks originate. Due to the cost (monetary and material) of pixel detectors however, the rest of the tracking system utilizes strip detectors, which have longer z extents but is still adequate because particles traversing radially outwards in space would anyway appear with lower densities in outer detector layers. Charged particles leave a trace of electron-hole pairs when they traverse the silicon wafers, allowing their spatial positions to be sampled at these layers. The magnetic field is required in order to bend their trajectories, so that their momenta can be measured from the curvature of their trajectories. In the limit of an ideally uniform magnetic field of strength B (in Teslas) and perfectly circular particle

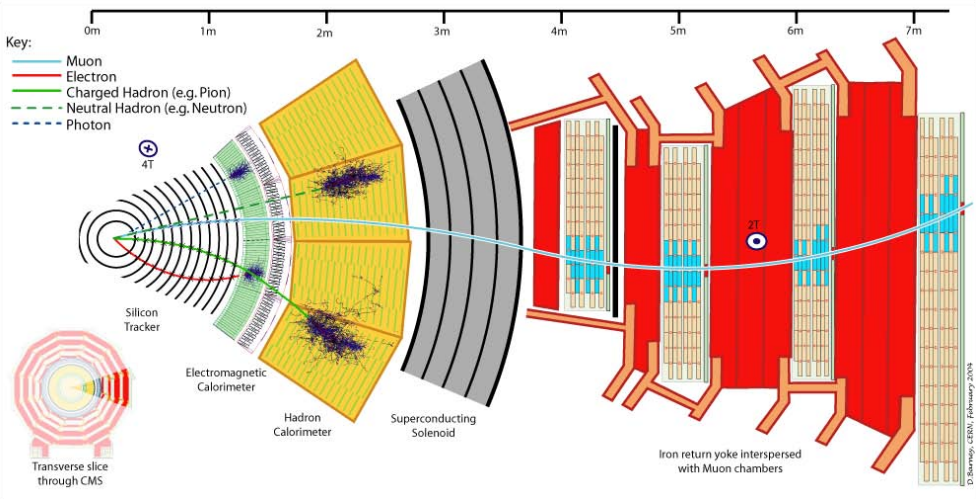

Figure 2.2.2: One sector of a transverse cross-section of the CMS barrel, showing the nominal trajectories and interactions of various types of particles.

trajectory of radius R (in meters), the transverse momentum of such a particle would be $p_{\mathrm{T}} = 0.3 \times B \times R$ (in GeV/c). Charged particles therefore require about $p_{\mathrm{T}} \gtrsim 0.6\,\mathrm{GeV}/c$ in order to escape the CMS tracker system; neutral particles generally pass unmeasured and undisturbed.

After traversing the volume of the tracker, particles impact the electromagnetic calorimeter (ECAL), which consists of a barrel (EB) design and an endcap (EE) design. The ECAL is designed to measure the energies of electrons/positrons and photons, which normally deposit all of their energy inside that instrument. Other particles i.e. charged hadrons also do deposit energy in the ECAL, but this fraction is small due to the high mass of these particles compared to electrons. The ECAL functions by initiating electromagnetic showers in an adequately deep layer of material with large atomic number. The showers result in a large number of low-energy electrons and photons whose total energy can be measured with conventional low energy particle detection techniques such as ionization and scintillation. Lead tungstate ($PbWO_4$) scintillating crystals are used at CMS because of their short radiation length, high scintillation speed and the radiation hardness, which allows for a compact calorimeter with very high granularity and an excellent energy resolution of $2.8\%/\sqrt{E/\,\mathrm{GeV}} \oplus 0.26\%$ with a negligible noise term. The crystals have a square front-face which is approximately 1 inch in width, which is about the Molière radius of this material. This means that the footprint of a single electron/photon in the ECAL would consist of about 90% of energy in a single crystal, but still have some extent into neighboring crystals. Due to the high material budget of the inner tracker however, about half of all electromagnetic (EM) objects undergo secondary interactions there, being bremsstrahlung for electrons/positrons and conversions for photons. This can lead to a spray of EM activity the ϕ direction due to sweeping out by the magnetic field, or even the appearance of satellite clusters. In

addition, in front of most of the endcap range a preshower device (ES) is placed, consisting of two layers of lead absorbers and silicon strip detectors. Its primary goal is to distinguish neutral pions that decay into two photons from prompt[2] photons by initiating EM showers, the profiles of which are then measured by the silicon detectors. It also improves the identification of electrons against minimum-ionizing particles, and the position determination of both electrons and photons due to its superior granularity.

Just outside of the ECAL in radius is the hadronic calorimeter (HCAL), used to measure the energies of hadrons. Particle showers in the HCAL are initiated and developed by strong-force interactions between the hadrons and the nuclei of heavy atoms. Scintillator layers sandwiched in between the absorber material in such detectors then provide an optical signal. The segmentation of the HCAL is significantly more coarse than that of the ECAL, with a 5×5 block of ECAL crystals situated in front of each HCAL tower. For the purposes of object reconstruction using only calorimeter information, such a ECAL-HCAL combination is grouped together as a single "calorimeter tower". The HCAL also has a barrel (HB) design and an endcap (HE) design. Outside these is the solenoidal magnet, which also functions as a showering layer for particularly extended hadronic showers. Due to the limited material depth of this system however, there can still be some amount of leakage outside of the solenoid, especially in very high energy events. There is therefore also a outer barrel hadron calorimeter (HO) that provides further energy measurements in several locations, although this information is not yet commonly used in event reconstruction. Coverage in the extreme forward region $3.0 < |\eta| < 5.2$ is provided by the forward hadron calorimeter (HF).

Both the electromagnetic and hadron calorimeters perform destructive measurements of particles, i.e. most EM particles are stopped by the ECAL, and most hadrons are stopped by the HCAL. Particles that continue traversing the detector in a largely unperturbed fashion include muons (a minimally ionizing particle), neutrinos, and perhaps some very weakly interacting BSM particles if those exist. The latter two types of particles cannot be detected with a generic collider setup. Muons on the other hand are sufficiently long-lived to form charged tracks that can be extended beyond the calorimetry by use of a suitable tracking detector, i.e. the muon chambers. Since the only tracking information may be used to determine muon momenta, a large lever arm is important to resolving this especially for TeV range particles. As such, the muon chambers themselves occupy a radial extent as large as that of the other sub-detectors combined. The chambers are embedded in the iron construction of the magnet's return yoke, such that muon momentum and charge measurements can also exploit the strong magnetic return field. Since the direction of the magnetic field is inverted however, this leads to the characteristic S-shaped muon tracks that has become a hallmark of the CMS detector. The detectors themselves utilize three types of gas-based technologies, the choices of which were driven by the need for fast response, excellent resolution, coverage of a very large total surface, operation in dense radiation environments, and so forth. These are

[2] "Prompt" is commonly used to refer to particles produced in the main reaction of interest, as opposed to those from soft radiative effects or hadron decays.

drift-tube (DT) detectors in the barrel region, with resistive-plate chambers (RPC) and cathode-strip chambers (CSC) forming the endcap. The CSC detectors extend in the forward direction beyond the RPC coverage, resulting in the muon chambers altogether spanning up to $|\eta| < 2.4$.

2.3 Event Reconstruction

Data collected in the detector can rarely be used in its raw form, because quantities of interest in most analyses are the presence and behavior of particles, not just the collections of hits observed in various detector elements. The process by which hits are interpreted in terms of particles and composite objects such as jets etc. is called event reconstruction, which is typically designed for maximal per-particle efficiency. Further identification and quality cuts are then applied at analysis level to suit the degree of required purity. In addition, calorimeter responses typically requires energy scale calibrations, which is performed insofar as possible per-channel. Nevertheless, there are many factors which cause residual dependencies to be seen at particle level, or even depending on the type and density of particles in the case of the HCAL. For example, there are non-uniformities in the amount of material *before* the calorimetry, which obviously cannot be parametrized by channel-level corrections since they depend on the particle trajectory. Due to the non-compensating nature of the HCAL (differing responses to EM versus hadronic energy deposits), the amount of energy recorded is not just linearly proportional to the true particle energy, but depends on the type of the incident particle plus details of the shower formation. All these effects motivate a need for a post-reconstruction stage whereby correction factors are applied based on properties of the reconstructed particles, or even on a jet basis.

There are two levels in which reconstruction is performed: a low-level re-assembly of signals that have been measured over the course of the many units comprising a single sub-detector system; and a high-level interpretation of these low-level objects in terms of particles. In the first category are the reconstruction of tracks in tracking-type detectors, out of which vertices can also be built, and clustering of energy deposits in calorimeter-type detectors. There are furthermore two philosophies according to which the high-level reconstruction is performed. The first is *topical*[3], i.e. aimed at reconstructing specific types of objects in specialized sub-detectors—photons in the ECAL, electrons in the ECAL and inner tracker, muons in the inner and muon trackers, jets in the calorimeters. There is no interplay between the various algorithms used to do so, a consequence of which is that the same information can participate in the reconstruction of more than one [type of] particle. In contrast the Particle Flow (PF) reconstruction method tries to correlate information in all sub-detectors and coherently assign them in terms of some number of electrons, muons, photons, charged and neutral hadrons that

[3] Also informally referred to as "standard" in the collaboration, but the author found this a bit awkward since Particle Flow reconstruction has since become very much a "second standard".

comprise the event. For example, muons are expected to deposit a minimum ionizing amount $\sim 3\,\text{GeV}$ of energy in the calorimeters, which is accounted for in PF reconstruction to prevent it from being assigned to nearby hadrons, but is irrelevant to the topical muon reconstruction since it does not help resolve the muon momentum. For electrons and muons, the topical and PF reconstructed objects are very similar in both algorithms and performance, up to some difference in parameter tunings that should anyway not significantly affect prompt particles (as opposed to those from hadron decays in jets). Where the PF method shines is in jet and global event reconstruction: use of tracking information significantly improves resolution, resolution of charged vs. neutral hadrons allows their different energy scales to be accounted for, exclusivity of reconstructed particles provides an easy way to use all of them at once when measuring quantities like momentum balance.

This analysis makes almost exclusive use of PF reconstructed objects, i.e. except when not yet feasible in the state-of-the-art software development. Relevant aspects of the reconstruction algorithms are summarized below.

2.3.1 Iterative tracking

Track finding is a pattern recognition problem in which the greatest challenge is the sheer number of combinatorial possibilities, what with the existence of 77 million channels. Of course, hardly any of these combinations could possibly be compatible with particles traveling outwards from the interaction point or secondary (possibly material-induced) vertices. First of all, disregarding "loopers" that lack enough momentum to escape the tracker and therefore curl back to smaller radii, one should only need to link hits in inner layers to progressively outer layers, or vice versa. Assuming that particle trajectories are approximately helical, there is also a maximum distance between hits in two consecutive layers that is still compatible with the particle being above a certain p_T threshold, leading to a finite road in which to look for the next hit. Alternatively, one can also pick two hits in an innermost and an outermost layer, and look in a football-shaped area between the two layers that is compatible with particles above some minimum p_T and of either sign in charge. All of the above observations form the back-bone of most tracking algorithms for silicon detectors, which may then differ in details of how to select "seeds" from which to grow the tracks, whether to go inwards-out or outwards-in, what trajectory functional form to fit the hits to, and so forth.

The CMS algorithm for general reconstruction of tracks in the inner tracking system [26] is inside-out and consists of five stages. First, particles may actually deposit signals in more than one channel in the pixel and strip detectors, which have to be combined into hits in a pre-tracking step. These hits are assigned a nominal position based on the charge deposition, which also has an estimated uncertainty. Second, seeds are formed from combinations of either three pixel hits (in different layers), or two hits (pixels and possibly selected strip layers) and either a vertex or a beam-spot constraint[4].

[4]Here the vertex is estimated using the pixel-triplet seeds. The beam-spot is a measurement of the

Third, a road search is performed to attach more and more hits to the track candidates. This starts from the initial helix built using the seed hits, which is extrapolated to the next layer taking into account multiple-scattering and energy loss effects in the expected material. All hits that are compatible with this extrapolated location and its uncertainty are then allowed to generate new track candidates, where each of the latter have their trajectories updated with the information of the added hit. This process continues until the last layer has been reached, in principle causing an exponential increase in the number of track candidates, but in practice this is controlled by pruning away low-quality candidates. Fourth, a final fit is performed per track candidate to estimate the helix parameters and uncertainties to high precision. Fifth and finally, spurious hits could have been included in the track candidates due to the looseness of the track finding criteria as required to retain high efficiency; these are removed by checking the compatibility of hits with the fitted trajectory, and removing outliers. On top of this, the reconstruction phase is followed by a cleaning phase, whereby tracks with bad fit qualities and/or are incompatible with the event interaction vertex/beam spot are removed.

To maximize efficiency and minimize the number of fake tracks while still staying within a reasonable time budget, the above procedure is actually iterated six times, starting with tight criteria to select an "easy" subset of clean, prompt, and relatively high-p_{T} tracks, which is then progressively relaxed to pick up low-p_{T} and displaced tracks. This helps because a large number of hits, i.e. those associated with high quality tracks, can be removed from the system after each of the iteration steps, leading to a reduction in the number of combinations that have to be dealt with in subsequent iterations. It is not unusual to see efficiencies and purities in the better than 90% level for promptly produced particles within tracker acceptance, although this can worsen significantly for particles in the dense cores of high-p_{T} jets.

2.3.2 Primary vertex reconstruction

2.3.3 Topical photon reconstruction

Electron/photon reconstruction in CMS is complicated by the interactions in the tracker material in front of the electromagnetic calorimeter. Electrons traversing the tracker layers radiate bremsstrahlung photons, such that the electron energy reaches the ECAL azimuthally spread because of the solenoidal magnetic field. The amount of radiated energy can be very large. Electrons with $p_{\mathrm{T}} = 10\,\mathrm{GeV}/c$ radiate about 50% of their energy in 50% of the cases, and up to 95% in 10% of the cases. These bremsstrahlung photons can in turn convert into e^+e^- pairs, which may in turn radiate, and so on leading to an EM "shower" and significant energy loss in the tracker. The rate of photon conversions is also about 50%, reflective of the average one radiation length of material in front of the ECAL.

average (i.e. not per-event) location of interactions in the transverse plane

Clustering is performed in order to collect all the energy originating from a single EM object. The Hybrid algorithm is used in the barrel, exploiting the η-ϕ grid arrangement of the crystals. It starts from "basic clusters" of 3×1 (η-ϕ) or 5×1 bars of crystals, and then performs a dynamical search for separated energy in the ϕ direction to form a "supercluster". Supercluster formation in the EE and ES proceeds similarly, but uses a slightly different algorithm Multi5×5 which adds together 5×5 basic clusters. Energy corrections are then performed on the superclusters, but due to the excellent ECAL resolution these are usually just at the 1% level.

Since superclusters are in common between electrons and photons, the latter have to be distinguished at the very least by requiring that there is no significant tracker activity along the trajectory of the photon, which is simply radially outwards from the interaction point. In addition, isolation and shower shape variables are typically applied by analysts in order to control the background from hadron decays. Photon conversions can also be identified by trying to reconstruct oppositely charged tracks with small opening angles consistent with the zero photon mass, and the number of these conversion track-pairs may provide further discrimination between single photons and two photons e.g. from decays of the neutral pion.

2.3.4 Muon reconstruction (topical, also used in PF)

Due to the different technologies comprising the muon spectrometers, a different hit reconstruction strategy is required for each. For the DT's the time-of-flight of muons from the interaction point to the DT cell is required to correct for the drift time. The CSC's and RPC's on the other hand collect signals on multiple strips, which must first be clustered to form hits. Furthermore, linear fits are first performed on the hits in each of the DT and CSC chambers, leading to muon "segments" a.k.a. track stubs, whereas RPC hits are used as-is.

There are three algorithms for high-level muon reconstruction in CMS [24], distinguished by how they use (or not) information from sub-detectors other than the muon chambers. The "standalone" muon reconstruction method only uses the muon chambers: segments in the innermost layers are used to seed a road-search, inside-out tracking algorithm similar to that for the inner tracking system, except using DT and CSC segments plus the RPC hits as input. The "tracker" muon method goes in the other extreme, starting from tracks reconstructed in the silicon tracker by the previously described algorithm, and only using the muon system as a "tag". That is, an inner track is either rejected or confirmed as a muon depending on the existing of compatible deposits in the calorimeters and/or muon segments. Finally, the "global" muon algorithm is something of a best-of-both worlds. It starts from tracks reconstructed by the standalone algorithm, then tries to attach to hits in these tracks to hits in the inner tracker system.

2.3.5 Particle Flow clusters

Energy deposits in the calorimeters are clustered in the reconstruction process because a single particle rarely deposits its energy in exactly one channel. The PF clustering algorithm selects cluster seeds as being channels with energy above a given threshold, and then grows these into topological clusters by iteratively collecting neighboring cells above a lower energy threshold. The cluster is assigned a nominal energy and position that is iteratively determined using information about the energies and relative positions of each cell in the cluster.

2.3.6 Particle Flow particles

Given the inner tracks, reconstructed muons, and calorimeter clusters explained above, the PF algorithm links these building blocks together into particles of various types [25]. In general, a particle can comprise of at most one charged-particle track, and/or several calorimeter clusters, and/or one muon track. The linking process must also remove double-counting of information about the particle from multiple sub-detectors, e.g. a muon could have all three of the possible elements, but only the muon track is relevant, and the inner track is probably the same as that which was used to reconstruct part/all of the muon track. The first stage in the PF linking process is a tentative one, and based on geometrical distance between elements. In particular, inner tracks are extrapolated to the calorimeters, and may be linked to any number of clusters within an acceptable (η, ϕ) distance of that extrapolated point. To account for bremsstrahlung photons emitted by electrons, tangents to the tracks are also allowed to link to clusters in the ECAL. Two calorimeter clusters (from different sub-detectors) are allowed to link when the position in the more coarse-grained calorimeter is within the envelope of the fine-grained one in (η, ϕ) space. Finally, inner and muon tracks are linked when they have an acceptable quality of fit. Elements that are either directly or indirectly linked according to these distances form a "block", which are thus by construction mutually exclusive.

The second stage of the PF algorithm involves a careful identification of each block as a particular type of particle, removing duplicate information, or discarding the block entirely.

Muon: If the muon track passes some quality criteria, it gives rise to a PF muon, and the track(s) are removed from the block. The expected energy deposit of $\sim 3\,\text{GeV}$ is also subtracted from the HCAL cluster energies where relevant.

Electron: Electrons tend do undergo bremsstrahlung radiation in the tracker, which can be used as a distinguishing criteria. If this and other tracking and calorimetric criteria are met, a PF electron is identified, in which case the track and ECAL clusters including those identified as bremsstrahlung photons are removed from the block.

Charged hadron: The calorimeter clusters may be interpreted as one or more charged hadrons. To determine this, all tracks that link to the given clusters are considered, with some disambiguation to ensure that tracks are only checked for the nearest HCAL cluster and/or the nearest ECAL cluster out of all those that they link to. If the total calibrated calorimetric energy exceeds the sum of track momenta, the ECAL clusters furthest from any track are removed from the list of clusters under consideration, because they are most likely from overlapping photons; this removal is to the point that the total calorimetric energy is just below or equal to the total track momentum. After removal of low-quality tracks that may cause an excess in track momentum above the calorimetric energy, each of the remaining tracks gives rise to a PF charged hadron. The momenta of these charged hadrons are taken from the track information unless the calorimetric energy is sufficiently compatible, in which case a fit of the tracker and calorimeter information are used to improve the measurement.

Neutral hadron or photon: If the total calibrated calorimetric energy is significantly more than the total track momentum in the above, the excess gives rise to neutral PF particles. An excess in ECAL energy is interpreted as a photon, and an excess in HCAL energy is interpreted as a neutral hadron. Photons and neutral hadrons are also created out of ECAL and HCAL clusters that are not linked to tracks.

Other than the use of tracking information, which has much better resolution than that of the hadron calorimetry in most cases, the PF algorithm also derives a lot of its power from the ability to perform particle-level and particle-type specific calibrations. These have direct consequences in improving jet resolution and therefore momentum balance as explained below.

2.3.7 Jet clustering algorithms

It is commonly said that jets arise because of QCD confinement, which prevents bare quarks and gluons from being observed but instead to fragment into colorless bound states, hadrons. However this does not on its own explain why there should be a large multiplicity of hadrons arising from a single quark/gluon, nor why they should all be collimated in a direction approximately that of the originating parton. Part of this is due to the showering behavior of high-energy partons, which furthermore prefers low-energy and/or small-angle radiations. For example, the probability density for a quark to radiate a gluon of energy E and at relative polar angle $\Delta\theta$ w.r.t. the direction of the quark goes like $\alpha_s/E\Delta\theta$. Showering goes on until the energy scale is low enough such that α_s becomes large and confinement kicks in, by which time there is typically already a huge number of branchings especially if the initial parton is very hard. Lastly, hadron

formation more or less preserves the directionality of the partons involved, which can informally be thought of as being because it is difficult to pull partons apart at this point.

For many studies, it is not enough just to reconstruct all these final-state hadrons, but to somehow move closer to the simple parton-level view of an interaction. This is served by organizing hadrons into jets, which cannot have a one-to-one correspondence to partons but are anyway the more observationally meaningful objects. Here the *sequential recombination* [79] class of jet clustering algorithms are some of the most commonly used in present-day high energy physics. Essentially, these algorithms attempt to trace the showering process backwards, by noticing that the most probable branchings are those that occur at small "distances" (to be defined). The algorithms thus all have a basic structure as follows:

1. Start with a list of input particles ("pseudo-jets").
2. Pick the pair of particles with closest distance d_{ij}.
   (a) If this minimum distance is larger than the maximum allowed distance R, stop.
   (b) Otherwise combine this pair into one new particle, e.g. by adding their 4-momenta, and repeat the procedure with the modified list of particles.

The distance definition $d_{ij} = \Delta \mathrm{R}_{ij}^2 \min(E_i^{2p}, E_j^{2p})$ for various integer values of p cover most of the algorithms in common use, and is motivated by the $\alpha_s/E\Delta\theta$ form of QCD branching probabilities. The choice $p = -1$ corresponds to the anti-k_T algorithm, which prefers to first cluster particles that are in close angular proximity, but *dis*favors clustering of soft particles when there are higher-energy alternatives. The latter property is nice because it results in jets that grow more or less circularly outward from hard cores, which is moreover stable against the presence of soft electronics noise or pile-up particles that may contaminate the event. Jet clustering in the CMS software system is provided by the external `fastjet` package [1].

2.3.7.1 Calorimeter jets and missing transverse energy (topical)

In the topical scheme, jets are reconstructed using only calorimetry information [23, 13]. The constituents of these jets are calorimeter "towers" created by performing (in the barrel) an unweighted sum of energies in a single HCAL cell and the 5×5 block of ECAL crystals contained within its footprint. A similar but more complex association is required for the endcap regions, but in the forward region there is only a single calorimeter which performs both EM and hadronic shower measurements. This is achieved by having two different lengths of Cherenkov light collection fibers in the device, long and short, both extending *inwards* towards the interaction point from the back of the device, and which effectively provides two sampling depths. The long fibers collect both EM and hadronic types of showers, whereas only the slower developing and

longer penetrating hadronic showers reach the short fibers. The asymmetry between energy measurements in the long/short fibers is thus used as a measure of the EM fraction of the shower. Each calorimeter tower is treated as a massless "particle" for the purposes of jet clustering.

In addition to the tower reconstruction, there is also a selection requirement to reduce the impact of soft calorimeter noise. There is usually a minimum E_{T} threshold required per tower, with different settings in various calorimeters. There are also some threshold requirements applied only to the ECAL energy sums for the barrel and endcap towers. A proper choice of these thresholds are particularly important for missing transverse momentum reconstruction, where the version called $\not\!\!E_{\mathrm{T}}$ is computed using all selected calorimeter towers.

One main implication of the use of calorimeter towers in jet and $\not\!\!E_{\mathrm{T}}$ reconstruction is that there is almost full overlap with information used by other objects, in particular electrons and photons, and to a lesser degree muons which may deposit a minimum ionizing amount of energy in the calorimeters. As such, there is often a need to disambiguate these objects e.g. when using both jets and electrons/photons in the analysis. This is most simply done by something like locating the nearest jet in ΔR to well-identified other objects, and discarding the jet if it is to close compared to the extent of these other objects, e.g. $\Delta\mathrm{R} < 0.3$.

2.3.7.2 PF jets and missing transverse momentum

In the PF scheme, jets are simply clustered using all or a subset of the PF particles as constituents. The choice between the two is up to the analyst, depending on whether there is need to perform prior clean-up or disambiguation of objects. For example, in running conditions with a high number of pile-up interactions, it can be important to first discard all charged particles that do not appear to originate from the primary vertex of choice. Analyses that involve one or more other types of objects, e.g. electrons and/or muons, may also want to distinguish a set of "good" (typically isolated) objects of these types that are excluded from the list of particles used to cluster jets, so that there is no overlap. The gain from using PF reconstruction [25] is most significant for low energy jets, since the calorimeter resolution is worst for soft particles whereas the tracker efficiency is reasonably high, resolution is good, and furthermore also accounts for the significant bending of charged particles by the magnetic field. The latter distorts the reconstructed directions of the jets, or even causes particles to be swept out of the maximum clustering distance altogether, both of which are recovered by the PF use of tracking information. For $p_{\mathrm{T}} < 100\,\mathrm{GeV}/c$ jets the η direction resolution is almost a factor of 2 better than calorimeter jets and with even more improvement at lower values of p_{T}; the ϕ direction resolution is a factor of 3 better. A similarly dramatic improvement is seen in the jet resolution and average response (a.k.a. jet energy scale). These are typically quantified using simulated events (see Section 4.1) by fitting a gaussian to the core of the distribution of responses $p_{\mathrm{T}}^{\mathrm{reco}}/p_{\mathrm{T}}^{\mathrm{gen}}$ and extracting the μ and σ param-

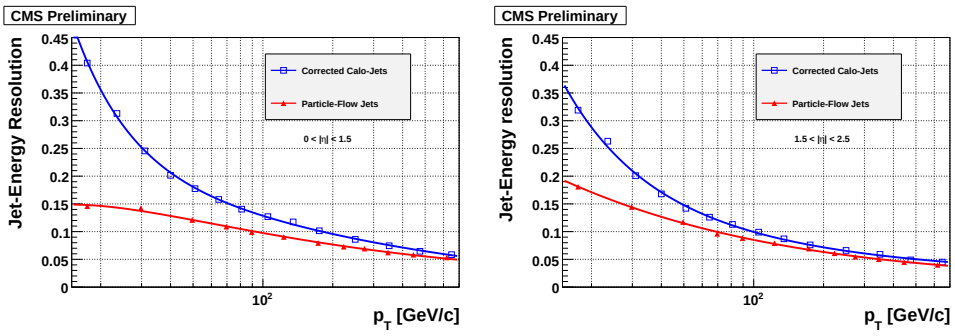

(a) Barrel (b) End-Caps

Figure 2.3.1: From [25]: Jet energy resolutions as a function of p_{T} for jet-energy-scale corrected calorimeter jets (open squares) and for Particle Flow jets (upwards triangles) in (a) the barrel and in (b) the endcaps. The resolution curves are fit to the quadrature sum of a constant term, a stochastic term and a noise term.

eters, where $p_{\mathrm{T}}^{\mathrm{reco}}$ is the transverse momentum of the reconstructed jet and $p_{\mathrm{T}}^{\mathrm{gen}}$ is the associated jet of simulated particles before interaction with the detector. For reasons explained in Section 2.3, the average response μ typically requires calibration, but for PF jets this correction factor is much smaller than that for calorimeter jets thanks to the particle-level calibrations performed as part of the algorithm. "Out-of-the-box" PF jets have an average response that is within a few percent of unity, compared to calorimeter jets for which this is 20% or more too low. Lastly, Figure 2.3.1 taken from [25] shows the significant improvement of the jet resolution σ due to PF reconstruction, which is around a 25% reduction even for $p_{\mathrm{T}}^{\mathrm{gen}} = 100\,\mathrm{GeV}/c$ jets and towards 50% for softer jets.

In all cases, the version of missing transverse momentum denoted as $\not\!\!E_{\mathrm{T}}$ is computed using all PF particles, since it is only by this full accounting that events are expected to balance (up to the contribution of invisible particles and measurement effects). Due to the significantly low average calorimeter jet response and non-inclusion of muon momenta, calorimeter $\not\!\!E_{\mathrm{T}}$ requires correction for both these factors, unlike PF $\not\!\!E_{\mathrm{T}}$ which can be used as-is. Since the identification and correction of very soft calorimeter jets are not well defined however, this energy scale correction can only be sensibly performed for jets with $p_{\mathrm{T}} \geq 20\,\mathrm{GeV}/c$ or so. This and the generally worse calorimeter resolution means that the PF $\not\!\!E_{\mathrm{T}}$ resolution can be 10 GeV or so better than that of calorimeter $\not\!\!E_{\mathrm{T}}$, with also a reduced bias in events with low intrinsic $\not\!\!E_{\mathrm{T}}$ (i.e. from neutrinos). From an analysis stand-point, selecting on PF $\not\!\!E_{\mathrm{T}}$ can result in around a factors of reduction in the QCD multi-jet background yield compared to a similar analysis performed using calorimeter $\not\!\!E_{\mathrm{T}}$.

Part II

A Search for Excess Events with Jets And Missing Transverse Momentum

Chapter 3

Scope and Search Design

3.1 A Conceptual Overview

Section 1.6 motivated a search in the jets plus $\not{E}_{\mathrm{T}}$ channel; however this specification is so generic as to be useless because of the huge cross-section of SM events with this same signature:

- W boson produced in conjunction with one or more jets, where the W boson decays into a charged lepton and a neutrino.
- Z boson produced in conjunction with one or more jets, where the Z boson decays into two neutrinos.
- Top quark pair production ($t\bar{t}$), with leptonic decay of at least one of the W bosons from the $t \to \mathrm{W}b$ prompt decay.
- Sub-leading: Di-boson (WW, WZ, ZZ) and single top production, with at least one leptonic decay.

In addition to the above channels—collectively the top/EWK background—where neutrino(s) constitute missing momentum in the event, it is possible to mis-reconstruct objects in the detector as explained in Section 2.3, leading to *apparent* (sometimes called "fake") missing momentum. Jets are the worst resolved objects in CMS, and if one considers that most of the proton-proton scattering cross-section goes into the production of so-called "QCD events" i.e. which have only jets in the final state, it comes as no surprise that there is also a significant mismeasurement-induced background to any $\not{E}_{\mathrm{T}}$ search. It is also possible for the detector to register spurious signals in the electronics, which when overlapping with real activity can be difficult to distinguish and is another means by which an otherwise well-balanced QCD event can appear to have high $\not{E}_{\mathrm{T}}$.

Several event selection criteria ("cuts") are imposed in order to reduce the SM background to a manageable level:

Lepton veto.

The non-QCD backgrounds, with the exception of the invisibly decaying Z boson, all contain one or more visible leptons in the final state. One may therefore consider vetoing all events that contain one or more identified leptons. This is clearly sub-optimal in case the BSM signal is lepton-rich, but it is nevertheless a choice made with knowledge of the existence of complementary searches in various leptonic channels.

High jet activity.

Since BSM particles are expected at a significantly higher mass scale than any of the SM background processes, the energy scale of the event is a good discriminator. Here there are several options, but the one chosen was H_{T}, defined as the scalar sum p_{T} of jets in the event. Furthermore, the electroweak and (to a certain extent) QCD production mechanisms tend to favor events with low jet multiplicities, whereas BSM events—especially when there are gluon partners involved, or long cascade decays as allowed by SUSY theories—tends to have many jets. A request for events to have ≥ 3 jets significantly reduces the electroweak and QCD backgrounds, and is not too inefficient even for signals with only two jets from the BSM particle decays, because a large portion of these events also have substantial ISR activity (Figure 1.5.2).

Noise pattern rejection.

High p_{T} noise has distinctive distributions due to the detector geometry and depending on the source of noise. For example single channels with very high energy readings and little surrounding activity are typically suspicious, as are long strips of activity along a direction coupled together by read-out electronics (e.g. η for the HCAL). Detailed temporal information about when the signal occurred is also a useful indicator since most types of noise and spurious sources are not compatible with the hypothesis that the particle has traveled outwards at roughly the speed of light from the time of occurrence of the collision event. Removing such suspicious-looking energy deposits or even rejecting events containing them has been found to be crucial for cleaning up $\not\!\!E_{\mathrm{T}}$ tails in the collected data. Lastly, a very simple but effective noise rejection criteria is simply to require that each event has a well-reconstructed collision vertex ("primary vertex"), as well as a healthy fraction of reconstructed tracks together with calorimeter activity. This is because noise in the calorimetry is expected to be highly uncorrelated with reconstructed particle tracks in the silicon tracker system. The latter is also essentially noise-free both because the per-channel noise rate is very low, and because it is highly unlikely that there should be such a coincidence of multiple noisy channels in such a way as to satisfy the pattern recognition requirements of track reconstruction.

$\not{E}_{\mathrm{T}}$-jet angular cuts.

Severe jet mismeasurements are required in order for QCD events to have high $\not{E}_{\mathrm{T}}$. Since the per-jet probability for this is low, most of these events are characterized by a single highly mismeasured jet. In the limit where the other jets are relatively well measured, the event $\vec{\not{E}}_{\mathrm{T}}$ tends to be aligned with the most mismeasured jet. Rejecting events with a small angle between $\vec{\not{E}}_{\mathrm{T}}$ and some jet is therefore a highly effective way of reducing the QCD background; however this does not come without a price in terms of signal inefficiency. The latter arises because even if the directions of the jets and DMC(s) in BSM events are completely uncorrelated, the finite 2π radians of angular space in the transverse plane means that one can rejects 5% of signal events per jet by imposing, say, a $\Delta\phi(\vec{\not{E}}_{\mathrm{T}}, \vec{p}_{\mathrm{T,jet}}) > 0.3$ requirement. This quickly compounds for signals with many jets in the final state, or if one carelessly includes as "jets" objects with too low a p_{T} such that the many stray particles in a typical event are also included. Furthermore, depending on the mass splitting between BSM states in cascade decay chains, the direction of jets and the DMC can actually be positively correlated. One compromise in order to retain high signal efficiency is to restrict this cut to only checking the leading (highest p_{T}) few jets in the event; a choice of the leading three jets was empirically found to be adequate.

3.1.1 $\not{E}_{\mathrm{T}}$ as a Signal-Background Discriminator

In the above discussion it is implicitly assumed that the main variable for separating signal from background should be $\not{E}_{\mathrm{T}}$. This is of course a rather literal and unsophisticated take on the definition of a "jets plus $\not{E}_{\mathrm{T}}$ search", and one may very well wonder if one cannot do better. The main conceptual disadvantage in using $\not{E}_{\mathrm{T}}$ (and also H_{T}) in a cut-and-count experiment is that it does not adjust to the mass scales of the BSM process. That is, a low $\not{E}_{\mathrm{T}}$ cut can maintain high efficiency for BSM models with low mass splittings between the produced BSM particle and the DMC into which it decays, but is sub-optimal for models with high mass splittings where a tighter cut could have been used to reject more background. Experimentally, $\not{E}_{\mathrm{T}}$ is also difficult because of its aforementioned sensitivity to mismeasurements and/or failures to reconstruct objects. To understand the high tail of the $\not{E}_{\mathrm{T}}$ distribution—especially for events collected in the fully hadronic channel—requires good control of the percent-level or smaller effects that cause top/EWK events to fail the lepton veto and QCD events to be misbalanced, and furthermore to understand the correlation of these effects with missing momentum in such events.

There are undoubtedly more clever variables to be used in lieu of $\not{E}_{\mathrm{T}}$. In fact, much effort has gone into devising variables that allow measurement of BSM particle masses, e.g. m_{T2} which has an endpoint (at least theoretically) at the produced particle mass and may also provide information about the DMC mass in some cases [67], and the "Razor" variable R and its companion quantity M_R which peaks near $M_\Delta \equiv (M^2_{\mathrm{produced}} - M^2_{\mathrm{DMC}})/M_{\mathrm{produced}}$ [76]. Assuming that the BSM particles are pair-produced, the final-

state objects in these events can be considered as being in two separate "hemispheres", each containing the decay products from exactly one of the initial produced particles. This fact is exploited by variables like m_{T2}, R, and M_R via hemisphere reconstruction[1], which then allows one to construct variables based on analogy to the simple two-body decay of a massive particle into a visible particle (the reconstructed hemisphere momentum) and an invisible particle (deduced from $\not{E}_{\mathrm{T}}$). These resolution of these variables tends to depend on how well the hemisphering algorithm performs in distinguishing the two BSM particle decay chains, and can be significantly degraded in the case of signals with high jet multiplicities and/or no significant spatial collimation of the decay products per hemisphere. Together with inevitable effects like contamination from ISR jets, imperfect experimental resolutions, and competing shapes of background distributions[2] of these variables, it typically turns out that no clear-cut edges or peaks can be observed especially in the fully hadronic search channel. Even so, it is clear that such mass-sensitive variables are desirable both for their performance in simple counting experiments as well as their potential to characterize [at least one aspect of] any excesses that may be seen.

That said, there is no reason to dismiss use of a variable because it has the unfortunate virtue of being *too* simple. In fact the average $\not{E}_{\mathrm{T}}$ in BSM events is also more or less proportional to M_Δ (Figure 3.1.1), and equi-signal-efficiency contours of a $\not{E}_{\mathrm{T}} > X$ (for some value of X) event selection has the same trend. Since $M_\Delta/2$ is the expected p_{T} of each of the outgoing particles from a 2-body decay of a particle produced at rest into one massive and one massless particle, it tends to generally provide a good scale dependence for quantities involving the momenta of final states, even for complex decay chains. For variables involving scalar sums of momenta like H_{T} (Figure 3.1.2), the trend is more proportional to the linear difference $M_{\mathrm{produced}} - M_{\mathrm{DMC}}$ a.k.a. the total available visible energy. The largest source of inefficiency for $\not{E}_{\mathrm{T}}$-based selections occurs in long cascade decays, where much of the available momentum may go to visible objects rather than the DMCs. Even without this though two DMCs can be produced anti-aligned in the transverse plane, simply by random coincidence especially if the initial BSM particles are produced almost at rest and therefore undergo more or less spherically symmetric decays. In this case the momenta of the DMCs can cancel each other out, resulting in events with low values of $\not{E}_{\mathrm{T}}$. In these cases one may recover some efficiency by using variables like M_R; on the whole however the two variables are quite comparable, and the main disadvantage of $\not{E}_{\mathrm{T}}$ is the practical one that it has a more difficult SM background. Actually, to combat the cross-section dependence of the signal yield a more performant variable would be something whose efficiency rises like some high power of M_{produced}, of course when deciding between variables with

[1] A typical hemisphere reconstruction algorithm collects objects together based on angular proximity, in a similar way to jet reconstruction algorithms. Other metrics e.g. minimizing the invariant mass of the summed momentum for each hemisphere may also be used.

[2] It is very difficult to resolve a broad peak on a broad background, especially if event counts are exponentially falling as a function of the variable in question.

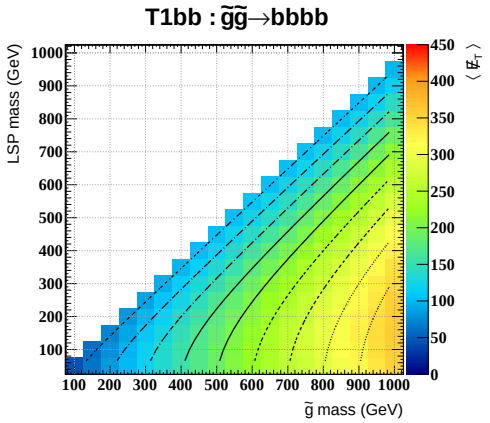

Figure 3.1.1: Average reconstructed $\not{E}_{\mathrm{T}}$ in simulated SUSY events, where each event consists of pair-produced gluinos that each undergo 3-body decay into two b quarks and the LSP. The overlaid lines indicate contours of equal $M_{\Delta}/2$, ranging from 50 GeV (diagonal) to 450 GeV (bottom right corner) in 50 GeV steps.

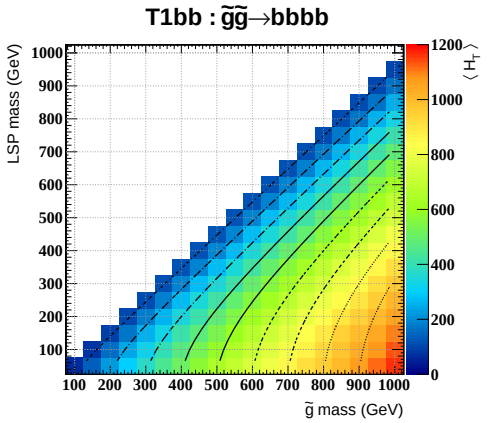

Figure 3.1.2: Average reconstructed H_{T} in simulated SUSY events, where each event consists of pair-produced gluinos that each undergo 3-body decay into two b quarks and the LSP. The overlaid lines indicate contours of equal $M_{\Delta}/2$, ranging from 50 GeV (diagonal) to 450 GeV (bottom right corner) in 50 GeV steps.

comparable background counts and signal efficiencies. For this something like $H_{\mathrm{T}} + \not{E}_{\mathrm{T}}$ can be competitive, although it has not yet been attempted here.

3.1.2 Background Estimation Philosophy

For most searches, the most time-consuming tasks—especially at technologically groundbreaking experiments like the LHC—are the background estimations. Reasons for this will be detailed in Section 4, but the fact that it is so is not too surprising given that a compatibility level with the background-only hypothesis of 0.1% (3 standard deviations) is required to claim evidence and 10^{-7} (5 standard deviations) to claim a discovery. This burden of proof means that not only does the central value of the background counts have to be predicted well, but also the systematic uncertainties on this number needs to be well understood. As such, quite a few searches are designed around particular variables and/or event selections that are designed to facilitate background estimations, e.g. by entirely removing some backgrounds, or because the behavior of background sources in these variables can easily be extrapolated from control regions using well-motivated trends.

The strategy followed here is more tedious but general. Data-driven methods are proposed for the estimation of all but the smallest cross-section SM processes, which

are anyway expected to be significantly reduced due to the lepton veto. These methods do not only predict the sufficient information of event counts after some particular set of search cuts. Instead, they predict a set of equivalent *events* per background with only very loose preselection requirements, which may then be manipulated in the usual way e.g. for the purposes of evaluating one or more cut flows. In this way, it is possible to generalize to a large variety of alternative cut flows and even new variables, in particular those that only involve jet kinematic quantities[3]. This flexibility also allows for the examination of many distributions other than those used to select the search region, which can be invaluable in understanding the data as well as gaining confidence about any observed excesses.

3.2 Object Definitions and Event Preselection Criteria

This analysis is performed using the full officially certified data sample collected by the CMS detector in the year 2010, corresponding to an integrated luminosity of $36\,\mathrm{pb}^{-1}$, and from the November 4 reprocessing campaign. In addition, Monte-Carlo (MC) simulations were used to generate samples of events from various SM background processes as they would appear in the detector. All data and simulated samples are listed in Appendix A, and the roles and parameters of MC simulations are explained in Section 4.

Unless stated otherwise, all objects used in this analysis have been reconstructed via the Particle Flow (PF) algorithm described in Section 2.3. The end product of PF reconstruction is the list of electrons, photons, muons, charged and neutral hadrons that comprise an event, as compiled from correlating information in various subdetectors. Jets are clustered out of *all* these objects, using the anti-k_T [79] algorithm with size parameter 0.5, and have their energy scales corrected to the MC-derived L2 and L3 levels, on top of which an additional residual correction is applied only when working with data events [88, 31]. One may legitimately wonder, why should an electron be allowed to cluster into or even become a jet? The quick but rather too glib answer is that of course jets do naturally contain electrons all the time, e.g. from decays of hadrons, pair-production in the tracker system, and so forth. The more apropos question is rather, why should *prompt* electrons—e.g. from decays of one-shell W's, or an immediate product of some BSM decay chain—be allowed to cluster into jets? It is in fact often desirable in analyses to work with disambiguated objects, whereby "interesting" electrons/photons/muons are maintained as a separate collection and jets are formed only out of the remaining particles as befits the QCD half of the event. However, this sophistication is rather unnecessary for a fully hadronic search which will anyway veto events with well-identified leptons, and furthermore does not make use of flavor information in any of search variable. The simpler route of constructing jets

[3] Cut flows that require further flavor and/or object identification criteria would require modifications to the background estimation methods.

from all available particles has thus been taken.

The following is a detailed description of the selection criteria outlined in Section 3.1. These are the cut flows that the background predictions must mimic, although particular prediction methods may start from different control samples, and/or only apply a subset of the search selections and emulate the rest. These details are deferred to the specific sections discussing the background predictions.

3.2.1 Trigger Requirement

Due to the high rate and cross-section of pp collisions, it is not possible to collect all events produced at CMS. It is also not advisable to collect a random subset of events, because by far most of these will be uninteresting low-energy multi-jet production. Instead, the CMS experiment utilizes a trigger system that selects events based on various kinematic and object identification criteria. Triggers and other layers of the experiment that participate in real time parallel to data taking are referred to as "online", as distinguished from the "offline" systems that work with stored data samples in a longer timescale. The online selection criteria are typically much simplified compared to quantities that may be used offline, due to the constraint of the software being able to run quickly enough to make immediate decisions about a huge input rate of events. The most salient example here is that the online jets are reconstructed using only the calorimeter systems and not the Particle Flow reconstruction described in Section 2.3, and also via the Iterative Cone [79] rather than anti-k_T clustering algorithm. Furthermore, the detailed p_T and η parametrized energy scale corrections are not applied to these jets, but only a simple scaling of the momenta of $|\eta| > 3$ jets by a factor of 0.7 is performed in order to account for the rather different HF energy scale.

The events used in this study are collected by trigger paths based on the online quantity HT, defined as the scalar sum of transverse energy of the subset of online jets which have $E_T > 20\,\text{GeV}$. Because the instantaneous luminosity of the experiment was increased over the course of the year, the HT threshold had to be similarly evolved in order to maintain a manageable data collection rate. The full data sample here is collected via the following triggers for the corresponding data collection run ranges:

Run Range	138560 - 147195	147196 - 148818	148819 - 149294
Trigger	`HLT_HT100U`	`HLT_HT140U`	`HLT_HT150U_v3`
HT threshold (GeV)	100	140	150

Due to differences in the emulation software compared to what was actually run online however, these trigger requirements were not imposed on the MC simulated samples. The data trigger efficiency with respect to the quantity H_T (to be defined below) used in the offline analysis has anyway been measured[4] to be 100% in the region

[4]This measurement is performed using a sample collected with a much lower threshold trigger, `HLT_Jet15U` which only requires presence of a single trigger jet with $p_T > 15\,\text{GeV}$, and is expected

$H_T \geq 300\,\text{GeV}$, with pessimistically 2% inefficiency allowed by the statistical uncertainty of the measurement.

3.2.2 Data Clean-up Filters

As discussed in Section 3.1.1, the variable $\not\!\!E_T$ is sensitive to non-collision-physics effects that plague any realistic detector, since these tend not to satisfy transverse momentum balance. The following selection criteria and event filters have been imposed to remove the bulk of these effects:

≥ 1 **good primary vertex.** A distinctive feature of collision events is that all particles originate from a single point in space. Since the tracking system can reconstruct the trajectory of particles, these primary vertex (PV) location(s) can be deduced, roughly speaking by looking for sets of tracks that coincide at approximately the same point. Requiring that each event has at least one high quality reconstructed primary vertex removes a significant portion that are purely calorimeter noise, and also those events where an interaction did occur but is so highly displaced from the center of the detector as to suffer from reconstruction problems. The quality criteria for these vertices is that they be within the expected luminous region of 24 cm in z and 2 cm in ρ from the origin, and that the vertex fit has greater than 4 degrees of freedom. The first vertex in the standard ordered list is referred to "the" primary vertex for the event. This ordering is by decreasing value of $\sum_{\text{track}}[\max(0, p_{\text{T,track}} - \delta p_{\text{T,track}})]^2$, where $p_{\text{T,track}}$ are the momenta of tracks collected into the vertex, and $\delta p_{\text{T,track}}$ the associated uncertainties on these momenta.

Tracking failure filter. Problems with track reconstruction in particular events can result in high $\not\!\!E_T$ due to the extensive use of track information to correct the energies of calorimeter deposits as performed in the Particle Flow reconstruction algorithms. These are rejected by requiring that $\sum p_{\text{T,track}} > 0.1 \sum p_{\text{T,jet}}$ for all events, where the left hand sum is over all tracks within $\Delta z < 1\,\text{cm}$ and $\Delta\rho < 0.2\,\text{cm}$ of the primary vertex, and the right hand sum is over all PF jets (no p_T or η requirements). In general, this and the primary vertex filters are very effective in cleaning up most of the visibly wrong events in the sample, because failure to reconstruct a sensible tracking view of the event is an indication that it is incompatible with various collision-centric hypotheses that are applied in the track reconstruction. Figure 3.2.1 is an example of a highly displaced event that is rejected by this filter, but not the primary vertex filter because there is a small population of tracks that appear to be originating from somewhere near the detector center. Figure 3.2.2 shows an event with a spectacular amount of activity in the muon chambers, all more or less aligned in the same direction and probably

from MC simulation studies to be fully efficient in the region of interest for the HT trigger efficiency turn-on.

what is called a "cosmic shower". This is an example of unexpected anomalies that this filter is robust enough to catch, at least with substantial enough frequency in order for them to be flagged so that dedicated filters may be designed.

Beam background rejection. The vacuum in the LHC beam pipe is not perfect, resulting in the occasional residual gas particle that may undergo elastic/inelastic scattering with the proton beams. Furthermore these and other particles e.g. as produced when the tails of beams scrape along collimators or beam pipe walls may form a halo of secondary particles that travel alongside the beam bunches. When particles from either of these sources are scattered at close enough proximity to enter the detector, they can create such high occupancies in the tracking system that part of the tracking algorithm is shut off by safety margins during event reconstruction. These pathological events are rejected by requiring that in events with more than 10 tracks, at least 25% of these tracks must pass the CMS standard "high purity" criteria.

Beam halo filter. Beam halo muons are particularly dangerous because of their long lifetimes and penetrating power, which allows them to occasionally traverse the CMS detector and leave energy deposits in the calorimeters. Although minimally ionizing particles, a beam halo muon traveling through the calorimeters tends to remain roughly parallel to the beam-line, thereby leaving a long train of energy deposits that are then interpreted by the collision-centric reconstruction algorithms as high transverse momentum jets. However this characteristic traversal pattern can be identified with beam halo specific algorithms, and afflicted events rejected from the data sample. The algorithm used in this study is the one utilizing measurements in the Cathode Strip Chamber (CSC) subdetector, and with the tight setting of identification criteria [4]. There is also a further source of non-collision muons that have some efficiency to be detected by this filter, i.e. those from cosmic rays which manage to make it to the LHC tunnel despite it being situated far underground. Most cosmic muons come through the vertical shaft that was used to lower the CMS detector into its cavern. Since the shaft is situated at a horizontal displacement from the detector itself, these muons also have a tendency to traverse the detector at a relatively shallow angle similar to that of beam halo muons. Dedicated cosmic muon reconstruction algorithms would provide higher efficiency rejection, but are not employed at this time.

HB-HE noise filter. Most of the noise in the barrel and endcap hadron calorimeters are rejected with a CMS standard filter. One type of cuts are based on counting the number of active channels per read-out unit of the calorimeter, thereby rejecting suspiciously high patterns of activity. The other type is based on timing information of the signals, in particular requiring that they exhibit physics-like pulse shapes.

(Additional) HCAL noise filter. Other than a suspiciously large number of firing channels per read-out unit, the HCAL can also exhibit single-channel noise. Newer software versions of the above filter include rejection for this type of noise, but for now the one data event (149063:19:21076423) exhibiting it has been removed by hand.

EE noise filter. A source of rare noise simultaneously affects the ECAL endcaps and the muon systems, and is rejected by requiring the number of energy deposits in the EE to be smaller than 2000.

3.2.3 Particle Flow Mis-reconstruction Filters

The reconstruction of tracks inside jets is difficult because of the large number of particles mostly collimated into a small region near the core of the jet. Since the momenta of tracks are deduced purely from pattern recognition, in the worst case scenario tracks can be reconstructed that have wildly unphysical momenta, either by a random coincidence of hits, or by joining up pieces from different particles. When a very large momentum (spurious) track is reconstructed, it can propagate into the PF reconstruction of the event in such a way as to significantly spoil the transverse momentum balance. This happens mostly for types of particles where there is little or no calorimetry information that can be used to constrain the momenta, e.g. muons. In fact, a substantial portion of what is naively reconstructed as muons inside jets are actually just a coincidence of tracks (real or not) with "punch-through" hits in the muon chambers that arise from leakage of showers past the hadron calorimeters, and the rare hadron that is energetic enough to survive the calorimetry and continues showering in the steel support structure/magnet return yoke in between the muon chambers. Inclusion of these so-called punch-through muons in the list of PF particles at best double-counts the actual particles which have already been accounted for in the calorimetry readout. These issues motivate the use of two event filters[5]:

Inconsistent PF muon filter. As explained in Section 2.3.4, muons may be reconstructed by either the "tracker" or "global" algorithms. Most real, high-p_{T} muons should be found by both algorithms, and requiring that a reconstructed muon be simultaneously a tracker and a global muon turns out to be a good quality criterion. An "inconsistent" muon is therefore defined to any muon with $p_{\mathrm{T}} > 100\,\mathrm{GeV}/c$ and yet either (a) not a tracker muon; or (b) not a global muon; or (c) has a tracker-only p_{T} that deviates by more than 10% from the global fit p_{T}. Events with one or more inconsistent PF muons are rejected.

[5]It is noted that there is in principle no need to reject events, but simply to remove the problematic muons from the event. The event rejection is just presently the technically easier route; software improvements are foreseen for the future.

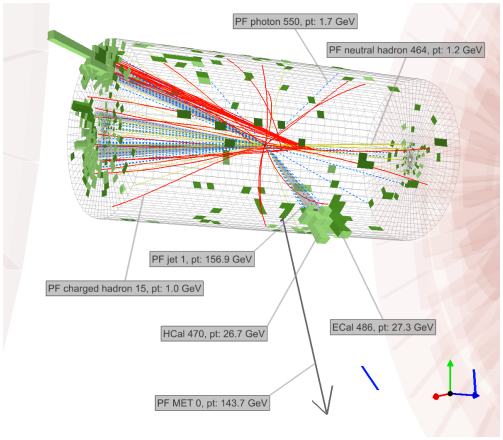

Figure 3.2.1: 3D detector view of event 882505300 of luminosity block 612 in run 148862, which has some tracks indicating that the actual hard collision is highly displaced from $z = 0$. The location of $z = 0$ can be seen as where the dotted blue photon tracks converge, since photons do not have tracking information and can only be assumed to originate from the detector center. The true origin of the collision is probably where the red charged hadron tracks converge. The right half of the event has failed to be reconstructed.

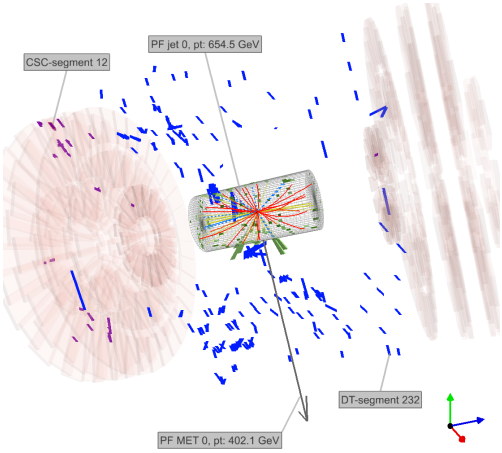

Figure 3.2.2: 3D detector view of event 790411869 of luminosity block 814 in run 149181, which has an enormous number of hits in the muon chambers. The leading jet reconstructed by the Particle Flow algorithm has $p_{\mathrm{T}} > 650\,\mathrm{GeV}/c$ because of "muons" that can randomly be reconstructed from the sheer combinatorial possibilities. In contrast the leading jet reconstructed only using the calorimeters has $p_{\mathrm{T}} = 150\,\mathrm{GeV}/c$, which is still rather high but not to such extreme. This event is flagged by the "tight" setting of the CSC beam halo identification algorithm.

Greedy PF muon filter. In the PF reconstruction algorithm, calorimeter deposits compatible with the trajectory of isolated muons are removed from the event, since the muon momentum is already accounted for. In the software version used here, this can erroneously remove deposits with energy larger than the magnitude of the muon's momentum, which is clearly non-physical. Events with one or more such "greedy" muons are rejected.

Furthermore, since the MC simulation closure tests have been performed with with effectively about $2.5\,\text{fb}^{-1}$ equivalent luminosity datasets, additional quality criteria are used to further reject punch-through muons that are not yet required for the $36\,\text{pb}^{-1}$ data measurement. These have *no effect in the data sample selection*, but are listed here because they are used in particular for the MC simulated samples relevant to the QCD background estimation:

Low-quality PF muon filter. A muon is defined to be low quality if it has momentum $p > 500\,\text{GeV}$ and yet does not pass the CMS standard `TMLastStationLoose` nor the `TM2DCompatibilityTight` identification criteria, and either (a) only have hits in the first muon station; or (b) have more than 10 hits in one station; or (c) are reconstructed with the global fit algorithm but do not penetrate to at least the third muon station or have some hits in first three stations that are not used in the fit. Events are rejected if they contain one or more low quality muons.

3.2.4 Background Feature Rejection

In order to remain sensitive to as wide a range of potential signals as possible, the search cuts in this analysis have been chosen in a background-centric way, i.e. just tight enough to exploit most of the rejection power for various backgrounds. The following core set of cuts are all low cost in terms of inefficiency when applied to fully hadronic BSM signals:

Muon veto. Tight-identified muons are required to have $p_\text{T} \geq 10\,\text{GeV}/c$ and $|\eta| < 2.4$, to satisfy the CMS standard `GlobalMuonPromptTight` quality criteria, to have tracks with ≥ 11 hits in the silicon tracker system, to be within $\Delta z < 1\,\text{cm}$ and $\Delta\rho < 0.2\,\text{cm}$ of the primary vertex, and to be isolated with $\text{iso}_\ell < 0.2$. Events are rejected if they contain one or more tight-identified muons. Here the lepton isolation variable is $\text{iso}_\ell = (\sum_{h^\pm}^{\Delta\text{R}<0.4} p_{\text{T},h^\pm} + \sum_{h^0}^{\Delta\text{R}<0.4} p_{\text{T},h^0} + \sum_{\gamma}^{\Delta\text{R}<0.4} p_{\text{T},\gamma})/p_\text{T}$, where $h^\pm$ are charged hadrons, h^0 are neutral hadrons, and γ are photons as reconstructed by the PF algorithm, and the sums run over all particles of the given type and within $\Delta\text{R} < 0.4$ of the direction of the lepton of interest.

Electron veto. Tight-identified electrons are required to have $p_\text{T} \geq 10\,\text{GeV}/c$ and $|\eta| < 2.5$ (excluding the barrel-endcap transition region $1.4442 < |\eta| < 1.566$), to have

at most one "lost" hit expected but not found along the track trajectory, and to be compatible with the primary vertex and isolated by the same criteria as described above for muons.

ECAL trigger primitive (TP) filter. About 1% of channels in the ECAL subdetector are masked due to being noisy, malfunctioning, or dead. These regions can be quite large especially when it is a case of a 5×5 block of crystals (corresponding to a "trigger tower") suffering from the loss of the same read-out electronics. When high p_{T} photons, electrons, and jets fall into such masked regions, this can result in otherwise balanced events appearing to have high $\not{E}_{\mathrm{T}}$. Fortunately, each trigger tower has an alternative, less fine-grained read-out interface for trigger purposes, and for a large number of towers this remains functional. Events are therefore rejected if there is a suspiciously large energy as read out via the trigger primitive information, i.e. energy $\geq 63.75\,\mathrm{GeV}$ which corresponds to the saturation value of this read-out mode.

Boundary energy (BE) filter. For masked ECAL towers where the TP information is not available, one may still try to identify remnants of activity in the surrounding channels. This is performed by summing the energies of all crystals that are nearest-neighbors of some crystal in this masked tower [58]. Events are rejected if this "boundary energy" exceeds $> 10\,\mathrm{GeV}$ for any ECAL tower with status code ≥ 14.

The last two filters, being the TP- and BE-based cuts, are referred to in general in the text as "ECAL hole filters". It is also noted that there is no associated veto for events containing the tau lepton. This is because tau identification is more difficult in terms of purity vs. efficiency, and is for now a future venture.

3.3 Topology-Driven Search Regions

The remaining sets of cuts are those that yield the most signal-background discrimination, and have already been prefaced in Section 3.1. The only fine print is that instead of $\not{E}_{\mathrm{T}}$, it is easier for the background estimation to work with the quantity $\vec{\not{H}}_{\mathrm{T}} \equiv \sum_{\mathrm{jet}} \vec{p}_{\mathrm{T,jet}}$, which is the so-called "missing H_{T}" because it computes the transverse balance of the event only using jets[6] above a threshold (though not necessarily the same as used in the computation of H_{T}). This does not mean that the procedures could never be generalized to predict $\not{E}_{\mathrm{T}}$ instead, but simply that it is not within the scope of the current study. All discussions that follow therefore pertain to $\not{H}_{\mathrm{T}} \equiv |\vec{\not{H}}_{\mathrm{T}}|$ in lieu of $\not{E}_{\mathrm{T}}$.

Four quantities are used to define regions of interest to this search:

[6] Recall that jets are clustered using all particles in the event, so there is no need to include other object types (in fact it would be double-counting to do so).

N_{jet} $\equiv$ Number of jets that have $p_{\text{T}} \geq 50\,\text{GeV}/c$ and $|\eta| \leq 2.5$
H_{T} $\equiv$ Scalar sum p_{T} of $p_{\text{T}} \geq 50\,\text{GeV}/c$, $|\eta| \leq 2.5$ jets
$\vec{\not{H}}_{\text{T}}$ $\equiv$ Vector sum $\vec{p}_{\text{T}}$ of $p_{\text{T}} \geq 30\,\text{GeV}/c$ jets (no η requirement)
$\Delta\phi_i$ $\equiv$ $\Delta\phi(\not{H}_{\text{T}}, \text{jet } i)$, where all jets are ranked in decreasing order of p_{T}, and $i = 1$ refers to the highest p_{T} jet.

The following search regions are identified:

	N_{jet}	$\Delta\phi_1$	$\Delta\phi_2$	$\Delta\phi_3$	H_{T} (GeV/c)	$\not{H}_{\text{T}}$ (GeV/c)
Baseline	≥ 3	≥ 0.5	≥ 0.5	≥ 0.3	≥ 300	≥ 150
High $\not{H}_{\text{T}}$					≥ 300	≥ 250
High H_{T}					≥ 500	≥ 150

The H_{T} threshold is required to be at least $300\,\text{GeV}/c$ in order to stay in the fully efficient region of the HT trigger efficiency. The N_{jet} and $\Delta\phi$ cuts have also not been varied at this time. What distinguishes the search regions are therefore the H_{T} and $\not{H}_{\text{T}}$ cuts. The baseline selection is a high statistics region which facilitates studies like that of the shapes of predicted background distributions. The high $\not{H}_{\text{T}}$ region is expected to have a very small QCD background, and has high efficiency for signals with short decay chains. The high H_{T} region is required in order to recover efficiency for signals with long cascade decays. It has however a substantial QCD background, i.e. almost half of the total. The complementarity of these search regions will be seen in Section 9.

3.3.1 Cut Flow Tables

For reference, the numbers of selected data events and rejection powers of the selection criteria listed in the previous section are shown in Table 3.1. The cuts are applied consecutively from the top to the bottom row of this table. The particular order in which the vetoes and filters are applied are not very important, because the events that they reject are almost entirely unique. The only significantly correlated cuts are the TP and BE filters, which can be understood since they address the same reconstruction issue. It turns out that these ECAL hole filters do not have much impact after the $\Delta\phi$ cuts; they are expected from MC simulation studies to help in rejecting QCD events with very high values of $\not{H}_{\text{T}}$, but there is not a substantial amount of such events to begin with in the high $\not{H}_{\text{T}}$ selection. In contrast, the PF mis-reconstruction filters are quite necessary especially in the high $\not{H}_{\text{T}}$ cut flow.

Table 3.2 shows the number of events expected in the search regions, also with the lepton veto and $\Delta\phi$ cuts relaxed to see how they affect the background composition as predicted via MC simulated samples (Appendix A.2). With only a $\not{H}_{\text{T}} \geq 150\,\text{GeV}/c$ selection, the background is half QCD, which the $\Delta\phi$ cuts remove with 88% efficiency. This cut also removes a substantial amount of top/EWK backgrounds, although the inefficiency for the LM1 signal benchmark point remains quite low. The lepton veto then removes a bit more than half of the remaining top/W backgrounds, i.e. about

Consecutive cuts	$\not{H}_T \geq 150$		**Baseline** $\not{H}_T \geq 150, \Delta\phi$		**High $\not{H}_T$** $\not{H}_T \geq 250, \Delta\phi$		**High H_T** $H_T > 500, \Delta\phi$	
HT trigger	601		200		37		69	
Muon veto	539	(10)	155	(23)	28	(24)	54	(22)
Electron veto	496	(8.0)	131	(16)	24	(14)	51	(5.6)
EE noise filter	495	(0.2)	130	(0.8)	23	(4.2)	50	(2.0)
Inconsistent μ filter	479	(3.2)	121	(6.9)	18	(22)	43	(14)
Greedy μ filter	475	(0.8)	120	(0.8)	17	(5.6)	43	
Beam halo filter	474	(0.2)	119	(0.8)	16	(5.9)	43	
Tracking failure filter	462	(2.5)	117	(1.7)	16		42	(2.3)
HCAL noise filter	461	(0.2)	116	(0.9)	15	(6.3)	41	(2.4)
TP filter	391	(15)	113	(2.6)	15		40	(2.4)
BE filter	379	(3.1)	111	(1.8)	15		40	

- $\Delta\phi$ refers to the cuts: $\Delta\phi_{1\text{-}2} \geq 0.5, \Delta\phi_3 \geq 0.3$

Table 3.1: Numbers of data events remaining after various consecutive stages of event clean-up criteria, starting from a preselection requiring ≥ 1 primary vertices, beam background rejection, HB-HE noise filter, $H_T > 300\,\text{GeV}$, and ≥ 3 jets. In parentheses are the percents of events rejected relative to the previous steps in the cut flow, with locations of zero rejection left blank for visual emphasis. Cuts with $> 5\%$ relative rejection power are highlighted in red.

$60\% - 70\%$ of the events with the W decaying eventually into a muon or electron (also counting subsequent decays of the tau in $W \to \tau\nu_\tau$). The veto is less efficient in $t\bar{t}$ events than W because the higher multiplicity of jets in the former leads in general to a higher probability for leptons to be non-isolated via accidental overlap with a jet, but also because the top quarks can be collimated in their decays. Lastly, the high-$\not{H}_T$ selection is almost fully efficient in rejecting QCD, and also $\geq 80\%$ of the top/W backgrounds, at almost the same cost in LM1 signal inefficiency as the high-H_T selection. In contrast the high-H_T selection retains more of the QCD background relative to the other SM processes, and is therefore complementary in terms of background composition. The LM0/LM1 benchmark points also illustrate the complementarity of the high-$\not{H}_T$ and high-H_T regions in terms of signal efficiency, since the high-H_T selection retains more of LM0 than the high-$\not{H}_T$ selection—even though LM0 is actually a lower mass scale point than LM1, it has more events with cascade decays.

The above identifies the following main backgrounds to this search, prediction methods of which will be presented in the associated sections:

W and $t\bar{t}$: [Section 5] These processes have high $\not{E}_T$ by way of leptonic decay(s) of the W boson(s), and only survive the search cuts if the lepton is a tau or is a muon/electron that failed the identification criteria in some way. The contribution due to fully hadronic decays of the W are covered by

Sample	$\not{H}_T \geq 150$		$\not{H}_T \geq 150$ $\Delta\phi$		**Baseline** $\not{H}_T \geq 150$ ℓ veto, $\Delta\phi$		**High $\not{H}_T$** $\not{H}_T \geq 250$ ℓ veto, $\Delta\phi$		**High H_T** $H_T > 500$ ℓ veto, $\Delta\phi$	
Data	482		180	(63)	111	(38)	15	(86)	40	(64)
SM	419		158	(63)	95	(38)	14	(85)	30	(69)
LM0	391		303	(23)	231	(24)	84	(64)	126	(45)
LM1	71.2		60.4	(15)	45.0	(25)	31.3	(30)	33.8	(25)
$Z \to \nu\bar{\nu}$	26.7		21.1	(21)	21.1		6.3	(70)	5.7	(73)
W	93.9		57.8	(38)	23.5	(59)	4.7	(80)	7.6	(68)
$\hookrightarrow \mu \vee \tau_\mu$	38%		39%		26%		20%		29%	
$\hookrightarrow e \vee \tau_e$	44%		45%		35%		20%		43%	
$\hookrightarrow \tau_h$	18%		16%		39%		60%		29%	
$t\bar{t}$	70.5		49.1	(30)	23.9	(51)	2.6	(89)	6.7	(72)
$\hookrightarrow \mu \vee \tau_\mu$	30%		31%		22%		33%		17%	
$\hookrightarrow e \vee \tau_e$	31%		31%		26%		33%		33%	
$\hookrightarrow \tau_h$	21%		20%		43%		33%		33%	
$\hookrightarrow$ (other)	18%		18%		9%		0%		17%	
QCD	222.0		27.0	(88)	24.6	(9)	0.2	(99)	9.9	(60)
Misc.	6.1		3.4	(44)	2.1	(38)	0.2	(90)	0.2	(90)

- $\Delta\phi$ refers to the cuts: $\Delta\phi_{1\text{-}2} \geq 0.5, \Delta\phi_3 \geq 0.3$
- "Misc." processes consist of WW, WZ, ZZ, tW, Wγ, Zγ, and Z/$\gamma^\star$

Table 3.2: Numbers of data events remaining after various consecutive stages of event selection cuts. In parentheses are the percents of events rejected relative to the previous steps in the cut flow, with locations of zero rejection omitted for visual emphasis. Cuts with relative rejection power between 40% and 80% are highlighted in blue, and those with rejection power $\geq$ 80% are highlighted in red. For the W and $t\bar{t}$ backgrounds the break-down into various (semi-leptonic) decay channels are also shown, and the $t\bar{t}$ (other) category consists mostly of di-leptonic decays.

the QCD background prediction, of which they are anyway a miniscule fraction.

$Z \to \nu\bar{\nu}$: [Section 6] This is an irreducible background in the sense of having no obvious handles by which it can be rejected.

QCD: [Section 7] This enters the search region by means of jet mismeasurements; if there is a noise contribution the noise has to overlap with real activity in order for it to survive the noise rejection cuts, in which case they are also considered as part of the jet resolution.

The W/top and invisible Z background estimations have been performed by others [85, 17, 15] and are only summarized in this document for completeness.

Chapter 4

Roles of Monte Carlo (MC) Simulation in Data Analysis

4.1 Event Generators and Detector Simulations

Given a function $f(q)$ defined in an n-dimensional space and a volume $\mathscr{V}$, Monte Carlo integration is a "brute force" technique that yields the integral $\int_{\mathscr{V}} d^n q f(q)$ almost regardless[1] of how complicated f and $\mathscr{V}$ might be. The naive MC integration algorithm [69] is simply:

1. Pick N random points $p^{(i)}$ within a simple volume $\mathscr{U}$ (e.g. box) that contains $\mathscr{V}$.
2. For each $p^{(i)}$, evaluate $f^{(i)} = f[p^{(i)}]$ if $p^{(i)}$ is within $\mathscr{V}$, or $f^{(i)} = 0$ otherwise.
3. The approximate integral is then $\int_{\mathscr{V}} d^n p f(p) \approx \mathscr{U} \sum_{i=1}^{N} f^{(i)}/N$.

MC integration is particularly appealing because of its flexibility, and ability to handle many-dimensional problems. For example, if $\mathscr{V}$ is not known analytically in the sense of a formulaic specification for the limits of integration for each of the $\int dp_k$, $k = 1, \ldots, n$, then it would not be possible utilize most deterministic integration techniques. For a fixed amount of computing time a.k.a. N, one can also always get a complete (if crude) answer out of MC integration, whereas deterministic techniques do not necessarily converge after an arbitrary number of steps. Another point is that it is not at all required for the space $\mathscr{U}$ to be sampled uniformly. One can concentrate the sampling of points into regions where f has interesting behavior, and use less points for regions where f is slowly varying. This is at cost that each $f^{(i)}$ in (3) must now be weighted by a factor that compensates for the over-sampling of some regions and under-sampling of others.

[1] Well, at least for sufficiently well-behaved functions and volumes. There is quite a bit of sophistication involved in performing MC integration of arbitrary functions in a sensible and efficient way; the interested reader is referred to other literature [82, 69].

All of the above has direct relevance for the problem of computing theoretical expectations to compare to data collected at a collider experiment. Typically, one identifies a few salient distributions that one wants to check, for example H_{T} and $\not{H}_{\mathrm{T}}$ in the context of this search. Because detector resolutions vary depending on the true properties of the object in question, it is typically (mathematically) impossible to "unfold" these data distributions in a unique way back to what the underlying true distributions must have been. In fact for most cases in high energy physics, one does not try to unfold data distributions back to the truth, but rather to smear theoretical distributions by expected detector resolutions to obtain data-like distributions to compare to. On top of this, the event selection criteria likely single out highly nontrivial regions over which the theory must be integrated in order to predict the distributions of interest.

This is of course a place in which MC integration steps in, and in a very conceptually natural way. The analogy to $f^{(i)}$ here is a full-blown *event*, which encodes not only particular quantities like the value of H_{T} and $\not{H}_{\mathrm{T}}$, but rather every piece of information from parton and hadron level down to the amount of energy deposited in various detector subsystems. Given the many qualitatively different effects to be modeled, the procedure is factorized into several stages:

Event generation. This initial stage predicts the physics that occurs at the instant of the collision, i.e. the scattering from initial into final states, decays of the latter (if any), and eventual hadron formation due to QCD confinement. For this the PYTHIA [82] event generator is probably the most widely used in CMS, although there are several other close contenders like Herwig [39]. Because there is not one universally applicable model that can describe the entire process, this calculation has to be broken up into perturbative versus non-perturbative parts. The main concepts are illustrated in Figure 4.1.1 and explained below:

Matrix Element (ME) calculation. For a given set of initial and final states, the computation of the scattering amplitude via matrix element methods is a staple of QFT textbooks [83]. In the language of the above, $f(p)$ would be the differential cross-section for such a process, with p being the phase space in which the reaction occurs and of which $\mathscr{V}$ is the kinematically allowed subspace. At this stage an event is fully specified by the n-dimensional vector x and the sampling of events is such that the frequency to have generated an event in a little volume $d^n p$ around p is $d^n p f(p)$. f consists of two aspects. The first is the parton distribution function (PDF), which provides the probability to find a parton of a particular flavor carrying a fraction x of the beam energy. These PDFs are obtained from fits of theoretically expected trends to experimental data, and for proton beams are available up to NLO expansions in the perturbation theory calculation. The second half is the usual calculation of the probability for these partons to scatter into the desired final state, which is completely specified by the QFT, and typically calculated to tree level.

Final state radiation (FSR). Colored and electrically charged particles in the final state radiate gluons and/or photons proportionally to the energy of said particle, and such radiative corrections can lead to qualitatively different event topologies i.e. promoting formally $2 \to 2$ ME processes to $2 \to 3$ $(4, \ldots)$ events in the final accounting of resolvable objects. In principle, these effects can all be calculated in the ME framework. In practice, this is rarely feasible because of the exploding dimensionality of the phase space, as well as divergences in the cross-section whenever the emitted particle is very soft or very collinear to the radiating parton. There is of course not a real singularity in the theory, but rather one arises because loop corrections that should have canceled the tree-level divergences have been neglected in the computation. As such, ME calculations involving massless partons have to be arbitrarily cut off in these problematic phase space regions. These missing pieces are then filled in by means of a complementary approximation, e.g. parton showers (PS). The latter is a technique by which all outgoing partons from the ME computation are evolved by asking the question of whether or not a branching like $q \to qg$, $g \to gg$, etc. should occur at some particular "time"[2]. The partons radiated in such a branching may themselves undergo branchings at some later time, and so on, leading to a showering behavior that progresses until some cut-off scale where QCD confinement kicks in.

Initial state radiation (ISR). Since ISR occurs when parton exchanges inside a hadron are interrupted by the hard scatter, one would naively have to model the collective behavior of all partons inside the hadron in order to predict what happens in case one of them should participate in a collision. This is clearly computationally difficult. Instead the trick used by software like PYTHIA is to start from the ME process, and evolve the incoming states *backwards* in time, via the same parton shower technology as for FSR.

Hadronization. QFT computations are perturbative, and appropriate at short scales where the strong coupling is small. It cannot be used to predict how partons are confined into hadrons, for which phenomenological models have to be used instead. The reader is referred to [82, 39] for details of two qualitatively different hadronization models.

Underlying event. The ME computation above is typically referred to as the "hard scatter" part of the event. After tracing backwards from the incoming states of the ME via the ISR showering algorithm, two initiating partons are identified, i.e. one per beam hadron. The remainder of the hadrons form beam remnants that have to be added into the event in an energy correlated, color-connected way. Actually there can also be multiple parton interactions

[2]Here "time" is not literally *time*, but rather some order parameter like the energy or (transverse) momentum scale of the branching.

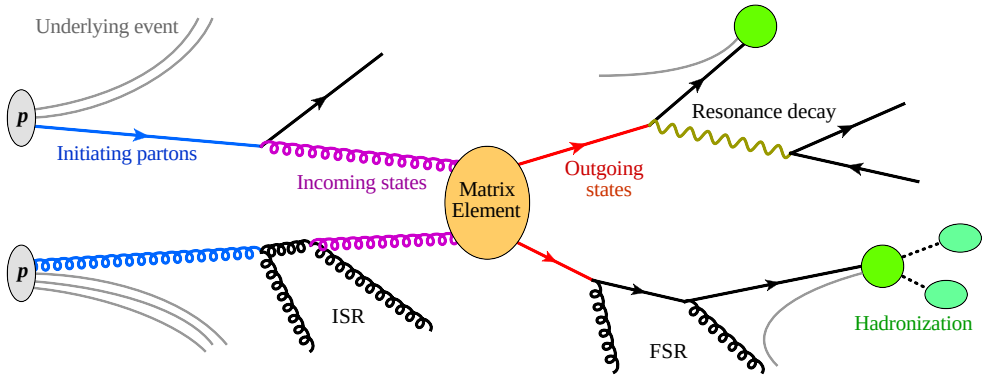

Figure 4.1.1: Illustration of various stages in the event generation process. Time can be thought of as flowing from the left to right, and the further the stage is away from the ME calculation, the less of it is known from first principles.

per event due to the composite nature of the beam hadrons, which may be correlated with the hard scatter in flavor, color, and momentum space. Both these sources of additional activity are collectively called the "underlying event", and have phenomenological knobs especially for the modeling of multiple parton interactions. One of the first tasks at a hadron collider is to adjust these knobs to best match observation, and the Z2 tune is the preferred one for LHC data although some samples were only available with an alternative D6T tune (see Appendix A).

Detector simulation. If event generation is complex, simulating the detector response is even more so. Here there is a "full" simulation option which encodes careful understanding of how particles interact with every piece of the detector, and is the first recourse for comparisons to data. All the MC simulated samples for SM processes used in this study utilize full detector simulation, as do selected SUSY signal benchmark points. However there is also a "fast" simulation option which utilizes parametrizations whenever possible, and is ideal for quick studies as well as generating very large numbers of events, because of the order-of-magnitude reduction in computing time that it provides. This fast simulation is used for all the BSM signal samples that scan over a grid of model parameter values. Major features of the two modes are highlighted below:

Full simulation. All particles from the event generation above are propagated from the interaction point through the magnetic field and the CMS detector geometry, allowing for in-flight decays. The geometry is a description of how every active element of the detector is positioned in space, as well as intervening inactive material that are nevertheless crucial to model because particles can interact with or even be stopped by them. The Geant4 [5]

software is used to describe energy loss in the detector material and simulates in detail electromagnetic and hadronic interactions that modifies particle trajectories and produces secondary particles as they travel through the detector. In the active detector elements, the passage of particles yield simulated hits. The final step in the detector simulation involves the emulation of the electronic read-out systems of the detector, also referred to as digitization. This process starts from the simulated hit positions and energy losses in the sensitive detectors, and aims to produce sampled signals that mimic the real data-acquisition conditions of CMS. It accounts for timing and position issues, charge drifts due to electromagnetic fields, electronics noise, malfunctioning channels, and so forth. These simulated signals are then processed in the same way as for data events.

Fast simulation. The parametrized simulation aims to maintain an agreement to within 1% of the detailed simulation. Instead of simulated signals in the read-out systems, what is delivered are reconstructed objects like tracks, calorimeter tower deposits and muons, of the same type as from the usual reconstruction, such that analysis software can be run transparently with both detailed and parametrized simulations. The particles from the event generation are also propagated through the magnetic field and unstable particles are decayed, but simplified versions of the detector geometry are used as the computational cost rises very quickly with the number of different elements that must be simulated. The reconstruction algorithms are also simplified. In the tracker, no pattern recognition is performed to search for tracks, but hits are fit to tracks along the actual simulated trajectories. Electromagnetic showers in the ECAL are simulated with a dedicated shower parametrization assuming a homogeneous calorimeter. As a second step, the energy distribution is sliced into a small array of crystals. Also in the HCAL the response is simulated using a dedicated parametrization for hadron showers, tuned on the full detector simulation with charged pions. For muons a simple parametrization of the detailed simulation efficiencies and resolutions is used, dependent on the muon momenta and pseudorapidities.

Pile-up interactions. Due to the high instantaneous luminosities of collisions at the LHC, several proton collisions can occur in the same bunch crossing. In general, only one of these collisions will contain a hard interaction of physics interest, while the other superimposed collisions will be soft minimum-bias or diffractive collisions. These overlapping interactions are referred to as pile-up collisions and some appropriate number of these should in principle have been overlaid on top of the main generated event before propagating it through the detector simulation. However this would have resulted in a large drain on computing resources because each event would take significantly longer to simulate. Instead, a pre-made bank of detector simulated minimum-bias samples are "mixed" into events of interest

at the level of hits in various detector elements.

4.2 The $\sqrt{s} \gg 2$ TeV Distrust of MC Predictions

In principle, if the current theory is to be tested, there should be no objection to comparing observations in data against calculations performed with said theory. There is however a more subtle point at play here: which aspect about the theory is it that is under question? As it stands, a disagreement with data can have at least three causes: (1) imperfect/incomplete calculation of SM theory; (2) imperfect modeling of the CMS detector; and (3) the presence of BSM events. If a discovery is to be made that can put into question the adequacy of the Standard Model, then it must necessarily discount (1) and (2). This is unfortunately not so obvious, because both involve various phenomenological parameters that have to be measured or tuned to match observation. This is obvious in the case of the detector modeling, which can furthermore not be fully determined using information from only laboratory tests of manufactured pieces. For example, there can be coherent electronics noise as seen in the EE and muon system in 2010 data collection runs, or (unintentional) mis-alignments in the detector assembly. It is also not always easy/quick to propagate this updated knowledge back into the simulation, which therefore tends to somewhat lag behind the state-of-the-art understanding of the detector.

Despite the success of QFT as a predictive theory, the full theoretical description of SM processes is also uncertain, due to complications explained in Section 4.1. A significant amount of effort over the course of years in hadron collider experiments go into verifying and tuning the phenomenological aspects to match data. The last comparable experiment is the Tevatron proton-antiproton collider, which operates at nearly $\sqrt{s} \sim 2\,\text{TeV}$, and has a very mature and reliable MC simulation as expected after more than one decade of operation. Now it has already been mentioned that the LHC runs at revolutionary energies, but there are also qualitative differences because it is a proton-proton collider. For example [21], the top quark pair-production cross-section is twenty times larger at the LHC due to an inversion of the main production mode from being quark-antiquark fusion to gluon-gluon scattering. On the other hand bottom quark pair-production and electroweak processes like W boson production is only larger by a factor of five. However, the W+multi-jet production cross-sections are orders of magnitude larger at the LHC, and for high center-of-mass energies the higher jet multiplicity cross-sections can even exceed that for lower jet multiplicities. This is a hint of the following aspects that will likely require re-tuning or higher precision theoretical calculations than have been tested at the Tevatron:

Gluon PDF. Many processes at the LHC are enhanced by gluon-gluon scattering diagrams, but the information about the gluon PDF is more uncertain than that for valence quarks of the proton. In fact, it shall be seen in Section 8.2 that the uncertainty in the theoretical modeling of the PDF and ISR in signal processes signif-

icantly degrades the strength of conclusions that can be drawn in some portions of parameter space; these uncertainties would also have affected MC simulations of SM backgrounds had they been used for predictions.

QCD radiation. Part of the theoretical modeling can be improved by evaluating matrix elements to higher precision, in particular the addition of extra QCD partons. The PYTHIA and Herwig software come with many built-in calculations for low-order (mostly $2 \to 2$, some $2 \to 3$) processes, but also have options to interface to external ME generators like MadGraph [61] and Alpgen [62]. The latter are dedicated to the generation of parton-level events for matrix elements with high multiplicities of final states (though still at tree level), and MadGraph in particular can compute arbitrary processes within a theory model of choice. Use of these external ME generators are of particular importance to BSM searches because the parton shower cannot be relied on to produce sufficiently hard and large-angle emissions on top of the partons from the ME, and may thereby underestimate the SM background with high multiplicity BSM-like final states. Except for the QCD processes[3], all other MC simulated samples used in this analysis have been generated with MadGraph.

ME-PS matching. The factorization of the event generation process into ME and PS approximations is arbitrary, and requires proper handling in order for the two descriptions to join up smoothly and without double-counting radiative effects. MadGraph and Alpgen both provide jet-based matching schemes, which have a tunable factorization/renormalization scale that must be empirically determined. A test by which the scale is varied up/down by a factor of two is traditionally used to demonstrate insensitivity to this unphysical parameter—or lack thereof, which can induce a large-ish systematic uncertainty. Unfortunately there is not (yet?) a similar matching scheme for photon radiation, which remains a caveat when simulating processes with one or more prompt photons in the ME calculation.

NLO K-factors. The change induced by a change in factorization/renormalization scale cannot correctly be interpreted as an uncertainty on the ME+PS calculation, although experimentalists have traditionally taken it as such, for lack of alternatives. The actual uncertainty can only be known by computing the size of the neglected terms in the ME computation, i.e. the NLO corrections. The ratio of NLO over LO computations are called NLO K-factors, and are in general phase-space and observable dependent. In [78] it is noted that there have been observations of dramatically large K-factors especially for high transverse momenta events. As an example, Figure 4.2.1 is a replica of the first figure in the afore-

[3]The reason for this is only pragmatic, i.e. because there were not enough events generated in the available MadGraph QCD sample in order for it to be sensible to use after the stringent event selection cuts in this analysis. Furthermore the MadGraph sample did not match as closely to the data as the PYTHIA sample, which might have been because it was only available with the D6T tune.

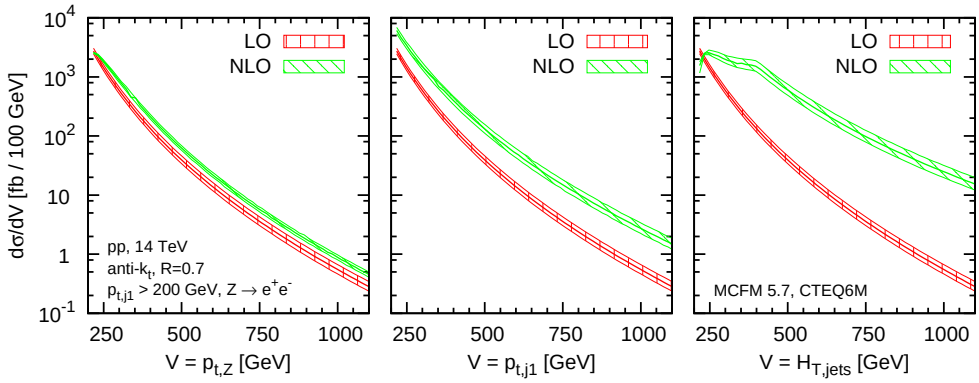

Figure 4.2.1: From [78]: The LO and NLO distributions for three observables in Z+jet production: the Z transverse momentum (left), the p_{T} of the hardest jet (middle), and the scalar sum of the transverse momenta of all jets (right). The bands correspond to the uncertainty from a simultaneous variation of the renormalization/factorization scale by a factor of two either side of a default $\mu = \sqrt{p_{\mathrm{T,j1}}^2 + m_{\mathrm{Z}}^2}$. The jet algorithm is anti-k_{T} with size parameter 0.7 and only events whose hardest jet passes a cut $p_{\mathrm{T}} > 200\,\mathrm{GeV}/c$ are accepted. The cross sections include the branching ratio $\mathrm{Z} \to e^+e^-$ and the $\sqrt{s} = 14\,\mathrm{TeV}$.

mentioned paper, and compares three observables in Z+jet events according to LO vs. NLO computations, for events with a leading jet of $p_{\mathrm{T}} > 200\,\mathrm{GeV}/c$. The Z p_{T} distribution is fairly well behaved, with an roughly constant K-factor of 1.5. However the leading jet p_{T} has a rising K-factor that reaches values of 4-6 at $p_{\mathrm{T}} \sim 1\,\mathrm{TeV}/c$, and the H_{T} K-factor is even more dramatic and approaches 100 at $1\,\mathrm{TeV}/c$. These large K-factors arise from the possibility to have NLO diagrams in which a soft/collinear Z was emitted, which make it into the jet p_{T} and H_{T} plots because there is no requirement on the boson p_{T}. This is not a problem per se if one only cares about events where the boson constitute a significant portion of the total momentum[4], but does illustrate that it is quite possible to run into a corner of phase space where LO computations are completely inadequate. For relatively low multiplicity, pure multi-jet production, general observables like H_{T} and the transverse momenta of leading jets can be predicted roughly to a factor of two (and not better) by the commonly used LO methods. It would seem though that caution is advisable for variables sensible to topological details, like angular or momentum correlation between jets, or those that probe extreme jet multiplicities.

In light of the above concerns, early searches in the CMS collaboration place a large emphasis on so-called data-driven methods, i.e. by which background predic-

[4]Note that this is different from just applying a high p_{T} requirement to the boson, because there would still be a problem if the energy scale of the event is so high that the boson is basically soft radiation.

tions are derived (almost) entirely from measurements in data control regions rather than by recourse to MC simulation. All the methods in this analysis follow this guideline. The discerning reader should however note that "data driven" does not mean "MC free", as the use of simulation is behind most of the search design, background prediction closure tests, various templates used for data fitting and modeling, extrapolations/parametrizations into regions of poor data statistics, cross-checks and bias and/or acceptance corrections for data-driven predictions, etc.

4.3 A Matter of Benchmarks

Although the design of search cuts is SM background motivated, it is impossible (or at least very ill advised) to completely ignore what BSM signal events may look like in these distributions. Furthermore, there is always a desire at the end of the day to analyze the results of the measurement in terms of compatibility with some signal hypotheses. In the case where an excess is seen, the ability to characterize it as a physically meaningful signal process will be invaluable to building confidence that it is not simply a statistical fluctuation/error in some background prediction or an unexpected background, and also to suggest confirming/distinguishing signatures to look for. If no excesses can be claimed, one would still like to know what signal models have been excluded so as to better focus efforts for the next round.

Unfortunately, here dark matter searches—especially those in the fully hadronic channel—suffer from the lack of a "smoking gun" distribution (e.g. mass peaks) that can be used to characterize observations in a model-independent way. On top of that, theoretical expectations are far less clear than they were when the W and Z bosons, or even the top quark, were discovered. Even the best-motivated models have very large allowed parameter spaces, but many parameter points which encode genuinely different physics are difficult to distinguish at a hadron collider. To avoid this divergence in the number of models that must be checked, the field has traditionally used restricted subspaces (such as the Constrained MSSM) which remove a lot of the complexity and redundancy. There is however significant dissatisfaction with results encoded in terms of these restricted subspaces, because they impose artificial and sometimes arbitrary constraints on kinematics and decay modes, and are not easy to translate to other spaces or models of theoretical interest.

To address this issue, the use of Simplified Model Spectra (SMS) has been proposed for studying and citing results of the LHC searches [49]. The gist of this idea is that the first stop when dealing with unknown physics is to simply work with *effective theories* rather than Lagrangians motivated by specific unification-scale concerns. As such, SMS are fully characterized by a (small) spectrum of BSM particles plus their production and decay modes. The continuous parameters are the masses and production cross-sections of the new particles, and their branching fractions into various modes, all of which can be taken as freely ranging and independent given the current lack of

knowledge. A further simplification employed in this document is to even work with SMS comprised of single topologies[5], which are given labels like the "T1bb" previously seen in Figures 3.1.1 and 3.1.2. This enables one to draw physically intuitive conclusions about how various results depend on a few model parameters. Appendix A contains details of how these samples have been generated in the MSSM language, but as explained in Section 1.5 the precise theoretical framework is unlikely to have visible experimental consequences—especially not for searches as simple as those discussed in this document. It is the view of the author that SMS are a particularly elegant language in which to phrase early discoveries, not because theoretical detail is unnecessary, but just premature.

[5] A "topology" should be thought of basically as a single Feynman diagram, but possibly up to including various decay channels for resonances, or flavor combinations of lepton partners.

Part III

Data-driven Background Estimations

Chapter 5

"Lost" Leptons in Top and W Production

These category of backgrounds cover the case of events where one or more W bosons, either from prompt W production, or from top production, undergoes leptonic decay. They then enter the search region if the charged lepton is a hadronically decaying tau, or otherwise if the electron/muon is out of geometric or kinematical acceptance, or is not identified/isolated. The electron and muon identification efficiency $\varepsilon^{\ell}_{\mathrm{ID}} = \varepsilon^{\ell}_{\mathrm{ID}}(p_{\mathrm{T},\ell}, \eta_{\ell})$ and isolation efficiency and $\varepsilon^{\ell}_{\mathrm{ISO}} = \varepsilon^{\ell}_{\mathrm{ISO}}(p_{\mathrm{T},\ell}, \Delta\mathrm{R}_{\ell,\mathrm{jet}})$ are measured using tag-and-probe techniques on Z events collected in data [85]. Here $\Delta\mathrm{R}_{\ell,\mathrm{jet}}$ is the distance between the lepton and the nearest $p_{\mathrm{T}} > 30\,\mathrm{GeV}/c$ jet[1] in the event, and is important in order to be able to treat the topologically different (Section 3.3.1) W and $t\bar{t}$ events on equal footing. The portion of the top/W background due to out-of-acceptance leptons is also very substantial, turning out to be about half of the total electron and muon contributions. Despite the high W mass which ensures that at least in its rest frame it should decay to high momentum leptons, in the lab frame W decays can appear quite asymmetric, with the charged lepton anti-aligned to its boost. Muons from tau decays also have to compete with the accompanying neutrino for momentum. Lastly, the $\not{H}_{\mathrm{T}}$ selection requirement tends to prefer the subset of events where the neutrino takes most of the W momentum, and all these effects result in a background with preferentially soft charged leptons.

The method by which this background is estimated is to start from a muon control sample, which differs from the preselection described in Section 3.2 only by:

- Collected with single muon triggers `HLT_Mu9` (for MC and data with run numbers below 147196) or `HLT_Mu15_v1` (for data with run numbers above 147196), instead of the HT triggers.
- Required to have exactly one muon with $p_{\mathrm{T}} > 20\,\mathrm{GeV}/c$ and $|\eta| < 2.1$, but oth-

[1] Excluding jets in a region $\Delta\mathrm{R} < 0.05$ around the lepton, because for reasons explained in Section 3.2 all leptons can also form or be part of a jet.

erwise satisfying the same identification and isolation requirements as for the lepton veto.

- The muon veto makes an exception only for the muon identified above. The electron veto is applied as usual.

This control sample of events differs only from the background to the search only by properties of the charged lepton, which is then manipulated as follows. Firstly, the muon selection has associated trigger, identification and isolation efficiencies that should be corrected for per event because of the kinematic and topology dependence of such efficiencies. This can be done by weighting each event in the control sample by a factor $1/\varepsilon^{\ell}_{\mathrm{ID}}\varepsilon^{\ell}_{\mathrm{ISO}}$ to correct to full efficiency. There is also an acceptance correction required to account for events with muons which have $|\eta| \geq 2.1$ or $p_{\mathrm{T}} \leq 20\,\mathrm{GeV}/c$ and therefore fail to be collected in the control sample. This correction is obtained from MC simulated $t\bar{t}$ and W samples as an overall scale factor. The final per-event correction factor for the muon control sample is therefore:

$$\frac{N^{\text{control-}\mu}_{\text{total}}}{N^{\text{control-}\mu}_{\text{in}}} \frac{1}{\varepsilon^{\ell}_{\mathrm{ID}}(p_{\mathrm{T},\ell},\eta_{\ell})\,\varepsilon^{\ell}_{\mathrm{ISO}}(p_{\mathrm{T},\ell},\Delta\mathrm{R}_{\ell,\mathrm{jet}})}$$

This corrected control sample can now be assumed to be the true number of events in each of the three flavor channels by lepton universality, which is then translated to the number of events in the background region as follows:

Non-identified/isolated e/μ. These are predicted by weighting each event in the control sample by the probability of its selected muon to be either out of the acceptance of the lepton veto selection, or to fail either identification or isolation. This is easiest done by considering that a lepton can only pass the requirements of the veto selection if it is all of: in acceptance, identified, and isolated, and then the probability of failing this is just one minus the aforementioned probability, i.e. $1-(N^{\text{veto-}\ell}_{\text{in}}/N^{\text{veto-}\ell}_{\text{total}})\,\varepsilon^{\ell}_{\mathrm{ID}}\varepsilon^{\ell}_{\mathrm{ISO}}$ for the desired lepton type (muon or electron). Note that even for the muon prediction this acceptance factor is different than that used to correct the control sample, because of the looser p_{T} and η requirements for leptons used in the event veto.

Hadronic tau decays. Here the selected muon is replaced by a tau jet, which are characterized by a low multiplicity of particles, typically a few pions and neutrinos. The tau-jet momentum is obtained by scaling the muon momentum with a factor drawn randomly from a response probability template obtained from MC simulated samples, where the response is defined as the ratio of the reconstructed tau-jet p_{T} over the true tau-lepton p_{T}. This procedure modifies the event by replacing the jet associated with the muon with the emulated tau-jet momentum, which is furthermore corrected for jet energy scale as would happen for any reconstructed jet. In order to probe the full response template this procedure is

Systematic uncertainty	Electron + muon	Hadronic tau
μ control sample statistics	$\pm 17\%$	$\sim \pm 30\%$
$\varepsilon^{\ell}_{\mathrm{ID}}$ and $\varepsilon^{\ell}_{\mathrm{ISO}}$ measurement statistics	-13% $+14\%$	$\pm 1\%$
Acceptance corrections (MC usage)	-5% $+5\%$	-5% $+6\%$
SM background in μ control region	-3% $+0\%$	$\pm 5\%$
$t\bar{t}$, W, Z sample kinematic differences	-10% $+10\%$	(n/a)
τ response template	(n/a)	$\pm 2\%$

Table 5.1: Systematic uncertainties for the lost lepton predictions.

repeated multiple times for each event. Each event is also weighted with a factor that accounts for the relative branching fractions for W decays into hadronically decaying tau leptons compared to that of $\mathrm{W} \to \mu\nu$.

The reader is referred to [85, 17] for details of these methods, including details about the evaluated systematic uncertainties. They are listed in Table 5.1 for reference. The largest uncertainty is just the statistical one of the control sample. For the lost electron/muon estimates the identification and isolation efficiency uncertainties have the next largest impact, which is not surprising since these inefficiencies contribute directly to the background. The sample dependence of these efficiencies also have some role, although most of it should have been controlled by the $p_{\mathrm{T},\ell}$ and $\Delta\mathrm{R}_{\ell,\mathrm{jet}}$ parametrizations. The smaller but not entirely negligible systematic uncertainties include those arising from use of MC simulated samples for the acceptance corrections. The potential SM background contamination (mostly QCD multi-jet production) can also be of comparable size. Finally, for the hadronic tau estimation the tau response template is derived from MC simulated samples and therefore have an uncertainty associated with the MC modeling. This is however one of the smallest systematic uncertainties.

Chapter 6

Invisible Decays of the Z Boson

In events where the Z boson is produced and decays invisibly, $\not\!\!E_{\mathrm{T}}$ is largely just the boson p_{T}. As such, the background estimation method exploits the relatively well-understood electroweak correspondence between the Z boson and photon. The production properties of photons and Z bosons are very different at energies below or of the order of the Z boson mass, but at higher energies the mass effect becomes asymptotically less important and they exhibit similar event topologies apart from electroweak coupling differences. In Figure 8 of [15] it is seen that the ratio $d\sigma_{\mathrm{Z}}(p_{\mathrm{T}})/d\sigma_{\gamma}(p_{\mathrm{T}})$ of differential production cross-sections of the two bosons ranges from about 0.8 at $p_{\mathrm{T}} \sim 100\,\mathrm{GeV}/c$, 1.2 at $p_{\mathrm{T}} \sim 150\,\mathrm{GeV}/c$, and is asymptotically about a factor of 2 at high boson p_{T}'s. Given the branching ratio of 20% for invisible decays of the Z and the high reconstruction efficiency of EM objects at the CMS detector, this means that the photon-to-Z translation retains high statistical power.

The prediction of of the $\mathrm{Z} \to \nu\bar{\nu}$ background from photons starts with the selection of a highly pure photon control sample, collected using the single-photon triggers listed in Table 6.1. In later data taking runs the triggers included a cleaning requirement that removed suspicious patterns of deposits in the EM calorimeters, in particular an isolated "spike" of activity in a single channel surrounded by no activity in a surrounding swiss-cross of channels. This was to prevent the trigger from dominantly collecting a type of luminosity-correlated noise that was identified early in the year. Other than this, the photon control sample satisfies the same preselection requirements as listed in Section 3.2.

For the offline analysis, the integration of photon identification and isolation within the PF framework is not yet in a mature state. As explained in Section 2.3.6, a "PF photon" is merely the leftover EM energy once the contributions from identified electrons, muons and charged hadrons have been subtracted, which clearly lacks the precision and background discrimination potential provided by the topical photon reconstruction of Section 2.3.3. The photons used here therefore refer to those from the latter, and in order to avoid double-counting of energies the nearest PF jet is removed from the event if it is within $\Delta\mathrm{R} < 0.1$ of the photon. This means that $\not\!\!E_{\mathrm{T}}$ is calculated as the negative

Run range	Trigger path	HLT photon p_{T} threshold
136033-137028	HLT_Photon20_L1R	20
138560-143962	HLT_Photon20_Cleaned_L1R	20
144010-144114	HLT_Photon25_Cleaned_L1R	25
146428-147116	HLT_Photon30_Cleaned_L1R	30
147196-148058	HLT_Photon50_Cleaned_L1R	50
148819-149442	HLT_Photon70_Cleaned_L1R	70

Table 6.1: List of photon triggers used to collect the photon control sample.

vectorial sum of transverse momenta of only jets recoiling against the photon, which is indeed the quantity directly comparable to $\not{H}_{\mathrm{T}}$ in $\mathrm{Z} \to \nu\bar{\nu}$ events. Photon candidates are distinguished from electrons by vetoing those that have a track seed in the pixel detector, required to be isolated in the tracker and calorimeters, and to have shower shape in the η coordinate be consistent with that of a single photon (rather than, say, decays of the meson $\pi^0 \to \gamma\gamma$). All events in the control sample are required to have at least one photon candidate, and the highest p_{T} such photon is selected as "the" photon in the event. There is no explicit cut on the p_{T} of the selected photon, only the one implicit from the trigger requirement, which is on overall fully efficient after an offline $p_{\mathrm{T},\gamma} > 75\,\mathrm{GeV}/c$ and as such also fully efficient for events that should contribute to all the search regions[1].

The remaining task is to derive the photon-to-Z translation factor for each of the search regions[2]. These are obtained using MC simulated γ+jets and $\mathrm{Z} \to \nu\bar{\nu}$ samples (Appendix A), but with scale factors to account for data-simulation differences, and systematic uncertainties derived from data insofar as possible. One complication arises from the break-down of the leading-order calculation of $\gamma+ \geq 2$ jets production for collinear and soft emissions of the photon, which the Z boson is protected from until very high energies thanks to its mass. As such, analogously to QCD radiation, the photon production mechanism also has to be factorized into perturbative and non-perturbative pieces, the former computed via ME methods and the latter modeled via a phenomenological photon fragmentation function. Other sources of photons without Z boson counterparts are those arising from hadron decays, and misidentified electrons. All of these differences are mitigated by imposing tight isolation requirements in the photon selection, after which the contaminations are at the $\leq 10\%$ level. Nevertheless, they must be properly and separately accounted for in the derivation of the translation factor, because all these sources are present in the data photon control sample, but not so of any single MC simulated sample. For example, the simulated γ+jets process contains the ME approximated piece, but most of the contribution to the fragmenta-

[1] Recall that even the loosest search region, the baseline selection, has a $\not{H}_{\mathrm{T}} \geq 150\,\mathrm{GeV}/c$ requirement which sort of translates to a $p_{\mathrm{T},\gamma} \geq 150\,\mathrm{GeV}/c$ region of importance, although the "turn-on" for this correspondence extends down to $p_{\mathrm{T},\gamma} \sim 100\,\mathrm{GeV}/c$.

[2] A $\not{H}_{\mathrm{T}}$ shape correction is not performed, although it could be in the future.

tion piece should be in the simulated multi-jet processes, and the two approximations are not properly matched (Section 4.2). The contaminations from hadron decays are also to be found in the multi-jet processes, and that from misidentified electrons would have dominant contributions from processes with one or more W and Z bosons in the final state. In practice, a separate translation/correction factor is derived for each of the following sources of photons:

Prompt (ME). This is the main σ_Z/σ_γ translation factor, and is obtained as the ratio of fully simulated events in $Z \to \nu\bar{\nu}$ over those in γ+jets samples, after the appropriate search cuts have been applied on these events. The γ+jets sample is further purified by requiring that the selected photon match to a generated photon from the ME calculation within $\Delta R < 0.2$. As such, it is orthogonal to the sources of contamination listed below, and includes the theoretical translation as obtained from ME calculations as well as the corrections for the simulated photon reconstruction and identification efficiencies. The latter efficiencies can be different from those in data, which incurs a measured scale factor correction as well as an associated uncertainty.

Fragmentation. The expected fraction of fragmentation photons that contaminate the data photon control sample is measured with a dedicated program JetPhox [9], which models the fragmentation contribution to NLO precision.

Hadron decays. The purity of the data photon control sample is measured using an isolation template method [37], and is found to be in good agreement with the MC simulation.

Misidentified electrons. The probability of an electron to be misidentified as a photon is measured using a tag-and-probe method with $Z \to e^+e^-$ events in data [80]. They are found to be negligible since this probability is $\sim 1\%$ and the contributing processes are at best (e.g. W boson production) comparable to prompt photon production in cross-section.

The data photon control sample is scaled down to correct for the sources of contamination, and then scaled by the σ_Z/σ_γ translation factor which is appropriate for a pure (prompt) photon sample. The combined scale factor is about 40%, with break-down and uncertainties as shown in Table 6.2. The reader is referred to [15] for details.

Source		Baseline $\not{H}_T \geq 150, \Delta\phi$			High $\not{H}_T$ $\not{H}_T \geq 250, \Delta\phi$			High H_T $H_T > 500, \Delta\phi$		
σ_Z/σ_γ	$\pm$ theory	0.41	$\pm$	6%	0.48	$\pm$	6%	0.44	$\pm$	4%
	$\pm$ acceptance		$\pm$	5%		$\pm$	5%		$\pm$	5%
	$\pm$ MC stat.		$\pm$	7%		$\pm$	13%		$\pm$	13%
Data/MC γ efficiency		1.01	$\pm$	2%	1.01	$\pm$	2%	1.01	$\pm$	2%
Fragmentation		0.95	$\pm$	1%	0.95	$\pm$	1%	0.95	$\pm$	1%
Hadron decays		0.94	$\pm$	9%	0.97	$\pm$	10%	0.90	$\pm$	9%
Electrons		1.00	$\pm$	1%	1.00	$\pm$	1%	1.00	$\pm$	1%
Combined scale factor		0.37	$\pm$	14%	0.45	$\pm$	18%	0.38	$\pm$	17%

Table 6.2: Translation/correction factors and corresponding systematic uncertainties contributing to the scale factor for predicting the $Z \to \nu\bar{\nu}$ background from the γ+jets control sample. The scale factors are derived for various search regions as shown in the columns.

Chapter 7

Mis-measurements in QCD Multi-jet Production

7.1 Overview

QCD is the most difficult background to model for SUSY searches in the all-hadronic, jets plus missing transverse energy channels. It requires a very good knowledge of the underlying "true" spectrum of particle jets and how they are manifested in the detector. Current theoretical knowledge of the former has large uncertainties, especially in the high-H_{T}, high jet multiplicity realm. In view of this, we developed a data-driven technique for estimating this background that we call the Rebalance and Smear (R+S) method. The QCD background estimates obtained with the R+S method have several beneficial qualities including being insensitive to contamination from non-QCD events—including any potential SUSY signal—in the data samples used to make the background estimates.

One of the most important quantities that the R+S method is designed to predict for QCD multi-jet events is $\vec{\not{H}}_{\mathrm{T}}$. Now even if one could detect all particles with perfect resolution, $\not{H}_{\mathrm{T}}$ would generally be non-zero because particles can fail to be included in jets by the jet algorithm used, and also jet p_{T}'s can fall below threshold. In a real detector, jets can also be mismeasured and this can produce large $\not{H}_{\mathrm{T}}$ particularly if one or more jets are far out in the tail of the response distribution. The main sources of tails in calorimetric jet resolution in CMS are muons and neutrinos from semi-leptonic decays of heavy flavor jets in $\sim 4\%$ of jets, and a comparably sized contribution from the $\sim$1% of masked or dead electromagnetic calorimeter (ECAL) cells. For Particle Flow (PF) jets, muons are reconstructed as part of the jet constituents; however the neutrino contribution remains. In addition, there is also a comparably sized population of low-response light flavored jets.

The R+S method is based upon the premise that if one were to have the true 3-momenta of a particle jet in an event, then the distribution of an ensemble of reconstructed jet momenta $p_{\mathrm{T}}^{\mathrm{reco}}$ can be modeled by a per-jet resolution function $r(p_{\mathrm{T}}^{\mathrm{reco}}|p_{\mathrm{T}}^{\mathrm{true}})$.

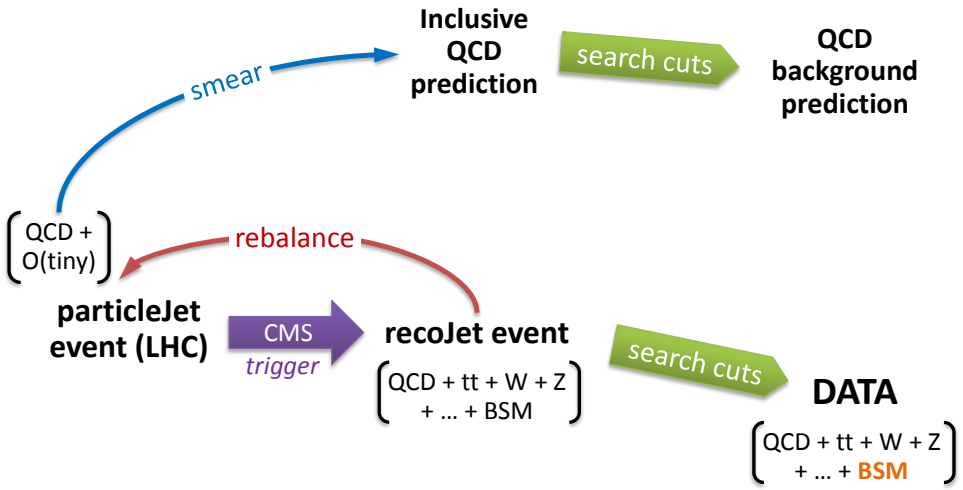

Figure 7.1.1: Overview of the R+S method.

The jet resolution is typically parametrized by at least two variables: $p_{\mathrm{T}}^{\mathrm{true}}$ and the pseudorapidity (η) of the jet. The latter accounts for variations in material and basic differences in construction and technologies of the calorimeter regions. The R+S method produces a prediction of the QCD background by starting from a "seed" sample where each "seed event" consists of "seed jets" that are good estimators of the true QCD particle jet momenta. The seed events are produced in the "Rebalance" step discussed below. In the "Smear" step a random value of the response $p_{\mathrm{T}}^{\mathrm{reco}}/p_{\mathrm{T}}^{\mathrm{true}}$ is drawn from the jet resolution distribution for each seed jet, and its true momentum is scaled by this factor in order to model the expected reconstructed momentum.

The Rebalance step allows one to bypass the need for precise theoretical understanding of QCD jet production by using real data as input—namely an inclusive multi-jet sample. This is mostly made up of QCD multi-jet events but has tiny contributions from fully hadronic W,Z and $t\bar{t}$ events and even tinier contributions from events with real $\not{H}_{\mathrm{T}}$—such as leptonic Standard Model (SM) events in which the lepton is not identified, or possibly even new physics signal events. None of these contributions matter because the Rebalance step suppresses them by melting them into the vast sea of QCD multi-jet events. This is done by making the reasonable assumption that if the true jet momenta for an n-jet event are denoted by $p_{\mathrm{T},i}^{\mathrm{true}}$ where $i = 1,\ldots,n$, then the likelihood of observing reconstructed jets with momenta $p_{\mathrm{T},i}^{\mathrm{reco}}$ can be written as $L = \prod_{i=1}^{n} r(p_{\mathrm{T},i}^{\mathrm{reco}}|p_{\mathrm{T},i}^{\mathrm{true}})$. Good estimators for the particle jet momenta can be obtained by maximizing the likelihood $\mathscr{L}$ as a function of $p_{\mathrm{T},i}^{\mathrm{true}}$, subject to the QCD transverse momentum balance constraint $\sum_{i=1}^{n} \vec{p}_{\mathrm{T},i}^{\mathrm{true}} + \vec{p}_{\mathrm{T,soft}}^{\mathrm{true}} = 0$. Here $\vec{p}_{\mathrm{T,soft}}^{\mathrm{true}}$ is the sum of all particles that are not clustered into seed jets and is approximated by the measured quantity $\vec{p}_{\mathrm{T,soft}}^{\mathrm{reco}}$. In other words, one adjusts all of the jet momenta in a manner consistent with expected measurement uncertainties to return the event back into approximate transverse momentum balance.

As shown in Figure 7.1.1, the rebalancing procedure is applied to data collected on jet or H_T triggers, stripping non-QCD events of their characteristic $\not{E}_T$, while "unfolding" real QCD events back to particle jet level. The resulting "pure" QCD sample is the desired seed event sample. The R+S method can thus be thought of as a filtration process in which one starts with a sample containing many sources and turns it into a very nearly pure QCD multi-jet sample to which one can apply search cuts to see what remains. In exactly this way one predicts just the QCD background in the RA2 search region. An important corollary of this aspect of the R+S method is that it predicts event-by-event jet kinematics—not just event counts—in the desired search region. The number of jets, p_T and η spectra of jets, ratios of p_T's of all pairs of jets, $\Delta\phi$ between pairs of jets, and $\Delta\phi$ between jets and the direction of $\not{H}_T$ have all been seen to be well modeled in Monte Carlo (MC) benchmark tests. This allows for great flexibility in the set of variables that can be used to either define a search region, or to characterize some observed new physics signal.

As noted above, the R+S method extracts the seed sample from *inclusive* data. There is no need for preselection cuts to suppress contamination by non-QCD events with high $\not{E}_T$. This is beneficial because cuts that suppress non-QCD events tend to bias QCD kinematics. For example, $\not{E}_T$ (or $\not{H}_T$) in QCD events typically depends on the H_T of the event, because the more energy that is present, the higher one can extend in mismeasurement of $\not{E}_T$. By rejecting events with significant $\not{E}_T$ in order to remove leptonic and signal events, one undesirably also depletes high-H_T portions of QCD phase space. The outcome is a bias in which one *under*-estimates the contribution of QCD events to the high $\not{H}_T$ tail. In contrast, the rebalancing part of the R+S procedure forces even high $\not{E}_T$ Beyond Standard Model (BSM) events, as well as SM events containing true $\not{E}_T$ from leptonic decays of vector bosons, to be converted into well balanced QCD-like events. Obviously in this case one does not reconstruct the correct initial state but, given the many orders of magnitude larger QCD cross-section, these events constitute a tiny sub-sample of all seed events and their impact is negligible. A minimal quality cut furthermore can be applied to reject suspicious events with very small values of the maximized likelihood. Note that the expected contamination from a CMS SUSY benchmark point LM0 (LM1) with high (moderately high) production cross-section is found to be less than 1.0 (0.1)% for asymptotically high $\not{H}_T$.

Concepts of the R+S method are presented in more detail in Section 7.2. Much of the program is dedicated to proofs of concept using MC simulated QCD samples, where only the $\hat{p}_T \geq 170\,\text{GeV}/c$ samples listed in Appendix A.2 have been used in order to have an equivalent luminosity of $2.5\,\text{fb}^{-1}$ or better. Results of the procedure applied to 2010 Collider data are given in Section 7.2.5. A crucial input to this methodology are the jet resolution functions, measured in a broad p_T and η range. Several methods [11, 7] have been developed to measure both the core and the non-Gaussian tails of the jet resolution from Collider data. For ease of reference, salient features of these methods are summarized in Section 7.3.1. Section 7.3.3 discusses additional parametrizations required to take into account event dependencies of the jet resolutions, in particular for the fraction

of heavy flavor jets. A correction to improve the performance of the R+S method is presented in Section 7.4; while significant for the calorimeter-jet based analysis, the size of this correction is only $\sim 5\%$ for the PF analysis. Systematic uncertainties are addressed in Section 7.5.

7.2 Basics of Rebalance+Smear method

7.2.1 Concept

Colored particles produced in high-energy collision events undergo fragmentation and hadronization, resulting in a spray of (meta-)stable hadrons that are quite well-collimated around the direction of the initial parton and roughly circular in η-ϕ space. The term "particle jets" (particleJets) is used in this document to distinguish between this underlying reality, and the reconstructed jets (recoJets) clustered from calorimeter deposits; in MC studies, the particle jet truth is available from clustering particles from the MC generator (genParticles) and are referred to as "genJets". If one were to take the vector sum of transverse momenta of all particle jets in a QCD event, conservation of transverse momentum makes this quantity nearly zero, to a level of O(10 GeV/c) due to inefficiencies of the clustering algorithm in collecting particles into jets. Nonzero magnitudes of $\not\!\!H_{\mathrm{T}}$ computed with reconstructed jets arise from some jets having been omitted from the vector sum, and/or imperfections in the measured momenta of jets that were included. This motivates the so-called "jet smearing" methods for QCD background prediction:

> Assume as input (1) the particleJet-level spectrum of QCD events[1], and (2) the probability distribution r of single-jet detector responses $p_{\mathrm{T}}^{\mathrm{reco}}/p_{\mathrm{T}}^{\mathrm{particle}}$. The recoJet-level spectrum of events can then be modeled by smearing the momentum of each particle jet in (1) by a random response drawn from (2).

(1) is assumed to be provided as a set of representative "seed" events, which are specified by at least the 3-momenta of all jets in the event. The jets to be smeared are referred to "seed jets". There is also typically some amount of "soft stuff" per event that is omitted from smearing, because the concept of "jet" becomes not very meaningful when so soft as to contain only single particles, and also because the jet resolution cannot be measured to arbitrarily low p_{T}. The simplest mode of smearing seed jets is to just scale the magnitude of their momenta by a random factor drawn from (2), i.e. leaving their directions unchanged. This is the procedure used throughout this study.

[1] For most of the purposes here, it is sufficient to consider an n-jet event as defined by the set of 3-momenta $\{\vec{p}_{\mathrm{T},i} | i = 1,\ldots,n\}$ of its jets, plus possibly some properties of these jets (e.g. flavor) to be discussed later. The term "spectrum of events" indicates the (multidimensional) probability distribution of $\{\vec{p}_{\mathrm{T},i}\}$ for a particular process like QCD. More loosely, "jet spectrum" is used to refer to the $\vec{p}_{\mathrm{T}}$ distribution of particular jets like the leading-p_{T} jet in events, and so forth.

The jet-smearing model is a vast simplification compared to use of fully-simulated (FullSim) Monte Carlo events, the latter being an established way of predicting data distributions from the detailed simulation of the particles propagating through and interacting with the detector volume. The driving motivation for this simplification is that allows for both inputs (1) and (2) to be [separately] measured from data itself, instead of having to simultaneously tune many MC event generation and detector simulation knobs to match observation. However, care must be taken that the approximation still adequately describes the measured QCD spectrum. The most obvious issue is that not all jets are equal in how they contribute to missing energy; in fact it would already be quite fortunate for simplicity's sake if the differences can be parametrized by just properties of the particle jet itself (as opposed to dependence on jet-jet or event-level correlations). Fortunately this seems to be more or less the case for the largest known factors:

- **Transverse momentum** : The CMS calorimeter resolution is known to improve significantly for higher p_{T} jets, even just considering the Gaussian/stochastic core of the response. The importance of various contributions to the non-Gaussian tails also exhibit p_{T}-dependence, such as the rising loss of hadrons that "punch-through" the calorimeters.

- $\eta - \phi$ **location** : Calorimetry at CMS consists of electromagnetic (ECAL) and hadron (HCAL) calorimeters, with the ECAL situated at a smaller radius than the HCAL, and together providing hermetic coverage up to $|\eta| < 5.2$. The calorimeters are segmented along z, being the electromagnetic barrel (EB) and end-cap (EE) detectors, and the hadron barrel (HB), end-cap (HE), and forward (HF) detectors[2]. These are distinguished as mechanically distinct calorimeters with different resolutions and energy scales. Part of the effort in jet reconstruction is to equalize the scale of the response across all η regions, but resolution shape differences remain. Furthermore, about 1% of the ECAL channels have been masked or are non-functional as the date of this writing, resulting in exceptionally low-response spots at particular $\eta - \phi$ locations. Appendix D describes how the fraction of "bad" ECAL channels within a $\Delta\mathrm{R} < 0.1$ cone of the jet axis may be used to parametrize how much a jet is affected by masked channels. A clear dependency is shown in Figure 7.2.1, for MC simulated QCD events prior to application of ECAL hole filters. Even for jets far from bad channels, as defined by having $f^{\mathrm{ECAL}}_{\mathrm{masked}} < 1\%$, there is a large sensitivity of the high response tail to a small region around $|\eta| \sim 1.3$ as shown in Figure 7.2.2.

- **Flavor**[3] : Quarks and gluons have different QCD showering/hadronization behaviors, leading to different particle compositions as well as jet shapes, and con-

[2]There is also the hadron outer (HO) calorimeter, but it is often neglected because it is not used by default in jet reconstruction.

[3]For MC-based studies, the flavor of a jet is determined according to the "algorithmic" definition as explained in [45]. In summary, this means that, in the stated order of precedence, a jet is called a "bottom

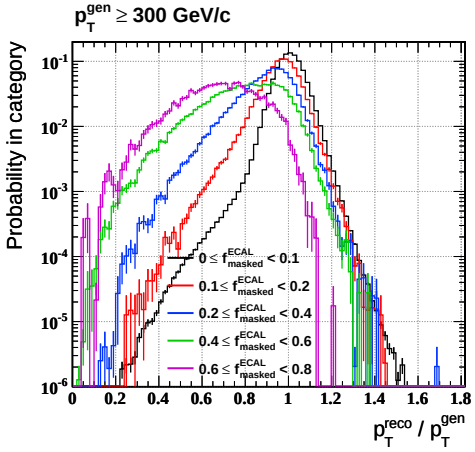

Figure 7.2.1: Resolution of genJets of $p_T \geq 300\,\text{GeV}/c$ over all η regions, and with values of $f_{\text{masked}}^{\text{ECAL}}$ as stated in the legend. Here the the leading two genJets in QCD samples are matched to the nearest recoJet within $\Delta R < 0.1$. No ECAL hole filters have been applied. All histograms are normalized to unit area.

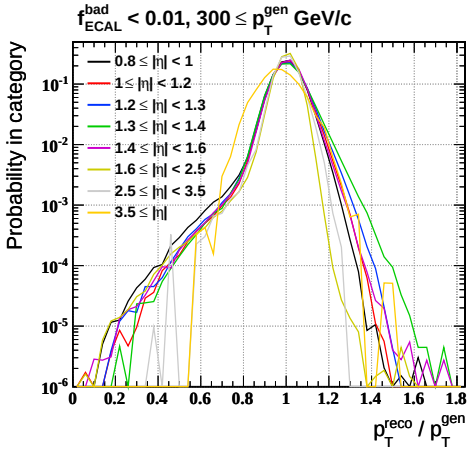

Figure 7.2.2: Resolution of genJets of $p_T \geq 300\,\text{GeV}/c$ with $f_{\text{masked}}^{\text{ECAL}} < 1\%$ and in various η regions as stated in the legend. Here the the leading two genJets in QCD samples are matched to the nearest recoJet within $\Delta R < 0.1$. For visual clarity, the histograms are shown by linearly interpolating between the centers of each bin. All histograms are normalized to unit area.

sequently different jet resolutions. The progressively better resolution of visible particles with higher p_T also means that decay of hadrons into invisible particles (i.e. neutrinos) grows to be one of the most significant sources of energy loss for jets with, say, $p_T > 100\,\text{GeV}/c$ or so. Heavy flavor (b and c) hadrons in particular have both higher branching ratios to semi-leptonic decays, as well as produce a harder spectrum of leptons because of their mass. Such jets have qualitatively different jet resolution shapes as shown in Figure 7.2.3 for jets in good regions of calorimetry.

The relative contributions of various populations contributing to the low response tail are shown in Figure 7.2.4. Since all jets that fall within regions of substantially many masked ECAL channels have cause to lose energy regardless of other properties, the jets are first categorized by $f_{\text{masked}}^{\text{ECAL}}$ if $f_{\text{masked}}^{\text{ECAL}} \geq 1\%$, for all flavors. The remaining population with $f_{\text{masked}}^{\text{ECAL}} < 1\%$ is then categorized by flavor. It is seen that for $p_{\text{T}}^{\text{gen}} \geq 300\,\text{GeV}/c$ jets the largest contributions in the region around $p_{\text{T}}^{\text{reco}}/p_{\text{T}}^{\text{gen}} \sim 0.6$ are from jets with $f_{\text{masked}}^{\text{ECAL}} \geq 20\%$, as well as those with $f_{\text{masked}}^{\text{ECAL}} < 1\%$ but either being b or light

jet" if it can be matched to a b-quark, a "charm jet" if it can be matched to a c-quark, and otherwise a quark or gluon jet based on the highest-p_T parton found within the matching cone.

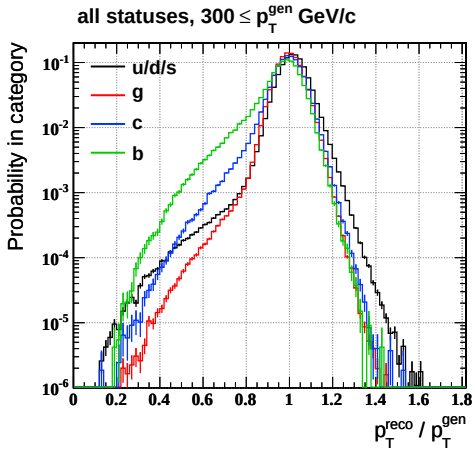

Figure 7.2.3: Resolution of genJets of $p_{\mathrm{T}} \geq 300\,\mathrm{GeV}/c$ over all η regions and $f_{\mathrm{masked}}^{\mathrm{ECAL}} < 1\%$. Jets are categorized by flavor as stated in the legend. Here the the leading two genJets in QCD samples are matched to the nearest recoJet within $\Delta\mathrm{R} < 0.1$. All histograms are normalized to unit area.

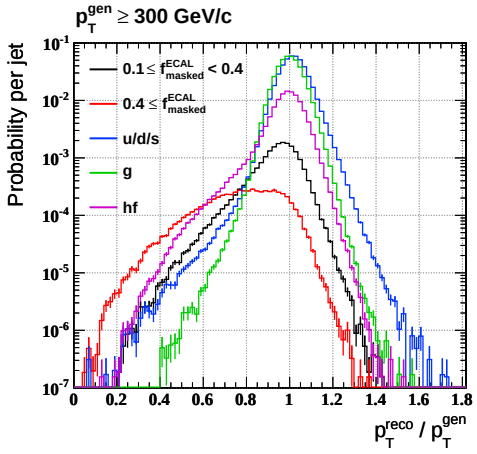

Figure 7.2.4: Resolution of genJets of $p_{\mathrm{T}} \geq 300\,\mathrm{GeV}/c$ over all η regions. Jets are categorized by $f_{\mathrm{masked}}^{\mathrm{ECAL}}$ and flavor as stated in the legend. Here the the leading two genJets in QCD samples are matched to the nearest recoJet within $\Delta\mathrm{R} < 0.1$. No ECAL hole filters have been applied. The histograms are normalized such that the sum of all categories has unit area, i.e. preserving the relative contribution of each population.

quark jets. All these three populations are roughly equal in size, although the non-b populations dominate towards very low response. In contrast, the $|\eta| \sim 1.3$ dependence of the high response tail is seen for all jet flavors. The light-quark jet population remains to be by far the dominant contribution to the high response tail for all η regions.

In practice, it is not possible to introduce arbitrarily many parametrizations: some jet properties such as flavor are experimentally difficult to determine with high enough efficiency/purity on a per-event basis, plus every parameter divides up the control sample by another dimension, leading to a divergence in statistical uncertainty. In the MC method demonstrations, the jet resolution has been parametrized with enough p_{T} bins to have a gradual change in shape between bins, fine η bins around the region $|\eta| \sim 1.3$, as well as $f_{\mathrm{masked}}^{\mathrm{ECAL}}$ as shown above. Details of these parametrizations are provided in Section 7.3.2, together with a comparison of the parametrizations used in the data measurement.

7.2.2 Seed Events from Data

The first and foremost proof-of-concept is provided by the closure of genJet smearing in MC studies, where one simply takes the genJets in QCD MC simulated events and smears them with the parametrized jet resolution functions. The more practical question however concerns how the two required inputs—particleJet-level seed events and jet resolution templates—can be obtained in data-driven ways. There is in fact a natural factorization of the two tasks, hence a discussion of jet resolution measurement methods is postponed to Section 7.3. The rest of this section describes a method of obtaining good seed events, assuming "perfect" jet resolution templates from MC as input.

Short of resorting to theoretical calculations e.g. as performed by Monte Carlo generators, the most obvious estimator of a particleJet-level event $\{\vec{p}_{\mathrm{T},i}^{\,\mathrm{particle}} | i = 1,\ldots,n\}$ is simply the set of reconstructed jet momenta $\{\vec{p}_{\mathrm{T},i}^{\,\mathrm{reco}} | i = 1,\ldots,n\}$. However it is intuitively obvious that smearing $\{\vec{p}_{\mathrm{T},i}^{\,\mathrm{reco}}\}$ cannot predict $\{\vec{p}_{\mathrm{T},i}^{\,\mathrm{reco}}\}$ itself, because the jets are now "doubly smeared" on top of the intrinsic detector resolution. This is especially prominent in the most important distribution to be predicted, i.e. causes a factor > 5 over-estimate of the number of QCD events with $\not{H}_{\mathrm{T}} > 150\,\mathrm{GeV}/c$. To understand how to mitigate this effect, one should consider how jet response contributes to $\not{H}_{\mathrm{T}}$. As mentioned in Section 7.2.1, $\not{H}_{\mathrm{T}}$ is nonzero at particle jet level only because some particles may not be clustered into jets, and some jets may not pass the required p_{T} threshold. This distinguishes an ***intrinsic*** $\not{H}_{\mathrm{T}}$ piece $\vec{p}_{\mathrm{T,soft}}^{\,\mathrm{particle}}$ that balances out jets above threshold, and appears in the transverse momentum conservation condition as:

$$\sum_{i \in \mathrm{jets}} \vec{p}_{\mathrm{T},i}^{\,\mathrm{particle}} + \vec{p}_{\mathrm{T,soft}}^{\,\mathrm{particle}} = 0 \qquad (\mathrm{for\,QCD}) \tag{7.2.1}$$

The reconstructed $\not{H}_{\mathrm{T}}$ is roughly a convolution of intrinsic and resolution-induced contributions. This is seen by first using Equation 7.2.1 to express the momentum of an arbitrary particle jet (say, k) as $\vec{p}_{\mathrm{T},k}^{\,\mathrm{particle}} = -\sum_{i \neq k} \vec{p}_{\mathrm{T},i}^{\,\mathrm{particle}} - \vec{p}_{\mathrm{T,soft}}^{\,\mathrm{particle}}$. Also recall that

reconstructed jets are approximately equal to their particleJet-level momenta up to a random scale-factor: $\vec{p}_{\mathrm{T},i}^{\,\mathrm{reco}} \approx r_i \times \vec{p}_{\mathrm{T},i}^{\,\mathrm{particle}}$ where r_i is the jet response. Substituting $\vec{p}_{\mathrm{T},k}^{\,\mathrm{particle}}$ into the definition of $\not{H}_{\mathrm{T}}$ gives:

$$\vec{\not{H}}_{\mathrm{T}} \equiv -\sum_i \vec{p}_{\mathrm{T},i}^{\,\mathrm{reco}} = -\sum_i r_i \times \vec{p}_{\mathrm{T},i}^{\,\mathrm{particle}} = -\sum_{i\neq k}(r_i - r_k) \times \vec{p}_{\mathrm{T},i}^{\,\mathrm{particle}} + r_k \times \vec{p}_{\mathrm{T,soft}}^{\,\mathrm{particle}} \tag{7.2.2}$$

It is convenient to choose the "reference" jet k such that $r_k \approx 1$, since it is unlikely that every single jet in the event is strongly mismeasured[4]. Equation 7.2.2 has the advantage of expressing $\not{H}_{\mathrm{T}}$ as a piece due to [relative] *mismeasurements* of jets, i.e. which has important contributions from those r_i very different from $r_k \approx 1$, and the aforementioned *intrinsic* piece $\vec{p}_{\mathrm{T,soft}}^{\,\mathrm{particle}}$. Since the magnitude of $\vec{p}_{\mathrm{T,soft}}^{\,\mathrm{particle}}$ is not large (for reasonably low seed jet p_{T} thresholds), it is the dominant contribution at low $\not{H}_{\mathrm{T}}$, and is more significant for events with many soft jets just below threshold. On the other hand, the contribution from jet mismeasurements dominate at high $\not{H}_{\mathrm{T}}$, and is mostly driven by a single badly reconstructed jet, preferentially with high $p_{\mathrm{T},i}^{\,\mathrm{particle}}$.

Completely analogously, $\not{H}_{\mathrm{T}}$ predicted from smearing seed jets can be written as:

$$\begin{aligned} \sum_{i\in\mathrm{seedJets}} \vec{p}_{\mathrm{T},i}^{\,\mathrm{seed}} + \vec{\not{H}}_{\mathrm{T}}^{\,\mathrm{seed}} &= 0 \qquad (\text{definition of } \vec{\not{H}}_{\mathrm{T}}^{\,\mathrm{seed}}) \\ \vec{\not{H}}_{\mathrm{T}}^{\,\mathrm{smeared}} &= -\sum_{i\neq k}(r_i - r_k) \times \vec{p}_{\mathrm{T},i}^{\,\mathrm{seed}} + r_k \times \vec{\not{H}}_{\mathrm{T}}^{\,\mathrm{seed}} \end{aligned} \tag{7.2.3}$$

One sees the problem with the recoJet smearing procedure: $\not{H}_{\mathrm{T}}^{\,\mathrm{seed}}$ is equal to the $\not{H}_{\mathrm{T}}$ of the measured event, so adding on top of this another mismeasurement-induced piece from smearing can only over-estimate by something like a factor of two. Section 4.2.2 of [50] shows how the badly mismeasured events, albeit very rare, retain "memory" of their original value of $\not{H}_{\mathrm{T}}$, and further smearing just (spuriously) promotes these events even further in the high $\not{H}_{\mathrm{T}}$ tail. Moreover, SUSY signal events would have exactly this same behavior, leading to a worse than 1:1 contamination in the QCD prediction.

The above observation suggests that good seed events should be required to not have problematically high values of $\not{H}_{\mathrm{T}}^{\,\mathrm{seed}}$. One could imagine only using events with low $\not{H}_{\mathrm{T}}$ (or $\not{E}_{\mathrm{T}}$), but since $\not{H}_{\mathrm{T}}$ is proportional to the amount of visible energy this results in a seed sample with jets biased towards low p_{T}. Furthermore, the true distribution of $\vec{p}_{\mathrm{T,soft}}^{\,\mathrm{particle}}$ is not of negligible magnitude, but rather is at least of the same order as the jet p_{T} threshold, so the low-$\not{H}_{\mathrm{T}}$ requirement also artificially truncates this contribution. Smearing such a seed sample tends to conversely under-predict $\not{H}_{\mathrm{T}}$, and at the end fine-tuning of the seed event selection is required for the cut biases and double smearing effects to cancel.

Instead, the trick pursued in the R+S method is to notice a so-far unexploited piece of information: $\vec{p}_{\mathrm{T,soft}}^{\,\mathrm{particle}}$ can be estimated by $\vec{p}_{\mathrm{T,soft}}^{\,\mathrm{reco}}$, the vector sum of reconstructed PF

[4] Even if it is so, the discussion remains qualitatively the same if one chooses k such that r_k is closest to 1 for all jets in the event

particles not included in jets above the seed jet p_{T} threshold[5]. With this one can imagine *constructing* a seed event that satisfies Equation 7.2.1, starting from $\vec{p}_{\mathrm{T},i}^{\,\mathrm{seed}} = \vec{p}_{\mathrm{T},i}^{\,\mathrm{reco}}$ and adjusting ("rebalancing") the momenta so that $\sum_i \vec{p}_{\mathrm{T},i}^{\,\mathrm{seed}} + \vec{p}_{\mathrm{T,soft}}^{\,\mathrm{reco}} = 0$. A procedure by which this can be accomplished is presented in Section 7.2.3. Here a very important property of the rebalancing procedure is noted: the predicted $\not{H}_{\mathrm{T}}$ is now robust against mismeasurements of $\vec{p}_{\mathrm{T},i}^{\,\mathrm{seed}}$ and $\vec{p}_{\mathrm{T,soft}}^{\,\mathrm{reco}}$. This is seen by writing the estimators as $\vec{p}_{\mathrm{T},i}^{\,\mathrm{seed}} = (1+\delta_i)\cdot\vec{p}_{\mathrm{T},i}^{\,\mathrm{particle}}$ and $\vec{p}_{\mathrm{T,soft}}^{\,\mathrm{reco}} = (1+\Delta_i)\cdot\vec{p}_{\mathrm{T,soft}}^{\,\mathrm{particle}}$, where δ_i and Δ_i are mismeasurement factors. With this and $\vec{p}_{\mathrm{T,soft}}^{\,\mathrm{reco}}$ in place of $\not{H}_{\mathrm{T}}^{\,\mathrm{seed}}$, the R+S equivalent of $\vec{\not{H}}_{\mathrm{T}}^{\,\mathrm{smeared}}$ (Equation 7.2.3) is:

$$\begin{aligned}
\vec{\not{H}}_{\mathrm{T}}^{\,\mathrm{R+S}} &= -\sum_{i\neq k}(r_i - r_k)\times\vec{p}_{\mathrm{T},i}^{\,\mathrm{seed}} + r_k\times\vec{p}_{\mathrm{T,soft}}^{\,\mathrm{reco}} \\
&= -\sum_{i\neq k}(r_i - r_k)(1+\delta_i)\times\vec{p}_{\mathrm{T},i}^{\,\mathrm{particle}} + r_k(1+\Delta_i)\vec{p}_{\mathrm{T,soft}}^{\,\mathrm{particle}} \\
&= \vec{\not{H}}_{\mathrm{T}} - \left[\sum_{i\neq k}(r_i - r_k)\cdot\delta_i\times\vec{p}_{\mathrm{T},i}^{\,\mathrm{particle}}\right] + r_k\Delta_i\cdot\vec{p}_{\mathrm{T,soft}}^{\,\mathrm{particle}} \qquad (7.2.4)
\end{aligned}$$

The rebalancing procedure proposed in Section 7.2.3 does not worsen the seed jet resolution (in fact it improves it somewhat), so δ_i is approximately Gaussian-distributed around 0 with a width of about 10% for $p_{\mathrm{T}} \sim 100\,\mathrm{GeV}/c$ jets and smaller than 8% for $p_{\mathrm{T}} > 200\,\mathrm{GeV}/c$. This means that $[\cdots]$ in Equation 7.2.4 is roughly an order of magnitude smaller than $\not{H}_{\mathrm{T}}$. The last term in the equation is similarly deemphasised by the factor of Δ_i—even though the resolution of soft particles is much poorer than that of high-p_{T} jets, it is helped by the fact that $\vec{p}_{\mathrm{T,soft}}^{\,\mathrm{particle}}$ is quite small in magnitude to begin with. Ergo $\not{H}_{\mathrm{T}}^{\,\mathrm{smeared}} \approx \not{H}_{\mathrm{T}}$, and seed events with highly mismeasured jets do not retain any particular preference for being smeared into events with high $\not{H}_{\mathrm{T}}$. The interested reader is referred Section 4.2.2 of [50] for supporting figures.

7.2.3 Maximum Likelihood Rebalancing

The maximum likelihood method [66] is an established way of obtaining approximately unbiased estimators for parameters of some model that describes a set of observables. In this context the observables are the measured jet momenta $\{\vec{p}_{\mathrm{T},i}^{\,\mathrm{reco}}\}$, the parameters to estimate are the true jet momenta $\{\vec{p}_{\mathrm{T},i}^{\,\mathrm{particle}}\}$, and the simplifying assumption $\vec{p}_{\mathrm{T},i}^{\,\mathrm{reco}} \parallel \vec{p}_{\mathrm{T},i}^{\,\mathrm{particle}}$ is made as discussed in Section 7.2.1. Assuming that the response of jets in a n-jet event are all uncorrelated, the likelihood for observing $\{\vec{p}_{\mathrm{T},i}^{\,\mathrm{reco}}\}$ if the true momenta are $\{\vec{p}_{\mathrm{T},i}^{\,\mathrm{particle}}\}$ is

[5] Technically, this is computed as $\vec{p}_{\mathrm{T,soft}}^{\,\mathrm{reco}} \equiv -\vec{\not{H}}_{\mathrm{T}} - \sum_{i\in\mathrm{jets}}\vec{p}_{\mathrm{T},i}$ in order to take advantage of the optimized choice of particles used in the computation of $\not{H}_{\mathrm{T}}$.

$$L_{\text{jets}} = L_{\text{jets}}(p_{\text{T},1}^{\text{true}}, \ldots, p_{\text{T},n}^{\text{true}}) = \prod_{i=1}^{n} r(p_{\text{T},i}^{\text{reco}} | p_{\text{T},i}^{\text{true}})$$

where $r(p_{\text{T},i}^{\text{reco}} | p_{\text{T},i}^{\text{true}})$ is the jet resolution function. $\{p_{\text{T},i}^{\text{max-}L}\}$ denotes the set of values at which $L_{\text{jets}}(p_{\text{T},1}^{\text{max-}L}, \ldots, p_{\text{T},n}^{\text{max-}L})$ is at a maximum, and is obtained via numerical minimization of $\min(-\ln L)$ using the MINUIT [53] software package. As explained in Section 7.2.2, it is of critical importance to impose the QCD transverse balance condition, Equation 7.2.1. If $\vec{p}_{\text{T,soft}}^{\text{reco}}$ is used as an estimator of $\vec{p}_{\text{T,soft}}^{\text{particle}}$, the equation $\sum_i \vec{p}_{\text{T},i}^{\text{true}} + \vec{p}_{\text{T,soft}}^{\text{reco}} = 0$ can be used to eliminate two of the n degrees of freedom. However, it turns out that a strict enforcement of this constraint results in somewhat delicate behavior of the maximum likelihood solution. This happens because the directions of the jets are fixed, so it is sometimes the case that a mistake in the angle of the measured $\vec{p}_{\text{T,soft}}^{\text{reco}}$ can only be compensated for by a very large distortion of the predicted $p_{\text{T},i}^{\text{max-}L}$. Such a pathology can be alleviated by loosening the event balance constraint, i.e. using a likelihood of the form:

$$L = L(p_{\text{T},1}^{\text{true}}, \ldots, p_{\text{T},n}^{\text{true}}, \vec{p}_{\text{T,soft}}^{\text{true}}) = \prod_{i=1}^{n} r(p_{\text{T},i}^{\text{reco}} | p_{\text{T},i}^{\text{true}}) \times R_{\text{soft}}(\vec{p}_{\text{T,soft}}^{\text{reco}} | \vec{p}_{\text{T,soft}}^{\text{true}}) \tag{7.2.5}$$

with $\vec{p}_{\text{T,soft}}^{\text{true}} \equiv -\sum_i \vec{p}_{\text{T},i}^{\text{true}}$. Somewhat sloppily (but to save on notation) $(\{p_{\text{T},i}^{\text{max-}L}\}, \vec{p}_{\text{T,soft}}^{\text{max-}L})$ henceforth denote the location of max L. The additional term R_{soft} is *chosen* to be of the form:

$$L_{\text{soft}} \equiv R_{\text{soft}}(\vec{p}_{\text{T,soft}}^{\text{reco}} | \vec{p}_{\text{T,soft}}^{\text{true}}) = \mathcal{G}\left(\frac{p_{x,\text{soft}}^{\text{reco}} - p_{x,\text{soft}}^{\text{true}}}{\sigma_{\text{T}}^{\text{soft}}}\right) \times \mathcal{G}\left(\frac{p_{y,\text{soft}}^{\text{reco}} - p_{y,\text{soft}}^{\text{true}}}{\sigma_{\text{T}}^{\text{soft}}}\right)$$

where $\mathcal{G}(x) \equiv \exp(-x^2/2)/\sqrt{2\pi}$ is the standard Gaussian function, and $\sigma_{\text{T}}^{\text{soft}}$ is an arbitrary width. The reader should understand that R_{soft} is *not* a resolution in the traditional sense of being a measure of how far a reconstructed quantity deviates from the true one. It is rather to be thought of as an empirical term that has been put in to impose the semi-loose constraint $\sum_i \vec{p}_{\text{T},i}^{\text{true}} + \vec{p}_{\text{T,soft}}^{\text{reco}} \approx 0$. This constraint cannot be too strict (e.g. a δ-function) also for the technical reason that most standard minimization packages, certainly MINUIT, exhibit very poor convergence behavior when faced with navigating near-singular functions. A choice of $\sigma_{\text{T}}^{\text{soft}} = 5\,\text{GeV}/c$ is used in the studies here, and it has been checked that the performance of the method is not sensitive to the precise choice of this width except that it should not be too small. Last but not least, it has also been seen that the maximum likelihood solution is highly insensitive to non-Gaussian tails in the jet resolution, i.e. using just the Gaussian core rather than the full shape for $r(p_{\text{T},i}^{\text{reco}} | p_{\text{T},i}^{\text{true}})$ results in at most percent-level differences in the predicted jet spectrum. Since it is quite a bit simpler (at a technical level) to use Gaussian resolutions, this is the prescribed standard for the method.

7.2.3.1 Caveat due to ECAL "holes"

The presence of localized regions of bad calorimetry as described in Section 7.2.1 has a consequence that the seed events do suffer from some distortion when they contain one or more jets falling into these troublesome spots. In particular, the rebalanced momenta of such jets are intrinsically low, and the angular reconstruction is also somewhat distorted away from the regions where there can be no recorded activity. This small fraction of events would not typically have posed a problem—except for the parametrization of the jet resolution by $f^{\text{ECAL}}_{\text{masked}}$. To explain by example, consider that all jets that fall in the regions where $f^{\text{ECAL}}_{\text{masked}} \geq 10\%$ or so tend to be strongly mismeasured. The rebalancing procedure can be set up to be able to correct for some level of the jet mismeasurement, by an appropriate input of the proper jet resolution for these poor calorimetry regions rather than an average core resolution dominated by well-behaved jets as explained above. The η and ϕ biases on the other hand cannot be addressed so simply. At any rate, these mismeasurements lead to a systematic underestimate of either the p_{T} or frequency of jets in regions with nonzero $f^{\text{ECAL}}_{\text{masked}}$, which in turn leads to an underestimate of $\not{H}_{\text{T}}$ caused by jets of substantially high p_{T} losing much of their energy due to high $f^{\text{ECAL}}_{\text{masked}}$.

The solution to this is to use the fact that the physics of interest in this search is symmetric under rotations in ϕ. Each rebalanced event is thus given a random rotation in ϕ—while preserving the p_{T}, η, and relative angles between all the seed jets—whereby the much larger population of events that originally had all jets in good regions now dominate the pool of rebalanced events everywhere.

7.2.4 Benchmark Performance in Monte Carlo

This section demonstrates the performance of the maximum likelihood R+S procedure when applied to QCD Monte Carlo simulated samples. MC-derived resolution templates are used for smearing the rebalanced seed jets, but the data-driven procedure is followed insofar as the resolutions being parametrized by only p_{T}, $f^{\text{ECAL}}_{\text{masked}}$, and η, with jet flavor accounted for by parametrized heavy flavor fractions (Section 7.3). Events are first rejected to model the ECAL hole filter effect as described in Section 7.3.2.1. A term to compensate for mismeasurements of $\{p^{\text{max-}L}_{\text{T},i}\}$ could have been included in L (Section 7.4.1), but is seen not to be needed for the PYTHIA6 QCD samples used here. The following figures are thus benchmark performance plots: what the ***R+S method can ideally achieve*** if jet resolution shapes and per-jet heavy flavor fractions are perfectly measured. A seed jet p_{T} threshold of $p^{\text{seed}}_{\text{T,min}} > 10\,\text{GeV}/c$ has been chosen to stay sufficiently below the smallest reconstructed jet threshold used in the RA2 analysis, i.e. the $p_{\text{T}} \geq 30\,\text{GeV}/c$ threshold for jets used to compute $\not{H}_{\text{T}}$. All seed events are preselected to have ≥ 2 seed jets—rebalancing is of course not meaningful for mono-jet events. This preselection has 100% efficiency since RA2 search cuts require ≥ 3 reconstructed

jets[6].

Figure 7.2.5 shows that when the R+S procedure is run on QCD MC simulated[7] events, the $\not{H}_T$ and H_T predictions are within 20% of the actual MC distributions. The closure in the jet and jet-jet correlation distributions in Figures 7.2.6 and 7.2.7 is at the 10-15% level before $\not{H}_T$ cuts, except for the region $p_{T,2}/p_{T,1} < 0.3$ which is anyway a very extreme tail containing only 4×10^{-5} fraction of events. The error bars in the Figures are "standard" in the sense that every seed event is re-used 100 times to predict 100 smeared events, and the prediction histograms are filled with weight 1/100 per smeared event. However as explained in Appendix E, this is not quite the proper thing to do, since the true uncertainty is in the statistical fluctuations of the seed sample. Since the inclusive QCD seed sample is very large, this statistical uncertainty tends to be negligible (order of one percent) compared to the uncertainty of the fully simulated QCD events to be compared to; therefore the error bars are dominated by the uncertainty of the latter. As such, the effort has only been made for a proper evaluation of the statistical uncertainty for the tabulated numbers, and not the plots which would anyway turn out to be visually very similar at the end. Table 7.1 summarizes the degree of closure for the prediction in various RA2 search regions. Depending on the region of interest, there is a residual 15-20% excess of events predicted by R+S. The only statistically significant excess occurs in the high H_T search region, where there is an 15% excess but only a 4% statistical uncertainty. There is also reason from the inclusive H_T distribution (i.e. before $\not{H}_T$ cuts, Figure 7.2.5) to suspect that there is an overall excess of 5-10% predicted events. This part of the bias would be accounted for by the $(\text{R+S})^N$ "rebalancing bias" systematic as explained in Section 7.5.3, leaving a residual discrepancy that is statistically compatible with being unbiased. However one can also more conservatively take the full size of the R+S vs. MC difference as a bias and systematic uncertainty, in lieu of the systematic uncertainty derived via $(\text{R+S})^N$.

7.2.4.1 Safety Against Non-QCD Contamination

A common concern of SUSY search background estimations is potential BSM contamination in the predicted background distributions, in particular $\not{H}_T$. For the R+S prediction this contamination can only cause an over-estimation of background events; this is undesirable because it reduces the power of the search, and . The same goes for contamination from the other SM backgrounds, which would be somewhat double-counted since they have already been covered by their respective background estimations. It is therefore a very important feature of the R+S prediction that it is largely unaffected by contamination from non-QCD processes with intrinsic missing energy: semi- and di-leptonic top, $W \to l\nu$, $Z \to \nu\bar{\nu}$, BSM, and so forth. This safety is a consequence

[6] In fact, a preselection of ≥ 3 seed jets is also 100% efficient.

[7] Here the $\hat{p}_T \geq 170\,\text{GeV}/c$ PYTHIA 6 samples have been used. The $\hat{p}_T < 170\,\text{GeV}/c$ samples contribute negligible number of events to the baseline selection and tighter search regions, but are responsible for a statistical fluctuation in the low H_T region that obscures the actual performance of the method.

	No $\Delta\phi$ cuts	**Baseline**	$\not{H}_{\mathrm{T}} \geq 250\,\mathrm{GeV}/c$	$H_{\mathrm{T}} \geq 500\,\mathrm{GeV}/c$
N(MC)	385 ± 3.7	31.8 ± 1.1	0.36 ± 0.11	23.5 ± 0.9
N(R+S)	445 ± 0.4	36.6 ± 0.2	0.49 ± 0.01	26.6 ± 0.1
N(R+S)/N(MC)	1.16 ± 0.01	1.15 ± 0.04	1.4 ± 0.4	1.13 ± 0.05

Table 7.1: Second row: Number of events predicted in a $100\,\mathrm{pb}^{-1}$ of integrated luminosity scenario, to pass various event selections as listed in the column headers. The first row is the yield according to the fully simulated PYTHIA 6 QCD sample. The second row is the R+S prediction when executed on this same MC sample. The last row is the ratio of the R+S predicted over actual MC yields. The uncertainties quoted are statistical only.

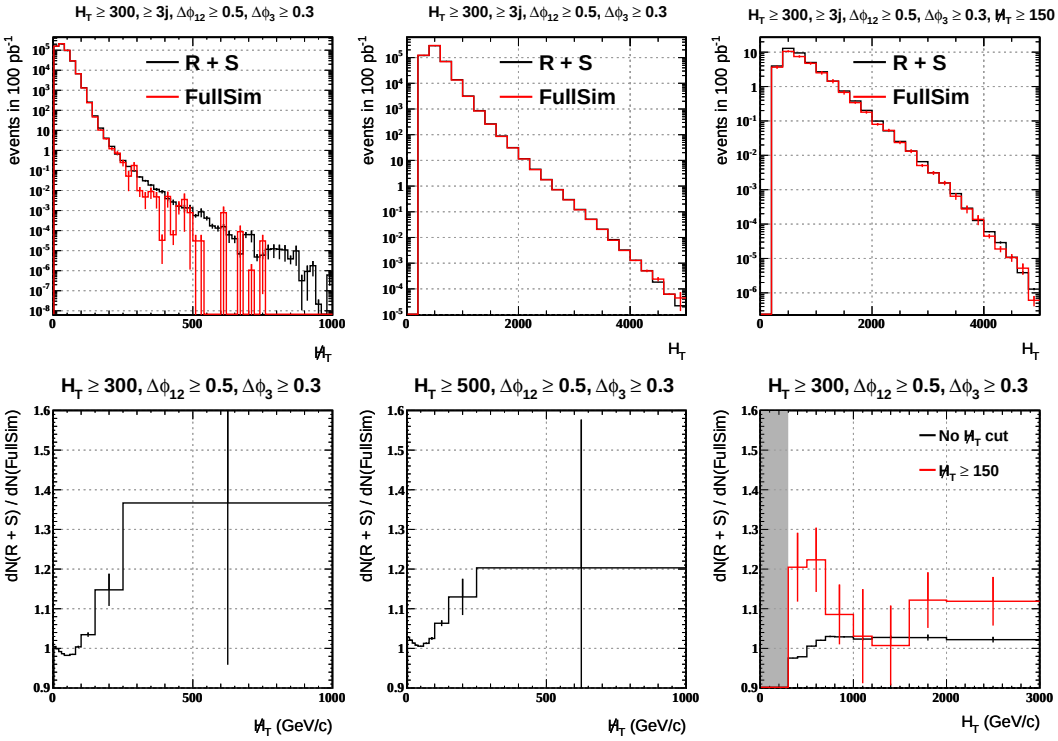

Figure 7.2.5: Maximum likelihood R+S prediction compared to fully simulated MC distributions, for events passing ≥ 3 jets, $H_{\mathrm{T}} \geq 300\,\mathrm{GeV}/c$ cuts, and $\Delta\phi(\not{H}_{\mathrm{T}}, \mathrm{jet})$ cuts as indicated in the legend. The top row show the spectra of events; the bottom row are the ratios of R+S over MC distributions of the above plots, plus those for the other search regions as indicated in the legend. The gray shaded area indicate where all denominators vanish.

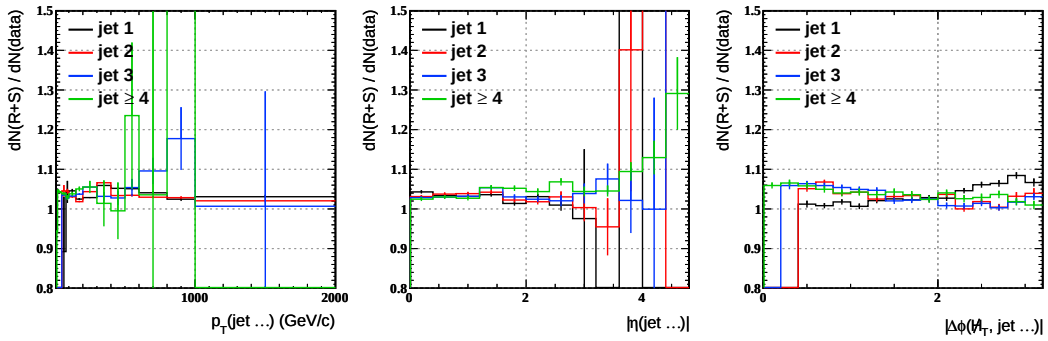

Figure 7.2.6: Maximum likelihood R+S prediction over fully simulated MC distributions, for events passing ≥ 3 jets, $H_{\mathrm{T}} \geq 300\,\mathrm{GeV}/c$, $\Delta\phi_{1\text{-}2} \geq 0.5, \Delta\phi_3 \geq 0.3$ cuts.

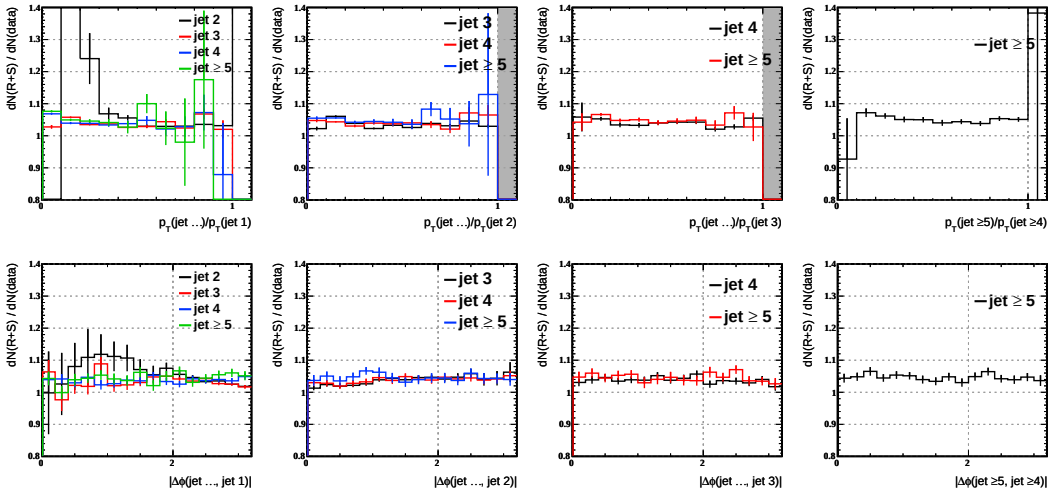

Figure 7.2.7: Maximum likelihood R+S prediction over fully simulated MC distributions, for events passing ≥ 3 jets, $H_{\mathrm{T}} \geq 300\,\mathrm{GeV}/c$, $\Delta\phi_{1\text{-}2} \geq 0.5, \Delta\phi_3 \geq 0.3$ cuts. The gray shaded area indicate where all denominators vanish.

of enforcing the QCD transverse balance condition (Equation 7.2.1) in the rebalancing part of the procedure. For non-QCD events, the transverse momentum conservation is instead $\sum_i \vec{p}_{\mathrm{T},i}^{\,\mathrm{particle}} + \vec{p}_{\mathrm{T,soft}}^{\,\mathrm{particle}} + \vec{p}_{\mathrm{T}}^{\,\mathrm{invisible}}$, where $\vec{p}_{\mathrm{T}}^{\,\mathrm{invisible}}$ is the total transverse momentum of "prompt" invisible particles: LSPs, and neutrinos not from jets. Analogous to the derivation of Equation 7.2.2, $\not\!\!H_{\mathrm{T}}$ in such non-QCD events has the form:

$$\vec{\not\!\!H}_{\mathrm{T}} \;=\; -\sum_{i\neq k}(r_i - r_k)\times \vec{p}_{\mathrm{T},i}^{\,\mathrm{particle}} + r_k \times \vec{p}_{\mathrm{T,soft}}^{\,\mathrm{particle}} + r_k \times \vec{p}_{\mathrm{T}}^{\,\mathrm{invisible}}$$

It is typically the last term that makes MHT large, since the rate of severe jet mismeasurement is much lower than the cross-section to produce a high-p_{T} SM boson that then decays leptonically, or the fraction of BSM events with high-p_{T} LSPs. Conversely, one sees that if this $\vec{p}_{\mathrm{T}}^{\,\mathrm{invisible}}$ piece could be removed from the picture, the MHT distributions of these non-QCD events should not be particularly different from that of a QCD event with the same multiplicity and p_{T} of jets. So long as their cross-sections are much smaller than that of QCD—as current knowledge expects—the R+S prediction remains safe. This "erasing" of $\vec{p}_{\mathrm{T}}^{\,\mathrm{invisible}}$ is in fact what happens in rebalancing. Intuitively, in order for the event to satisfy $\sum_i \vec{p}_{\mathrm{T},i}^{\,\mathrm{seed}} + \vec{p}_{\mathrm{T,soft}}^{\,\mathrm{reco}} = 0$ after rebalancing, $\vec{p}_{\mathrm{T}}^{\,\mathrm{invisible}}$ must have been absorbed into the [visible] momenta of the seed jets. The only danger is if one or more seed jets are rebalanced to have extraordinarily high p_{T}, or if $p_{\mathrm{T,soft}}^{\text{max-}L} \gg p_{\mathrm{T,soft}}^{\mathrm{reco}}$. Both these situations are very unlikely according to the resolutions for jets and soft stuff used to compute the QCD event likelihood (Equation 7.2.5), and have obvious consequences to the value of the maximized likelihood, L^{max}.

In Section 4.5.2 of [50], it is shown that for the calorimeter-jet based analysis, the non-QCD SM contamination of the QCD prediction is below 0.5% in the region $\not\!\!H_{\mathrm{T}} \sim 150\,\mathrm{GeV}/c$, and below 1% everywhere. The contamination from two SUSY benchmark points LM0 and LM1 are respectively 2.5% and 1.2% in the region $\not\!\!H_{\mathrm{T}} \sim 250\,\mathrm{GeV}/c$, and less than 1.5% (1%) in the region $\not\!\!H_{\mathrm{T}} \sim 150\,\mathrm{GeV}/c$. A cut on L^{max} which retains all but 0.5% of QCD events reduces all non-QCD SM contributions to a fraction of a percent, and even the high cross-section SUSY benchmark point LM0 produces at most a 1% contamination at asymptotically high $\not\!\!H_{\mathrm{T}}$. However, since less than one QCD event is expected in the high $\not\!\!H_{\mathrm{T}}$ search region in 2010 Collider data anyway, and the level of potential contamination is negligible compared to all other uncertainties, no effort has been made to apply this cut at this time.

7.2.5 QCD Prediction for 2010 Collider Data

Figure 7.2.8 shows that when the R+S procedure is run on Collision 2010 data, the H_{T} prediction is within 20% of the data distribution before $\not\!\!H_{\mathrm{T}}$ cuts. The high $\not\!\!H_{\mathrm{T}}$ bins and low H_{T} bins for the $\not\!\!H_{\mathrm{T}} \geq 150\,\mathrm{GeV}/c$ region (rightmost plot) look to be underestimated because they contain top and electroweak contributions that are present in data but not in the R+S prediction—however when added together with MC estimates for the non-QCD backgrounds, the full prediction is compatible with data. The predicted

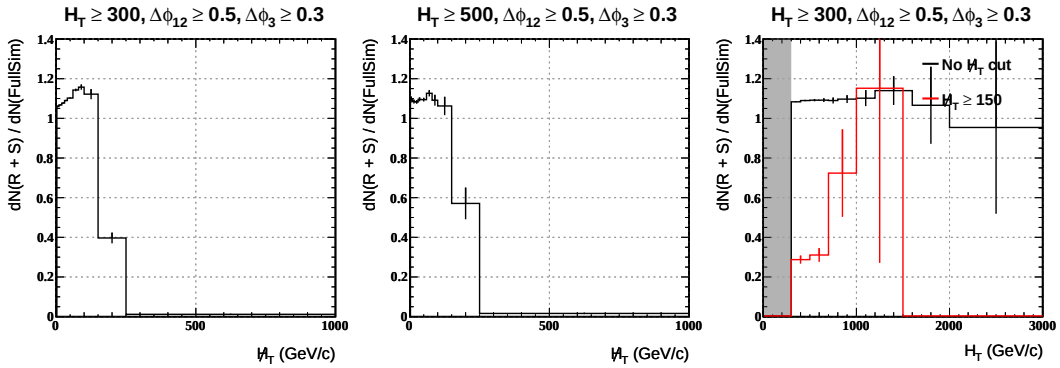

Figure 7.2.8: Maximum likelihood R+S prediction compared to Collision 2010 data, for events passing ≥ 3 jets, $H_T \geq 300\,\text{GeV}/c$ cuts, and $\Delta\phi(\not{H}_T, \text{jet})$ cuts as indicated in the legend. The gray shaded area indicate where all denominators vanish.

jet η distribution shows a bit of distortion in the region around $|\eta| \sim 3$, which is to be investigated. Otherwise all jet and jet-jet correlation distributions in Figures 7.2.9 and 7.2.10 are within 10% of the data before $\not{H}_T$ cuts, which is fully QCD-dominated.

Table 7.2 lists the number of predicted events for various RA2 search regions, as well as systematic uncertainties as evaluated via the methods in Section 7.5.1. Signs have been provided for the change in number of R+S predicted events as induced by the various sources. Uncertainties specified in the form $\pm X\%$ can be assumed to induce more or less symmetric, e.g. Gaussian-distributed variations around the central value over an ensemble of experiments. Uncertainties in the form $^{+X\%}_{-Y\%}$ have an asymmetric variation around the central value, the exact shape of which becomes unimportant since there are many uncertainties of roughly comparable sizes, and the Central Limit Theorem comes into play. Finally, uncertainties with a single sign, i.e. $+X\%$ (or $-X\%$, although not present here) should be understood as upper (lower) bounds on the size of a deviation that should only be positive (negative) according to physics principles. In all of the present cases these are taken to be the full size of an expected bias due to that source. The presence of asymmetric uncertainties induces a shift in the central value of the prediction, and the biases should all be subtracted. This combination has been done in [16] and the results included in Table 7.2 for ease of reference.

7.3 Input jet resolutions

7.3.1 Jet Resolution Measurement Methods

The R+S method as described in Section 7.2 makes use of jet resolutions in two forms:

1. *For rebalancing* : The function $\sigma(p_T^{\text{particle}}|\eta)$, being the trend of the Gaussian core width as a function of p_T^{particle} and in bins of jet η. The functional form

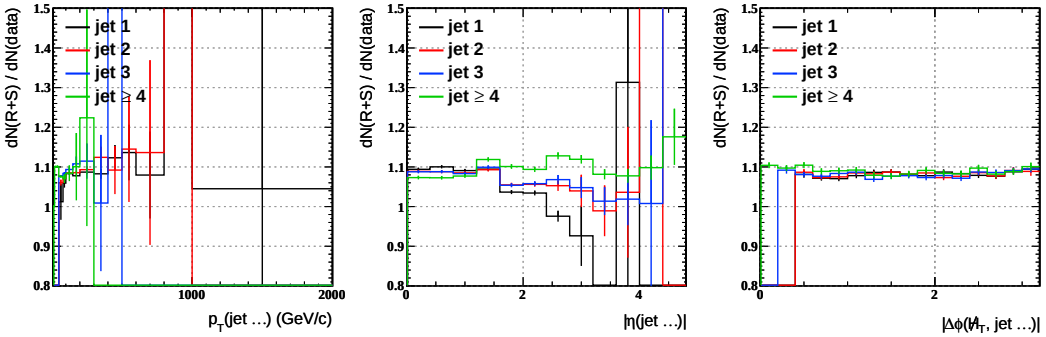

Figure 7.2.9: Maximum likelihood R+S prediction over Collision 2010 data, for events passing ≥ 3 jets, $H_{\mathrm{T}} \geq 300\,\mathrm{GeV}/c$, $\Delta\phi_{1\text{-}2} \geq 0.5, \Delta\phi_3 \geq 0.3$ cuts.

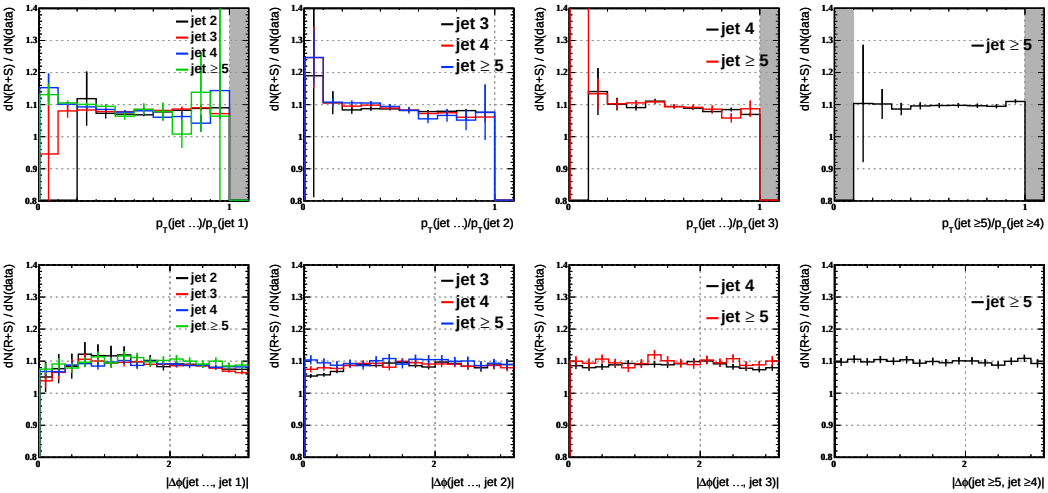

Figure 7.2.10: Maximum likelihood R+S prediction over Collision 2010 data, for events passing ≥ 3 jets, $H_{\mathrm{T}} \geq 300\,\mathrm{GeV}/c$, $\Delta\phi_{1\text{-}2} \geq 0.5, \Delta\phi_3 \geq 0.3$ cuts. The gray shaded area indicate where all denominators vanish.

		Baseline $\not{H}_T \geq 150$	**High** $\not{H}_T$ $\not{H}_T \geq 250$	**High** H_T $H_T > 500$
Nominal prediction		39.4	0.18	19
Bias-corrected prediction		29.7	0.16	16
Seed sample statistics	(symmetric)	$\pm 2.3\%$	$\pm 23\%$	$\pm 3.3\%$
Resolution core	(asymmetric)	$+14\%$ -25%	$+0\%$ -52%	$+15\%$ -21%
Resolution tail	(asymmetric)	$+43\%$ -33%	$+56\%$ -78%	$+48\%$ -34%
Flavor trend	(symmetric)	$\pm 1\%$	$\pm 12\%$	$\pm 0.3\%$
genJet smearing closure	(box)	$+14\%$	$+30\%$	$+7\%$
Rebalancing bias	(box)	$+10\%$	$+10\%$	$+10\%$
Soft stuff estimator	(box)	$+3\%$	$+19\%$	$+4\%$
Control sample trigger	(box)	-5%	-5%	-5%
RA2 search trigger	(symmetric)	$\pm 1\%$	$\pm 1\%$	0%
Lepton veto	(box)	$\pm 5\%$	$\pm 0.05\%$	$\pm 0.2\%$
Pile-up effects	(box)	$\pm 2\%$	$\pm 10\%$	$\pm 2\%$
Total uncertainty		51%	64%	49%

Table 7.2: Second row: Number of events predicted for $36\,\text{pb}^{-1}$ of Collision 2010 data via the R+S method, for various event selections as listed in the column headers. Third row: Bias corrected numbers, to be used in limit setting. The following rows contain the systematic variations (relative) expected from various sources. Sources in italics are biases that should be corrected, with the full size of the bias taken as the systematic uncertainty. The bottommost row is the "overall" systematic uncertainty as combined according to [16].

used to model the shape of the resolution core is of course not limited to just being Gaussian; the salient requirement here is that it should be a well-behaved analytical form so as to have good convergence when used in the minimization software. As previously noted, it is not important for this functional form to also model tails of the jet resolution.

2. *For smearing* : A histogram $r(p_{\mathrm{T}}^{\mathrm{reco}}/p_{\mathrm{T}}^{\mathrm{particle}}|\eta,\ldots)$ of the full jet response probability distribution, parametrized by as many variables as required to capture the detector and physics dependence. A functional form may also be used; however histograms are assumed in this study since they provide more flexibility.

The most direct way of measuring the reconstructed jet resolution is to select events with one very well-measured object to provide the estimation of $p_{\mathrm{T}}^{\mathrm{particle}}$, which should from conservation of transverse momentum be balanced against the probe jet. Photon plus one jet events are ideal candidates for such a measurement, since the photon resolution is order of magnitude better than that of jets. Details of two photon-based resolution measurements are presented in [7]. Unfortunately, the photon production cross-section is three orders of magnitude smaller than that of multi-jet production, which means that for low integrated luminosities these measurements are insufficient to populate the high-p_{T}, low-probability response tails that the QCD background method must predict. As such, a complementary method using di-jet events has been developed in [11] to measure the resolution over a wider range in p_{T}, η, and response. The basic idea is to write down the likelihood of observing a reconstructed di-jet event, given an input $p_{\mathrm{T}}^{\mathrm{particle}}$ spectrum and jet resolution function $r_{\vec{b}}$ described by a set $\vec{b}$ of free parameters. This likelihood is used to obtain maximum likelihood estimators for $\vec{b}$. The performance of this method degrades for low $p_{\mathrm{T}}^{\mathrm{particle}}$ events, where the photon-based measurements naturally take over in importance.

In light of the limited integrated luminosity available in the 2010 Collider data, rather than direct measurements the mode has instead been to derive MC-data scale factors. This makes use of high MC statistics to assist in describing p_{T} and η trends, as well as the full shape of the resolution distributions. Current indications are that the core resolutions are a few percent (relative) wider in data than in MC, which is modeled by an additional smearing of the MC resolution functions. The combined result [11] from all the above methods is used to obtain the R+S data prediction in Section 7.2.5. On top of this, the fraction of jets with response in the tails of the resolution shape may also be slightly higher in data than in MC; for this the shape of the MC resolution tails are assumed to be correct, and a simple scaling of the tail probability is performed. The only caveat is that both a scaling of the distribution at response below unity ("low" tail) and a scaling of the distribution at response above unity ("high" tail), can induce the same change in the asymmetry distribution. The nominal modification is obtained by equally scaling both lower and upper tails of the resolution in order to induce the observed scaling of the asymmetry tail. This is similarly done scaling either only the lower tail, only the upper tail, or both tails equally, to induce the maximum/minimum

scaling of the asymmetry tail that is compatible with its uncertainty band. The envelope of all these variations is taken as the systematic uncertainty band for the jet resolution distribution. This prescription, details of which are in Appendix C, is in fact overly conservative because of course all these variation methods are mutually exclusive, so the actual band cannot possibly be the full size of this envelope. Improvements are foreseen for the future, but is not important yet for the present search.

7.3.2 Jet Resolution Parametrizations

Four variables for parametrizing the jet resolution have been identified in Section 7.2.1, being $p_{\mathrm{T}}^{\mathrm{particle}}$, η, jet flavor, and $f_{\mathrm{masked}}^{\mathrm{ECAL}}$. In order to economize on the total number of bins in which the jet resolution shape must be resolved, the following strategy is adopted:

- All jets are first classified by $f_{\mathrm{masked}}^{\mathrm{ECAL}}$. Jets with $f_{\mathrm{masked}}^{\mathrm{ECAL}} \geq 0.01$ are classified into ten $f_{\mathrm{masked}}^{\mathrm{ECAL}}$ bins with lower edges $0.01, 0.05, 0.1, 0.15, 0.2, 0.3, 0.4, 0.5, 0.6, 0.8$.

  - In order to support the effects of the TP and BE filters, which act only on masked channels of particular status values (13 for TP, 12 and 14 for BE), a further parametrization by channel status is required for jets with $f_{\mathrm{masked}}^{\mathrm{ECAL}} \geq 0.01$. Three bins are used, one for status 13, one for status 12+14, and the last for all other statuses. Here the "status" for a particular jet is determined as that with the highest weighted contribution as described in Appendix D.

- Jets with $f_{\mathrm{masked}}^{\mathrm{ECAL}} < 0.01$ are further classified by flavor: b, c, or light flavor (lf) otherwise.

- For all of the above categories ($f_{\mathrm{masked}}^{\mathrm{ECAL}}$ and flavor), jets are classified into nine $|\eta|$ bins. For very high η values, the limited center-of-mass energy of the collision results in the high p_{T} regions being poorly populated; therefore a different uppermost inclusive p_{T} bin is used for various η regions:

$\lvert\eta\rvert$ bin(s)	Lower edges of p_{T} bins
(*all*)	0,4,6,8,10,12,14,16,18,20,25,30,35,40,45,50,55,60,70,80,90,100,$\cdots$
$[0, 0.8)$	$\cdots$,120,140,160,180,200,250,300,350,400,500,600,700,800,1000,1400,1800, 2500
$[0.8, 1)$	$\cdots$,120,140,160,180,200,250,300,350,400,500,600,700,800,1000,1400,1800
$[1, 1.2)$	$\cdots$,120,140,160,180,200,250,300,350,400,500,600,700,800,1000,1400
$[1.2, 1.3)$	$\cdots$,120,140,160,180,200,250,300,350,400,500,600,700,800,1000
$[1.3, 1.4)$, $[1.4, 1.6)$, $[1.6, 2.5)$	$\cdots$,120,140,160,180,200,250,300,350,400,500,600,700,800
$[2.5, 3.5)$	$\cdots$,120,140,160,180,200,250,300
≥ 3.5	$\cdots$,100

7.3.2.1 ECAL Hole Filter Probabilities

The rebalancing step predicts an inclusive particle level QCD spectrum. Even if the ECAL hole filters were to be applied as a preselection of seed events before rebalancing, the rotation step (see Section 7.2.3.1) would wash out this information to the negligible level. The net effect would be that the depletion of events with jets near ECAL holes would not be modeled, which in turn results in an overestimate of the predicted $\not\!\!H_{\mathrm{T}}$ due to this oversampling of the ECAL hole contribution.

The ECAL hole filter effect can be modeled by a parametrized per-jet probability to cause the event the fail the filters. Both these filters have associated objects that are used to evaluate the filter decision. For the TP filter, these are all ECAL trigger primitives with saturated energy readings (63.75 GeV). For the BE filter, these are the boundary energy objects constructed by collecting all ECAL hits around the border of a contiguous masked region. In both cases a direction can be defined for these objects by computing the arithmetic mean position in η-ϕ. The afflicted jet can then be identified as the one closest in ΔR to the filter object. The fraction of times in which a jet is tagged as associated with the filter object is then recorded as a function of p_{T}, η, $f^{\mathrm{ECAL}}_{\mathrm{masked}}$, and the ECAL status code. Here the p_{T} to be used should be the particle-jet level momenta, in order to avoid correlations with the reconstructed jet response. In the case of MC studies, this can be done by using genJets as probes. Alternatively the probability map can be made (or at least verified) in a data-driven way by "fixing" the momenta of reconstructed jets with $f^{\mathrm{ECAL}}_{\mathrm{masked}} \geq 1\%$ by adding back the component of the $\not\!\!E_{\mathrm{T}}$ vector that is parallel (not anti-parallel) to the jet. For now, the MC-derived map has been used for the results of Section 7.2.4.

As part of the smearing step, a random number is then drawn for each jet and the event rejected with the frequency predicted by the abovementioned probability map. Despite the latter being derived using MC (in order to access $p^{\mathrm{true}}_{\mathrm{T}}$), for the data prediction the event rejection probability is properly computed with respect to the time-dependent list of masked channels for the particular run in which the seed event was

taken. In other words, the rejection probability of "new" masked regions that may develop in the course of data taking, are modeled by the measured rejection probability of a masked region of similar configuration.

7.3.3 Jet Resolution Event Dependencies

Of the three identified populations causing most of the low/high jet response tails as described in Section 7.2.1, the heavy flavor jet production fractions are expected to have some event dependence that needs to be accounted for, while in contrast the proximity to calorimeter holes is a purely geometric effect that can be parametrized just by $f^{\mathrm{ECAL}}_{\mathrm{masked}}$. As explained in Section 7.3.1, the control samples used to measure the jet resolutions are not the same as the search sample, which means that the resolution tails may not be present in exactly the correct sizes. Furthermore, it may not be possible to use a single rescaled resolution function if this "correct size" depends on the physics of the event, such as the number of jets and/or energy scale of the collision. This is the case for heavy flavor (hf) production, where (roughly speaking) the different production modes involve Feynman diagrams with different numbers of final states and different preferences for the momenta and flavor of these final states. Section 4.4.1 of [50] explains how this is sufficiently modeled by further categorizing the jet resolution templates as being from hf jets.

In [89], it is seen that the PYTHIA and MadGraph Monte Carlo generators may bracket the heavy flavor observations in data. This suggests using the hf trends in both these Monte Carlo samples in order to obtain an expectation of how much a proper parametrization would affect the R+S prediction[8]. The smearing procedure is therefore modified as follows:

1. Assume as input $b_n^k = b_n^k(p_{\mathrm{T}})$ and $c_n^k = c_n^k(p_{\mathrm{T}})$, the probability in an n-jet event for a rank-k jet of the given p_{T} to be a b- and c-jet respectively.

    - All jets with $|\eta| > 2.5$ are ignored for the construction of b_n^k (c_n^k), i.e. jet counting is performed with $p_{\mathrm{T}} > 50\,\mathrm{GeV}/c$, $|\eta| \leq 2.5$ jets, and for ranking the list of jets within $|\eta| \leq 2.5$ are ordered by decreasing p_{T}. This is in preparation for data-driven measurement where heavy flavor jets may be distinguished by tracker-based quantities such as vertexing or muon reconstruction, both of which have an acceptance limit of $|\eta| \lesssim 2.4$. It is anyway the case that jets with $|\eta| > 2.5$ have ≥ 3 times smaller leptonic fraction than central jets, which together with the much smaller rate of forward jets renders their precise heavy flavor content unimportant.

2. For each seed jet, draw a random choice with probability b_n^k to be a b-jet and c_n^k to be a c-jet; otherwise the jet is labeled as being of "light flavor" (lf).

[8] A data-driven procedure [22] is planned for a future update.

3. Draw a random response from the jet resolution functions categorized by the choice in (2).

The use of separate b and c flavor trends rather than a combined hf trend is motivated by the b fraction being about 25% different in PYTHIA vs. MadGraph Monte Carlo generated events, whereas the c fraction difference is almost twice as large (~50%).

Presently, all MC indications are that the heavy flavor population does not become a significant contribution to the $\not{H}_{\mathrm{T}}$ spectrum of QCD until $\not{H}_{\mathrm{T}} \geq 250\,\mathrm{GeV}/c$ or so. Since the expected number of QCD events in this region is below an event for the 2010 Collision data, compared to tens of events from other backgrounds, it should be sufficient to concentrate on a strategy that is adequate for the high-H_{T} region. In the latter search region which only utilizes a $\not{H}_{\mathrm{T}} \geq 150\,\mathrm{GeV}/c$ cut, the smallness of the heavy flavor contribution makes it sufficient to evaluate its impact as just a systematic uncertainty. This is treated in Section 7.5.2.

7.4 Corrections to the R+S method

7.4.1 Finite seed jet resolution

The rebalancing procedure starts from reconstructed jet momenta $\{\vec{p}_{\mathrm{T},i}^{\,\mathrm{reco}}\}$ in a measured event and obtains estimators $\{\vec{p}_{\mathrm{T},i}^{\,\text{max-}L}\}$ of the true momenta $\{\vec{p}_{\mathrm{T},i}^{\,\mathrm{particle}}\}$. These estimators have some residual "resolution" $p_{\mathrm{T},i}^{\,\text{max-}L}/p_{\mathrm{T},i}^{\,\mathrm{particle}} \neq 1$, which was significant for the calorimeter-jet based analysis. This is detailed in Section 4.6.1 of [50], together with the introduction of an empirical "p_{T} cooling" factor into the likelihood function L for each jet to encourage their rebalanced momenta to flavor slightly lower values. In other words, the modified likelihood function to be maximized is:

$$L_{\mathrm{cooled}}(p_{\mathrm{T},1}^{\mathrm{true}},\ldots,p_{\mathrm{T},n}^{\mathrm{true}}) \;=\; L(p_{\mathrm{T},1}^{\mathrm{true}},\ldots,p_{\mathrm{T},n}^{\mathrm{true}}) \times \prod_{i=1}^{n} f_{\mathrm{cool}}(p_{\mathrm{T},i}^{\mathrm{true}}) \qquad (7.4.1)$$

For simplicity, the same cooling function is used for all seed jets in the event. The functional form is arbitrary and very different shapes have been shown in [50] to produce the same effect when tuned to result in a flat predicted-over-observed jet multiplicity distribution. For a simple choice of a monotonically decreasing function $\ln f_{\mathrm{cool}}(p_{\mathrm{T}}) \equiv 0.1(A-1)\Delta/[p_{\mathrm{T}}-1+0.1(A-p_{\mathrm{T}})]$, an arbitrary choice of $A = 50$ is made and the following is carried out to determine Δ:

1. For a given jet multiplicity predicted-over-observed ratio histogram, fit a line in the range $3 \leq \mathrm{N(jet)} \leq 6$.

2. For the data measurement, the slope of this line is plotted in Figure 7.4.2 as a function of Δ.

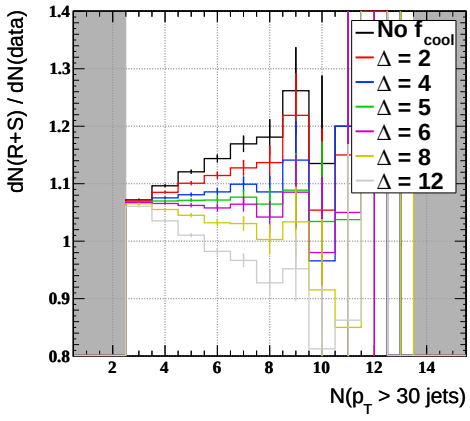

Figure 7.4.1: Ratio of R+S over Collision data distributions of the number of $p_{\mathrm{T}} > 30\,\mathrm{GeV}/c$ jets, when the f_{cool} correction term is included in the modified likelihood L_{cooled}. The parameters of f_{cool} are chosen to be $A = 50$ and the value of Δ is varied as stated in the legend. Events are required to have ≥ 3 jets and $H_{\mathrm{T}} > 300\,\mathrm{GeV}/c$.

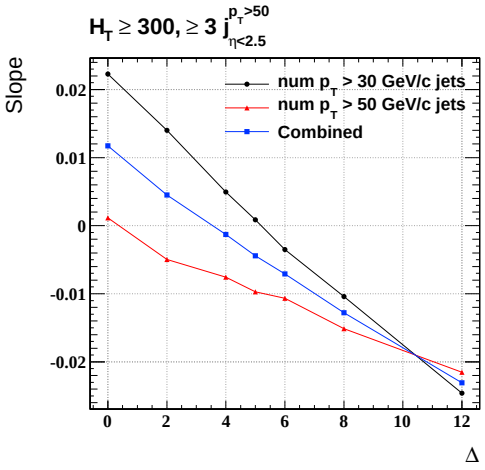

Figure 7.4.2: Slope of linear fits to the ratio of R+S over Collision data jet multiplicity distributions. The "Combined" points are the average of all other points (i.e. for various definitions of jet counting) for the same Δ value.

3. Find the value Δ_0 at which the slope is 0. This is taken to be the optimal value of Δ.

In practice one wants to use more than one p_{T} threshold for the jet counting histograms used to tune f_{cool}, because they probe distortions in different regions of the jet p_{T} spectrum. In these studies two thresholds, $p_{\mathrm{T}} > 30\,\mathrm{GeV}/c$ and $p_{\mathrm{T}} > 50\,\mathrm{GeV}/c$ have been used, in which case a simple arithmetic average of the two slopes is taken as the tuning variable a function of Δ. This is the "Combined" trend shown in Figure 7.4.2, from which the value $\Delta_0 \sim 3.5$ is obtained for the data measurement and used for the results of Section 7.2.5. The prediction for the Monte Carlo closure test does not seem to require any correction.

It is important to note that this derivation of the p_{T}-cooling correction factor can be executed in a completely data-driven way. The non-QCD contamination in the jet multiplicity distribution used to tune this factor is expected to be minimal up to very high jet multiplicities. SM backgrounds with real missing energy constitute less than 1% contamination. A high cross-section signal such as the SUSY benchmark point LM0 can result in a 10% and rising contamination at very high jet multiplicities (≥ 8 from MC expectations), but can easily be circumvented by only using the region $3 \leq$

N(jet) ≤ 6 as described in the procedure.

At any rate, this correction is very small since Particle Flow jets are already very well-measured. The total effect on the $\not{H}_T$ distribution prediction is within 5%. It is noted though that there is still an overall $\sim 10\%$ bias in the number of predicted events, as is evident from the offset of the $\Delta = 5$ ratio plot in Figure 7.4.1. This is understood to be still due to this same seed jet resolution effect as discussed in this Section, but which the selected functional form does not manage to correct. Future improvements are foreseen; for now, this is taken as a bias and a systematic uncertainty.

7.5 Systematic Uncertainties

7.5.1 Jet resolution variations

Jet resolution shape uncertainties

The jet resolution fitting/measurement methods [11, 7] provide systematic variations on the measured shapes and gaussian core trends. These are classified as being from the core up/down and tail up/down variations. Figure 7.5.1 shows the effect of this variation for the high-H_T search region, which is the one of most relevance since QCD is one half of the total background (compared to being negligible in the high-$\not{H}_T$ search region). The envelope ranges from 4% at $\not{H}_T \sim 0$ to 50%-60% at $\not{H}_T \geq 250\,\text{GeV}/c$. A similar variation envelope is seen in the $H_T \geq 300\,\text{GeV}/c$ selection.

genJet smearing closure

Inadequacies in how the jet resolution is defined, and/or what to parametrize it by, can be seen in the gen-jet smearing closure test, which is unaffected by whatever biases might be present in the seed jets due to the rebalancing procedure. This is in fact responsible for most of the discrepancy visible in Figure 7.2.5. The full size of this difference in the gen-jet smeared prediction compared to the fully simulated MC prediction is taken as both a bias correction and a systematic uncertainty. The source of this bias is explained in Appendix B.

7.5.2 Event dependence of flavor fractions

Section 7.3.3 explains how it is possible to account for the event dependence of the fraction of heavy flavor jets by further parametrizing the jet resolution by flavor. Given the expected small difference in the QCD prediction due to this variation, a systematic uncertainty is evaluated by comparing the prediction (in data) when the PYTHIA Monte Carlo heavy flavor trends are used, to that when the MadGraph MC trends are used. These MC generators are seen to have quite different flavor fractions, on the 25% level for bottom and 50% for charm respectively. The difference induced by this variation is very small in the $\not{H}_T \geq 150\,\text{GeV}/c$ search regions, in particular only 0.3% in

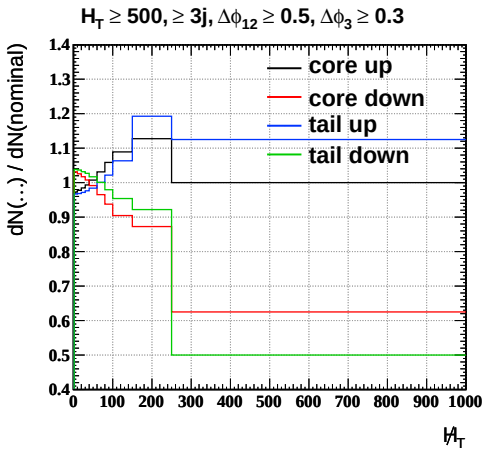

Figure 7.5.1: Ratio of predictions with various core/tail up/down variations of the input jet resolutions, over the one with the nominal jet resolutions. This is for events with ≥ 3 jets, $H_{\mathrm{T}} \geq 500\,\mathrm{GeV}/c$, $\Delta\phi_{1\text{-}2} \geq 0.5, \Delta\phi_3 \geq 0.3$, using 2010 Collision data.

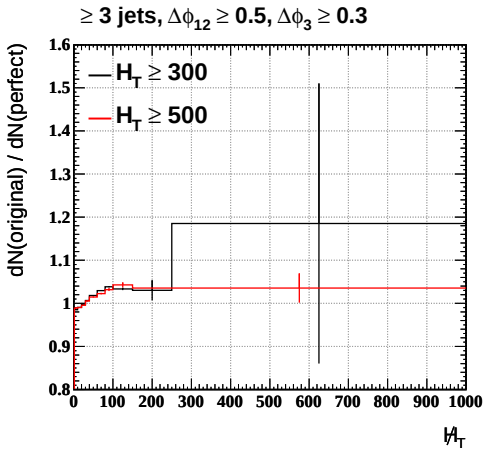

Figure 7.5.2: Ratio of the second iterated R+S prediction using the original soft stuff in the event vs. the "perfect" one obtained from knowledge of the rebalanced jets in the previous iteration (before smearing). This is for events predicted to pass the RA2 search selections, using 2010 Collision data.

the high-H_T search where QCD is an important background. A more careful evaluation of the flavor trend dependency would be necessary for the high-$\not{H}_T$ search region; however the QCD contribution there is negligible in the 2010 data, and this would be a future improvement. Therefore the PYTHIA MC flavor trends are used in producing the nominal R+S prediction, and the difference with respect to MadGraph is taken as a systematic uncertainty.

7.5.3 Rebalance + Smear (R+S) Method

Statistics of Control Sample

The bootstrap method introduced in AppendixE is used to evaluate the statistical uncertainty due to the inclusive seed sample. This is seen to be quite large in the high-$\not{H}_T$ search region, being about 23%, but less than 4% in the high-H_T search region. 100 pseudo-datasets have been used for this estimation.

Trigger (In)efficiency

As stated in [16], the RA2 search sample can be collected using H_T triggers for data taken in 2010. The simplicity and inclusiveness of this trigger makes it also possible for the QCD control sample of seed events for smearing to be collected with the same trigger. However since the momenta of jets are modified by both the rebalancing and smearing procedures, it is expected that there will be migration of events in and out of the sample boundary. For example, an event passing the trigger selection and with offline $H_T = 300\,\text{GeV}/c$ can, after rebalance and smear, predict an $H_T = 250\,\text{GeV}/c$ event which falls outside of the search region. Conversely, an event with offline $H_T = 250\,\text{GeV}/c$ can predict a $H_T = 300\,\text{GeV}/c$ event inside the search region. The latter situation can create an inefficiency in the QCD prediction if a substantial fraction of the predicted $H_T \geq 300\,\text{GeV}/c$ events should come from a lower-H_T sample than collected by the available trigger.

A proper accounting of trigger efficiencies is performed by correcting for the trigger inefficiency in the R+S prediction, and then applying the trigger efficiency (if lower than 100%) for QCD events passing the RA2 search selection. The R+S trigger inefficiency can be obtained in data by comparing the prediction made with events collected with the H_T triggers to that made with events collected with a "control" trigger HLT_Jet15U. The latter is highly prescaled and does not provide enough events to evaluate the difference in predicted events after the full sets of search cuts to any accuracy. Therefore a very conservative upper bound is taken from the only statistically significant observed difference before $\not{H}_T$ cuts, which is in the region $300 < H_T < 350\,\text{GeV}/c$.

Lepton Veto

The efficiency of the RA2 lepton vetoes in rejecting QCD events is percent level after all other search cuts. As such, any uncertainties associated with this is expected to be

insignificant compared to the other systematic uncertainties from the R+S prediction method and input jet resolutions. Since the method itself does not predict the efficiency of lepton vetoes, the lepton vetoes are applied as a preselection of the seed sample. The veto efficiency according to the PYTHIA 6 QCD MC sample (with pile-up) is then used as an upper bound on the uncertainty. For the baseline search region this has a somewhat uncomfortably large value of 5%; however this is solely due to one very highly weighted MC event, and the uncertainty on this number is almost 100%. If this event were to be removed, the veto inefficiency would have been $0.1\% \pm 0.08\%$. Nevertheless, the very conservative 5% is taken as the uncertainty, and anyway the baseline selection does not contribute to the RA2 exclusion limits. For the other search regions the veto inefficiency is well below 1%.

Rebalancing bias and soft stuff uncertainty

One method for evaluating biases due to the rebalancing procedure is to use the events predicted by a first iteration $(\text{R+S})^1$ of the method as a "data-tuned Monte Carlo" with which R+S biases can be studied. In other words, the jet-smearing method predicts QCD events, with the "particle jets" being the rebalanced seed jets, the "reconstructed jets" being the ones after smearing, and the "true jet resolution" being that used to smear the jets. Using these events to quantify the impact of various systematics would be akin to doing the same evaluations with Monte Carlo events, except that this has the benefit of by construction matching closely the actual observed QCD spectrum and detector conditions. This method also does not double-count the biases caused by the resolution input, since as mentioned the inputs used in the next iteration are by construction perfect.

It can also be used to probe the size of potential biases caused by using $\vec{p}^{\,\text{reco}}_{\text{T,soft}}$ as an estimator of $\vec{p}^{\,\text{true}}_{\text{T,soft}}$. The latter is known in the second iteration $(\text{R+S})^2$ as being the negative sum of the particle jets (a.k.a. rebalanced jets from the first iteration). One can then take the difference between $(\text{R+S})^2$ predictions given $\vec{p}^{\,\text{reco}}_{\text{T,soft}}$ as input compared to using $\vec{p}^{\,\text{true}}_{\text{T,soft}}$ as input. This ratio of predictions is shown in Figure 7.5.2, where one sees that the soft stuff bias may induce a shape distortion of the predicted $\not{H}_{\text{T}}$ distribution, which is to be expected since it contributes directly to the balancing of the event. In both the Collision data as well as the QCD MC simulated samples, the predicted bias is in ≥ 3 jet, $H_{\text{T}} \geq 300\,\text{GeV}/c$ events, with very little variation as a function of jet kinematic and jet-jet correlation variables—i.e. it looks mostly like an overall excess in event selection efficiency. This same 15% is taken for this rebalancing-induced uncertainty in the search regions.

High-pileup luminosity scenario

When working with data in a luminosity scenario where pile-up is important, the rebalancing procedure (Section 7.2.3) is not quite correct because it solves for the true jet momenta by imposing the single-interaction QCD balance condition Equation 7.2.1.

While this equation still remains true in the case of multiple primary interactions, a more restrictive condition applies for all interactions A:

$$\left[\sum_i \vec{p}_{\mathrm{T},i}^{\,\mathrm{particle}} + \vec{p}_{\mathrm{T,soft}}^{\,\mathrm{particle}}\right]_A = 0$$

where $[\cdots]_A$ indicates a sum over exactly those momenta belonging to interaction A. Since the rebalancing procedure only has the information that $\sum_A [\cdots]_A = 0$, it may not get the solutions for $\{\vec{p}_{\mathrm{T},i}^{\,\text{max-}L}\}_A$ and $\{\vec{p}_{\mathrm{T,soft}}^{\,\text{max-}L}\}_A$ as correctly as it could have if the tighter constraints were available. However, assuming that the bias in these true momenta—and the fraction of "merged" jets containing particles from more than one interaction—remains small, the jets from the additional primary interactions are still correctly accounted for in the R+S prediction.

The difference between the prediction when performed for a subset of events with exactly one reconstructed primary vertex, versus that performed for the inclusive sample, is taken as a systematic uncertainty. This estimate is conservative because the differences are actually statistically compatible with there being no difference.

Part IV

Analysis of the Results

Chapter 8

Excess or Exclusion?

8.1 The Statistics of Hypothesis Testing

In the heydays of bubble chamber experiments and even beyond, it was not uncommon to claim discoveries without quantification of the word "significant". The discovery of the Υ meson at Fermilab, W boson at CERN, B mesons ad CLEO are examples spanning the decade between the 1970's and 1980's, all of which are hallmarks of experimental particle physics [81]. There has however since been an evolution towards having definitive standards, and the modern high energy physicist is surely inured to the understanding that terms such as "evidence" and "discovery" come with precise price tags. For this the field has borrowed heavily from the study of mathematical statistics, in particular the subject of hypothesis testing. The basic questions of a search-type analysis are simple: Given a hypothesis H_0, is the data compatible with H_0? And: If there is an alternative hypothesis H_1, is the data more compatible with H_1 than H_0? Unfortunately though the answer is *not* simple, most of the time starting with the return question: What do you mean [by "compatible"]?

Forgetting for the moment how such things may be obtained, suppose that one has the probability distribution functions (p.d.f.[1]) for the two hypotheses, $f_0(X)$ and $f_1(X)$ for H_0 and H_1 respectively, where the test statistic X is some vector of quantities that characterize the observation, e.g. the yield in a particular search region. The first task is to identify a critical region $\mathscr{C}$ where observations $X \in \mathscr{C}$ should result in H_1 being preferred over H_0. It is not always obvious what shape this region should take, even in the case of one-dimensional test statistics. For example, one would like that H_0 and H_1 be localized in X-space, and in such a way that there is a specific direction of movement that goes "further" away from the region preferred by H_0 and "nearer" towards that preferred by H_1. The simplest such case is illustrated in Figure 8.1.1 for the one-dimensional problem, in which case it is rather obvious that smaller values of X should be preferred for H_0 and larger values for H_1. One can thus define the critical

[1] Not to be confused with the parton distribution functions, PDF's, though of course these are themselves also p.d.f.'s.

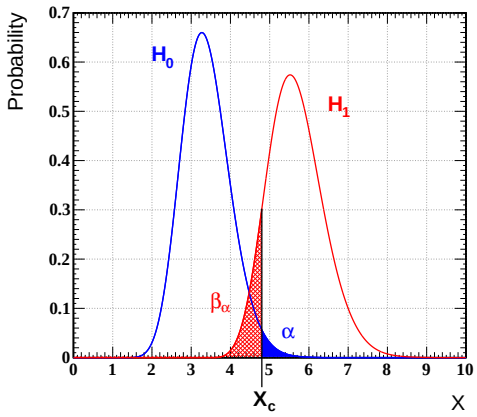

Figure 8.1.1: Illustration of p.d.f.'s $f_0(X)$ for the H_0 hypothesis (blue, left) and $f_1(X)$ for the H_1 hypothesis (red, right). The critical region is above X_c, and α (solid shaded area) and β (hatched area) are the probabilities to make errors of types I and II respectively.

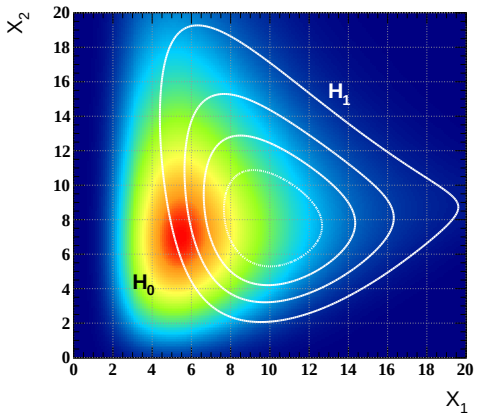

Figure 8.1.2: Illustration of p.d.f.'s for $f_0(X)$ for the H_0 hypothesis (temperature plot, left peak) and $f_1(X)$ for the H_1 hypothesis (white contours, right peak), for a 2-dimensional test statistic $X = (X_1, X_2)$.

region to be the set of points for which $X > X_{\mathscr{C}}$ for some $X_{\mathscr{C}}$; fortunately this is the case for the simple 1-channel counting experiment as are all the search regions in this analysis. Unfortunately the generalization to higher dimensionality is not unambiguous, because of the infinite number of ways in how such a boundary can be drawn. This complication can be seen by considering an example of the probability distributions for a 2-dimensional test statistic $X = (X_1, X_2)$ as shown in Figure 8.1.2. This is especially tricky in the case where X_1 and X_2 are not uncorrelated in the sense that the joint p.d.f. cannot be factorized into a product of two 1-dimensional p.d.f.'s. It is however highly desirable—e.g. to utilize the full power of combining channels (shape analysis) rather than separately evaluating the significance of each. Such a development is foreseen for the future.

In the above framework, one is now prepared to answer the questions below.

8.1.1 Probability distributions, including systematic uncertainties

Before any calculations can be performed, one needs to specify the form of $f_0(X)$ [and $f_1(X)$]. In the case of a counting experiment where H_0 is the background-only hypothesis and H_1 the background-plus-signal hypothesis, these would trivially be Poisson distributed about B and $S+B$ where B and S are the mean expected background and

signal yields respectively. The complication that arises is because B and S are only determined up to various systematic uncertainties, which furthermore tend to come from multiple sources. A discussion of the many ways in which systematic uncertainties can be treated can be found in [70], but is beyond the scope of this document. Instead only the conceptually simple Bayesian treatment is used, whereby one integrates over the nuisance parameters that the background/signal predictions depend on. That is, the predicted background yield depends on these parameters in some known way, but the true values of the parameters are themselves not known. Instead, in the Bayesian language one assumes that one knows the prior probability distributions of these parameters, and can therefore integrate over all possible values of the nuisance parameters, effectively smearing the f_0 and f_1 distributions by this lack of knowledge. The caveat is that the procedure should handle the case where B comprises of multiple estimations of different backgrounds, with possibly correlated (also with S) sources of systematic uncertainties.

The first observation is that it is traditional in the field to enumerate systematic uncertainties by source, and associated "$\pm 1\sigma$" changes in the estimations allowed by these uncertainties. Naively one should be able to write the predicted yield of a particular background as $B = B_0 + \sum_i \delta B_i$ where B_0 is the central predicted value and δB_i is the (unknown) variation that could be induced by the i^{th} source of systematic effects. This decomposition holds so long as the sources of systematic effects are uncorrelated[2], in which case the joint probability distribution of all these δB_i also factorizes into a product of the individual p.d.f.'s, $\text{Prob}(\delta B_1, \delta B_2 \ldots) = \prod_i \pi_i(\delta B_i)$ where π_i are the aforementioned prior probability distributions. The generalization to multiple backgrounds, signal[3] and their uncertainties, still assuming that they are all uncorrelated, is just:

$$\begin{aligned} S+B &= S_0 + \sum_k B_0^{(k)} + \sum_{i,a\in\{S,B\}} \Delta_i^{(a)} \\ \text{Prob}(\Delta_1, \ldots) &= \prod_{i,a\in\{S,B\}} \pi_i^{(a)}(\Delta_i^{(a)}) \end{aligned}$$

where $B_0^{(k)}$ is the central estimated value of the k^{th} background, $\Delta_i^{(B)}$ are uncertainty-induced variations of all the background estimations and $\Delta_i^{(S)}$ that of the expected signal yield, with prior probabilities $\pi_i^{(B)}$ and $\pi_i^{(S)}$ respectively. The H_0 and H_1 probability

[2]This is simply a linear expansion assuming that the terms second order in systematic deviations are relatively unimportant. One may also want to distinguish multiplicative uncertainties, which should be parametrized as $B_0 \times \prod_i (1+\delta B_i)$ instead. However this does not make much of a difference unless the uncertainties are all large and/or far tails need to be sampled.

[3]The following discussion is also applicable to f_1, which is simply a case where the signal terms are removed.

distributions are then computed up to a normalization constant as:

$$
\begin{aligned}
f_0(X) &\propto \left[\prod_i \int \pi_i^{(B)}(\Delta_i^{(B)}) d\Delta_i^{(B)}\right] \frac{(\sum_k B_0^{(k)} + \sum_j \Delta_j^{(B)})^X \exp[-(\sum_k B_0^{(k)} + \sum_j \Delta_j^{(B)})]}{X!} \\
f_1(X) &\propto \left[\prod_{i,a\in\{S,B\}} \int \pi_i^{(a)}(\Delta_i^{(a)}) d\Delta_i^{(a)}\right] \\
&\quad \times \frac{(S_0 + \sum_k B_0^{(k)} + \sum_{j,b} \Delta_j^{(b)})^X \exp[-(S_0 + \sum_k B_0^{(k)} + \sum_{j,b} \Delta_j^{(b)})]}{X!}
\end{aligned}
\tag{8.1.1}
$$

where the integrand simply encodes the Poisson fluctuation around the (systematically uncertain) expected yield B (or $S+B$).

A classic objection against Bayesian statistics is regarding the subjectiveness in what to select for prior distributions. This is not so much of a problem for the π_i distributions since they can in principle be obtained from physics understanding about the source of the uncertainty, i.e. if a distribution of $B^{(k)}$ values due to the i^{th} systematic uncertainty was available, one would just take that distribution. Due to the amount of work required to evaluate this however, it is rarely practical. Instead what one can do is to assume to the best of one's knowledge a "reasonable" form for π_i based on how that uncertainty was obtained. The following types of shapes were used in this analysis[4]:

Distribution	**For uncertainties…**	$\pi(\Delta)$
Poisson	…of statistical origin, with N_{control} events in control sample entering with weight w.	$\frac{(N_{\text{control}})^{\Delta/w}\exp(-N_{\text{control}})}{(\Delta/w)!}$
Box	…estimated as upper/lower bounds.	$\begin{cases} \frac{1}{\Delta_{\max}-\Delta_{\min}}, & \Delta_{\min} < \Delta < \Delta_{\max} \\ 0, & \text{otherwise} \end{cases}$
Gaussian	…estimated as symmetric 1σ intervals.	$\frac{\exp[-(\Delta-\mu)^2/2\sigma^2]}{\sqrt{2\pi\sigma^2}}$
Dimidated gaussian	…estimated as asymmetric "1σ" intervals.	$\frac{1}{\sqrt{2\pi}} \times \begin{cases} \exp[-\frac{(\Delta-\mu)^2}{2\sigma_+^2}]/\sigma_+, & \Delta > \mu \\ \exp[-\frac{(\Delta-\mu)^2}{2\sigma_-^2}]/\sigma_-, & \Delta < \mu \end{cases}$

[4]When assessing the far tail of the H_0 distribution as required to claim a discovery, it would furthermore become important to also consider shapes with longer tails.

The remaining issue is that of correlated uncertainties, but this is actually a non-issue because with a bit of work, it should always be possible to define all the systematic uncertainties in such a way that they are indeed uncorrelated. For example, the MC jet energy scale (JES) uncertainty can affect several background estimations if they use MC information in some way, and definitely affects the signal modeling. In this case the naive writing would have resulted in multiple terms $\Delta_{\text{JES}}^{\text{signal}} + \Delta_{\text{JES}}^{b1} + \Delta_{\text{JES}}^{b2} + \ldots$ for signal and backgrounds $b1$, $b2$ etc., each with presumably the same form π_{JES} of the prior distribution but different impacts $\pi_{\text{JES}}(\Delta^{(k)}|\delta_{\text{JES}+}^{(k)}, \delta_{\text{JES}-}^{(k)})$ where $\delta_{\text{JES}\pm}^{(k)}$ are the yield variations induced by varying the jet energy scale by "1σ" up/down. All these should be collapsed into a single term Δ_{JES} with prior distribution $\pi_{\text{JES}}(\Delta_{\text{JES}}|\delta_{\text{JES}+}^{\text{signal}} + \delta_{\text{JES}+}^{b1} + \ldots, \delta_{\text{JES}-}^{\text{signal}} + \delta_{\text{JES}-}^{b1} + \ldots)$ since they are fully correlated. Another example is when two or more background estimations utilize overlapping control samples, but this can be handled in the same way with a bit of book-keeping to split the predictions up into completely correlated and completely uncorrelated pieces. To avoid this amount of work one may also prefer to treat as uncorrelated the positively correlated pieces, which is permissible because it results in a larger a.k.a. more conservative spread in the distribution of predicted background yields.

Lastly, it should be said that when the background predictions have many systematic uncertainties of comparable absolute sizes (and sufficiently finite in distribution), the Central Limit Theorem of probability theory ensures that the combined distribution will be approximately normally distributed. This is often used to justify a simple addition by quadratures of the sizes of each uncertainty. The caution here is that the change in the predicted yields often depend non-linearly on the "knobs" that one turns to evaluate the size of each systematic effect, leading to asymmetric uncertainties. This happens especially when the variations are large, and/or intrinsically almost one-sided e.g. for efficiencies near 0 or 100%. Even if the dependence was mostly linear, large uncertainties can cause the gaussian p.d.f. assumption to break down because a substantial portion of the probability content is in some unphysical region like that of negative event yields. The combination of such uncertainties is not entirely obvious, and ofttimes used prescriptions e.g. adding the up/down uncertainties separately in quadratures or linearly do not make mathematical sense. In fact these ad hoc prescriptions go so far as to break the convergence properties of the Central Limit Theorem: consider when all the "up" sizes are larger than the "down" sizes, where the separate summation "technique" will preserve or even enhance the difference after adding many sources. One should at the very least symmetrize the up/down halves to obtain an approximate root-mean-square deviation (RMS) of the asymmetric distribution before adding sources together in quadratures, although it is debatable as to whether the symmetrization should be done linearly (i.e. an arithmetic average) or in quadratures. All these issues [41] are precluded by the combination procedure detailed above.

8.1.2 Significance a.k.a. p-value of a measurement

Given $f_0(X)$, one would first like to know if a discovery has been made, i.e. an observation outside of bounds acceptable to the background-only ("null") hypothesis H_0. This is done by simply checking if the data falls within the critical region $\mathscr{C}$, i.e. without recourse to any particular signal model. The definition of $\mathscr{C}$ comes from considering the types of errors that can be made in the choice between H_0 and H_1:

Type I: H_1 is selected even though H_0 is true, which occurs with probability $\alpha \equiv \int_{X\in\mathscr{C}} dX\, f_0(X)$.

Type II: H_0 is selected even though H_1 is true, which occurs with probability $\beta_\alpha \equiv \int_{X\notin\mathscr{C}} dX\, f_1(X)$.

The regions corresponding to these probabilities are illustrated in Figure 8.1.1. Since a mistake of type I is the more embarrassing one to make, the selection of $\mathscr{C}$ aims to make the probability of this as small as is feasible. In modern high energy physics the convention is typically to define a $\alpha = 3\sigma \approx 0.135\%$ critical region for "evidence" and a $\alpha = 5\sigma = 2.87\times10^{-7}$ region for a "discovery". The choice to express probability content in the form $n\sigma$—i.e. the integral above n standard deviations of the normal distribution—is convenient to avoid proliferation of very small numbers.

For a particular counting experiment that has observed X_D events in data, the significance a.k.a. p-value of this observation is defined as

$$p_B^D \equiv \int_{X>X_D} f_0(X)\, dX$$

Therefore $p_B^D \leq 3\sigma\,(5\sigma)$ would constitute evidence (discovery).

8.1.3 Limits on signal yield

When no evidence/discovery can be claimed, one would instead like to know what maximum yield of signal could be present in and still be compatible with the data. This can be obtained from Equation 8.1.1 by applying Bayes' theorem, which gives (up to a normalization constant) $f_1(S_0|D) \propto f_1(D|S_0)\Pi(S_0)$. That is, Equation 8.1.1 gives the likelihood $f_1(D|S_0) = f_1(D)$ of observing $X = D$ given the signal yield S_0, which can be re-interpreted as the probability for S_0 given D at cost of a prior distribution $\Pi(S_0)$. The latter is in fact the controversial part about the Bayesian treatment here, since there should be no information injected into the calculation by this arbitrary choice. A flat prior distribution for the signal yield has been chosen for the results in Section 8.2, as well as neglecting the systematic uncertainties on the signal yield. This leads to the following formula for the signal p.d.f.:

$$f_1(S_0|D) \propto \left[\prod_i \int \pi_i^{(B)}(\Delta_i^{(B)})d\Delta_i^{(B)}\right] \times \frac{(S_0+\sum_k B_0^{(k)}+\sum_j \Delta_j^{(B)})^D \exp[-(S_0+\sum_k B_0^{(k)}+\sum_j \Delta_j^{(B)})]}{D!}$$

where D is the number of events observed in data. The value of $S_0^{\max}$ such that $\int_{S_0<S_0^{\max}} f_1(S_0|D)dS_0 = \text{C.L.}$ provides a limit on the number of signal events that could be present and still be compatible with D to the desired confidence level C.L.

8.1.4 Excluding signal models

Given a particular signal model, one may also go in the direction of hypothesis testing. The characterization of a discovery is a nontrivial task that is beyond the scope of this document to discuss. On the other hand in the case of no evidence/discovery, it is quite a standard task to determine which signal models have been excluded because they would have contributed enough events to be discrepant with the background-only yield. One might be tempted to do this just by evaluating the confidence level of the H_1 hypothesis, $\text{CL}_{S+B} \equiv \text{Prob}(X \leq X_D|H_1)$, and exclude H_1 if this probability is small enough, say $< 5\%$. However this has a defect in that whenever the observation X_D is very small, many signal hypotheses can be excluded even though the compatibility of X_D with the background-only hypothesis is also rather poor. That is, if one assumes for a moment that the B-only hypothesis H_0 is true, then an observation $X_D \ll B$ is understood to be a downward fluctuation by $B - X_D$ which although unfortunate may nevertheless occur due to the probabilistic nature of experiments. However by comparing X_D to the $S+B$ hypothesis H_1, this missing $B - X_D$ events are allowed to enhance the contribution from signal roughly speaking by $S \to S + (B - X_D)$. In such a way one may even conclude that the H_0 hypothesis is itself excluded by $\text{CL}_B < 5\%$ via such an observation. This does not make the use of CL_{S+B} wrong per se, but "only" conceptually disturbing.

A commonly used solution is to normalize the H_1 confidence level to that of H_0, i.e. using the modified confidence level $\text{CL}_S \equiv \text{CL}_{S+B}/\text{CL}_B$ [73, 55]. Furthermore, rather than just the event count X as assumed in the discussion above, the optimal test statistic to use is actually the likelihood ratio $f_1(X)/f_0(X)$. The probability distributions of CL_{S+B} and CL_S must thus be computed via a change of variables, which is technically easiest via MC integration techniques. One of the present prescriptions of the CMS collaboration is to exclude a particular signal model S if $\text{CL}_S < 5\%$, i.e. at 95% confidence level (C.L.). The surface bounding the set of all excluded points in BSM parameter space is called the exclusion limit. For the purposes of search design, or for comparing to the observed limit, it is also common to compute the expected limit, which is simply the one evaluated at the median of the background-only test statistic.

8.1.4.1 Signal contamination

The caveat in using data-driven background predictions is that they can be prone to contamination from signal events, which typically results in an excess of predicted background events and can therefore not be neglected because it would cause the limit to become too optimistic. In such a case one has first to subtract the expected signal contamination from the predicted background, i.e. by executing the affected background estimation methods on the MC simulated signal samples and computing the induced yield. This unfortunately complicates the procedure, also because it makes the derived limits difficult to port to other models especially for theorists who would then have to mock-up background predictions in some way. It has however been noted[86] that for some searches it is possible to anticipate how the contamination would modify the background prediction, e.g. by a simple prescription that expresses how much contamination would result from a given total signal yield. For example, most of the signal contamination in this search affects the lost lepton predictions, which due to the same closure properties as when performed on background events, more or less[5] also predicts the number of signal events with lost leptons. In the case of the $S+B$ hypothesis, this actually has an even simpler form because subtraction of the lost-lepton contribution from the S term, which would already only contain contributions from fully hadronic or lost-lepton events, would leave just the fully hadronic piece. This is pleasant because it allows one to use MC truth information to only evaluate the fully hadronic component of the signal, but does not apply to the B-only hypothesis that is required in the CL_S method. Nevertheless, it provides an easy way to estimate the impact of signal contamination, which is also conservative in the case of using the CL_S method with only modification of the $S+B$ hypothesis.

8.1.5 Search power

Suppose for a moment that one adopts the naive but conceptually simpler prescription of citing evidence (discovery) if $p_B^D = \int_{X>X_D} f_0(X)\,dX \leq 3\sigma\,(5\sigma)$, and otherwise excluding a signal if $\int_{X<X_D} f_1(X)\,dX < 5\%$. In a hypothetical space of all possible signal models, it is easy to see that these two regions are not mutually complementary, because of a "gray area" in which the signal yield is too high to be excluded, and yet too low to be conclusive according to the deliberately stringent conditions imposed by the field. Using a test statistic other than X for signal exclusion, e.g. the likelihood ratio as for the CL_S method, would modify this border, but the conclusion would remain the same.

This non-complementarity has direct implications in the task of optimizing or studying the performance of a search, because it is not obvious that a choice that would maximize the exclusion limit would also maximize discovery potential, and vice versa. Here a classic measure of discovery potential is the search power $1-\beta_\alpha$, i.e. the probability

[5] This would have been exact except for the MC-derived acceptance correction factors.

that a particular signal, if present, would cause a discovery to have been made. All this is further complicated in the typical case where there are many more than one candidate signal models, because it is highly unlikely that one would be able to simultaneously maximize the performance w.r.t. each of them.

Instead, it is recommended in [71] that one should maximize the size of the region satisfying

$$1 - \beta_\alpha(\vec{m}) > \text{C.L.}$$

where C.L. is the desired confidence level chosen for limit setting (here 95%), and $\vec{m}$ indexes a particular signal model in the space of model parameters. This "sensitivity region" has the nice property of being one in which the experiment is *conclusive* in the sense of either resulting in an exclusion or otherwise a discovery, with no possible in-between. The choice to maximize the size of the region rather than some form of combined/average power also precludes preferring a search that has better power in regions of already high power, thereby neglecting coverage.

8.2 Prediction vs. Measurement in $36\,\text{pb}^{-1}$

The expected numbers of background events in various search regions (Section 3.3), as obtained from the estimation methods detailed in Sections 5, 6, and 7, are reported in Table 8.1. The numbers of events observed in data are all slightly below the expected background yield, but then the search regions are not uncorrelated. The statistical and systematic uncertainties are combined as explained in Section 8.1.1 and the RMS of the resulting p.d.f.'s cited here. Sadly, all observations have p-values within 1σ, so only a limit on the allowable signal yield could be obtained (Section 8.1.3), which turns out to be about half of the data yield in all search regions. The $\not{H}_\text{T}$ spectrum observed in the data (Figure 8.2.1) has in fact a few events strewn along the far tail, all of which have been examined for and do not exhibit any obvious instrumental or reconstruction problems. The most striking such event was recorded on October 26, 2010, and is present in all three search regions. The transverse projection view of this event is shown in Figure 8.2.2. It has quantities $\not{H}_\text{T} = 693\,\text{GeV}/c$ and $H_\text{T} = 1132\,\text{GeV}/c$, yielding an approximate center-of-mass energy scale of $\not{H}_\text{T} + H_\text{T} = 1.83\,\text{TeV}/c$ i.e. 36% of the available beam-beam collision energy. None of the jets in the event are identified as originating from heavy flavor, and none of all possible jet-jet and jet-jet-jet invariant mass combinations are compatible with the W boson or top quark masses. The direction of $\vec{\not{H}}_\text{T}$ is also far from any of the known masked channels in the EM calorimeter, as well as from any of the reconstructed jets or high-p_T track activity in the event.

Given the lack of evidence for any real excess, exclusion limits have been set for several types of signal models. The first and traditional set are the Constrained MSSM (CMSSM) family of models [12], which has 5 free parameters as opposed to the 120 free parameters in the MSSM. This dramatic reduction is performed by imposing several constraints that, although arbitrary, are consistent with experimental data and cos-

Background	Baseline $\not{H}_T \geq 150$	High $\not{H}_T$ $\not{H}_T \geq 250$	High H_T $H_T > 500$
$Z \to \nu\bar{\nu}$	26.3 ± 4.8	7.1 ± 2.2	8.4 ± 2.3
$t\bar{t}/W \to e, \mu + \ldots$	33.0 ± 8.1	4.8 ± 1.9	10.9 ± 3.4
$t\bar{t}/W \to \tau_h + \ldots$	22.3 ± 4.6	6.7 ± 2.1	8.5 ± 2.5
QCD multi-jets	29.7 ± 15.2	0.2 ± 0.1	16.0 ± 7.9
Total SM background	111.3 ± 18.5	18.8 ± 3.5	43.8 ± 9.2
Observed in $36\,pb^{-1}$ data	111	15	40
95% C.L. limit signal yield	40.4	9.6	19.6

Table 8.1: Predicted background event yields from the data-driven methods, in various search regions. The last line is the maximum number of signal events that could be present in and still be compatible with the data to 95% C.L..

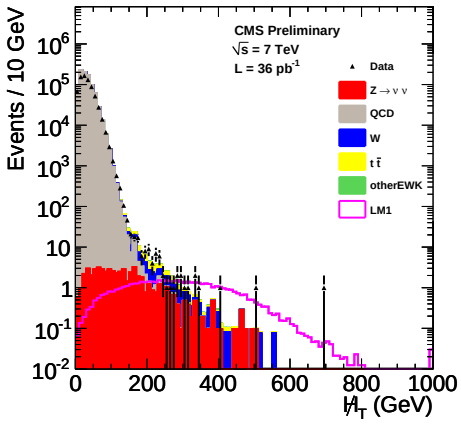

Figure 8.2.1: Differential $\not{H}_T$ distribution for various MC simulated samples (stacked except for the example signal model point LM1), with that of $36\,pb^{-1}$ of CMS data overlaid.

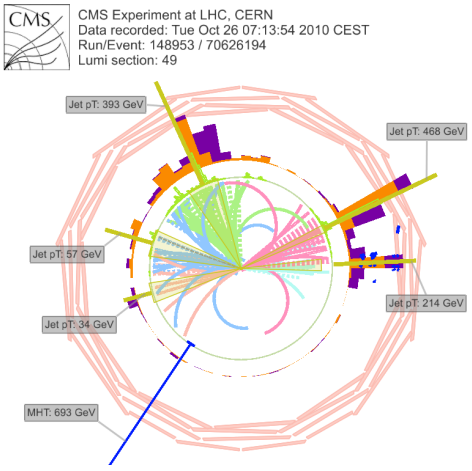

Figure 8.2.2: r-ϕ view in the detector display of event 70626194, in luminosity section 49 of run 148953. This is the event with highest $\not{H}_T$ that passed search selections.

mological considerations, as well as retains a large range of phenomenology in the resulting models. Two of these parameters, m_0 and $m_{1/2}$, control the electroweak scale squark and gluino masses, and are therefore scanned over in fine (10 GeV) steps. The other three parameters are fixed to have values $\tan\beta = 10$, $\mu > 0$, and $A_0 = 0$; a fully hadronic search would anyway be insensitive to changes in these. The signal samples are generated using the full simulation, and have associated experimental as well as theoretical uncertainties. The largest experimental contribution to the uncertainties arises from the modeling of the jet energy scale and jet resolution, the next largest being the measurement of the total integrated luminosity. The measurement of the trigger efficiency, and modeling of the lepton veto and various clean-up filters (Section 3.2.2) are all percent-level in uncertainty. On the whole the combined experimental uncertainties are on the order of 10%, typically smaller, and do not have any significant impact on the conclusions. The theoretical uncertainty in the signal modeling are larger, the worst one being the factorization and renormalization scale uncertainties on the NLO cross-section calculations, which can be $\sim 15\%$. Contributions from uncertainties of the parton distribution functions and initial state radiation are smaller, i.e. a few percent, and final state radiation uncertainties are negligible. Signal contamination in the background predictions is computed using the same MC simulated signal samples, per point in the $(m_0, m_{1/2})$ parameter space plane, and removed from the expected background yield prior to the evaluation of the limit. This affects the muon control sample of the lost lepton predictions, which yields a contamination of around 3 to 5 events in the region near the limit curve. The photon control sample for the $Z \to \nu\bar{\nu}$ prediction could in principle be similarly prone, but CMSSM models do not have any particular source of isolated photons, and therefore this contamination is negligible. Lastly, the R+S method for the QCD multi-jet background prediction is intrinsically safe against signal contamination.

Figure 8.2.3 shows the observed and expected CL_S limits in the CMSSM $(m_0, m_{1/2})$ parameter plane for this search, labeled as "Jets+MHT". The contour is the envelope selecting the best sensitivity of either the high-H_T or high-$\not{H}_T$ search regions. These have complementary purviews, the high-$\not{H}_T$ selection being more powerful in the large $m_{1/2}$ region, while the high-H_T selection excludes more of the large m_0 region. For reference, shaded regions excluded by various past experiments are also shown, whereby one sees the significantly higher reach of this search. The exclusion from an ATLAS search [40] in the same fully hadronic final state can be seen in Figure 8.2.4—although not really comparable due to differences in the limit computation method—in which case it would have exceeded that of the Razor exclusion by about 50-60 GeV in $m_{1/2}$ in the region $m_0 < 500$ GeV, but less than the Jets+MHT exclusion by 100 GeV or more in $m_{1/2}$ in the region $m_0 > 500$ GeV. A few other searches performed by the CMS collaboration on the same data are shown as further contour lines, in particular the trio of other fully hadronic searches labeled as "α_T", "$\alpha_T + b$-tag[6]", "Razor", in red, whereas the leptonic searches are indicated by cyan lines. The "α_T" searches utilize an event

[6] This corresponds to RA1b in Section .9.2.

shape observable α_T [56, 72] which provides a very strong rejection of the QCD multi-jet background, and is powerful for signal models with low jet multiplicities and high $\not{E}_T$. Thanks to a higher signal acceptance however, this analysis manages to strongly exceed the α_T limits in spite of a larger background count. The Razor-based search is very comparable, and in fact complementary in the large m_0 and large $m_{1/2}$ regions. The degradation of the Razor-based limits compared to those of this search at high $m_{1/2}$ is also due to the cascade decay chains, where the higher multiplicity of final-state objects means that it is easier to confuse the hemisphere reconstruction required by Razor and attendant variables. On the other hand at high m_0 the simpler topologies are in the Razor search's favor and the ≥ 3 jet selection penalizes this search. Lastly, the leptonic searches all appear to provide looser constraints, because the branching ratios to the relevant topologies are significantly smaller than unity; this is also the reason the $\alpha_T + b$-tag search gives a smaller excluded region compared to the vanilla α_T search. Lastly, Figure 8.2.5 shows the excluded region for this search in the $(m_{\tilde{q}}, m_{\tilde{g}})$ plane, which is a transformation of the $(m_0, m_{1/2})$ parameters and is more physically intuitive to think about. The production cross-section is largest when the squark and gluino masses are of comparable sizes, because of a strong enhancement from the squark-gluino associated production process, and falls off as the squark mass grows higher than that of the gluino. This trend is reflected in the excluded region, which is largest near the diagonal where it reaches masses of almost 700 GeV, and falls off to $m_{\tilde{g}} \sim 500$ GeV for asymptotically high squark mass.

Despite their utility as common ground by which searches can be compared, there is dissatisfaction amongst both theorist and experimentalist communities regarding results expressed only in a few slices of some constrained sub-space. The reason has been explained in Section 4.3, i.e. that there is no obvious way to generalize from these slices to any wider questions of interest. This happens because the signal selection efficiencies are strongly dependent on the production-decay topologies, and each point in say the $(m_0, m_{1/2})$ plane consists of some complicated admixture of topologies. As such, the exclusion of $m_{\tilde{g}} < 500$ GeV/c models for pretty much any value of $m_{\tilde{q}}$ as seen from Figure 8.2.5 certainly does not mean that this region is excluded in any conceivable model, or even "many" conceivable models. This motivates a turn towards simplified models in the following chapter.

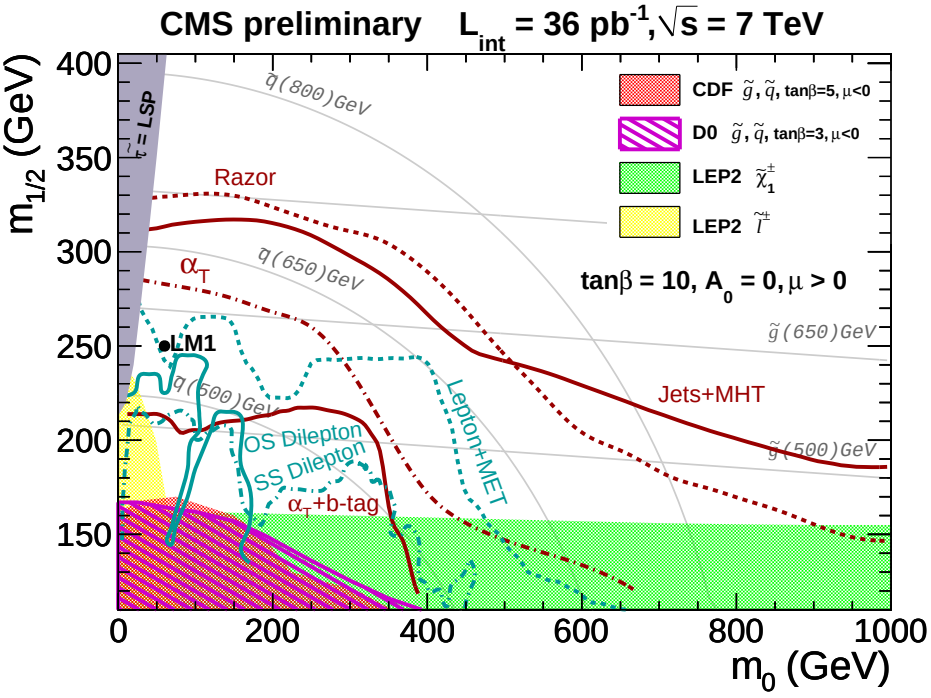

Figure 8.2.3: Excluded regions in CMSSM $(m_0, m_{1/2})$ plane by various CMS collaboration searches using 2010 data, and compared to several past experiments. This search is indicated as "Jets+MHT".

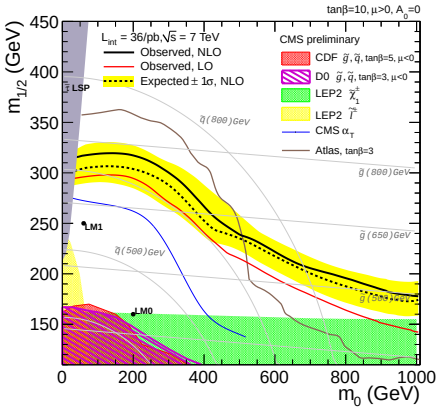

Figure 8.2.4: Excluded regions in CMSSM $(m_0, m_{1/2})$ plane by this search compared to several past experiments and the present experiment ATLAS, also at the LHC. The yellow shaded region around the exclusion contour is the $\pm 1\sigma$ uncertainty band.

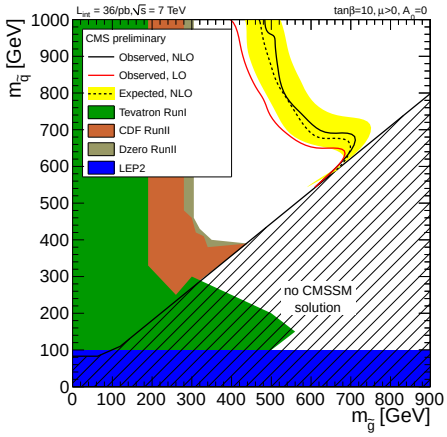

Figure 8.2.5: Excluded regions in CMSSM $(m_{\tilde{g}}, m_{\tilde{q}})$ plane by this search compared to several past experiments. The yellow shaded region around the exclusion contour is the $\pm 1\sigma$ uncertainty band.

Chapter 9

The SUSY Frontier, 2010

9.1 Performance of This Search

The importance of planning/evolving a search towards getting the most out of data may be obvious, but the metric by which to do so is less easily defined when the form of the signal is not well known. Much of the design principles explained in Section 3 have been trigger and background motivated, particularly the H_{T} and $\not{H}_{\mathrm{T}}$ cuts. The relatively low integrated luminosity of $36\,\mathrm{pb}^{-1}$ made it such that these simple search regions were already quite sufficient; however orders of magnitude more delivered data is expected just by the end of the year 2011. There will be more handles that can and will have to be used in order to maintain a competitive edge, especially since the current search regions are rather high in background count.

In preparation for this, it is of interest to consider the strengths and weaknesses of this search in terms of a range of "high priority" simplified models [44]. While a large set, they are still quite finite and covers many staple features that could be present in some of the more popular BSM models (Section 1.4). Within the constraint of remaining a fully hadronic jets and missing momentum search, only topologies that are salient and distinguishable are discussed in the following. The mnemonics used to refer to each of these are in Table 9.1, and the SUSY language is used without significant loss of generality (Section 1.5.1). The reader should keep in mind that theoretical uncertainties on the SMS models have not been evaluated in these studies, as they are rather dependent on details of the MC event generation software, and are in a sense not a question of whether one could observe an excess in these channels but rather whether one would be able to characterize an excess as being from so-and-so model. Characterization is not the main concern of the performance studies here, therefore this aspect has been neglected for technical simplicity. It is however known from [16] that the largest uncertainties are those associated with ISR and PDF modeling, and affect mostly the low mass-splitting, low produced particle mass regions. Experimental uncertainties in the signal simulation also affect mostly the same regions, the largest of which is the jet energy scale uncertainty which is accounted for here, the rest of which is negligible in

comparison and were thus neglected. Even the jet energy scale uncertainty has little impact on the exclusion limits or the sensitivity region. More information about the MC simulated samples used in this study are found in Appendix A.3.

In the context of the CMS SUSY searches of 2010, this search is referred to as Reference Analysis 2 (RA2). This label is used to distinguish these from studies of other searches in the following section. For brevity the high-$\not{H}_T$ and high-H_T searches are denoted as MHT+ and HT+ respectively, and the baseline search selection is assumed unless otherwise stated. This part of the study only involves the predicted rather than observed performance, in order not to base conclusions on fluctuations in the data. Since the expected limit is not sensitive to the issues that motivated use of the CL_S method (Section 8.1.4), the simpler procedure of computing CL_{S+B} with event yields (not likelihood ratios) is used. Unless stated otherwise, the signal contamination is also assumed to be zero, as would happen if complementary regions could be used to bound this in or subtract it from the data-driven background predictions. Such robustness is certainly a desired development for the future.

8.1.4.1

9.1.1 Single-stage decay topologies

The simplest models one can build and with high cross-section are those with pair-production of gluinos or squarks, which then undergo direct decay into the LSP. Furthermore, the squark-gluino pair production topology has been omitted for simplicity, although attractive because of the significant boost in cross-section should it be present. For this search the phenomenology would anyway look like something in between the squark-squark and gluino-gluino production events, since there is not (yet) any specific cut that should be tested against this topology in particular. Eliminating the squark-gluino production modes leads to a particularly simple class of models parametrized by exactly two mass parameters, i.e. that of the produced particle and of the LSP. The following is an examination of the $\tilde{b}\tilde{b} \to bb$ and $\tilde{g}\tilde{g} \to bbbb$ topologies; the $\tilde{g}\tilde{g} \to tttt$ topology, although nominally also a single-stage decay, is not yet accessible due to the high gluino mass scale required to produce two on-shell tops. The reader may also wonder why the sbottom production mode has been chosen rather than pair-production of light-flavor squarks, which have higher cross-sections. The reason for this is solely pragmatic, i.e. that for the 2010 fully hadronic searches that do not utilize b-tagging, there is very little distinction between signal events with light or heavy flavor jets. As such, one can kill two birds with the same stone, i.e. for this search the $\tilde{b}\tilde{b} \to bb$ topology can be thought of as equivalent to the $\tilde{q}\tilde{q} \to qq$ topology, but simultaneously allows comparison with the b-tag based searches in topologies of their interest.

For a fixed event selection, the quantity that determines the performance of the search in one signal model over the other is mostly just the signal selection efficiency. To understand this one can examine the efficiency plots as a function of mass parameters for various models, e.g. Figure 9.1.1. However this rapidly gets cumbersome because of

Feynman Diagram	Mnemonic	Produced particle	Final state(s)	
			1st stage	2nd stage
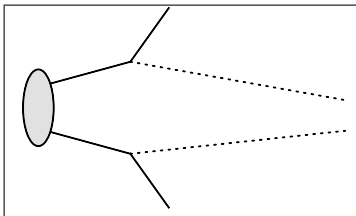	$\tilde{b}\tilde{b} \to bb$	$\tilde{b}$	b	
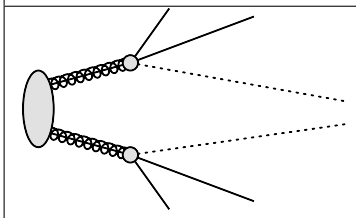	$\tilde{g}\tilde{g} \to bbbb$	$\tilde{g}$	$b\bar{b}$	
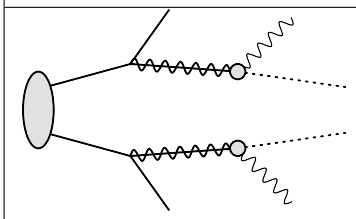	$\tilde{q}\tilde{q} \to qWqW$ $\tilde{q}\tilde{q} \to qZqZ$	$\tilde{q}$	q q	W Z
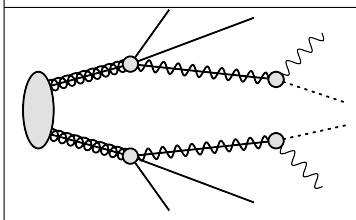	$\tilde{g}\tilde{g} \to qqWqqW$ $\tilde{g}\tilde{g} \to qqZqqZ$ $\tilde{g}\tilde{g} \to tbWtbW$	$\tilde{g}$	$q\bar{q}'$ $q\bar{q}$ $t\bar{b}$	W Z W
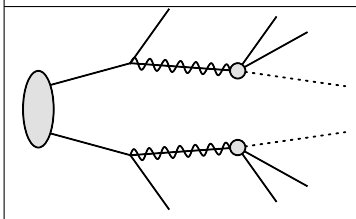	$\tilde{q}\tilde{q} \to q\ell\nu q\ell\nu$	$\tilde{q}$	q	$\ell\nu$
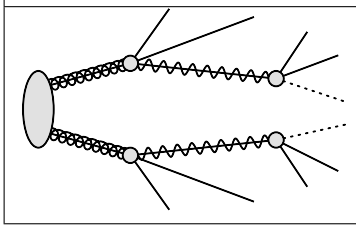	$\tilde{g}\tilde{g} \to qq\ell\nu qq\ell\nu$	$\tilde{g}$	$q\bar{q}$	$\ell\nu$

Table 9.1: SMS topologies and their mnemonics. Here q is any of the light-flavor quarks (u,d,s,c). The listed final states exclude the neutralino LSP, which always occurs at the last stage of the decay.

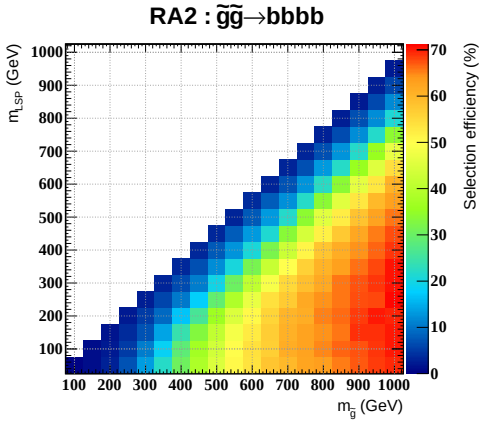

Figure 9.1.1: Efficiency of the baseline search selection on the $\tilde{g}\tilde{g} \to bbbb$ SMS topology, as a function of the produced and LSP masses.

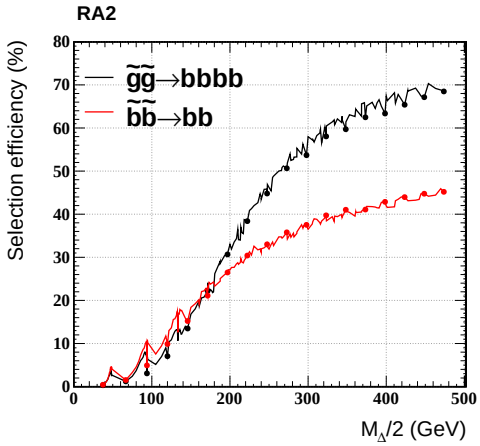

Figure 9.1.2: Efficiency of the baseline search selection on the $\tilde{g}\tilde{g} \to bbbb$ and $\tilde{b}\tilde{b} \to bb$ topologies, as a function of $M_\Delta/2$.

the large number of topologies and the lack of an obvious way to "overlay" 2D plots[1]. Instead, it was noticed in Section 3.1.1 that the variable $M_\Delta/2 = (m_{\tilde{g}}^2 - m_{\text{LSP}}^2)/2m_{\tilde{g}}$ pretty much sets the scale of visible and invisible transverse momenta in BSM pair-production events. Exploiting this, a plot like Figure 9.1.1 can be condensed into a 1-dimensional profile graph like in Figure 9.1.2 by taking each model point (i.e. represented by the squares) and entering it with x-coordinate being $M_\Delta/2$ for that point. This would in principle create a band in the 1D graph, except that since there are a finite grid of points in the 2D version, they instead show up as a jagged line. Although this seems like a dramatic reduction, the reader is reminded that no information is actually omitted in such a 1D version, because deviations from the $M_\Delta/2$-controlled trend would show up as a scatter in the y-coordinate for a small range in $M_\Delta/2$. This occurs in the upcoming plots especially when plotting scalar sum variables for topologies with ≥ 2 visible objects, which for reasons discussed in Section 3.1.1 are more appropriately parametrized by $m_{\text{produced}} - m_{\text{LSP}}$. For reference, the points for the lowest LSP mass ($m_{\text{LSP}} = 50\,\text{GeV}$) are shown as dots, and moving to the left of one such point corresponds to an increase in m_{LSP} (until the next such point). The fact that these light-LSP points look fully correlated with the dips in the MHT+ graph in Figure 9.1.2 is exactly because in Figure 9.1.1 it looks like there is an overall lower efficiency for selecting models with $m_{\text{LSP}} \sim 50 - 100\,\text{GeV}$ regardless of the gluino mass, which is due to the $\not{H}_{\text{T}} \geq 150\,\text{GeV}/c$ selection requirement.

Various search selections and SMS topologies can be compared by means of $M_\Delta/2$

[1] One can take a ratio w.r.t. some reference topology at the very least, but this doesn't really reduce the number of plots to be examined and correlated by eye.

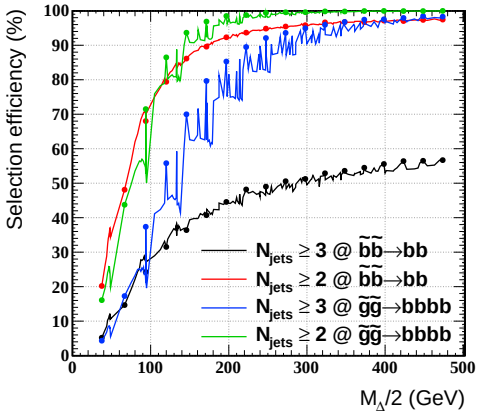

Figure 9.1.3: Efficiency w.r.t. the full sample (no other selections) of jet multiplicity cuts on single-stage SMS topologies, as a function of $M_\Delta/2$.

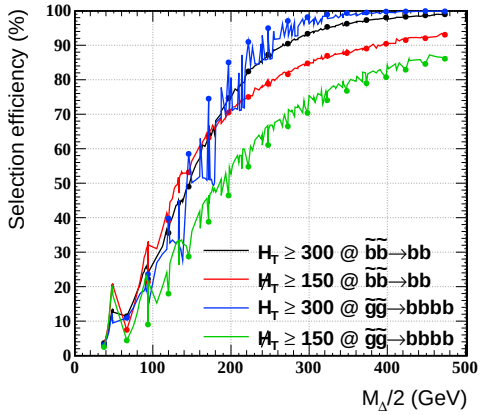

Figure 9.1.4: Efficiency w.r.t. the full sample (no other selections) of H_T and $\not{H}_\mathrm{T}$ cuts on single-stage SMS topologies, as a function of $M_\Delta/2$.

profiles. Figure 9.1.2 starts with the efficiency of the baseline search selection, which is by construction higher than any of the other regions. Even here there is a clear loss of signal events in the squark-squark topology $\tilde{b}\tilde{b} \to bb$ compared to the gluino-gluino one, which is also not asymptotically efficient. The difference between squark-squark and gluino-gluino topologies is attributable to the ≥ 3 jets selection requirement, which as shown in Figure 9.1.3 is only 50% efficient for the inclusive $\tilde{b}\tilde{b} \to bb$ sample since it requires events to have at least one hard ISR/FSR jet. A ≥ 2 jet requirement would however be a bit more efficient for squark-squark than gluino-gluino production, since the gluino decays into two jets of comparable p_T whereas the squark delivers the same momentum into a single jet, thereby suffering less threshold effects. A higher p_T threshold on one or both leading jets may be sufficient to trade in for the relaxed multiplicity requirement and still maintain a decent level of background, especially in the high-$\not{H}_\mathrm{T}$ search region where there is negligible QCD background, or if the cut is placed in the second jet, which tends to have lost energy in high-$\not{H}_\mathrm{T}$ QCD events. On the other hand the asymptotic $\lesssim 70\%$ efficiency for the $\tilde{g}\tilde{g} \to bbbb$ topology is mostly due to the $\not{H}_\mathrm{T}$ selection as seen in Figure 9.1.4, which is also responsible for a little of the $\tilde{b}\tilde{b} \to bb$ inefficiency. Relaxing the $\not{H}_\mathrm{T}$ selection is more difficult because this is the cut that controls most of the QCD yield, but it might be possible if supplemented with other QCD suppression variables, or if $\not{E}_\mathrm{T}$ could be used in lieu of $\not{H}_\mathrm{T}$.

Figures 9.1.5 and 9.1.6 show the effect of tighter $\not{H}_\mathrm{T}$ and H_T cuts a.k.a. the other two search selections on these two topologies. The baseline selection efficiency on the most performant topology, $\tilde{g}\tilde{g} \to bbbb$, is maintained in all plots as a point of reference. The feature of note here is that the MHT+ and HT+ cuts are almost of equivalent impact on

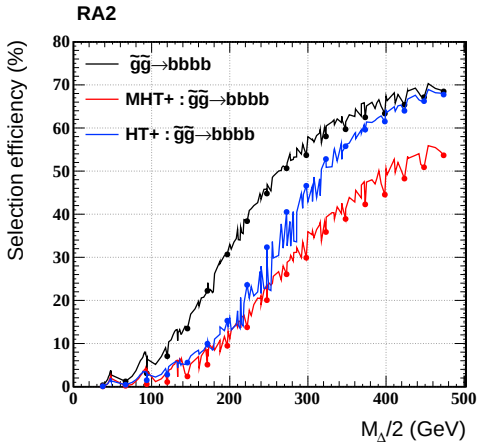

Figure 9.1.5: Efficiency of the various search selections on the $\tilde{g}\tilde{g} \rightarrow bbbb$ topology, as a function of $M_\Delta/2$.

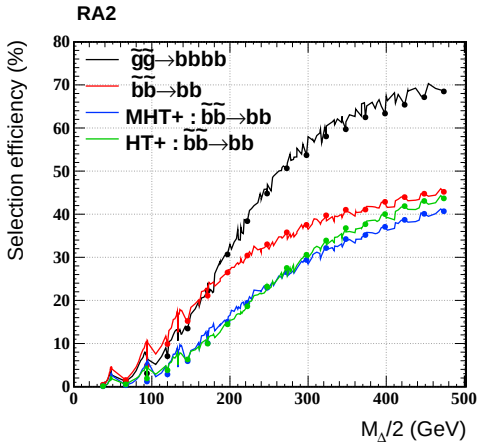

Figure 9.1.6: Efficiency of the various search selections on the $\tilde{b}\tilde{b} \rightarrow bb$ topology, as a function of $M_\Delta/2$.

the $\tilde{b}\tilde{b} \rightarrow bb$ topology, which seems promising for the MHT+ selection given that it has half the background count of the HT+ selection. This is also why it will be seen that the MHT+ region has better search power even for the $\tilde{g}\tilde{g} \rightarrow bbbb$ topology where it is less efficient than the HT+ selection. In all these cases however, the tighter search regions are most inefficient in the region of small $M_\Delta/2$, which is expected since these models have little visible or invisible p_T. This would especially be a region to watch out for in terms of ensuring coverage when the search cuts are tightened for higher luminosities.

Signal efficiencies provide insight into potential regions of improvement, but at the end of the day must be "multiplied" by the signal cross-sections in order to provide a proper measure of the search performance. This is because it is unwise to spend much effort improving regions of low efficiency but anyway high expected cross-sections, at the cost of intrinsically penurious regions. Here a word of caution should be said that the absolute cross-sections tend to be the most theory-dependent quantities, not because of modeling uncertainties (PDF/ISR/scale/...) even though they can be significant, but because cross-sections depend on the spins of the produced BSM particles as well as the number of participating species. For example, UED cross-sections are about an order of magnitude higher than those predicted by SUSY from basic spin considerations [42]. As another example, the squark-squark production cross-sections in SUSY can easily be halved by having decoupled left- vs. right-handed squarks. This means that it remains to maintain coverage with evolving luminosities of even those regions in SMS parameter space that have nominally been excluded by some assumed cross-section. What remains true though is that the power-law dependency $1/M^{\gamma}_{\text{produced}}$, $\gamma \sim 5-6$ is motivated from basic phase space considerations and should more or less always hold. Since overall correction factors do not modify the relative positioning of contour lines,

it is therefore still meaningful to judge a search by the region in mass parameter space that it excludes or has power in. This is done in the following.

Section 8.1.5 motivates the use of size of the sensitivity region—defined as the region in which there is $> 95\%$ probability of seeing a 3σ excess due to signal—as a figure of merit for search design. This is compared to the expected exclusion regions in Figures 9.1.7 and 9.1.8 for the two single-stage SMS topologies, which are to be interpreted as covering the regions from the lower left corner up to the drawn contour lines. The gray shaded region (upper left triangle) indicates where this topology is kinematically prohibited. The most striking feature is that there is quite a substantial "gray zone" in between the two types of regions, which can be reduced by about half by relaxing the search power requirement to $> 50\%$ ("toss a coin and hope for luck"). While nice in order to keep the sensitivity regions from vanishing from the plots altogether, this is not done because the $> 95\%$ requirement may expose some features that are not detectable by the looser criteria. For example the MHT+ search seems to have a dip in sensitivity compared to the baseline and HT+ selections, although the reader is warned that this is not conclusive due to the coarseness of the simulated SMS grids, which could also use an increase in the number of generated events for low-efficiency region near the diagonal. Secondly, the $\tilde{b}\tilde{b} \to bb$ topology was actually normalized to the $\tilde{q}\tilde{q}$ (light squark) production cross-section[2] because that is the more relevant channel for this search. The penalty at which it appears to be w.r.t. the gluino-gluino topology is purely driven by the factor of ~ 5 smaller cross-section, and in fact if the topology had been scaled to the gluino pair-production cross-section, it would have had a slightly *larger* exclusion/sensitivity region. This is despite the lower $\tilde{b}\tilde{b} \to bb$ selection efficiency due to the ≥ 3 jet requirement, but happens for reasons that can be seen from Figures 9.1.5 and 9.1.6: the more performant (tighter) search regions anyway reduce the $\tilde{g}\tilde{g} \to bbbb$ selection efficiency, which is now comparable to that of $\tilde{b}\tilde{b} \to bb$ up to the region $M_\Delta/2 \gtrsim 300\,\text{GeV}$, which is not yet probed with the present integrated luminosity. That said, the squark-squark topology is certainly one that needs to be selected with higher efficiency than gluino-gluino topologies because of the cross-section penalty. The reader who compares Figure 8.2.5 though will see that the presence of squark-gluino associated production modes can significantly boost the discovery potential, although in a non-discovery scenario statements about squarks would still be rather inconclusive at least without making specific model assumptions.

To conclude, squark-squark production topologies in general deserve attention in order to keep the selection efficiencies as high as possible (for a fixed amount of background), due to the more uncertain nature of the cross-section compared to gluino production. This can very dramatically (but unsurprisingly) be achieved by relaxing the ≥ 3 jet selection to ≥ 2, although this might come at too significant of a cost in background counts.

[2]The reader may multiply this cross-section roughly by 1/4 in order to obtain that for $\tilde{b}\tilde{b}$ production, but this would result in quite an uninterestingly blank plot.

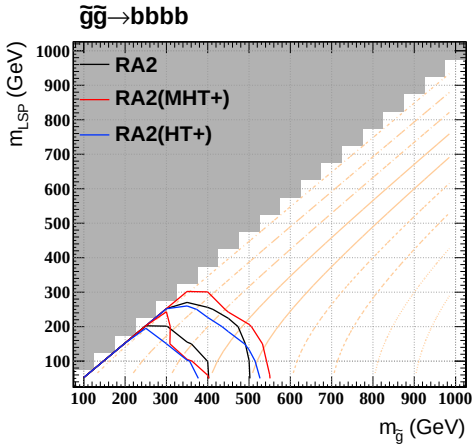

Figure 9.1.7: Expected exclusion limits (larger region set) vs. sensitivity region (smaller region set) for various search selections and the $\tilde{g}\tilde{g} \rightarrow bbbb$ model. The diagonal lines indicate contours of equal $M_\Delta/2$, ranging from 50 GeV (diagonal) to 450 GeV (bottom right corner) in 50 GeV steps.

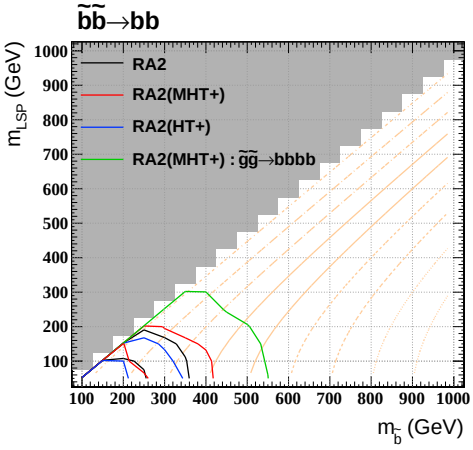

Figure 9.1.8: Expected exclusion limits (larger region set) vs. sensitivity region (smaller region set) for various search selections and the $\tilde{b}\tilde{b} \rightarrow bb$ model, with the best performing topology $\tilde{g}\tilde{g} \rightarrow bbbb$ shown for reference.. The diagonal lines indicate contours of equal $M_\Delta/2$, ranging from 50 GeV (diagonal) to 450 GeV (bottom right corner) in 50 GeV steps.

9.1.2 Two-stage decay topologies

The second stage of the two-stage decay topologies in Table 9.1 all involve electroweak particles, since the simplifying assumption that the gluino decays are 3-body has been made. They can therefore be classified as either containing Wor Z bosons in the decay chain, versus those where the decays are via an off-shell slepton[3]. The top-rich $\tilde{g}\tilde{g} \to tbWtbW$ topology is neglected because it has very poor acceptance in this search, given the lepton veto and intrinsically high gluino mass required to produce an on-shell top.

Figure 9.1.9 shows the efficiency of the baseline selection on the Wand Z topologies. The W topologies are systematically lower, because of a larger branching ratio to leptons that may then cause the event to be rejected by the lepton veto. Since they are otherwise kinematically similar, the Z topologies are focused on henceforth. The main feature here is that even though the squark-squark production events now have comparable or better efficiency than that of gluino-gluino production, the overall efficiency is a bit lower than that of the one-stage gluino decay. This inefficiency is due to the $\not{H}_{\mathrm{T}} \geq 150\,\mathrm{GeV}/c$ requirement, which is here also anti-correlated with high visible activity because of the competition between the W boson and the LSP for the boost of the chargino. Figure 9.1.10 shows that the MHT+ selection is systematically less efficient than the HT+ selection, and in general the squark-squark and gluino-gluino topologies remain very similar in efficiency. In the diagonal strip $m_{\mathrm{LSP}} > m_{\mathrm{produced}} - 2m_{\mathrm{Z}}$ (similarly for m_{W}) however, the gluino undergoes 3-body decay into two effectively massless visible objects (leptons or jets) and the LSP, which means that the latter can obtain more momentum than in a similar case where the Z (W) boson was produced on-shell and thus reserves a larger share of the energy-momentum. Furthermore, final-state objects that would otherwise be visible fall below selection thresholds and/or have lower reconstruction efficiencies when very soft, thereby contributing to $\not{H}_{\mathrm{T}}$ rather than H_{T}. It is thus in this low $M_{\Delta}/2$ region where the efficiencies of the MHT+ and HT+ converge that the cleaner MHT+ region can compete with the more efficient HT+ selection. This yields exclusion/sensitivity regions like that in Figure 9.1.11. The shape of the regions is now rather convex and also does not cover as much range in gluino masses as when it underwent single-stage decay (compare Figure 9.1.7). These depletions might be recoverable by using $M_{\mathrm{eff}} \equiv \not{H}_{\mathrm{T}} + H_{\mathrm{T}}$ instead of $\not{H}_{\mathrm{T}}$ as the main discriminating variable, of course relaxing the $\not{H}_{\mathrm{T}}$ preselection (required to control QCD) insofar as possible.

The impact of signal contamination on the exclusions of the $\tilde{g}\tilde{g} \to qqZqqZ$ and $\tilde{g}\tilde{g} \to qqWqqW$ topologies are estimated by the RA2-specific trick noted in Section 8.1.4.1, i.e. testing against only the fully hadronic part of the signal. Figure 9.1.13 shows that the $\tilde{g}\tilde{g} \to qqZqqZ$ exclusion is barely affected, since the branching ratio to visible leptons is only 10%. On the other hand Figure 9.1.14 shows a rather dramatic reduction

[3]The chargino in these topologies was constrained to have mass only 30 GeV above that of the neutralino LSP, and then underwent 3-body decay. The motivation here was to design a topology that challenged the ability of di-lepton searches to resolve soft leptons. Topologies where the slepton is on-shell are of course also important, and furthermore can have varied phenomenology for appropriate searches; however these are beyond the scope of this document.

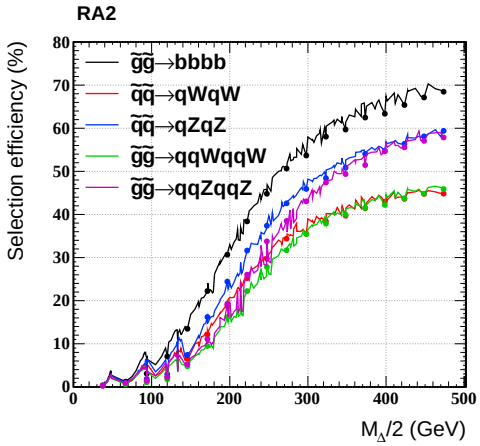

Figure 9.1.9: Efficiency of the baseline search selection on the two-stage decay topologies involving Wand Z bosons, as a function of $M_\Delta/2$.

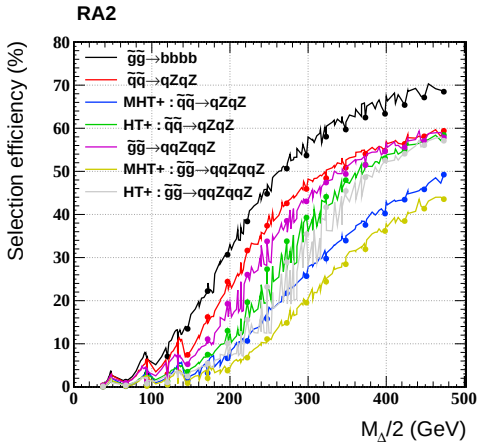

Figure 9.1.10: Efficiency of the various search selections on the two-stage decay topologies involving Z bosons, as a function of $M_\Delta/2$.

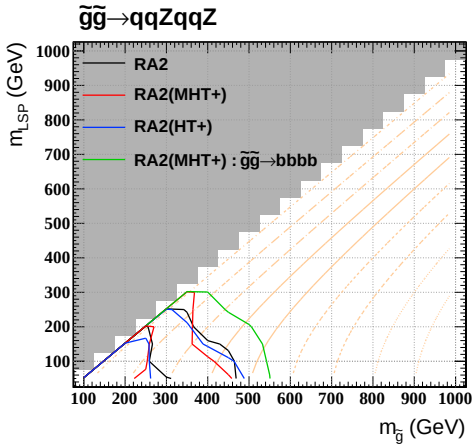

Figure 9.1.11: Expected exclusion limits (larger region set) vs. sensitivity region (smaller region set) for various search selections and the $\tilde{g}\tilde{g} \rightarrow qqZqqZ$ model, with the best performing topology $\tilde{g}\tilde{g} \rightarrow bbbb$ shown for reference. The diagonal lines indicate contours of equal $M_\Delta/2$, ranging from 50 GeV (diagonal) to 450 GeV (bottom right corner) in 50 GeV steps.

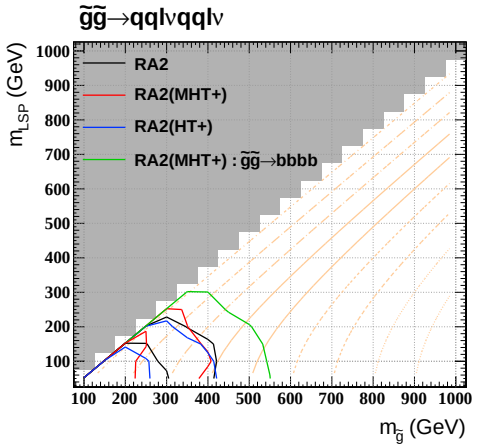

Figure 9.1.12: Expected exclusion limits (larger region set) vs. sensitivity region (smaller region set) for various search selections and the $\tilde{g}\tilde{g} \rightarrow qq\ell\nu qq\ell\nu$ model, with the best performing topology $\tilde{g}\tilde{g} \rightarrow bbbb$ shown for reference. The diagonal lines indicate contours of equal $M_\Delta/2$, ranging from 50 GeV (diagonal) to 450 GeV (bottom right corner) in 50 GeV steps.

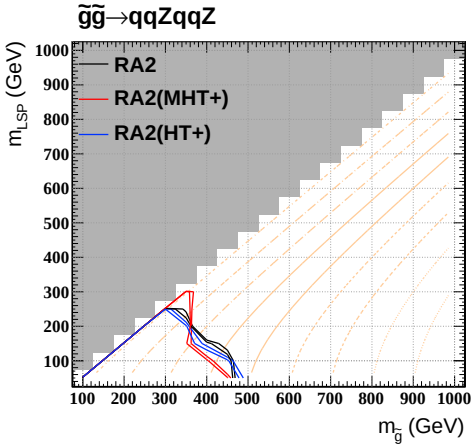

Figure 9.1.13: Expected exclusion limits for various search selections and the $\tilde{g}\tilde{g} \rightarrow qqZqqZ$ model, without (larger region) and with (smaller region) signal contamination accounted for. The diagonal lines indicate contours of equal $M_\Delta/2$.

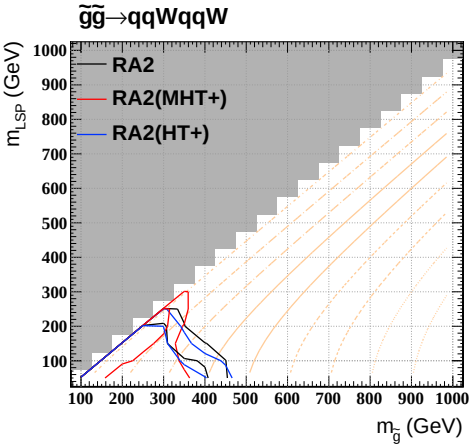

Figure 9.1.14: Expected exclusion limits for various search selections and the $\tilde{g}\tilde{g} \rightarrow qq\ell\nu qq\ell\nu$ model, without (larger region) and with (smaller region) signal contamination accounted for. The diagonal lines indicate contours of equal $M_\Delta/2$.

of the MHT+ search region exclusion of the $\tilde{g}\tilde{g} \rightarrow qqWqqW$ topology, in particular the high $M_\Delta/2$ region. The other search regions are less affected, but still substantially so.

The off-shell slepton topologies always have two visible leptons per event, with equal branching ratios for all three flavors. As such, according to Section 8.1.4.1 one would expect this search to be completely insensitive to these type of signals. If the signal contamination could somehow be mitigated however, hadronic searches like this one can help recover what are low-efficiency regions for the leptonic searches, i.e. where the leptons are soft, out of acceptance, or non-isolated because of high and angularly correlated jet activity as can happen in busy signal topologies with collimated decay chains. For low $M_\Delta/2$ in the $\tilde{g}\tilde{g} \rightarrow qq\ell\nu qq\ell\nu$ topologies the leptons remain soft, leading to a comparable selection efficiency to all other topologies discussed so far. For large produced and low LSP masses, the leptons can receive a significant boost from the decay of the intermediate chargino, leading to a "strip" around $m_{\text{LSP}} \sim 100\,\text{GeV}$ that has progressively harder leptons as a function of $m_{\tilde{g}}$ and therefore a smaller selection efficiency as shown in Figure 9.1.15. This deviation from the $M_\Delta/2$ trend is due to the constraint that the chargino mass is always 30 GeV above the LSP mass. The efficiency of the other search selections are shown in Figure 9.1.16,whereby one sees that the overall efficiency never exceeds 35% even in the baseline selection. Still, this leads to an exclusion/sensitivity region (Figure 9.1.12) that is quite comparable to that of the Z topologies, which is understood because the search does not yet probe the problematic

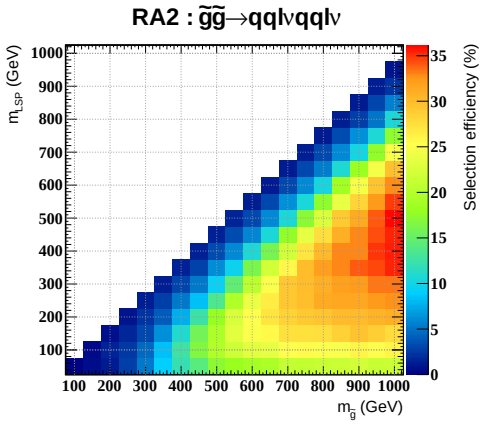

Figure 9.1.15: Efficiency of the baseline search selection on the $\tilde{g}\tilde{g} \to qq\ell\nu qq\ell\nu$ topology, as a function of produced and LSP masses.

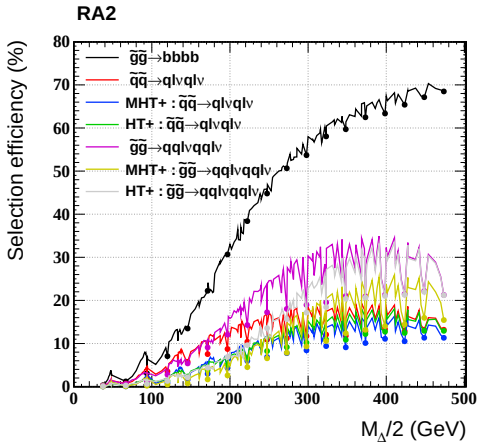

Figure 9.1.16: Efficiency of the various search selections on the two-stage decay topologies involving off-shell sleptons, as a function of $M_\Delta/2$.

high $M_\Delta/2$ region.

9.2 Selected Searches at the CMS Experiment

An exercise similar to that in Section 9.1 can be performed for other dark matter searches run by the CMS collaboration, with an eye to obtaining a global picture of what is covered and what not as of the 2010 round of searches. Since the sensitivity versus exclusion regions do not seem to be qualitatively different except for the tendency of the former to vanish off the plots, a choice to examine just the expected limits was made. Also, due to time limitations only a subset of analyses were evaluated, corresponding to the search regions identified in Table 9.2. The selection criteria used to define these regions were validated to be within a few percent, most to within a couple of percent, of those reported by the analysts themselves for various SUSY benchmark points. The reader should nevertheless keep in mind that these are "emulated" results and may be lacking in various ways. For example, only the largest experimental uncertainties on the signal simulation have been accounted for, some via crude upper-bounds, and do not seem to have much effect on the exclusion limits. Signal contamination has not been accounted for, resulting in somewhat idealized results, although not out of possibility if further work is done to make the methods robust. There are also some searches missing from the survey that should provide more coverage in specific areas. Table 9.3 lists the various topologies and the corresponding salient analyses covered here.

Analysis	Region	Selection Criteria	
RA2 [33]			$\Delta\phi_{1\text{-}2} \geq 0.5, \Delta\phi_3 \geq 0.3$,
	(MHT+)	$\not{H}_T \geq 250\,\text{GeV}/c$	≥ 3 jets
	(HT+)	$H_T \geq 500\,\text{GeV}/c$	$H_T > 300, \not{H}_T > 150$
RA1b [38]	$\geq 1\,b$, $\alpha_T > 0.55$, $p_{T,j1\text{-}2} > 100$, $H_T > 350, \not{H}_T/\not{E}_T < 1.25$		
RA2b [35]	**(1b)**	$= 1$ b-tagged jet	$\Delta\phi(\not{E}_T, j1\text{-}3) \geq 0.3$,
	(≥1b)	≥ 1 b-tagged jets	≥ 3 jets
	(≥2b)	≥ 2 b-tagged jets	$H_T > 300, \not{E}_T > 150$
MT2 [27]	**(≥3j)**	≥ 3 jets, $M_{T2} > 200$	$\Delta\phi(\not{E}_T, j) \geq 0.3$,
	(≥4j, ≥1b)	≥ 4 jets, $\geq 1\,b$-tagged $M_{T2} > 120, H_T \geq 450$	$p_{T,j1} > 100$, $H_T > 300$, $\lvert\not{H}_T - \not{E}_T\rvert < 70, \not{E}_T > 30$
RA4 [34]	$p_{T,\ell 1} \geq 20$, no other leptons, ≥ 4 jets, $H_T > 500, \not{E}_T > 250$		
RA5 [32]	**(e,μ)**	≥ 1 same-sign e/μ pair, ≥ 2 jets, $H_T > 300, \not{E}_T > 30$	

Table 9.2: Search regions in various analyses surveyed in this study. All momentum units are in GeV/c. The RA2, RA1b, RA2b, and MT2 searches all include lepton vetoes (at least in the used search regions).

In the following, all three RA2 search regions are rendered in the same color (black), since the number of visually distinguishable colors are finite and each analysis has been assigned a unique color. The three RA2 curves can be resolved using the plots in Section 9.1.

9.2.1 b-rich topologies

Figures 9.2.1 and 9.2.2 show the all-b final state topologies, for squark-squark and gluino-gluino production respectively. These demonstrate the power of the b-tag searches RA1b, RA2b, and one of the MT2 regions, compared to generic jet-based searches that do not make use of b-tags (RA2 and another of the MT2 regions). The curves are more or less coincident in the $\tilde{b}\tilde{b} \to bb$ topology, where also one sees that the ≥ 2 b-tag selection of RA2b is already inefficient compared to its ≥ 1 b-tag selection. It seems that four b quarks in the final state are required to bring out the true advantage of these searches, as seen by comparing Figure 9.2.2. Here the uncertainties for the RA2b and MT2 searches are approximated by 20% and 15% respectively, and if any substantial signal contamination is present and accounted for, may cause the limits to degrade appreciably. Also, the large uncertainty on the RA2b background estimation makes the limit significantly systematics-driven (and therefore the computation here must be taken with a larger grain of salt), unlike all the other searches surveyed here. A factor of two decrease in the background uncertainty can improve the RA2b($\geq 2b$) limit by $\sim 100\,\text{GeV}$ in the mass parameters space. As it is, the b-tag based searches are formally better than the generic ones in the limit of a (roughly) maximal multiplicity

	SMS Topology	RA2	RA1b	RA2b	MT2	RA4	RA5
Generic	$\tilde{g}\tilde{g} \to qqqq$	$\surd$			$\surd$		
Heavy flavor	$\tilde{g}\tilde{g} \to bbbb$	$\surd$	$\surd$	$\surd$	$\surd$		
	$\tilde{g}\tilde{g} \to tttt$	$\surd$	$\surd$	$\surd$	$\surd$		
	$\tilde{g}\tilde{g} \to tbWtbW$	$\surd$	$\surd$	$\surd$	$\surd$	$\surd$	$\surd$
EWK boson	$\tilde{g}\tilde{g} \to qqWqqW$	$\surd$			$\surd$	$\surd$	$\surd$
	$\tilde{g}\tilde{g} \to qqZqqZ$	$\surd$			$\surd$	$\sim$	
Slepton	$\tilde{q}\tilde{q} \to q\ell\nu q\ell\nu$	S				$\surd$	
	$\tilde{g}\tilde{g} \to qq\ell\nu qq\ell\nu$	S				$\surd$	$\surd$

Table 9.3: List of analyses surveyed in this study, and the topologies for which they were enlisted under. "S" indicates that signal contamination may be an issue, even though neglected here. "$\sim$" indicates analyses that may not be so relevant to the corresponding topology, but were surveyed anyway. Only the gluino production topologies are listed, but the corresponding squark production topologies are also included in practice.

of b-quarks in the final state, but not dramatically so, and does not help recover the difficult $\tilde{b}\tilde{b} \to bb$ topology, which would have vanished from the exclusion plot had it not been scaled to the $\tilde{q}\tilde{q}$ production cross-section instead of the smaller single-flavor one.

The other b-rich topologies are those that include top quarks in the final state, which are intrinsically difficult because the produced BSM particle mass has to be substantially high if it is to produce an on-shell top quark[4]. However they also have the advantage of the W boson from top quark decays (and possibly elsewhere in the decay chain) which may decay leptonically, permitting them to be picked up by leptonic searches. As seen in Figure 9.2.3, the same-sign di-lepton (SSLL) search is the most performant in this topology, although the overall exclusion region is still rather small. The single-lepton search does not perform comparably well, which could be due to its rather tight $\not{E}_{\mathrm{T}} > 250\,\mathrm{GeV}$ requirement. The fully hadronic searches are also penalized because about half of the events have an isolated lepton, while such searches rely on a large signal efficiency rather than very clean search regions like the SSLL search, which managed despite a $< 5\%$ selection efficiency for this topology. The other topology, $\tilde{g}\tilde{g} \to tttt$, does not show up visibly in the exclusion plots because the lowest allowed gluino mass is nearly 400 GeV. Its phenomenology is anyway very similar to that of the $\tilde{g}\tilde{g} \to tbWtbW$ topology, except for a bit harder jets due to having fewer stages in the decay. The efficiencies of various searches in this topology are shown in Figure 9.2.4, where it is seen that RA2 actually maintains the highest efficiency, but is nevertheless too high background to yield a competitive limit.

The CMS collaboration SUSY physics analysis group does not seem to have a ded-

[4]Off-shell top quark decays, although conceivable, did not seem to be within the technological capability of the PYTHIA event generator, at least without instruction from the author himself.

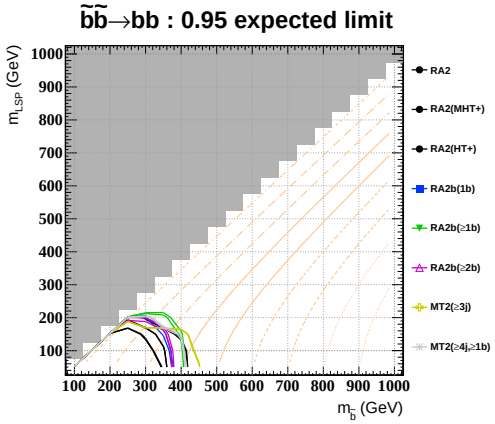

Figure 9.2.1: Expected exclusion limits for various searches and the $\tilde{b}\tilde{b} \to bb$ model (scaled to the $\tilde{q}\tilde{q}$ production cross-section so as to be visible).

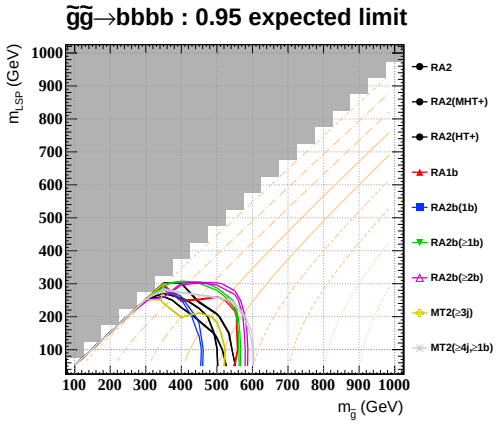

Figure 9.2.2: Expected exclusion limits for various searches and the $\tilde{g}\tilde{g} \to bbbb$ model.

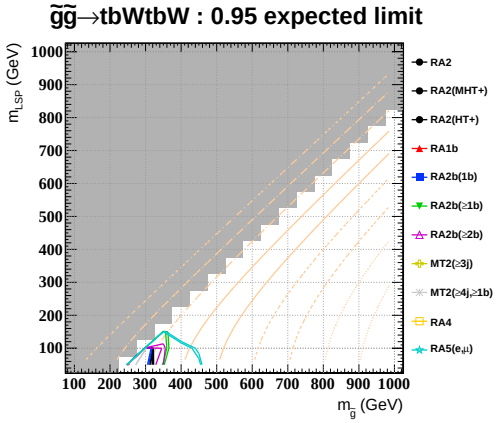

Figure 9.2.3: Expected exclusion limits for various searches and the $\tilde{b}\tilde{b} \to bb$ model (except scaled to $\tilde{q}\tilde{q}$ production cross-section).

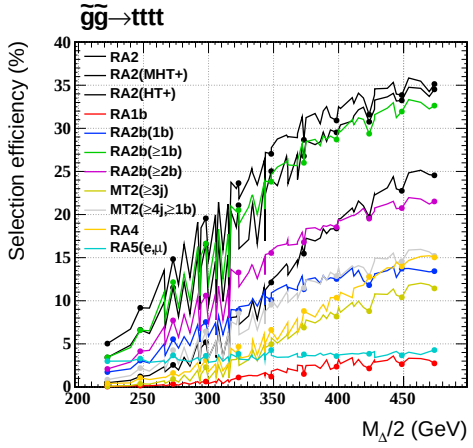

Figure 9.2.4: Efficiency of selecting the $\tilde{g}\tilde{g} \to tttt$ model, for various searches. The highest efficiency RA2 line is the baseline selection, followed by the HT+ and lastly the MHT+ selection.

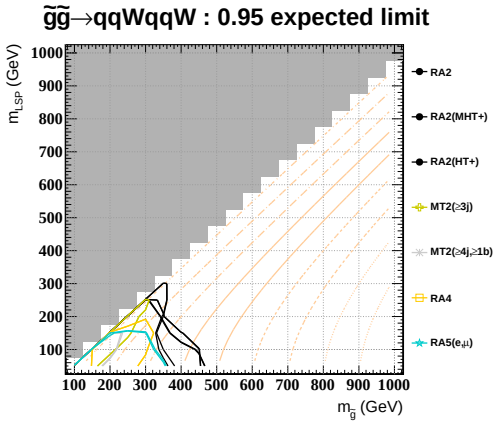

Figure 9.2.5: Expected exclusion limits for various searches and the $\tilde{g}\tilde{g} \to qqWqqW$ model.

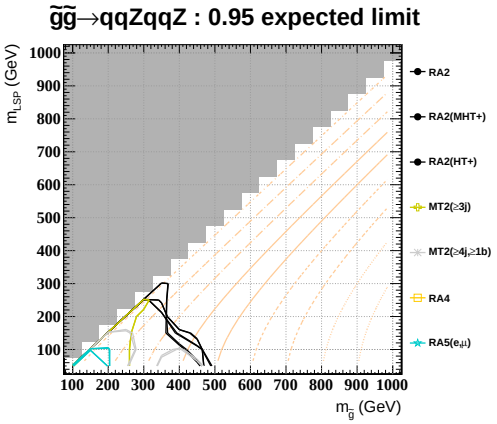

Figure 9.2.6: Expected exclusion limits for various searches and the $\tilde{g}\tilde{g} \to qqWqqW$ model.

icated top plus dark matter search, which might help recover coverage of this topology. However, a suitable combination of same-sign and opposite sign di-lepton searches, or a relaxation of the single leptonic search requirements, might already go very far in improving this direction.

9.2.2 Cascade decays with W and Z bosons

Figures 9.2.5 and 9.2.6 show the exclusion limits in gluino-gluino production and cascade decay topologies with W and Z bosons respectively in the final state, where RA2 still provides the most coverage. The squark-squark topologies are similar except that coverages are squeezed by the lower production cross-sections, and are thus omitted for conciseness. Here the leptonic searches tend to be penalized by the leptonic branching ratio in the case of electroweak bosons, especially the Z boson which only has 7% decays into electrons or muons, and therefore barely shows up at all for RA5 and is not present for RA4. RA4 also develops a "hole" in its coverage of the very low gluino mass region of the $\tilde{g}\tilde{g} \to qqWqqW$, which is probably due to its tight $H_{\mathrm{T}} > 500\,\mathrm{GeV}/c$ and $\not{E}_{\mathrm{T}} > 250\,\mathrm{GeV}$ requirements. This is nevertheless the type of topology in which it might be useful to combine hadronic and leptonic dark matter searches, in hopes of improving the limits or discovery power. It was seen from Figure 9.1.9 that the efficiency of the RA2 baseline selection on the $\tilde{g}\tilde{g} \to qqWqqW$ topology was about 30% less than that on the $\tilde{g}\tilde{g} \to qqZqqZ$ topology, which somewhat sets the scale of possible improvements. Furthermore, unless improved the RA2 search would be sensitive to signal contamination in these topologies, although it was seen in Section 9.1.2 that the $\tilde{g}\tilde{g} \to qqZqqZ$ topology exclusion remains quite stable.

The last feature of note is the fact that the MT2 exclusion in Figure 9.2.6 seems

to form two island separated roughly by the $M_\Delta/2 \sim 150\,\text{GeV}$ line (third from the diagonal). This is not an accident of statistics, but in fact shows up as a depletion in the strength of the limit along several bins in the mass parameters plane. A similar but less severe effect is also seen in the RA2 expected limits. This corresponds to the $m_{\text{LSP}} = m_{\text{produced}} - 2m_{\text{Z}}$ threshold above which the Z boson is produced off-shell and below which it is produced on-shell, for reasons explained in Section 9.1.2.

9.2.3 Cascade decays with (off-shell) sleptons

Figure 9.2.7 shows the good coverage of the SSLL search RA5 in the off-shell slepton topology, compared to other searches in this survey. Assuming that the opposite sign di-lepton search has comparable performance, a combination of these two searches should result in a significantly stronger limit. Furthermore, including the search regions already in RA5 that utilize tau leptons and also go lower in the p_{T} of the leptons should also result in a performance gain. The performance of RA4 is actually comparable to that of RA2, although the latter should not be considered as robust since it would vanish if signal contamination cannot be subtracted. Figure 9.2.8 shows the efficiency of various search selections on this topology, whereby one sees that the RA5 efficiency seems to again be in the vicinity of 5%. The RA4 efficiency is lower than the latter in the vicinity where it would have helped to set a competitive limit, although it has an interesting rise towards high $M_\Delta/2$ where there is a possibility for events to contain hard leptons, whereas the RA5 efficiency remains almost constant. There is evidently a preference for events in the $\tilde{g}\tilde{g} \to qq\ell\nu qq\ell\nu$ topology to have one hard lepton, but not two, at large $M_\Delta/2$. As such, single lepton searches may be a good way to supplement di-lepton ones even in topologies with nominally two leptons.

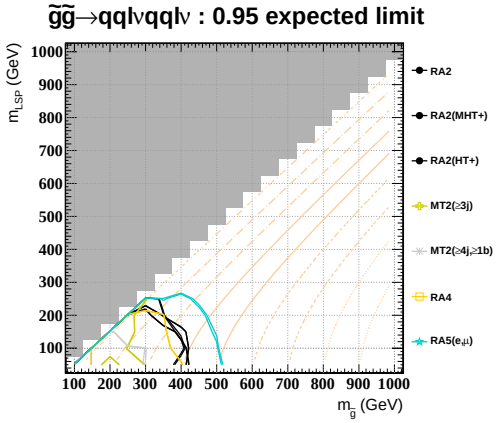

Figure 9.2.7: Expected exclusion limits for various searches and the $\tilde{g}\tilde{g} \to qq\ell\nu qq\ell\nu$ model.

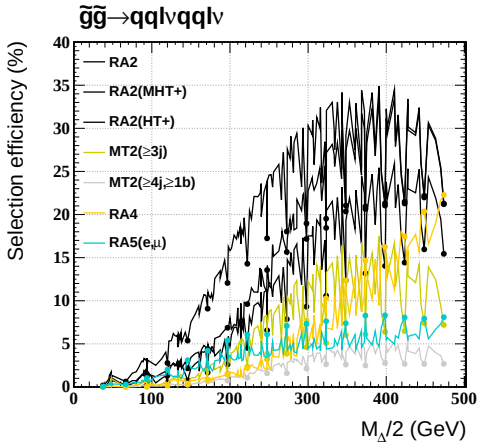

Figure 9.2.8: Efficiencies for selecting events in the $\tilde{g}\tilde{g} \to qq\ell\nu qq\ell\nu$ model, for various searches.

Chapter 10

Conclusion and Future Prospects

A generic dark matter search in the fully hadronic channel was performed using $36\,\mathrm{pb}^{-1}$ integrated luminosity of data collected by the CMS detector at the LHC experiment, corresponding to all the available certified pp collision data in 2010. Data-driven background estimation methods were introduced for each of the major Standard Model backgrounds, which actually covers all the SM processes that have substantial cross-sections. One is irreducible, from Z+jets events where the Z decays into neutrinos. The second largest population comes from W+jets and top pair production events where one or more W bosons decay into an electron or muon that is not identified or a tau that decays hadronically. The last but most complicated background arises from QCD multi-jet production, where the missing momentum originates from jet mismeasurements, heavy-flavor decays, or instrumental effects. A novel method for estimating the latter background was developed, based on the principle of unfolding a sample of inclusive data events back to well-balanced, particle-level truth, and then smearing these particle-jets by the measured detector resolution in order to "simulate" a sample of detector-level events.

All the background estimation methods predict events, not just counts after cuts, and should be easily extendible to other variables beyond the simple missing-transverse-momentum based search regions presently utilized. There are three such search regions, one with minimal $\not{H}_\mathrm{T}$ and H_T cuts based mostly on background considerations, and on top of these one region with high $\not{H}_\mathrm{T}$ and a complementary region with high H_T. All data observations within these regions are within 1σ of the expected background yields. As such, limits on the maximum allowable signal yields have been set, corresponding to about 10 events in the tightest (high $\not{H}_\mathrm{T}$) search region. Excluded regions in the CMSSM $(m_0, m_{1/2})$ parameter plane have been constructed, indicating that this search exceeds a previously published α_T-based analysis by CMS collaborators, and is competitive w.r.t. the ATLAS collaboration limits. Information about this search in terms of Simplified Model Spectra have also been published, although not repeated here.

In preparation for future evolutions, a study was performed of the search performance in terms of a variety of SMS models, in particular focusing on means by which

to present and quantify this information. The transverse momentum scale variable $M_\Delta/2 = (m^2_{\text{produced}} - m^2_{\text{LSP}})/2m_{\text{produced}}$ adequately parametrizes most efficiencies of cuts placed on vector sum momenta variables, whereas the linear difference $m_{\text{produced}} - m_{\text{LSP}}$ is more appropriate for scalar sum variables. This holds even in the case of long cascade decays, so long as the constraints on the masses of the intermediate particles are some fraction of the produced-LSP mass splitting rather than, say, forced to be at a fixed mass difference. Profiling quantities like selection efficiencies in terms of this variable allows one to reduce the dimensionality of the visually difficult to process 2-dimensional distributions, and the spread for a small range in $M_\Delta/2$ retains information about whether or not there are other "hidden" model parameters at play.

The actual quantity to maximize in order to obtain the most out of data would be the sensitivity region of the search, defined as the volume of BSM model parameter space in which the search power exceeds the confidence level at which models are prescribed to be excluded. In general the expected limit and sensitivity regions are qualitatively similar, except for the latter being about half the size when requiring 3σ evidence potential with $> 95\%$ probability; as such it probably makes little difference whether one or the other is optimized. However the smallness of the sensitivity regions means that there was actually not that much in terms of BSM mass parameters that was discoverable with the $36\,\text{pb}^{-1}$ data. This situation should rapidly change given that already more than ten times that integrated luminosity has been collected as of this date in 2011.

Out of the 2010 exercise, some obvious regions of poor signal efficiency were identified for this search: squark-squark topologies with only two parton in the final state, which were at best 50% depleted by the ≥ 3 jet selection; low $M_\Delta/2$ strips, where there is little visible or invisible momentum (albeit having substantial amounts of invisible *energy*); and a transition region between those covered well by the high-$\not{H}_{\text{T}}$ and high-H_{T} selections, for events with long cascade decays. The naive ways to improve upon this would be to relax the search to ≥ 2 jets, possibly with more stringent p_{T} cuts on leading jets, and also to use the variable $M_{\text{eff}} \equiv \not{H}_{\text{T}} + H_{\text{T}}$ in lieu of tight $\not{H}_{\text{T}}$ requirements. The feasibility of these remain to be seen, as there is always also the need to keep background yields under control. All this of course does not preclude the introduction of more clever and targeted variables, perhaps even exploiting kinematic properties of events that one knows have such small mass splittings as to be almost invisible except for recoil against an ISR jet. As work in this direction has yet to be done however, this document ends on this note.

Lastly, a survey of a subset of dark matter searches run by the CMS collaboration was also performed using the same SMS models as utilized to study the RA2 search performance. It is seen that fully hadronic searches like RA2 lead in terms of extracting information about topologies consisting of light-flavor jets in the final state, and also if the final state contains up to two W or Z bosons. The performance unsurprisingly worsens for topologies with more leptons in the final state, where in particular the dilepton searches take over in performance, not only for the topologies with decays via

sleptons, but also those with four or so W bosons (possibly from top quark decays). Most of the studied gluino pair-production topologies are presently covered by either the generic hadronic searches or the di-lepton ones, although the squark pair-production topologies suffer more from low and highly model-dependent cross-sections. The *b*-tag based searches can also have significantly better coverage than a generic jets search in the case of topologies with many (≥ 4) *b*-quarks in the final state, although a reduction of the background uncertainty would make these limits more stable. However the jet kinematic selection cuts in the single lepton search seem a bit too harsh for it to do as much good as it could have in the large category of events with one lepton in the final state, or when a second lepton fails to be identified.

Part V

Appendices

Appendix A

Software, Data and Simulated Samples

This analysis is performed with user code in CMS software version 3.8.7, with most samples (re-)reconstructed using versions 3.8.5, 3.8.6, or 3.8.7.

A.1 Data Samples

The full 36 pb^{-1} integrated luminosity of 2010 Collision data has been used to derive the results in this study. The subset of data used is collected via an `OR` of all H_{T} triggers (`HLT_HT100U`, `HLT_HT140U`, and `HLT_HT150U_v3`), and is located in the following datasets:

Run range	Dataset	$\int \mathscr{L} dt$ (pb^{-1})
136035-141955	`/JetMETTau/Run2010A-Nov4ReReco_v1/RECO`	0.285
141956-146427	`/JetMET/Run2010A-Nov4ReReco_v1/RECO`	2.895
146428-147195	`/Jet/Run2010B-Nov4ReReco_v1/RECO`	5.057
147196-149294	`/MultiJet/Run2010B-Nov4ReReco_v1/RECO`	27.907

Only events in the list of luminosity sections certified for general use of the November 4 2010 reprocessed data (`https://cms-service-dqm.web.cern.ch/cms-service-dqm/CAF/certification/Collisions10/7TeV/Reprocessing/Cert_136033-149442_7TeV_Nov4ReReco_Collisions10_JSON.txt`) have been used.

Several of the background estimation methods utilize orthogonal control samples, which are therefore located in other datasets. The muon control sample for the lost lepton estimations (Section 5) is obtained from the muon dataset:

Run range	Dataset	$\int \mathscr{L} dt$ (pb^{-1})
136035-144144	`/Mu/Run2010A-Nov4ReReco_v1/RECO`	3.2
146240-149442	`/Mu/Run2010B-Nov4ReReco_v1/RECO`	32.9

The photon control sample for the invisible Z estimation is obtained from the electron-photon dataset for early runs, which was later split into separate electron and photon datasets:

Run range	Dataset	$\int \mathscr{L} dt$ (pb^{-1})
136035-144144	/EG/Run2010A-Nov4ReReco_v1/RECO	3.18
146240-149442	/Photon/Run2010B-Nov4ReReco_v1/RECO	32.96

A.2 Monte Carlo Samples

The utility of MC simulated datasets is explained in Section 4. The simulated processes used in this study are listed in Table A.1[1].

A.3 Simplified Model Spectra (SMS) Samples

The samples used in this study were privately produced, using CMS software version 3.8.7 and the fast rather than full simulation. The cross-sections were obtained from NLO computations by Prospino [14], and shown in Figure A.3.1 for the range of masses used in this study.

[1]There are also several QCD multi-jet datasets that have been pre-filtered to enhance various aspects like heavy flavor or lepton production. These have not been used here (despite possibly matching the wildcards in Table A.1).

Dataset (and Remarks)	σ (pb)	$\int \mathscr{L} dt$
/QCD_Pt_*_TuneZ2_7TeV_pythia6 /QCD_Pt_170to300_TuneZ2_55M_7TeV_pythia6 In main use, for large size and good agreement with data.	Table A.2	
/QCD_Pt_*_TuneZ2_7TeV_pythia6/Fall10-E7TeV_ProbDist _2010Data_BX156_START38_V12-v1 Mixed with pile-up conditions similar to 2010 data. Same events as non-pileup samples at event generation level.	Table A.2 (sans the extra 55M in the 170-300 bin)	
/QCD_TuneD6T_HT-100To250_7TeV-madgraph	7×10^6	1.432
/QCD_TuneD6T_HT-250To500_7TeV-madgraph	171000	27.3
/QCD_TuneD6T_HT-500To1000_7TeV-madgraph	5200	1414
/QCD_TuneD6T_HT-1000_7TeV-madgraph	83	20642
Too low statistics in the 250-500 bin for the R+S checks. Used in the $Z \to \mu^+\mu^-$ estimation for fragmentation photons.		
/GJets_TuneD6T HT-40To100_7TeV-madgraph	23620	94
/GJets_TuneD6T HT-100To200_7TeV-madgraph	3476	305
/GJets_TuneD6T HT-200_7TeV-madgraph	485	2355
Prompt photon samples used in the invisible Z estimation method.		
/TTJets_TuneD6T_7TeV-madgraph-tauola/ Fall10-START38_V12-v2	165	8452
/WJetsToLNu_TuneD6T_7TeV-madgraph-tauola	31300	478
/WJetsToLNu_TuneZ2_7TeV-madgraph-tauola	31300	478
/ZinvisibleJets_7TeV-madgraph	5760	376
/LM0_SUSY_sftsht_7TeV-pythia6	39	5631
/LM1_SUSY_sftsht_7TeV-pythia6	4.9	44733

Table A.1: Fully simulated Monte Carlo datasets used in this study, with cross-sections and equivalent luminosities. Dataset names end with /Fall10-START38_V12-v1 unless otherwise specified. The cross-sections are scaled to NLO expectations for the top and EWK processes.

$\hat{p}_T$ of sample (GeV/c)	Cross section (pb)	Equivalent luminosity (pb^{-1})
0 to 5	4.8×10^{10}	1.1×10^{-5}
5 to 15	3.7×10^{10}	4.5×10^{-5}
15 to 30	8.1×10^{8}	6.6×10^{-3}
30 to 50	5.3×10^{7}	6.1×10^{-2}
50 to 80	6.3×10^{6}	0.5
80 to 120	7.8×10^{5}	3.5
120 to 170	1.1×10^{5}	26
170 to 300	2.4×10^{4}	2.3×10^{3}
300 to 470	1.2×10^{3}	2.6×10^{3}
470 to 600	70	2.9×10^{4}
600 to 800	16	1.3×10^{5}
800 to 1000	1.8	1.1×10^{6}
1000 to 1400	0.33	3.3×10^{6}
1400 to 1800	0.01	9.3×10^{7}
1800 to ∞	3.6×10^{-4}	1.5×10^{9}

Table A.2: Equivalent luminosity of events generated in each $\hat{p}_T$ bin that the PYTHIA 6 QCD MC sample (Table A.1) is comprised of.

Dataset	Process
/T1bb_GlGlToBBBB_38xFall10-v2/StoreResults-T1bb_GlGlToBBBB_38xFall10-v2	$\tilde{g}\tilde{g} \to bbbb$
/T1tb_GlGlToTBTB_38xFall10/StoreResults-T1tb_GlGlToTBTB_38xFall10	$\tilde{g}\tilde{g} \to tbWtbW$
/T5z_SqSqToQZQZ_38xFall10/sakoay-T5z_SqSqToQZQZ_38xFall10	$\tilde{q}\tilde{q} \to qZqZ$
/T6z_GlGlToQQZQQZ_38xFall10/sakoay-T6z_GlGlToQQZQQZ_38xFall10	$\tilde{g}\tilde{g} \to qqZqqZ$
/T5_SqSqToQWQW_38xFall10/sakoay-T5_SqSqToQWQW_38xFall10	$\tilde{q}\tilde{q} \to qWqW$
/T6_GlGlToQQWQQW_38xFall10/sakoay-T6_GlGlToQQWQQW_38xFall10	$\tilde{g}\tilde{g} \to qqWqqW$
/T7off_SqSqToQLNuQLNu_38xFall10/sakoay-T7off_SqSqToQLNuQLNu_38xFall10	$\tilde{q}\tilde{q} \to q\ell\nu q\ell\nu$
/T8off_GlGlToQQLNuQQLNu_38xFall10/sakoay-T8off_GlGlToQQLNuQQLNu_38xFall10	$\tilde{g}\tilde{g} \to qq\ell\nu qq\ell\nu$
/T10bb_SbSbToBB_38xFall10/sakoay-T10bb_SbSbToBB_38xFall10	$\tilde{b}\tilde{b} \to bb$

Table A.3: Fast simulated SMS Monte Carlo datasets used in this study.

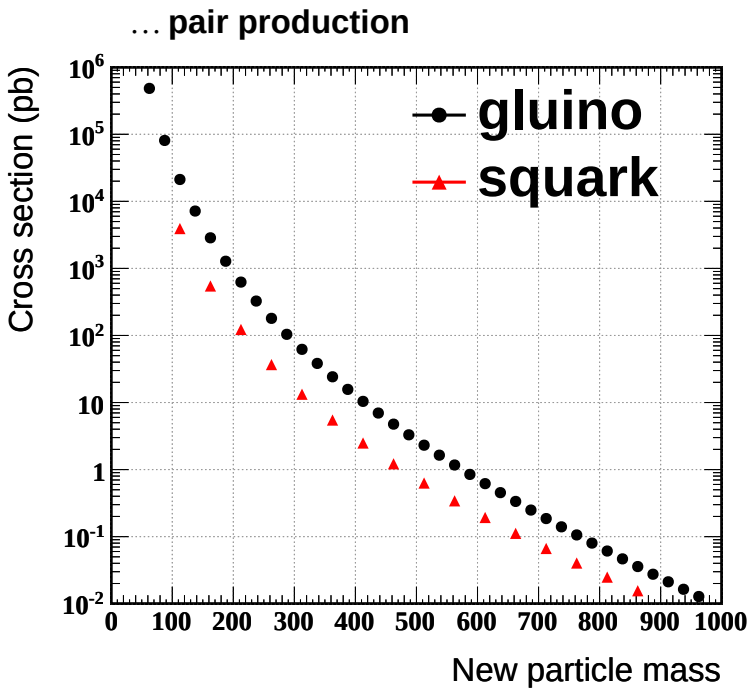

Figure A.3.1: Cross-sections for gluino-gluino and squark-squark pair production in the MSSM.

Appendix B

"Ideal" genJet Smearing

The genJet smearing procedure was introduced in Section 7.2.2. At first glance, this may seem like a test that *must* close, for is it not basically a tautology?

The answer is "no". All template-based methods have the property that if the template (a.k.a. the jet resolution) is created using a population with a different composition than that of the target sample to which it is to be applied, the prediction will be incorrect up to the level by which the composition modifies the template. More subtly, one can even apply the template to the same population with which it was derived, and yet end up with a biased prediction by afterwards applying cuts that select a special subset of events, or by examining variables that are sensitive to particular population features. For example, to predict variables like H_{T} it is typically fine to treat all jets as independent, but variables like $\not{H}_{\mathrm{T}}$ can in fact be strongly affected by jet-jet correlations or peculiarities that preferentially occur in some event topologies. This is why templates are typically parametrized by observable quantities in order to adapt to the target sample and any cuts that modify the sample composition. In anticipation of this, the resolutions used in this section are parametrized as explained in Section 7.3.2 and 7.3.3. Assuming for a moment that there are no missing parametrizations, one should now be in a position to obtain perfect closure, especially when using exactly the same MC simulated sample as from which the resolutions were obtained.

Unfortunately, the answer is still "no". The problem lies in the fact that jets are composite objects, and their resolution is not easily parametrized by single-object properties like is highly adequate for leptons and photons. There is not really a "parton level" momentum that can be uniquely assigned to a given jet—even a given genJet—as already seen in Section 4.1, the evolution from parton[s!] to jets is complex, probabilistic, and also environment dependent. Supposing that one gives up on the parton-centric view, and is willing to take a genJet-centric view to the level of including some shape information in the parametrization in order to account for the distribution of particles within that particular genJet, the problem would still remain. This is because of a second caveat, i.e. that of how particles appear in the detector. Jets are comprised of the occasional high p_{T} particle, but mostly soft ones whose trajectories tend to be significantly

modified by the magnetic field and also interactions with the detector material. The use of tracking information in the PF reconstruction helps very much in mitigating this, but cannot be fully efficient, cannot correct the neutral population, and also cannot unfold material interactions (bremsstrahlung, pair-production etc.) back to the original particle. As such, there is always some degree of distortion in the detector vs. true views of particles in an event, which can lead to different clustering decisions especially for sub-leading jets. There is therefore always some kind of arbitrary matching scheme that has to be used to link a genJet to a corresponding recoJet, and traditionally the field has used a simple ΔR requirement. In order to make use of resolution measurements that use this scheme, the studies in this document also follow suit. For completeness, the matching algorithm is as follows:

- Loop through all genJets in decreasing order of p_{T}:
  - For a given genJet, find the nearest recoJet in ΔR. If $\Delta\mathrm{R} < 0.1$, call this a match, and remove the recoJet from the list of those available to be matched.
  - Repeat until there are no more genJets to be matched.

Since the only place in which this is used is to construct the jet resolution, which also only utilizes the leading two genJets per event, further sophistication is irrelevant.

Figure B.0.1 shows how the genJet smeared $\not{H}_{\mathrm{T}}$ and H_{T} distributions compare to the fully simulated distributions from the same MC simulated QCD sample, in terms of ratio plots. For the inclusive sample, i.e. without any event selection criteria, the genJet smeared distributions do indeed match the fully simulated ones to within $1\% - 2\%$ except for a small region i.e. the first bins which are $\sim 4\%$ discrepant. However, proceeding to a $H_{\mathrm{T}}^{\mathrm{true}} \geq 300\,\mathrm{GeV}/c$, ≥ 3 genJets selection starts to bring out some features especially in the high $\not{H}_{\mathrm{T}}$ region. Here the selection criteria have been applied to genJets in order to make it clear that this deviation arises from simply looking at a population subset, and not because the cuts are not predicted well by the genJet smeared quantities. Figure B.0.2 shows an even larger distortion—now even in the rather robust H_{T} variable—when the angular cuts $\Delta\phi_i \equiv \Delta\phi\left(\not{H}_{\mathrm{T}}, \text{jet } i\right)$ are applied on the smeared and fully simulated events. These cuts strongly probe jet-jet correlations, and although not very large in magnitude, there is clearly a bias in the prediction. Given that the high end of the H_{T} distribution is under-predicted in the $\Delta\phi_{1\text{-}2} \geq 0.5, \Delta\phi_3 \geq 0.3$ region, and yet the $\not{H}_{\mathrm{T}}$ distribution is over-predicted at high $\not{H}_{\mathrm{T}}$ for the same selection, it can also be inferred that there is some cancellation of the full size of the $\not{H}_{\mathrm{T}}$ bias by the depletion of high H_{T} events. This is a first hint of the many ***compensating biases*** that can be induced in predictions involving $\not{H}_{\mathrm{T}}$ and other vector-based variables. These compensations are rarely conceptually satisfactory because it is not easy to tell what their individual sizes are and to prove that they remain canceled out in reality.

The particular bias above is known to be due to the genJet definition. genJets are traditionally defined simply by clustering particles from the event generation (after

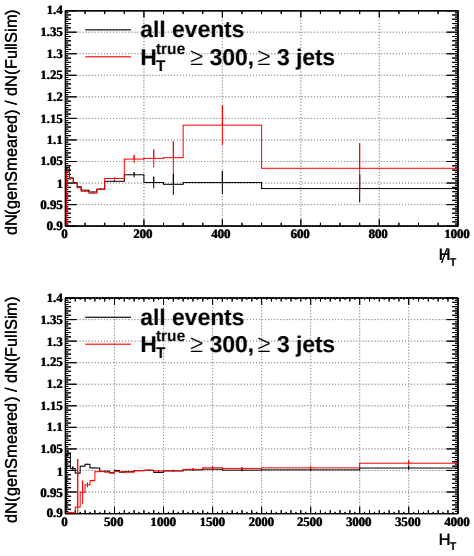

Figure B.0.1: Ratio of (standalone-)genJet smeared over fully simulated MC distributions, for all events in black and for those with $H_{\mathrm{T}}^{\mathrm{true}} \geq 300\,\mathrm{GeV}/c$ and ≥ 3 genJets ($p_{\mathrm{T}} \geq 50\,\mathrm{GeV}/c, |\eta| < 2.5$) in red.

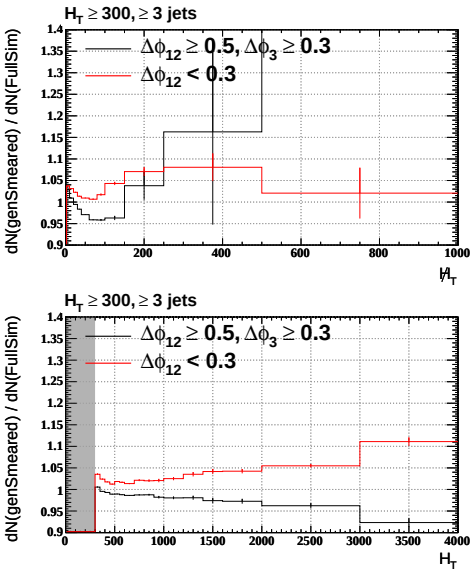

Figure B.0.2: Ratio of (standalone-)genJet smeared over fully simulated MC distributions, for events with $H_{\mathrm{T}} \geq 300\,\mathrm{GeV}/c$, ≥ 3 jets, and $\Delta\phi$ cuts as indicated in the legends. The gray shaded area is where the denominator vanishes. The out-of-scale last bin in the $\not{H}_{\mathrm{T}}$ ratio plot has value 2.7 ± 1.2.

hadronization, but before interaction with the detector) with the same jet reconstruction algorithm as used for recoJets. However this means that such "standalone" genJets are completely blind to systematic biases in the recoJet directions due to features of the detector, proximity to other radiation, and so forth. Deviations in the recoJet vs. genJet angular locations are also not possible to model with the smearing method used here, which is just to scale the magnitude of the jet momenta by a random response. It is possible to extend this to also smear the jet directions, but this does also cannot induce systematically biased directions without using some knowledge of the event topology.

An alternative definition are the ***reco-defined (redefined) genJets***: For a given recoJet, a 1-1 correspondent genJet is defined by collecting all stable genParticles that fall within the recoJet area. Since the anti-k_T algorithm with size parameter 0.5 is used to cluster jets in this study, this includes all genParticles whose momentum falls within a $\Delta R < 0.55$ cone with respect to the recoJet axis. Whenever there is an ambiguity as to which (overlapping) jets to assign a genParticle to, the jet with a reconstructed constituent closest to the genParticle is chosen. Furthermore, the η and ϕ direction of the redefined genJet is fixed to be the same as that of the recoJet, i.e. only the p_T information is taken from the vector sum of genParticles. This may seem like a somewhat artificial prescription, but is in fact a practical one, because the most natural data-driven estimate of particle jet momenta would be the recoJets themselves. It is neither necessary nor completely well-defined to try to go all the way back to some unmeasurable collection of "true particle jets", only to have to modify them in some complex way in order to predict reconstructed jets that can be different in magnitude, direction, as well as multiplicity. Instead the idea is to start from only those particles that contribute energy to a clustered recoJet, and just model the calorimeter response of this fixed set of particles.

Figures B.0.3 and B.0.4 are the same series of closure plots as previously, except now using redefined genJets everywhere in the jet resolution derivation and smearing procedures. The H_T distributions are now well predicted at least in the $H_T \geq 300\,\text{GeV}/c$ region[1], and with the removal of the previously compensating H_T bias, the bias in the $\not{H}_T$ distribution is now more obvious.

The last clue is that even though the non-correspondence of genJets vs. recoJets has been mitigated by the use of redefined genJets, this does not remove the problem that e.g. a for a fixed $p_T^{\text{gen}} = 200\,\text{GeV}/c$, whether the jet is the third jet in a high H_T event or the first jet in a lower H_T event makes a difference to its resolution. This environment dependence can however be handled by parametrizing the jet resolution by proximity in ΔR to the nearest other jet of $p_T^{\text{gen}} \geq 10\,\text{GeV}/c$. This leads to Figures B.0.5 and B.0.6, where it is seen that most of the biases have been reduced to a 5% or better level. Due to constraints on the available data resolution measurements, which were all performed with the traditional use of standalone genJets, this parametrization cannot actually be

[1] Recall that these simulated QCD samples start with $\hat{p}_T \geq 170\,\text{GeV}/c$, which roughly corresponds to $H_T^{\text{true}} \gtrsim 2 \times 170\,\text{GeV}/c = 340\,\text{GeV}/c$. So the deviation seen in the region below this in Figure B.0.3 is some kind of leakage below the approximate H_T cut.

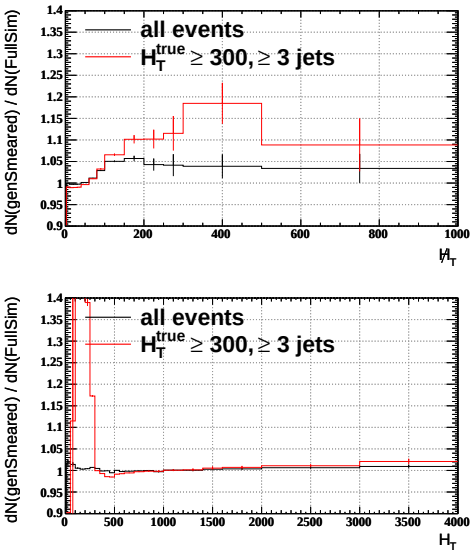

Figure B.0.3: Ratio of redefined genJet smeared over fully simulated MC distributions, for all events in black and for those with $H_{\mathrm{T}}^{\mathrm{true}} \geq 300\,\mathrm{GeV}/c$ and ≥ 3 genJets ($p_{\mathrm{T}} \geq 50\,\mathrm{GeV}/c, |\eta| < 2.5$) in red.

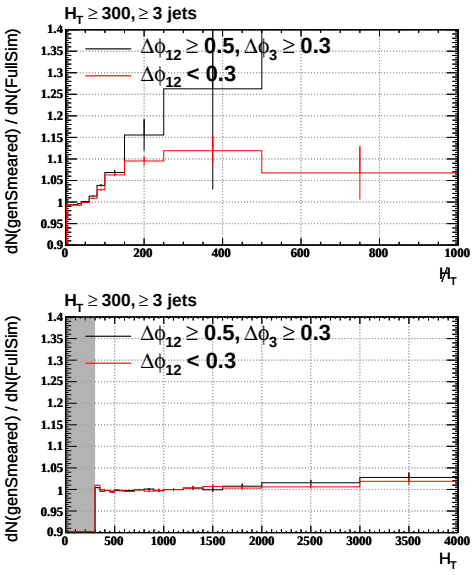

Figure B.0.4: Ratio of redefined genJet smeared over fully simulated MC distributions, for events with $H_{\mathrm{T}} \geq 300\,\mathrm{GeV}/c$, ≥ 3 jets, and $\Delta\phi$ cuts as indicated in the legends. The gray shaded area is where the denominator vanishes. The out-of-scale last bin in the $\not{H}_{\mathrm{T}}$ ratio plot has value 2.8 ± 1.2.

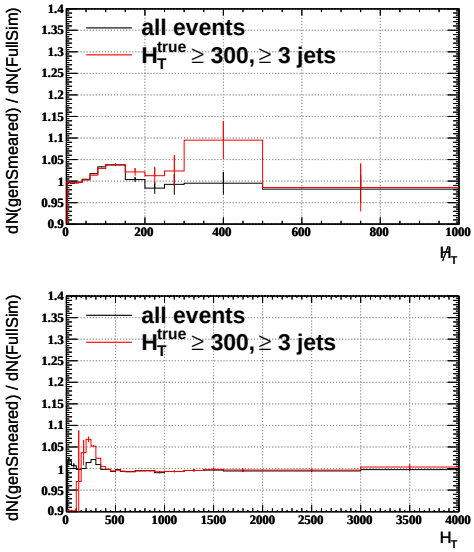

Figure B.0.5: Ratio of redefined genJet smeared over fully simulated MC distributions, for all events in black and for those with $H_{\mathrm{T}}^{\mathrm{true}} \geq 300\,\mathrm{GeV}/c$ and ≥ 3 genJets ($p_{\mathrm{T}} \geq 50\,\mathrm{GeV}/c, |\eta| < 2.5$) in red. Here the jet resolution is parametrized by ΔR to the nearest other jet.

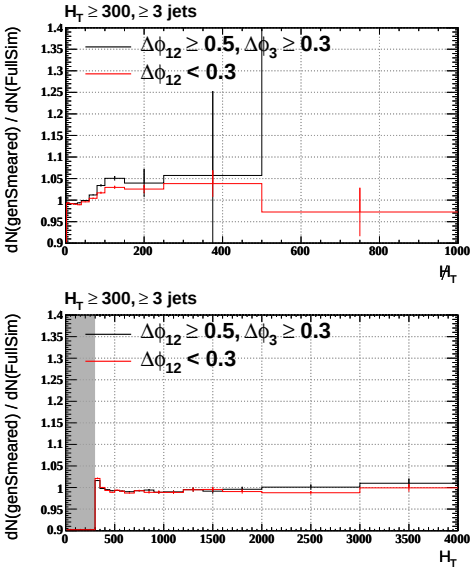

Figure B.0.6: Ratio of redefined genJet smeared over fully simulated MC distributions, for events with $H_{\mathrm{T}} \geq 300\,\mathrm{GeV}/c$, ≥ 3 jets, and $\Delta\phi$ cuts as indicated in the legends. Here the jet resolution is parametrized by ΔR to the nearest other jet. The gray shaded area is where the denominator vanishes. The out-of-scale last bin in the $\not{H}_{\mathrm{T}}$ ratio plot has value 2.7 ± 1.2.

used in the R+S measurement. This induces a lack of closure in the prediction that has to be taken as a bias and systematic uncertainty in the results of Section 7.2.5. The full bias according to Figure B.0.4, i.e. without the H_{T} bias cancellation, is conservatively taken for this purpose.

Appendix C

Interpretation of Asymmetry Tail Scaling Factors

The measurement [11] provides the scale factors $\mathrm{SF}^{A}_{1.5\text{-}2.5}$ and $\mathrm{SF}^{A}_{\geq 2.5}$ by which the regions $1.5\sigma_A < A < 2.5\sigma_A$ and $\geq 2.5\sigma_A$ in the asymmetry distribution $A \equiv (p_{\mathrm{T},1} - p_{\mathrm{T},2})/(p_{\mathrm{T},1} + p_{\mathrm{T},2})$ for MC simulation QCD events should be scaled in order to match observations in data, with σ_A being the width of the simulated asymmetry distribution. However this has an ambiguous interpretation in terms of scale factors for the jet resolution resolution distribution, because an infinite number of variations of the resolution shape can produce the same variation in the asymmetry distribution. In order to convert this to a usable correction to and uncertainty band for the resolution distribution, a simplifying assumption was made i.e. that a $\mathrm{SF}^{A} > 1$ observation should only be explained by a $\mathrm{SF}^{r} > 1$ scale factor for some region in the resolution shape, and similarly for a $\mathrm{SF}^{A} < 1$ observation. The task is then to identify which part of the resolution distribution these SF^{r} should be applied to, and what the allowed ranges of SF^{r} values are.

Since the SF^{A} measurements correspond to extrapolations to perfect di-jet events, a toy simulation of such events are created by drawing a random "$\hat{\mathrm{p}}_{\mathrm{T}}$" from the distribution $p^{\mathrm{gen}}_{\mathrm{T},1}$ of transverse momentum of the leading genJet in actual QCD events (as predicted by the simulation), here referred to as $p^{\mathrm{ave}}_{\mathrm{T}}$. Each toy di-jet event then has two perfectly back-to-back jets with genJet-level momenta equal to this simulated $\hat{\mathrm{p}}_{\mathrm{T}}$, and are smeared to simulate their "reconstructed" momenta using random numbers drawn from the resolution distribution in the appropriate η and $p^{\mathrm{ave}}_{\mathrm{T}}$ bins. Since the η is arbitrary, each toy event is actually re-used for all of the η bins that the SF^{A} measurements are available in. Figure C.0.1 shows an example of the distribution of responses for the toy jet with the worst mismeasurement $|p^{\mathrm{reco}}_{\mathrm{T}} - p^{\mathrm{gen}}_{\mathrm{T}}|$ in each of these toy di-jet events. For $A \geq 1.5\sigma_A$ there are clearly two populations in the low (response < 1) and high (response > 1) tail regions, both of which contribute to the same asymmetry window; this is true for all other $p^{\mathrm{ave}}_{\mathrm{T}}$ and η bins. In real di-jet events this structure is somewhat smeared out due to the possibility of the third jet in the event being responsible for

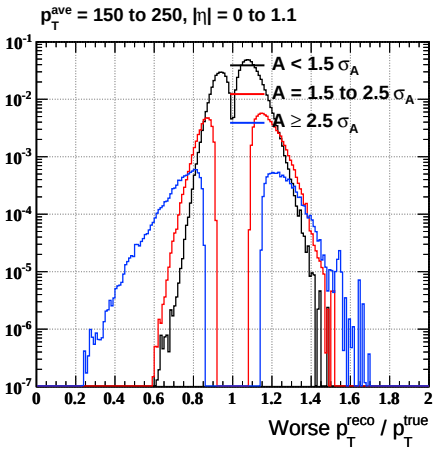

Figure C.0.1: Resolution of the most mismeasured jet in toy di-jet events, binned by the region of the asymmetry that they contribute to.

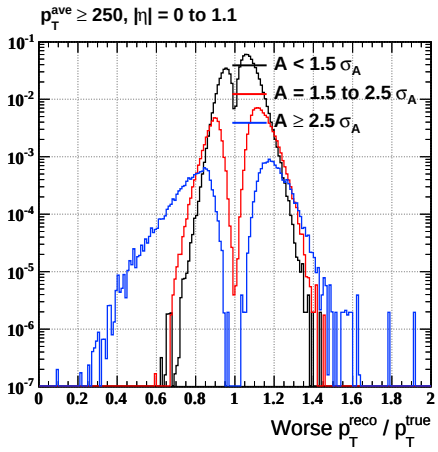

Figure C.0.2: Resolution of the most mismeasured jet in real di-jet events with $p_{\mathrm{T},3} < 5\% \times p_{\mathrm{T}}^{\mathrm{ave}}$, binned by the region of the asymmetry that they contribute to.

some amount of the asymmetry, e.g. Figure C.0.2. However the structure remains very comparable, and the four populations are identified as $\rho^{r<1}_{A=1.5\text{-}2.5}$ and $\rho^{r>1}_{A=1.5\text{-}2.5}$ for the lower asymmetry window and $\rho^{r<1}_{A\geq 2.5}$ and $\rho^{r>1}_{A\geq 2.5}$ for the upper window respectively. The high tail is a bit more prominent than expected from considering the shape of the jet resolution, which is broader towards low rather than high responses. This is an artifact of the $p_{\mathrm{T}}^{\mathrm{ave}}$ binning effect, i.e. if one or more jets fluctuate upwards in response, the event enters into a higher $p_{\mathrm{T}}^{\mathrm{ave}}$ bin, and there are more of these due to the falling spectrum than vice versa.

The rest of the procedure is to scale the ρ^r_A populations in such a way that the total scaling of the $\rho^{r<1}_{A=1.5\text{-}2.5} + \rho^{r>1}_{A=1.5\text{-}2.5}$ populations is equal to that of the asymmetry scale factor $\mathrm{SF}^A_{1.5\text{-}2.5}$, and similarly for the other asymmetry window. For example, if only $\rho^{r<1}_{A=1.5\text{-}2.5}$ is scaled, then it must account for the full increase by $\mathrm{SF}^A_{1.5\text{-}2.5}$, whereas if $\rho^{r>1}_{A=1.5\text{-}2.5}$ is also scaled, the scaling of each individual piece would be smaller. The ratio of the modified resolution shapes are then taken over the original shape, resulting in the transformation maps shown in Figure C.0.3. The black lines in these plots are what would be obtained by scaling both halves of the resolution by an equal factor to account for the asymmetry scale factors, and are taken as the nominal interpretation. The green lines correspond to the same scaling but now to account for $\mathrm{SF}^A \pm \delta\mathrm{SF}^A$, where $\delta\mathrm{SF}^A$ are the systematic uncertainties on the scale factors; they therefore form a 1σ uncertainty band for the nominal scaling if this method of equal scaling is assumed. However it is also possible to scale only the lower tails or only the upper tails, the $\pm 1\sigma$ bands of which are represented by the red and blue lines respectively. For reference, the

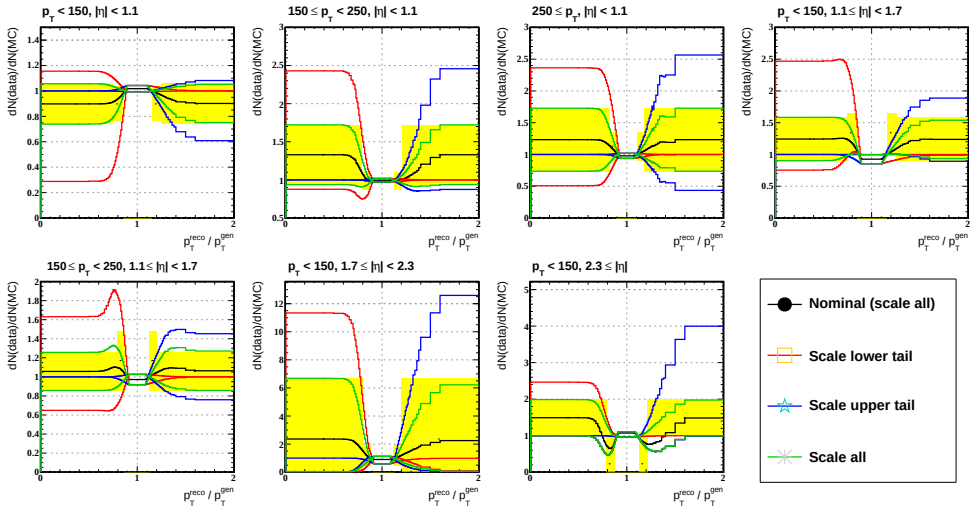

Figure C.0.3: Ratios of scaled over original resolution shapes, for various options in which sides of the resolution shape to scale in order to account for a particular asymmetry window scale factor.

yellow shaded areas show the bands that would have been obtained by naively scaling square windows $1.5\sigma_r < |r| < 2.5\sigma_r$ and $|r| \geq 2.5\sigma_r$ in the resolution by the same scale factors $\mathrm{SF}^{A}_{1.5\text{-}2.5}$ and $\mathrm{SF}^{A}_{\geq 2.5}$ as for the asymmetry distribution, where $\sigma_r = \sqrt{2}\sigma_A$ is the equivalent width in the response distribution for a given asymmetry distribution width.

To evaluate the R+S uncertainty band, the maximum envelope induced by all these variations (green, red, and blue) is taken. This gives a differential scale factor which can then applied to MC truth resolutions in the various bins as explained in Section 7.3.2. The scale factor is assumed to be universal i.e. no dependence on the parametrization bins have been accounted for.

Appendix D

Masked ECAL Locations and the $f^{\mathrm{ECAL}}_{\mathrm{masked}}$ Parameterization

Figure D.0.1 shows the η-ϕ locations of ECAL channels that have been masked. The list of masked channels in the actual detector varies by about 10% depending on the particular period of data taking. In contrast the currently used MC samples have been generated with a fixed set of masked channels; the Figure here corresponds to parameters stored in the global tag START38_V12, and is the same for all MC samples listed in Section A.2 (ranging from global tags START38_V10 to START38_V14). Since the distribution of particles within a jet falls off strongly w.r.t. the axis of the jet, if its axis was to coincide with the center of one such block of bad channels, it would have a much higher tendency to lose a significant amount of energy. One might thus imagine parametrizing the jet resolution by distance (typically ΔR) from the jet axis to the center of the nearest bad ECAL block. However a much stronger correspondence is given by a first-principles calculation of the average expected energy loss for the distribution of particles comprising a "typical" jet, as described below. This parametrizations has the desirable benefit of removing most of the residual dependence on the size of the masked region, that the ΔR-to-center parametrizations instead suffers from.

In the CMS jet reconstruction algorithms, the momentum of a jet is defined as the vectorial sum of 4-momenta of its constituents, with spatial component $\vec{p}_{\mathrm{jet}} \equiv \sum_i \vec{p}_i$. One may imagine modeling it instead as a continuous distribution of energy, i.e. $\vec{p}_{\mathrm{jet}} \sim \int \sin\theta \, d\theta \, d\phi \, \rho(\theta,\phi)\, \hat{r}$ where r, θ, ϕ are the usual spherical coordinates and ρ a momentum density function; here all particles are assumed to be emitted radially outwards from the origin. Since only the transverse momentum is invariant under any boosts along z that the event may be produced with, it is more convenient to work in terms of the transverse momentum density $\rho_{\mathrm{T}}(\theta,\phi) \equiv (\sin\theta) \times \rho(\theta, phi)$. Furthermore, the average distribution of particles in QCD jets is circularly symmetric about the jet axis $(\eta_{\mathrm{jet}}, \phi_{\mathrm{jet}})$ in η-ϕ space, where $\eta \equiv$ -$\ln\tan(\theta/2)$ is the so-called pseudorapidity. Transforming to η has the important feature that in this coordinate system the distribution of particles about the jet axis is again z-boost invariant. This allows the use of a generic

$\rho_{\mathrm{T}}(\eta\text{-}\eta_{\mathrm{jet}}, \phi\text{-}\phi_{\mathrm{jet}})$ "template" that is invariant under translations in η_{jet} and ϕ_{jet}. This template should in principle be jet-p_{T} dependent, but this is not so important to model. Figure D.0.2 shows the template used in this study, which is technically created by filling a 2D histogram of $\Delta\phi \equiv \phi\text{-}\phi_{\mathrm{jet}}$ vs. $\Delta\eta \equiv \eta\text{-}\eta_{\mathrm{jet}}$ distances of each constituent of $p_{\mathrm{T}}^{\mathrm{gen}} \geq 200\,\mathrm{GeV}/c$ jets in a QCD Monte Carlo sample. Each entry is weighted by the p_{T}-fraction carried by the constituent, where the fraction is used so as to be less jet-p_{T} dependent. The reconstructed jet constituents have been used in order to account for the asymmetry induced by the CMS magnetic field, which sweeps particles out in ϕ. Also, since the effect of interest is to model the loss of electromagnetic energy, only electrons and photons have been included in the list of jet constituents.

Given all of the above, and after the θ to η coordinate transformation, the momentum flux of such an "average jet" out of an area $\mathscr{A}$ in η-ϕ space is:

$$\begin{aligned}\vec{p}_{\mathscr{A}} \;=\; & \int_{\mathscr{A}} \cosh^{-1}\eta \, d\eta \, d\phi \, \rho_{\mathrm{T}}(\eta\text{-}\eta_{\mathrm{jet}}, \phi\text{-}\phi_{\mathrm{jet}}) \\ & \times \left[\hat{x}\cosh^{-1}\eta\,\cos\phi + \hat{y}\cosh^{-1}\eta\,\sin\phi + \hat{z}\tanh\eta\right]\end{aligned}$$

Denoting the integration over all space as $\vec{p}_{\infty}$, and the integration over only regions of masked calorimetry as $\vec{p}_{\mathrm{masked}}^{\mathrm{ECAL}}$, this leads to defining the effective masked ECAL fraction as $f_{\mathrm{masked}}^{\mathrm{ECAL}} \equiv |\vec{p}_{\mathrm{masked}}^{\mathrm{ECAL}}|_{\mathrm{T}}/|\vec{p}_{\infty}|_{\mathrm{T}}$, a.k.a. the average fraction of lost transverse momentum. Here $|\cdot|_{\mathrm{T}}$ denotes the magnitude of the given vector in the transverse plane. Monte Carlo integration techniques are used to evaluate $\vec{p}_{\mathrm{masked}}^{\mathrm{ECAL}}$, in particular so that the footprint of each masked ECAL tower in η-ϕ space can be accounted for in the area of integration. Figure D.0.3 show the values of $f_{\mathrm{masked}}^{\mathrm{ECAL}}$ as a function of η and ϕ, in regions corresponding to various binned ranges as listed in Section 7.3.2.

In a completely analogous way, the Gaussian jet profile probability function can be used to compute the weighted fraction of bad ECAL channels that have a particular status code value. The population with highest such fraction at a particular η-ϕ location of interest is defined to be "The" ECAL status code for that location. This map is shown in Figure D.0.4. Figure D.0.4 gives an example of how successfully the $f_{\mathrm{masked}}^{\mathrm{ECAL}}$ parametrizations follows the contours of the actual average MC jet response (50% quantile); similar agreement is seen for other quantiles of the jet resolution distribution. Figures D.0.5 and D.0.6 compare the ΔR parametrizations and $f_{\mathrm{masked}}^{\mathrm{ECAL}}$; the correlation with jets of lower response is clearly more linear for the $f_{\mathrm{masked}}^{\mathrm{ECAL}}$ parametrizations.

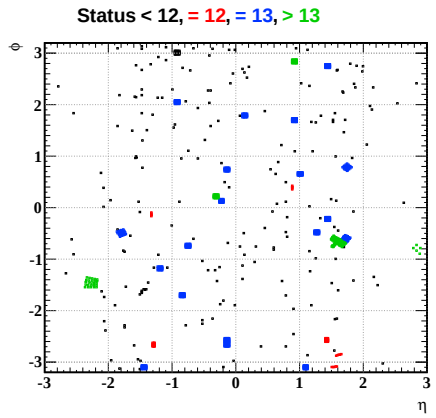

Figure D.0.1: η-ϕ locations of masked (i.e. status > 0) ECAL channels. Channels of various statuses are shown in colors stated in the title.

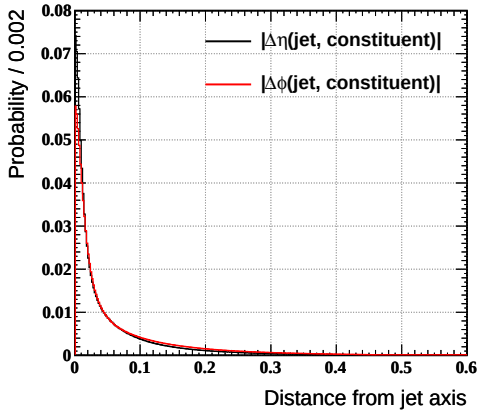

Figure D.0.2: 1-dimensional projections of the average transverse momentum distribution $\rho_{\mathrm{T}}(\eta - \eta_{\mathrm{jet}}, \phi - \phi_{\mathrm{jet}})$ of particles within $p_{\mathrm{T}} \geq 200\,\mathrm{GeV}/c$ reconstructed jets.

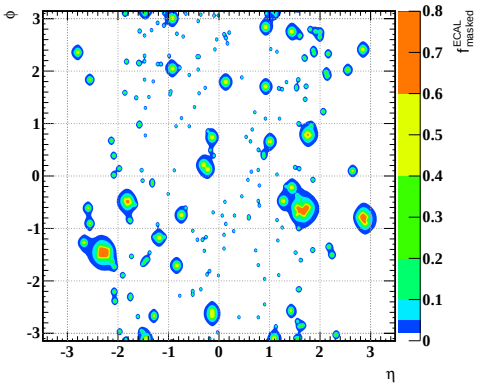

Figure D.0.3: Areas covered by various $f_{\mathrm{masked}}^{\mathrm{ECAL}}$ binning ranges, as a function of η and ϕ. The uncolored regions correspond to $f_{\mathrm{masked}}^{\mathrm{ECAL}} < 2\%$.

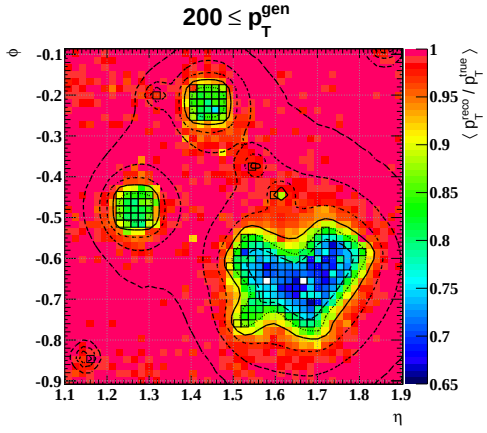

Figure D.0.4: Average response for $p_{\mathrm{T}}^{\mathrm{gen}} \geq 200\,\mathrm{GeV}/c$ jets, overlaid with contour lines indicating the various regions defined by the $f_{\mathrm{masked}}^{\mathrm{ECAL}}$ binning ranges (compare Figure D.0.3). The square boxes indicate the positions of masked ECAL channels.

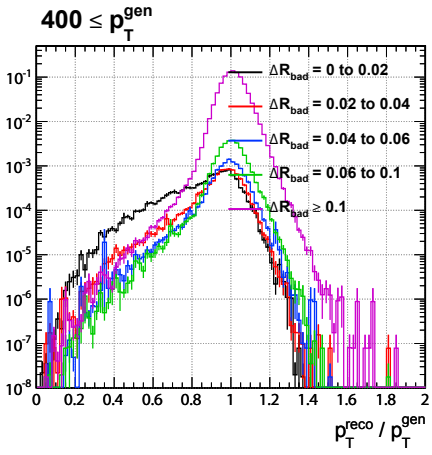

Figure D.0.5: Resolution of jets for various distances to the nearest bad ECAL block.

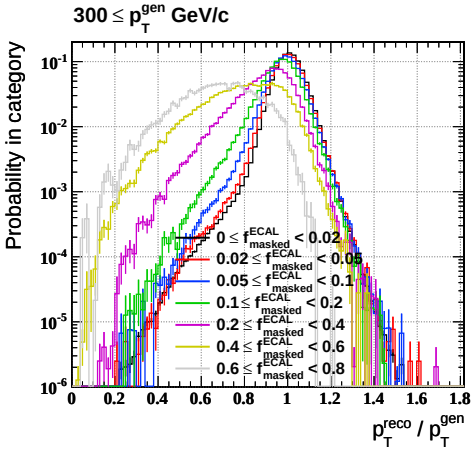

Figure D.0.6: Resolution of jets for various values of fraction of bad ECAL channels within $\Delta R < 0.1$ of the jet axis.

Appendix E

Statistical Uncertainty via Bootstrap Method

It is mentioned in Section 7.2.4 that it is insufficient to evaluate the systematic uncertainty on the R+S prediction due to the statistical uncertainty of the seed sample by naively taking the sum-of-weights in quadratures per histogram bin. The reason for this is illustrated by Figure E.0.1, which shows the contribution to some predicted variable due to a single seed event in two types of method. The left figure is the perhaps more familiar case where every input event makes a single contribution to the prediction, e.g. using an isolated muon control sample to predict a non-isolated sample by weighting the event by the isolation inefficiency. The right figure is the present case where every seed event can be used to make a spectrum of possible predictions, i.e. by smearing it more than one time. In the first case every input affects exactly one bin in the predicted histogram; in the second case the predicted bins can be correlated due to a single underlying input event. In other words, a statistical fluctuation in the seed sample may result in a shape change over a large range of the final prediction.

The bootstrap method [43] prescribes using the same data as used for the main measurement to generate an ensemble of pseudo-datasets, with which statistical properties of the prediction may be studied. That is, if there are N events in the data, then one can construct a pseudo-experiment by randomly drawing N events *with replacement* from the data (i.e. each event has a chance to be picked more than once). In such a way, 100 pseudo-experiment histograms are created for the predicted $\not{H}_{\mathrm{T}}$ and other distributions. Then the pseudo-experiment spread is computed per bin of each histogram as the quoted statistical uncertainty for that bin. The reader is however cautioned that one must not assume that this means the bins in the predicted histograms are able to fluctuate independently of each other. When evaluating the uncertainty on the number of events in the search region, e.g. $\not{H}_{\mathrm{T}} \geq 150\,\mathrm{GeV}/c$, the histograms are re-binned prior to computing the statistical uncertainty so as to properly account for the correlation between events in the entire region of interest.

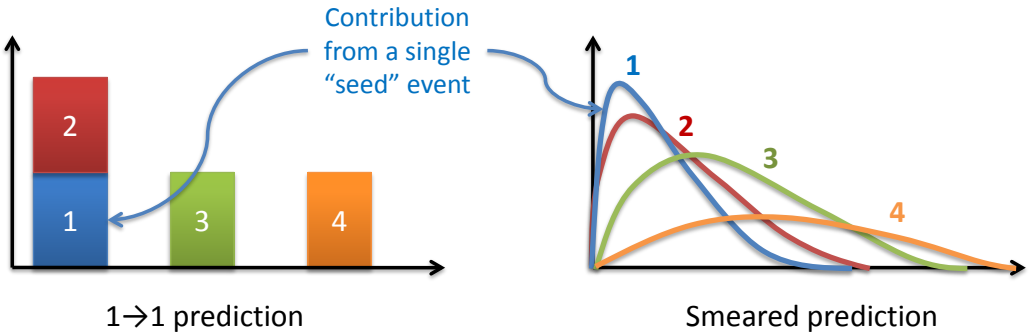

Figure E.0.1: Contribution due to a single event in (left) the case where each event makes a single prediction; and (right) the case where each event makes a smeared prediction.

Bibliography

[1] *FastJet: A Code for fast k(t) clustering, and more*, 2006. 31

[2] G. et al. Abbiendi. Precision electroweak measurements on the Z resonance. *Physics Reports*, 427(5-6):257 – 454, 2006. ISSN 0370-1573. doi: DOI:10.1016/j.physrep.2005.12.006. URL http://www.sciencedirect.com/science/article/B6TVP-4JD0GYD-1/2/6698a46ba8621d4438c39124ad678c2c. 13

[3] G. et al. Abbiendi. Measurement of the $e^+e^- \to W^+W^-$ cross section and W decay branching fractions at LEP. *Eur. Phys. J.*, C52:767–785, 2007. doi: 10.1140/epjc/s10052-007-0442-0. 13

[4] D. Acosta, G. Di Giovanni, J. Gartner, R. Remington, J. Yelton, A. Deisher, V. Gaultney, T. Micelli, and G. Williams. Beam Halo Event Identification in CMS Using the CSCs, ECAL, and HCAL. *CMS AN-2010/111*, 2010. 43

[5] S. Agostinelli, J. Allison, K. Amako, J. Apostolakis, H. Araujo, P. Arce, M. Asai, D. Axen, S. Banerjee, G. Barrand, F. Behner, L. Bellagamba, J. Boudreau, L. Broglia, A. Brunengo, H. Burkhardt, S. Chauvie, J. Chuma, R. Chytracek, and G. Cooperman. GEANT4: A simulation toolkit. *Nucl. Instrum. Meth.*, A506:250–303, 2003. doi: 10.1016/S0168-9002(03)01368-8. 55

[6] A. A. et al. Aguilar-Arevalo. Event Excess in the MiniBooNE Search for $\bar{\nu}_\mu \to \bar{\nu}_e$ Oscillations. *Phys. Rev. Lett.*, 105:181801, 2010. doi: 10.1103/PhysRevLett.105.181801. 10

[7] E. Albayrak, A. Bhatti, D. Elvira, S. Sharma, and M. Zielinski. Measurement of Full Jet Energy Resolution using Photon+Jets Events for Estimation of QCD Background to SUSY RA2 Analysis. *CERN-CMS-AN-2010/421*, 2010. 72, 89, 95

[8] N. Arkani-Hamed, A. G. Cohen, E. Katz, and A. E. Nelson. The littlest Higgs. *JHEP*, 07:034, 2002.

[9] Patrick Aurenche, Michel Fontannaz, Jean-Philippe Guillet, Eric Pilon, and Monique Werlen. A New critical study of photon production in hadronic collisions. *Phys. Rev.*, D73:094007, 2006. doi: 10.1103/PhysRevD.73.094007. 68

[10] C. Autermann, A. Bhatti, and G. Lungu. RA2 sensitivity in constrained MSSSM. *CMS AN-2011/034*, 2011.

[11] Christian Autermann, Christian Sander, Peter Schleper, Matthias Schroder, and Hartmut Stadie. Measurement of the Jet p_T Response Function in QCD Di-jet Events using an Unbinned Maximum Likelihood Method. *CERN-CMS-AN-2010/341*, 2010. 72, 89, 95, 148

[12] Marco et al. Battaglia. Proposed post-LEP benchmarks for supersymmetry. *Eur. Phys. J.*, C22:535–561, 2001. doi: 10.1007/s100520100792. 109

[13] G L et al. Bayatian. *CMS Physics Technical Design Report Volume I: Detector Performance and Software*. Technical Design Report CMS. CERN, Geneva, 2006. There is an error on cover due to a technical problem for some items. 31

[14] W. Beenakker, R. Hopker, and M. Spira. PROSPINO: A program for the PRO-duction of Supersymmetric Particles In Next-to-leading Order QCD. 1996. 138

[15] Kelly Beernaert, Steven Lowette, and Piet Verwilligen. Data-driven Prediction of the Invisible Z Background using Photons for the RA2 Inclusive Hadronic SUSY Search. *CMS AN-2010/403*, 2010. 51, 66, 68

[16] Riccardo Bellan, Mariarosaria D'Alfonso, Sue Ann Koay, Steven Lowette, Nick McColl, Elizabeth Mullin, Roberto Rossin, and Joseph Incandela. Search Optimization and Limit Setting Using Simplified Model Spectra for the RA2 Inclusive Hadronic SUSY Search. *CERN-CMS-AN-2010/404*, 2010. 86, 88, 97, 115

[17] Riccardo Bellan, Mariarosaria D'Alfonso, Sue Ann Koay, Steven Lowette, Nick McColl, Roberto Rossin, and Joseph Incandela. Data-Driven Prediction of the Hadronically Decaying Tau Background for the RA2 Inclusive Hadronic SUSY Search. *CMS AN-2010/402*, 2010. 51, 65

[18] A. et al. Belyaev. Dictionary of LHC Signatures. *Pramana*, 72:229–238, 2009. doi: 10.1007/s12043-009-0019-6. 13

[19] G. Bertone, D. Hooper, and J. Silk. Particle dark matter: evidence, candidates and constraints. *Physics Reports*, 405:279–390, January 2005. doi: 10.1016/j.physrep.2004.08.031. 9

[20] M. Bradac. Dark matter: Revealing the invisible with 2 cosmic supercolliders the 'bullet cluster' 1E0657-56 and MACSJ0025-1222. *Nucl. Phys. Proc. Suppl.*, 194: 17–21, 2009. doi: 10.1016/j.nuclphysbps.2009.07.002. 8

[21] John M. Campbell, J. W. Huston, and W. J. Stirling. Hard Interactions of Quarks and Gluons: A Primer for LHC Physics. *Rept. Prog. Phys.*, 70:89, 2007. doi: 10.1088/0034-4885/70/1/R02. 57

[22] Robert Ciesielski and Anwar Bhatti. Response function for heavy flavor jets. *CERN-CMS-AN-2010/422*, 2010. 92

[23] CMS Collaboration. Performance of Jet Algorithms in CMS. *CMS-PAS-JME-07-003*, 2007. 31

[24] CMS Collaboration. Muon Reconstruction in CMS. *CMS-PAS-MUO-08-001*, 2008. 28

[25] CMS Collaboration. Particle Flow Event Reconstruction in CMS and Performance for Jets, Taus, and MET. *CMS-PAS-PFT-09-001*, 2009. 29, 32, 33

[26] CMS Collaboration. Track reconstruction in the CMS Tracker. *CMS-PAS-TRK-09-001*, 2009. 26

[27] CMS Collaboration. Search for supersymmetry in hadronic final states using M_{T2} in the first $30\,\mathrm{pb}^{-1}$ of 7 TeV pp collision data. *CMS AN-2010/459*, 2010. 127

[28] CMS Collaboration. Electron reconstruction and identification at $\sqrt{s}$ = 7 TeV. *CMS-PAS-EGM-10-004*, 2010.

[29] CMS Collaboration. Photon reconstruction and identification at $\sqrt{s}$ = 7 TeV. *CMS-PAS-EGM-10-005*, 2010.

[30] CMS Collaboration. MET Performance in pp Collisions at $\sqrt{s}$=7 TeV. *CMS-PAS-JME-10-009*, 2010.

[31] CMS Collaboration. Jet Energy Corrections determination at $\sqrt{s}$=7 TeV. *CMS-PAS-JME-10-010*, 2010. 40

[32] CMS Collaboration. Search for new physics with same-sign di-leptons at the LHC. *CMS-PAS-SUS-10-004*, 2010. 127

[33] CMS Collaboration. Search for new physics with the jets and missing momentum signature. *CMS-PAS-SUS-10-005*, 2010. 127

[34] CMS Collaboration. Search for new physics with single-leptons at the LHC. *CMS-PAS-SUS-10-006*, 2010. 127

[35] CMS Collaboration. A Search for New Physics using Events with b-tagged Jets and Missing Energy in pp collisions at 7 TeV. *CMS-PAS-SUS-10-012*, 2010. 127

[36] CMS Collaboration. Search for supersymmetry in events with a Z boson and missing energy. *CERN-CMS-PAS-SUS-11-012*, 2010.

[37] CMS Collaboration. Measurement of the Differential Isolated Prompt Photon Production Cross Section in pp Collisions at $\sqrt{s}$ = 7TeV. *CMS-PAS-QCD-10-037, in preparation*, 2011. 68

[38] CMS Collaboration. A Search for New Physics in b-tagged dijet and multi-jet events with Missing Energy in pp collisions at 7 TeV. *CMS-PAS-SUS-10-011, in preparation*, 2011. 127

[39] G. Corcella, I.G. Knowles, G. Marchesini, S. Moretti, K. Odagiri, P. Richardson, M.H. Seymour, and B.R. Webber. HERWIG 6.5: an event generator for Hadron Emission Reactions With Interfering Gluons (including supersymmetric processes). *JHEP*, 01:010, 2001. 53, 54

[40] Joao Barreiro Guimaraes et al. da Costa. Search for squarks and gluinos using final states with jets and missing transverse momentum with the ATLAS detector in $\sqrt{s} = 7$ TeV proton-proton collisions. 2011. 111

[41] G. D'Agostini. Asymmetric Uncertainties: Sources, Treatment and Potential Dangers. *arXiv:physics/0403086*, 2004. 105

[42] AseshKrishna Datta, Gordon L. Kane, and Manuel Toharia. Is it SUSY? *arXiv:hep-ph/0510204v1*, 2005. 120

[43] B. Efron. *The Jackknife, The Bootstrap and Other Resampling Plans*, volume 38 of *CBMS-NSF Regional Conference Series in Applied Mathematics*. SIAM, Philadelphia, 1982. 155

[44] Daniele Alves et al. Simplified Models for LHC New Physics Searches. 2011. 115

[45] Thomas Speer et al. Algorithms for b jet identification in cms. *CERN-CMS-AN-2009-085*, 2009. 74

[46] Katherine Freese, Brian Fields, and David Graff. Death of stellar baryonic dark matter. 2000. 9

[47] F. Gianotti. Physics at the LHC. *Phys. Rept.*, 403:379–399, 2004. doi: 10.1016/j.physrep.2004.08.027.

[48] Kim Griest and Marc Kamionkowski. Unitarity Limits on the Mass and Radius of Dark Matter Particles. *Phys. Rev. Lett.*, 64:615, 1990. doi: 10.1103/PhysRevLett.64.615. 9

[49] LHC New Phyics Working Group. Signatures of New Physics at the LHC, 2010. URL http://www.lhcnewphysics.org/. 60

[50] The CMS SUSY RA2 group. Inclusive search for SUSY at CMS with the jets plus missing momentum signature. *CERN-CMS-AN-2010/260*, 2010. 78, 79, 85, 92, 93

[51] Christopher T. Hill and Elizabeth H. Simmons. Strong dynamics and electroweak symmetry breaking. *Phys. Rept.*, 381:235–402, 2003. doi: 10.1016/S0370-1573(03)00140-6.

[52] Jay Hubisz and Patrick Meade. Phenomenology of the littlest Higgs with T-parity. *Phys. Rev.*, D71:035016, 2005. doi: 10.1103/PhysRevD.71.035016. 12

[53] F. James and M. Roos. Minuit: A system for function minimization and analysis of the parameter errors and correlations. *Comput. Phys. Commun.*, 10:343–367, 1975. doi: 10.1016/0010-4655(75)90039-9. 80

[54] N. et al. Jarosik. Seven-Year Wilkinson Microwave Anisotropy Probe (WMAP) Observations: Sky Maps, Systematic Errors, and Basic Results. *Astrophys. J. Suppl.*, 192:14, 2011. doi: 10.1088/0067-0049/192/2/14. 8

[55] Thomas Junk. Confidence Level Computation for Combining Searches with Small Statistics. *Nucl. Instrum. Meth.*, A434:435–443, 1999. doi: 10.1016/S0168-9002(99)00498-2. 107

[56] Vardan et al. Khachatryan. Search for Supersymmetry in pp Collisions at 7 TeV in Events with Jets and Missing Transverse Energy. *Phys. Lett.*, B698:196–218, 2011. doi: 10.1016/j.physletb.2011.03.021. 112

[57] N. V. Krasnikov and S. I. Bityukov. Incorporating systematics and statistical uncertainties into exclusion limits. Prepared for PHYSTAT2003: Statistical Problems in Particle Physics, Astrophysics, and Cosmology, Menlo Park, California, 8-11 Sep 2003.

[58] Hongxuan Liu, Kenichi Hatakeyama, Ulla Gebbert, Konstantinos Theofilatos, and Will Flanagan. Studies on ECAL Dead and Masked Channel Contributions to High MET and MHT. *CMS AN-2010/354*, 2010. 47

[59] Michael Loewenstein and Alexander Kusenko. Dark Matter Search Using Chandra Observations of Willman 1, and a Spectral Feature Consistent with a Decay Line of a 5 keV Sterile Neutrino. *Astrophys. J.*, 714:652–662, 2010. doi: 10.1088/0004-637X/714/1/652.

[60] C. Macesanu, C. D. McMullen, and S. Nandi. Collider implications of universal extra dimensions. *Phys. Rev.*, D66:015009, 2002. doi: 10.1103/PhysRevD.66.015009.

[61] Fabio Maltoni and Tim Stelzer. MadEvent: Automatic event generation with MadGraph. *JHEP*, 02:027, 2003. 58

[62] Michelangelo L. Mangano, Mauro Moretti, Fulvio Piccinini, Roberto Pittau, and Antonio D. Polosa. ALPGEN, a generator for hard multiparton processes in hadronic collisions. *JHEP*, 07:001, 2003. 58

[63] Stephen P. Martin. A Supersymmetry Primer. 1997. 11

[64] Richard Massey, Thomas Kitching, and Daisuke Nagai. Cluster Bulleticity. 2010. 8

[65] Barbara Mele. Top quark rare decays in the standard model and beyond. 1999. 13

[66] K. et al. Nakamura. Review of particle physics. *J. Phys.*, G37:075021, 2010. doi: 10.1088/0954-3899/37/7A/075021. 79

[67] Mihoko M. Nojiri, Yasuhiro Shimizu, Shogo Okada, and Kiyotomo Kawagoe. Inclusive transverse mass analysis for squark and gluino mass determination. *JHEP*, 06:035, 2008. doi: 10.1088/1126-6708/2008/06/035. 37

[68] Troy A. Porter, Robert P. Johnson, and Peter W. Graham. Dark Matter Searches with Astroparticle Data. 2011.

[69] William H. Press, Saul A. Teukolsky, William T. Vetterling, and Brian P. Flannery. *Numerical Recipes: The Art of Scientific Computing, Third Edition (2007)*. Cambridge University Press. ISBN-13: 978-0521880688. 52

[70] Giovanni Punzi. Incorporating Systematics in Limits. July 2003. URL http://www-cdf.fnal.gov/physics/statistics/notes/Syst_in_limits_report.pdf. 103

[71] Giovanni Punzi. Sensitivity of searches for new signals and its optimization. *arXiv:physics/0308063*, 2003. 109

[72] Lisa Randall and David Tucker-Smith. Dijet Searches for Supersymmetry at the LHC. *Phys. Rev. Lett.*, 101:221803, 2008. doi: 10.1103/PhysRevLett.101.221803. 112

[73] Alexander L. Read. Presentation of search results: The CL(s) technique. *J. Phys.*, G28:2693–2704, 2002. doi: 10.1088/0954-3899/28/10/313. 107

[74] M. Reuter and H. Weyer. Running Newton constant, improved gravitational actions, and galaxy rotation curves. *Phys. Rev.*, D70:124028, 2004. doi: 10.1103/PhysRevD.70.124028. 8

[75] Thomas G. Rizzo. Probes of universal extra dimensions at colliders. *Phys. Rev.*, D64:095010, 2001. doi: 10.1103/PhysRevD.64.095010. 12

[76] Christopher Rogan. Kinematical variables towards new dynamics at the LHC. 2010. 37

[77] L. J. Rosenberg and K. A. van Bibber. Searches for invisible axions. *Phys. Rept.*, 325:1–39, 2000. doi: 10.1016/S0370-1573(99)00045-9. 10

[78] Mathieu Rubin, Gavin P. Salam, and Sebastian Sapeta. Giant QCD K-factors beyond NLO. *JHEP*, 09:084, 2010. doi: 10.1007/JHEP09(2010)084. 58, 59

[79] Gavin P. Salam. Towards Jetography. *Eur. Phys. J.*, C67:637–686, 2010. doi: 10.1140/epjc/s10052-010-1314-6. 31, 40, 41

[80] M. Sani, S. Simon, M. Pieri, J. Branson, E. Sudano, C. Palmer, and A. Holzner. Photon Efficiency Measurements using Tag and Probe. *CMS AN-2010/292*, 2010. 68

[81] Pekka K. Sinervo. Signal significance in particle physics. *CDF/PUB/STATISTICS/PUBLIC/6031*, 2002. 101

[82] Torbjorn Sjostrand, Stephen Mrenna, and Peter Z. Skands. PYTHIA 6.4 Physics and Manual. *JHEP*, 05:026, 2006. doi: 10.1088/1126-6708/2006/05/026. 14, 52, 53, 54

[83] M. Srednicki. *Quantum field theory*. Cambridge, UK: Univ. Pr., 2007. 3, 53

[84] Gerard 't Hooft and M. J. G. Veltman. DIAGRAMMAR. *NATO Adv. Study Inst. Ser. B Phys.*, 4:177–322, 1974. 4

[85] Jan Thomsen, Jula Draeger, Christian Autermann, Christian Sander, and Peter Schleper. W and ttbar background estimation for all-hadronic searches for new physics. *CMS AN-2010/203*, 2010. 51, 63, 65

[86] N. Toro. Private communication. 108

[87] Erik P. Verlinde. On the Origin of Gravity and the Laws of Newton. *JHEP*, 04: 029, 2011. doi: 10.1007/JHEP04(2011)029. 8

[88] Mikko Voutilainen, Francesco Pandolfi, Daniele del Re, Sinjini Sengupta, Ricardo Eusebi, Mithat Kaya, Ozlem Kaya, and Philipp Schieferdecker. Absolute jet energy correction uncertainty. *CMS AN-2010/304*, 2010. 40

[89] L. Wehrli, A. Rizzi, C. Graband, L. Sala, M. Baarmand, B. Dorney, S. de Visscher, and P. Otyugova. Measurement of $B\bar{B}$ Angular Correlations Based on Secondary Vertex Reconstruction in CMS. *CERN-CMS-AN-2010/347*, 2010. 92